

Peng Zhao *Editor*

Magnetic Levitation

Innovation of Density-Based
Applications

 Springer

Magnetic Levitation


Peng Zhao
Editor

Magnetic Levitation

Innovation of Density-Based Applications

 Springer

Editor

Peng Zhao 

School of Mechanical Engineering

Zhejiang University

Hangzhou, Zhejiang, China

ISBN 978-981-99-8313-1

ISBN 978-981-99-8314-8 (eBook)

<https://doi.org/10.1007/978-981-99-8314-8>

© The Editor(s) (if applicable) and The Author(s), under exclusive license to Springer Nature Singapore Pte Ltd. 2024

This work is subject to copyright. All rights are solely and exclusively licensed by the Publisher, whether the whole or part of the material is concerned, specifically the rights of translation, reprinting, reuse of illustrations, recitation, broadcasting, reproduction on microfilms or in any other physical way, and transmission or information storage and retrieval, electronic adaptation, computer software, or by similar or dissimilar methodology now known or hereafter developed.

The use of general descriptive names, registered names, trademarks, service marks, etc. in this publication does not imply, even in the absence of a specific statement, that such names are exempt from the relevant protective laws and regulations and therefore free for general use.

The publisher, the authors, and the editors are safe to assume that the advice and information in this book are believed to be true and accurate at the date of publication. Neither the publisher nor the authors or the editors give a warranty, expressed or implied, with respect to the material contained herein or for any errors or omissions that may have been made. The publisher remains neutral with regard to jurisdictional claims in published maps and institutional affiliations.

This Springer imprint is published by the registered company Springer Nature Singapore Pte Ltd.

The registered company address is: 152 Beach Road, #21-01/04 Gateway East, Singapore 189721, Singapore

Paper in this product is recyclable.

Preface

Magneto-Archimedes Levitation (MagLev) has gained its spotlights in the accurate, sensitive, and untethered testing of diamagnetic and low-magnetic objects. Ever since Whitesides's research group proposed the original MagLev structure back in 2009, where the objects submerged in paramagnetic solutions levitated stably between two like-pole-facing permanent magnets, researchers have successfully applied MagLev in density measurement of various samples. As density is one of the innate characteristics of materials, magnetic levitation comes in handy in the revelation of density profiles of the testing samples, leading to further density-based analysis, characterization, and separation of different materials.

Due to the unique merits of volume-free, fast speed, low cost, and user-friendliness, magnetic levitation has also evolved over time from the limited function of density measurement. Because magnetic levitation is capable of untethered density measurement regardless of the precise volume of the object, the spectrum of measurable samples was expanded from only macroscale to microscale, where powders and droplets were successfully levitated and measured. The living materials like cells were also successfully measured and analyzed via magnetic levitation, thus broaden the application of MagLev from materials science to the field of bioengineering. Different designs, optimizations, and variations of MagLev setup were proposed, introducing more complicated distributions of magnetic forces, and complex applications such as assembly, manipulation, and separation were made possible.

In this book, we provide a comprehensive overview of the magnetic levitation, from its history and basic theories, to the multiple dimensions of its applications in different research fields. We start from a brief introduction of magnetism and magnetic materials in Chap. 1, with a slight touch of physics, to provide the background of magnetic levitation. In Chap. 2, we discuss the route of evolution of magnetic levitation and three typical types of applications. Chapter 3 is about the theories, with Maxwell's equation being the center, along with forces on magnetic materials, followed by Chap. 4, where the phenomenon of stable levitation is discussed in detail, revealing the basic principle of density-based magnetic levitation. Then

we move on to the density-based measurement applications, from the configuration of two like-pole-facing square magnets (Chap. 5), to the optimization of this classic device (Chap. 6). Then, we introduce the application cases in mechanical engineering (Chap. 7), chemistry (Chap. 8), and bioengineering (Chap. 9). Finally, in the last two chapters we expand the magnetic levitation from merely density test to other more sophisticated applications such as manipulation (Chap. 10) and separation (Chap. 11), ending on a note of unlimited potential and serving as a hint of undiscovered applications of magnetic levitation method.

This book would benefit the audience in the field of mechanical engineering, chemistry, materials science, and bioengineering, since magnetic levitation method has proved itself suitable for the density-based analysis and applications of materials of different scales. Under the collaborate efforts from researchers around the world, magnetic levitation is already a novel instrument applicable in multiple fields. The analysis in this book will help the audience deeply understand the mechanism of magnetic levitation, and it can serve as an instruction for the magnetic levitation procedure or guidebook for the magnetic levitation setup. With our viewpoints and thoughts about MagLev running through this book, we hope that this book may spark the audience's interest toward magnetic levitation method and enlighten them to further develop MagLev method.

Hangzhou, China
September 2023

Peng Zhao

Contents

1	Magnetism and Magnetic Materials	1
	Peng Zhao, Daofan Tang, Jun Xie, and Chengqian Zhang	
2	Development of Magneto-Archimedes Levitation	17
	Peng Zhao, Jun Xie, Haonan Sun, and Chengqian Zhang	
3	Magnetic Forces	33
	Chengqian Zhang, Zhezai Hu, Huangzhe Dai, and Peng Zhao	
4	Stable Levitation	47
	Chengqian Zhang, Zhezai Hu, Jun Xie, and Peng Zhao	
5	Standard MagLev Testing Method	67
	Jun Xie, Yifeng Pan, Hao Chen, and Peng Zhao	
6	Optimization of MagLev	91
	Jun Xie, Zhengchuan Guo, Chengqian Zhang, and Peng Zhao	
7	Magnetic Levitation in Mechanical Engineering	123
	Jun Xie, Ruoxiang Gao, Daofan Tang, and Peng Zhao	
8	Magnetic Levitation in Chemistry	145
	Jun Xie, Baocai Zhang, Xuemei Li, and Peng Zhao	
9	Magnetic Levitation in Medicine and Bioengineering	163
	Chenxin Lyu, Chengqian Zhang, Daofan Tang, and Peng Zhao	
10	Manipulation via MagLev	181
	Daofan Tang, Chengqian Zhang, Zhezai Hu, and Peng Zhao	
11	Separation via MagLev	193
	Chengqian Zhang, Jun Xie, Chenxin Lyu, and Peng Zhao	

Chapter 1

Magnetism and Magnetic Materials



Peng Zhao, Daofan Tang, Jun Xie, and Chengqian Zhang

1.1 Introduction

Magnetism, a captivating natural phenomenon, has intrigued human curiosity and scientific inquiry for centuries. The ability of certain materials to exert attractive or repulsive forces on other objects without direct physical contact has given rise to a rich history of exploration and discovery. From the enigmatic lodestones of ancient times to the sophisticated magnetic materials of today's technological advancements, the study of magnetism has continuously evolved, revealing profound insights into the fundamental nature of matter and the intricate interplay of forces.

This chapter embarks on a journey through the annals of history to unveil the origins and evolution of magnetism. We delve into the enigmatic discoveries that laid the foundation for our understanding of magnetism's various facets, encompassing both its inherent characteristics and its diverse manifestations. The exploration extends to the diverse classifications of magnetism, each with distinct properties and behaviors, contributing to its multifaceted presence in the natural world.

Furthermore, a comprehensive exploration of magnetic materials is presented, ranging from naturally occurring ferromagnetic substances to meticulously engineered artificial materials with tailored magnetic properties. The intricate relationship between magnetism and materials science has paved the way for transformative applications across industries, from telecommunications and electronics to medicine and renewable energy.

P. Zhao (✉) · D. Tang · C. Zhang

The State Key Laboratory of Fluid Power and Mechatronic Systems, College of Mechanical Engineering, Zhejiang University, Hangzhou, China

e-mail: pengzhao@zju.edu.cn

J. Xie

College of Mechanical Engineering, Zhejiang University of Technology, Hangzhou, China

1.2 A Brief History of Magnetism

Magnetism considered as one of the basic properties of materials has been known for a long time. The historical record of utilizing magnetism of materials can be traced back to the eleventh century. “Sinan”, a lodestone carved in the shape of a Chinese spoon can be regarded as the prototype of the navigational compass. The invention of magnetic compass enabled the long-distance voyages, which promoted the great discovery of America by Christopher Columbus in 1492 and the earlier discovery of Africa by Cheng Ho in 1433 (Fig. 1.1).

It was Hans Christian Oersted that discovered the relationship between electricity and magnetism in 1820. This professor at the University of Copenhagen noticed by accident that a compass needle could be deflected by a current-carrying wire. The other experiments followed, with André-Marie Ampère, who in 1820 discovered that the current-carrying coil was equivalent to a magnet, which launched the revolution of electromagnetism; Michael Faraday, who discovered electromagnetic induction in 1821 and demonstrated the principle of the electric motor by steel magnet; James Clerk Maxwell who was inspired by previous experiments, unified electricity, magnetism and optics into Maxwell’s formulation. The Maxwell’s formulation is summarized in the four equations:

$$\epsilon_0 \nabla \cdot \mathbf{E} = \rho \quad (1.1)$$

$$\nabla \cdot \mathbf{B} = 0 \quad (1.2)$$

$$(\frac{1}{\mu_0}) \nabla \times \mathbf{B} = \mathbf{j} + \epsilon_0 \partial \mathbf{E} / \partial t \quad (1.3)$$

$$\nabla \times \mathbf{E} = -\partial \mathbf{B} / \partial t \quad (1.4)$$

Fig. 1.1 The prototype of the navigational compass “Sinan” [1], which can be traced back to the Spring and Autumn period of ancient China (771–685 BCE). Copyright Wikimedia Commons



where Eq. 1.1 describes the properties of the electric field. In general, the electric field can be either the electric field of free charge or the induced electric field excited by a changing magnetic field, while the induced electric field is a vortex field, whose electric displacement line is closed and does not contribute to the flux of the closed surface. Equation 1.2 describes the properties of the magnetic field. Magnetic fields can be excited by conduction current or displacement current of changing electric field. Their magnetic fields are vortex fields, and magnetic induction lines are closed lines, which do not contribute to the flux of closed surfaces. In Eq. 1.3, the law of excitation of electric field by changing magnetic field is described. And in Eq. 1.4, the law of conduction current and excitation of magnetic field by changing electric field is described.

During the late 19th and early twentieth centuries, the study of magnetic materials and phenomena experienced significant advancements. In 1885, German physicist Carl W. von Siemens discovered that the magnetic properties of a material could be enhanced by subjecting it to high temperatures and then cooling it in the presence of a magnetic field. This process, known as magnetic annealing or quenching, later became instrumental in the production of permanent magnets.

In 1911, Dutch physicist Heike Kamerlingh Onnes observed certain materials, like mercury, exhibiting zero electrical resistance at extremely low temperatures. This phenomenon, termed superconductivity, is now known to have a close connection with magnetism and has led to the development of numerous groundbreaking technologies, including MRI machines and particle accelerators.

In the 1920s, German physicist Wolfgang Pauli developed a magnetic theory based on electron configurations, providing a framework for explaining the magnetic properties of atoms and molecules. Known as Pauli paramagnetism, this theory laid the foundation for understanding the magnetic behavior of electrons in atoms and molecules.

In the 1930s, French physicists Pierre Weiss and Louis Néel formulated a magnetic theory that explained the behavior of ferromagnetic materials, such as iron, in terms of the alignment of their magnetic domains. This theory, now referred to as the Weiss-Néel theory, provided insights into the properties of magnetic materials and the relationship between magnetism and other physical properties, such as electrical conductivity.

In the 1950s and 1960s, the discovery of spintronics opened up new possibilities for using electron spins, in addition to their charge, to manipulate electronic devices for data storage and processing. Spintronics has been widely applied in various devices, including magnetic hard drives, spin-based transistors, and magnetic sensors.

In recent years, the study of magnetism has been a dynamic and vibrant field, continuously yielding new discoveries and breakthroughs. Some current areas of active research include magnetic nanoparticles and their applications in biomedicine, the development of novel materials with exotic magnetic properties, and the exploration of the interplay between magnetism and topology in quantum materials.

In the research on magnetic nanoparticles, scientists are constantly advancing in the development of new synthesis methods and characterization techniques to obtain

Fig. 1.2 Modern clinical magnetic resonance imaging (MRI) scanner. Copyright Wikimedia Commons



more precise and efficient magnetic nanoparticles. These nanoparticles hold tremendous potentials in the field of biomedicine, serving as carriers for drug delivery to target specific cells or tissues, thereby enhancing therapeutic efficacy and reducing side effects. Additionally, magnetic nanoparticles are employed in magnetic hyperthermia, where the application of a magnetic field guides the particles to release heat at the site of a tumor, achieving precise thermal therapy. Furthermore, researchers are exploring the utilization of magnetic nanoparticles in diagnostic imaging techniques, such as magnetic resonance imaging (MRI), which is widely used in medical diagnostics (Fig. 1.2).

In parallel, the investigation of new materials with exotic magnetic properties, such as topological insulators, has become a major focus of magnetic research. Topological insulators, as novel topological quantum materials, are captivating due to their unique electronic structures and quantum phenomena. Researchers are diligently working on synthesizing novel topological insulators and exploring their potential applications in quantum information processing, spintronics, and energy conversion. These materials possess distinct properties and potential advantages in quantum information handling and energy conversion, arousing significant interest in the scientific community.

The exploration of the relationship between magnetism and topology in quantum materials has also become a highly pursued topic. Some quantum materials exhibit peculiar topological magnetic properties, such as topological magnetic monopoles and skyrmions. The presence of these unique topological structures gives rise to magnetic behavior in materials that is entirely distinct from that observed in traditional materials, showcasing important scientific significance and potential applications. Researchers are delving into the fundamental physics of topological magnetic materials to understand their unique electronic behaviors and corresponding magnetic phenomena.

The field of magnetism research continues to expand and deepen, offering novel perspectives on understanding the fundamental properties of matter and the behavior

of electrons in solids. The emergence of new materials and phenomena holds great promise for advancing various domains and unlocking new possibilities.

1.3 Sources of Magnetism

Magnetism can arise from a variety of sources, including the movement of charged particles, and the orbital and spin moments of elementary particles. In this section, we will explore these sources of magnetism in more detail.

1.3.1 Movement of Charged Particles

The movement of charged particles, such as electrons or ions, is one of the most common sources of magnetism. When charged particles move, they create a magnetic field around them that can interact with other magnetic fields or with other charged particles. This effect is known as electromagnetic induction and is the basis for many electrical devices, such as generators and motors.

The fundamental relationship between moving charges and magnetism is described by Ampere's law, which states that the magnetic field (\mathbf{B}) generated by a closed loop of current-carrying wire is directly proportional to the current (I) passing through the loop and inversely proportional to the distance (r) from the wire. Mathematically, Ampere's law is represented as:

$$\oint \mathbf{B} d\mathbf{L} = -\mu_0 \cdot \sum I \quad (1.5)$$

where μ_0 is the permeability of free space, a fundamental constant in physics.

The magnetic field produced by moving charges follows certain rules:

1. **Magnetic Field Around a Straight Current-Carrying Wire:** The magnetic field lines form concentric circles around the wire, with the direction given by the right-hand rule. The direction of the magnetic field is tangential to the circles and depends on the direction of the current flow through the wire.
2. **Magnetic Field of a Current Loop:** In a closed loop carrying a current, the magnetic field lines follow a pattern similar to that of a bar magnet, with a north and south pole. Inside the loop, the magnetic field lines point in one direction, while outside the loop, they point in the opposite direction.
3. **Magnetic Field of a Solenoid:** A solenoid is a long, tightly wound coil of wire. It behaves like a magnet, with the north and south poles determined by the direction of the current through the coil.

In magnetic materials, such as iron or nickel, the movement of electrons within atoms and between neighboring atoms results in the creation of magnetic fields due

to the circulating currents associated with the motion of these charged particles. In ferromagnetic materials, for example, the movement of electrons in certain electron bands leads to the alignment of their spins, resulting in a macroscopic magnetic field that gives rise to the material's magnetization.

The concept of moving charges and their associated magnetic fields is essential for understanding various magnetic phenomena and applications, such as magnetic fields around electric currents, magnetic induction in transformers, the operation of electric motors and generators, and the behavior of magnetic materials in response to external magnetic fields. It also underlies the principles behind technologies like magnetic resonance imaging (MRI) and magnetic storage devices like hard drives.

1.3.2 *Orbital and Spin Moments of Elementary Particles*

At the microscopic level, magnetism is the result of the angular momentum of elementary particles, which are determined by the intrinsic magnetic properties of the electrons and the way they interact with the nuclei of the atoms. The electron which is the main source of magnetic moments in solid, has two distinct sources of angular momentum, one is connected with orbital motion around the nucleus, and the other is spin.

Orbital moments, also known as orbital magnetic moments, refer to the magnetic moment associated with the motion of charged particles, such as electrons, around the atomic nucleus in an atom. The structure of an atom is based on the Bohr model which proposes that an atom consists of a positively charged nucleus at its center, composed of protons and neutrons, surrounded by negatively charged electrons moving in circular orbits around the nucleus. The electrons in an atom can only exist in certain discrete energy levels or orbits around the atomic nucleus, and each energy level corresponds to a specific value of the electron's energy. This magnetic moment arises from the circulating electric currents created by the orbital motion of the electrons. Orbital moments contribute to the overall magnetization of materials

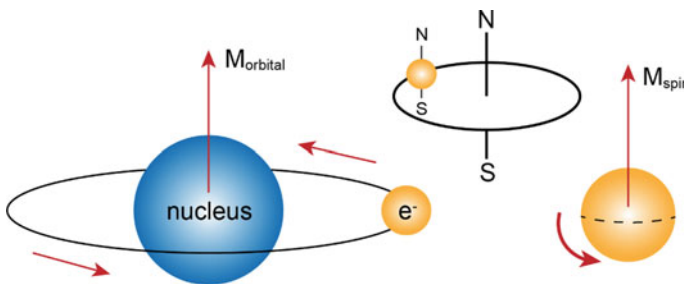


Fig. 1.3 Illustration of orbital moments and spin moments

combined with the spin moments and plays a significant role in phenomena like paramagnetism or diamagnetism.

Spin is a form of intrinsic angular momentum that particles possess due to their quantum nature. It is a fundamental property of elementary particles, and it is not related to their physical rotation. It is important to note that spin is not the same as classical spin, as particles are not spinning around their axis like macroscopic objects. Instead, it is a purely quantum property that describes the angular momentum of particles in the context of wave-particle duality. Spin is quantized, meaning that it can only take discrete values. For example, electrons have a spin of $1/2$, which means their intrinsic angular momentum can be either “spin up” or “spin down,” corresponding to opposite orientations of the magnetic moment. The presence of spin gives rise to an intrinsic magnetic moment associated with the particle. This magnetic moment behaves like a tiny magnetic dipole, creating a magnetic field around the particle. Spin magnetic moments interact with external magnetic fields. When a particle with spin is placed in a magnetic field, its magnetic moment tends to align with the field direction. This interaction is fundamental in many magnetic phenomena.

Generally, an electron remains both spin and orbital moments at the same time, which is coupled by spin-orbit interaction to generate a total electronic angular momentum with resultant magnetic moment. The coupling between the intrinsic spin and orbital motion causes energy level shifts in the atom or material, leading to the splitting of energy levels into multiple sub-levels. This phenomenon is known as fine structure splitting. The energy difference between the split levels is small, but it has significant implications for atomic spectra and magnetic properties. For example, in atoms with partially filled electron shells, the coupling between the electron’s spin and its orbital motion results in different energy levels for different electron spin orientations. This energy difference between the spin-up and spin-down states leads to a net magnetic moment for the atom, contributing to the overall magnetism of the material. In materials with heavy elements or strong spin-orbit coupling, the modification of magnetic moments can lead to various magnetic phenomena, such as magnetic anisotropy, where the magnetic properties depend on the direction of the external magnetic field. Spin-orbit coupling also plays a crucial role in the behavior of magnetic materials in response to external magnetic fields.

1.4 Types of Magnetism

In theory, all materials possess magnetism due to the intrinsic property of electron spin, which is a fundamental characteristic of elementary particles composing matter. However, the type of magnetism exhibited by different materials varies. A typical example of a magnetic material is a ferromagnet, such as a permanent magnet. In general, there are six main types of magnetic behavior exhibited by materials: paramagnetism, diamagnetism, ferromagnetism, antiferromagnetism, and ferrimagnetism (Fig. 1.4).

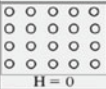
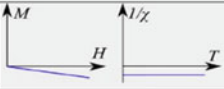
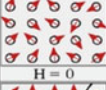




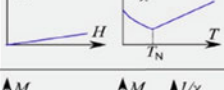
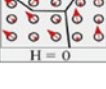
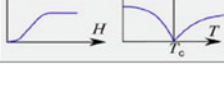
Magnetism	Examples	Magnetic behaviour	
Diamagnetism	Bi, Si, Cu, inert gases Susceptibility small and negative (-10^{-6} to -10^{-5})		Atoms have no magnetic moments. 
Paramagnetism	Al, O ₂ , MnBi Susceptibility small and positive (10^{-5} to 10^{-3})		Atoms have randomly oriented magnetic moments. 
Ferromagnetism	Fe, Ni, Co, Gd Susceptibility large (generally > 100)		Atoms are organized in domains which have parallel aligned magnetic moments. 
Antiferromagnetism	Cr, MnO, FeO Susceptibility small and positive (10^{-5} to 10^{-3})		Atoms are organized in domains which have antiparallel aligned moments. 
Ferrimagnetism	Fe ₂ O ₄ , MnFe ₂ O ₄ , NiFe ₂ O ₄ Susceptibility large (generally > 100)		Atoms are organized in domains which have a mixture of unequal antiparallel aligned moments. 

Fig. 1.4 Summary of the main types of magnetism and their features. Reproduced with permission from Ref. [2]. Copyright 2016 Elsevier

Paramagnetism is a magnetic phenomenon observed in materials, in which the internal magnetic moments tend to align with the external magnetic field under its influence. It is considered a relatively weak form of magnetism primarily originating from the behavior of electron spin moments within the material. When exposed to an external magnetic field, the unpaired electron spin moments tend to align with the field, giving rise to a temporary magnetic moment in the material, a phenomenon referred to as alignment. However, it is important to note that the alignment in paramagnetism is only partial, and at elevated temperatures, thermal motion disrupts the alignment, leading to a weakening of the overall magnetization. Paramagnetic materials exhibit a magnetization strength directly proportional to the external magnetic field; however, this magnetization is weaker in comparison to other magnetic behaviors such as ferromagnetism. Understanding the underlying principles of paramagnetism is significant for comprehending material magnetism and designing magnetic materials with tailored properties.

Diamagnetism is a magnetic property that is observed in materials and exhibits a weak magnetic field repulsion when subjected to an external magnetic field. In contrast to paramagnetism, diamagnetic materials tend to align their internal magnetic moments opposite to the direction of the external magnetic field. This behavior is primarily associated with the electron orbital magnetic moments within the material. When exposed to an external magnetic field, the electron orbital magnetic moments generate a weak magnetic field that opposes the direction of the external field. Diamagnetism arises due to the response of the electron orbital magnetic moments to the external magnetic field. The orbital motion of electrons around the atomic nuclei gives rise to tiny current loops, generating an intrinsic magnetic moment. When placed in an external magnetic field, these magnetic

moments experience a torque that aligns them in a direction opposite to the applied field, leading to a weak repulsion. The magnetic response of diamagnetic materials is relatively weak compared to other magnetic behaviors like ferromagnetism. Furthermore, diamagnetism is particularly prominent at elevated temperatures due to the influence of thermal energy. At higher temperatures, thermal motion disrupts the alignment of electron orbital magnetic moments, accentuating the diamagnetic behavior.

Ferromagnetism refers to the phenomenon in which the materials exhibit a robust permanent magnetization when exposed to an external magnetic field. The origin of ferromagnetism lies primarily in the interaction between electron spin and orbital magnetic moments, as well as the exchange interaction between neighboring atoms. Within ferromagnetic materials, electrons possess both spin and orbital magnetic moments. When subjected to an external magnetic field, the electron spin moments tend to align with the direction of the field, while the orbital magnetic moments also orient themselves in the same direction. This mutual interaction between spin and orbital magnetic moments spontaneously aligns the electron magnetic moments in ferromagnetic materials, resulting in a macroscopic and intense magnetization. Moreover, the exchange interaction between neighboring atoms causes the electron spin moments of adjacent atoms to align parallelly, further enhancing the material's magnetic properties and enabling ferromagnetic materials to sustain permanent magnetization, even in the absence of an external magnetic field, displaying a strong magnetic effect. It is crucial to acknowledge that magnetic moments in ferromagnetic materials are not homogeneously distributed across the entire material. On the contrary, the material is segmented into numerous small regions, each with its distinct magnetic moment alignment, known as magnetic domains. The interfaces between different magnetic domains are referred to as domain walls. In the absence of an external magnetic field, the magnetic moments of individual domains cancel each other out, resulting in the material not demonstrating macroscopic magnetization. However, when an external magnetic field is applied, the domain walls can move and reconfigure, allowing the magnetic moments throughout the entire material to align entirely, forming a strong magnetic state.

Antiferromagnetism, in contrast to ferromagnetism, is characterized by neighboring atoms' magnetic moments aligning in opposite directions, resulting in a net magnetic moment of zero for the material. Ferromagnetic and antiferromagnetic materials share a fundamental characteristic—atomic magnetic moments contributed by electron spins. In other words, antiferromagnetic materials also possess strong magnetic moments within their atoms; however, the electron magnetic moments of neighboring atoms align in opposite directions, leading the material to exhibit no macroscopic magnetization. Antiferromagnetic substances are relatively less common, with most of them only existing at low temperatures. If the temperature exceeds the Néel temperature, they typically transition to become paramagnetic.

Ferrimagnetism represents an intermediate state between ferromagnetism and antiferromagnetism, where, in the presence of an external magnetic field, electron spin and orbital magnetic moments tend to align partially with the field's direction. However, in ferrimagnetic materials, the magnetic moment arrangement is partially

opposite; the electron magnetic moments of neighboring atoms only align partially in opposite directions, resulting in a smaller overall magnetic moment at the macroscopic scale. Ferrimagnetic properties arise from materials composed of constituents possessing at least two different magnetic moments, typically found in compounds or alloys. Common examples of ferrimagnetic substances include magnetite (Fe_3O_4) and ferrites.

Superparamagnetism [3] refers to the magnetic behavior exhibited by single-domain ferromagnetic materials when the particle size is smaller than the critical size. Below the Curie temperature but above the blocking temperature, superparamagnetic materials display characteristics of paramagnetism, and hence are termed superparamagnetic. These materials exhibit a significantly higher magnetic susceptibility under the influence of an external magnetic field compared to typical paramagnetic materials. The internal electron spin and orbital magnetic moments in superparamagnetic materials tend to align with the direction of the external magnetic field. Another crucial factor influencing superparamagnetism is the exchange interaction. Within the material, there exists an exchange interaction between electrons, promoting the alignment of unpaired electron spins and leading to the formation of long-range ordered magnetic structures, thus enhancing the overall magnetic moment of the material.

1.5 Magnetic Materials

Materials that can react in some way to a magnetic field are known as magnetic materials. Experiments show that any substance can be more or less magnetized in an external magnetic field, though the degree of magnetization varies. Most materials exhibit weak responses to an external magnetic field and are classified as either diamagnetic or paramagnetic. Ferromagnetic and ferrimagnetic materials, on the other hand, are strong magnetic materials, often referred to as magnetic materials. Magnetic materials are generally classified into soft magnetic materials and hard magnetic materials based on the ease of their magnetization.

1.5.1 *Hard Magnetic Materials*

Hard magnetic materials, also known as permanent magnetic materials or permanent magnets, refer to functional materials that can retain their magnetism for an extended period after being magnetized and can withstand a certain level of external magnetic field interference. The main technical magnetic parameters for permanent magnets include: saturation magnetization, remanent magnetization, intrinsic coercivity, maximum energy product, squareness of hysteresis loop, Curie temperature, and magnetic susceptibility. Some of these parameters are intrinsic to the material and are mainly determined by its crystal structure and chemical composition, with

little influence from the manufacturing process. These parameters include saturation magnetization and Curie temperature. The remaining parameters are structure-sensitive and are influenced not only by the intrinsic magnetic properties of the material but also by the manufacturing process, grain size, orientation, microstructure, and other factors.

Permanent magnetic materials exhibit a significant response to an external magnetic field, forming magnetization curves or hysteresis loops (Fig. 1.5), which characterize the relationship between the magnetization intensity M or magnetic induction B and the magnetic field strength H during the magnetization process. The technical saturation hysteresis loop refers to the curve of magnetization intensity M or magnetic induction B of permanent magnetic materials as the external magnetic field gradually decreases from a certain direction's saturation field to the reverse saturation field and then returns to the initial direction's saturation field. From Fig. 1.5, it can be observed that after removing the external magnetic field, hard magnetic materials still possess a residual magnetization along the direction of the external magnetic field, denoted as M_r . The residual magnetization strength not only depends on the saturation magnetization of the permanent magnetic material but also on factors such as the orientation distribution of internal crystal grains and the characteristics of the magnetic domain structure.

Figure 1.6 illustrates a significant and rapid increase in the strength of hard magnetic materials, specifically represented by the maximum energy product, $(BH)_{\max}$, over the span of approximately 100 years. For instance, the $(BH)_{\max}$ value for KS steel is 7.6 kJ m^{-3} , whereas the latest Nd-Fe-B magnets exhibit a strength approximately 60 times greater than that of KS steel.

Japanese researchers have made significant contributions to the development of hard magnetic materials. In 1931, Mishima invented MK steel [5], an Fe-Ni-Al

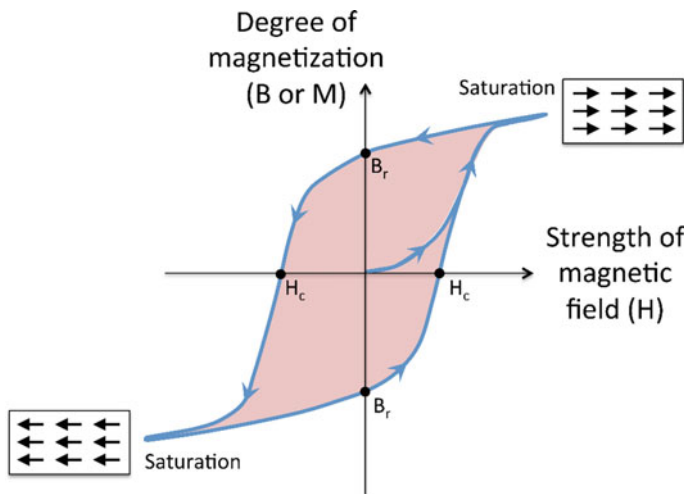
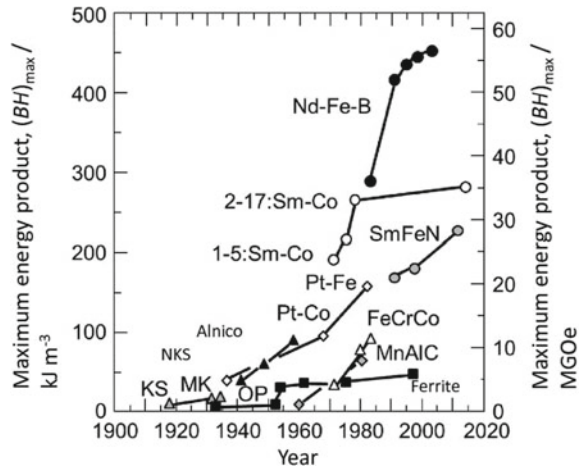


Fig. 1.5 Hysteresis loop for hard magnetic materials. Copyright Wikimedia Commons

Fig. 1.6 Trends in $(BH)_{\max}$ in hard magnetic materials. Reproduced with permission from Ref. [4]. Copyright 2019 Springer Nature



alloy with two-phase separation morphology, which formed the basis of current alnico magnets and exhibited a $(BH)_{\max}$ of 9.6 kJ m^{-3} . Subsequently, Kato and Takei invented oxide powder magnets in 1933 [6], based on oxides rather than conventional alloy magnets, laying the foundation for modern ferrite magnets. These oxide powder magnets consisted of a mixture of CoFe_2O_4 and Fe_3O_4 and exhibited a high coercive field strength (H_cJ) of around 80 kA m^{-1} , representing a groundbreaking discovery in comparison to previous alloy magnets [7].

The development of MK steel and NKS steel in 1934 by Honda, Masumoto, and Shirakawa led to the creation of alnico magnets. Additionally, various Mn-based magnets and Pt-based magnets with coercive force were reported during the same period. In 1971, Iida et al. [7] produced an Fe–Cr–Co magnet with magnetic shape anisotropy, similar to alnico magnets, which is the only current magnetic material that can be cold worked.

The discovery of Sm–Co magnets in 1966 marked the beginning of the era of rare earth magnets. Hoffer and Strnat measured the magnetic properties of YCo_5 and reported its high magneto-crystalline anisotropy [8]. Subsequently, SmCo_5 magnets with high saturation magnetic polarization J_s and extremely high magneto-crystalline anisotropy constant K_u were mass-produced. The addition of Cu to CeCo_5 and SmCo_5 alloys led to two-phase-separated Sm–Co magnets, with the main phase of $\text{Sm}_2\text{Co}_{17}$ exhibiting excellent temperature properties and higher $(BH)_{\max}$ than SmCo_5 magnets. However, Nd–Fe–B magnets, discovered in 1983 by Sagawa et al. [9] and Croat et al. [10], surpassed $\text{Sm}_2\text{Co}_{17}$ magnets in terms of $(BH)_{\max}$ and became the most powerful permanent magnets.

The current most impactful permanent magnets on technology and people's lives are ferrite magnets and Nd–Fe–B magnets. Ferrite magnets, developed from oxide powder magnets based on CoFe_2O_4 , have a favorable cost-performance ratio due to their cheap raw material price and chemical stability. Nd–Fe–B magnets, with a main phase of $\text{Nd}_2\text{Fe}_{14}\text{B}$, are currently the most powerful permanent magnets

with excellent magnetic properties, making them suitable for various applications. Nd–Fe–B magnets can be classified as sintered magnets, hot-worked magnets, and bonded magnets, each with specific fabrication processes and properties.

Hard magnetic materials are temperature-sensitive, and as the temperature rises, their magnetic properties gradually decline. At a specific temperature known as the Curie temperature, the magnetization strength vanishes. Once a magnetic material is heated beyond its Curie temperature, it permanently loses its magnetic properties. Temperatures exceeding the Curie temperature cause irreversible structural changes in the magnetic domains, resulting in permanent damage that cannot be restored through magnetization.

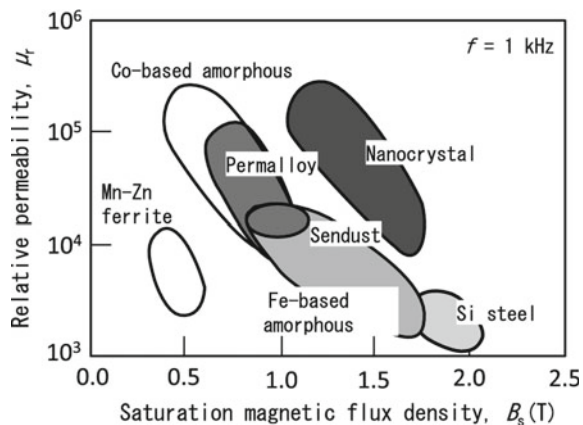
1.5.2 Soft Magnetic Materials

Soft magnetic materials are a type of materials that are sensitive to magnetic fields and can be easily magnetized and demagnetized. They have low coercivity and high magnetic permeability, which means they can quickly undergo magnetization and demagnetization under the influence of an external magnetic field while producing minimal energy loss.

The development of magnetic materials saw significant progress in the early twentieth century. In 1913, Elemen discovered that Fe–Ni alloys containing 30–90% Ni exhibited high magnetic permeability, leading to the creation of “permalloy.” Subsequent investigations in 1923 focused on heat treatment methods for the Fe–80%Ni alloy, which demonstrated that rapid cooling from 600 °C improved initial permeability [11] (Fig. 1.7).

In Fe–Ni alloys, the presence of a Ni₃Fe order phase at compositions of 50–85% Ni, and the order–disorder transformation occurring at 503 °C, impacted magnetic permeability. Slow cooling from high temperatures caused the order phase to

Fig. 1.7 Relationship between saturation magnetic flux density and permeability in soft magnetic materials. Reproduced with permission from Ref. [12]. Copyright 2019 Springer Nature



appear, resulting in reduced magnetic permeability with crystal magnetic anisotropy. However, the addition of third elements, such as Mo or Cr, was found to suppress the regular phase and produce high permeability with good reproducibility, even with slow cooling. This research led to the development of Mo permalloy and Cr permalloy.

In 1932, Masumoto and Yamamoto developed Sendust [13], an Fe–Si–Al alloy containing 5–11% Si and 3–8% Al, which exhibited high magnetic permeability. However, higher Si and Al contents resulted in the precipitation of intermetallic compounds Fe_3Si and Fe_3Al , making the alloy hard and brittle. Despite this, Sendust found various applications, including in magnetic heads during the development of magnetic recording technology.

Si steel, or magnetic steel, was developed by Hadfield in 1900, and Goss later introduced a method for producing oriented Si steel sheets with a specific crystallographic texture, known as Goss texture [14]. Non-oriented Si steel sheets are used in rotary machines, while oriented Si steel sheets find applications in transformers. The addition of Si to Fe reduced magneto-crystalline anisotropy and magnetostriction constant, λ . Fe–6.5%Si alloy with low λ was developed by Takada et al. [15] in 1988, and mass production became possible in 1994. This alloy is used as a low-noise magnet core material for high-frequency applications [16]. Recent developments have achieved even higher Si content through a siliconizing technique, offering high magnetic flux density and low Fe loss for applications such as reactors, supporting high-frequency ranges [17].

Amorphous alloys are known for their low magneto-crystalline anisotropy and high permeability due to the absence of a crystal phase and pinning at domain walls. These alloys are fabricated using the liquid quenching method. In 1975, Masumoto and Kimura [18] discovered that nanocrystals of 10–20 nm precipitated during low-temperature annealing of amorphous alloys to form stable aggregates. This nanocrystalline magnetic material exhibits high saturation magnetic flux density and permeability. The presence of a crystal phase did not significantly reduce the saturation magnetic flux density and permeability due to various factors, such as the ferromagnetic nature of the remaining amorphous phase, averaging out of magneto-crystalline anisotropy through exchange coupling between nanocrystals, low magnetostriction, and the small size of nanocrystals that prevents the formation of pinning sites for domain walls [12].

Soft magnetic materials based on metals often encounter issues with eddy currents and heat generation at high frequencies due to their low electrical resistance. To address this problem, materials with thin bodies or small particles have been developed to reduce eddy current losses. However, soft ferrites, which contain Fe oxide such as Fe_2O_3 , are an exception to this issue because of their high electrical resistance. They can be used for high-frequency applications even with low magnetization.

The main types of ferrites include MnZn ferrite ($(\text{MnZn})\text{O}\cdot\text{Fe}_2\text{O}_3$) and NiZn ferrite ($(\text{NiZn})\text{O}\cdot\text{Fe}_2\text{O}_3$), both having a spinel structure and represented by the general formula MFe_2O_4 or $\text{MO}\cdot\text{Fe}_2\text{O}_3$ (M: metal with valence 2).

MnZn ferrite is commonly utilized at frequencies of several megahertz or lower in wideband transformers and noise filters. Its composition results in zero magneto-crystalline anisotropy and magnetostriction, leading to a high permeability with large crystal grains, facilitating easy movement of domain walls. Additionally, MnZn ferrites have the highest saturation magnetic flux density. However, their electrical resistance is lower than other spinel ferrites, which can result in larger magnetic losses at frequencies exceeding several megahertz. A solution to this issue involves precipitating a phase with high electrical resistance in the grain boundaries. For frequencies up to several hundred megahertz, which is higher than those used for MnZn ferrite, NiZn ferrite is employed as a magnetic core material in transformers and inductors. NiZn ferrites possess high electrical resistance, making them suitable for use in such applications.

References

1. Kingdon, A. The south pointing spoon. *Hakai Magazine*; 2019.
2. Palagummi S, Yuan FG. Magnetic levitation and its application for low frequency vibration energy harvesting. *Struct Health Monit (SHM) Aerosp Struct*. 2016; 213–51.
3. Bean CP, Livingston JD. Superparamagnetism. *J Appl Phys*. 1959;30(4):120–9.
4. Cui J, et al. Nanomagnetic encoding of shape-morphing micromachines. *Nature*. 2019;575(7781):164–8.
5. Mishima T, Makino N. Studies on industrialization of “MT” permanent magnet (I) on the chemical composition and additional elements. *Tetsu-to-Hagane*. 1957;43(5):556–60.
6. Kato Y, Takei T. Permanent oxide magnet and its characteristics. *J Instit Electr Eng Japan*. 1933;53:408–12.
7. Iida S, Iwasaki S, Iwama Y, et al. *Hard magnetic materials*. Tokyo: Maruzen; 1976.
8. Hoffer G, Strnat K. Magnetocrystalline anisotropy of YCo5 and Y2Co17. *IEEE Trans Magn*. 1966;2(3):487–9.
9. Sagawa M, Fujimura S, Togawa N, et al. New material for permanent magnets on a base of Nd and Fe. *J Appl Phys*. 1984;55(6):2083–7.
10. Croat JJ, Herbst JF, Lee RW, et al. Pr-Fe and Nd-Fe-based materials: a new class of high-performance permanent magnets. *J Appl Phys*. 1984;55(6):2078–82.
11. Barrett WF. On the electrical conductivity and magnetic permeability of various alloys of iron. *Sci Trans Royal Dublin Soci*. 1900; 67.
12. Sugimoto S. History and future of soft and hard magnetic materials. In: *Magnetic material for motor drive systems: fusion technology of electromagnetic fields*. 2019. p. 261–77.
13. Masumoto H. On a new alloy “Sendust” and its magnetic and electric properties. *J Japan Inst Metals*. 1937;1:127–35.
14. Goss NP. Electrical sheet and method and apparatus for its manufacture and test. U.S. Patent, No. 1,965,559. 1934.
15. Takada Y, Abe M, Masuda S, et al. Commercial scale production of Fe-6.5 wt.% Si sheet and its magnetic properties. *J Appl Phys*. 1988;64(10):5367–536.
16. Okami Y, Abe M, Yamaji T, et al. Continuous siliconizing technology of 6.5% silicon steel sheet. *Tetsu-to-Hagane*. 1994;80(10):777–782.
17. Hiratani T, Oda Y, Namikawa M, et al. Development of Si gradient steel sheet with high saturation magnetic flux density and low iron loss at high frequency. *Mater Jpn*. 2014;53(3):110–2.
18. Masumoto T, Kimura H. Crystallization processes in an Fe-base amorphous alloy (Fe-P-C) quenched from the liquid phase. *J Jpn Inst Metals*. 1975;39(3):273–80.

Chapter 2

Development of Magneto-Archimedes Levitation



Peng Zhao, Jun Xie, Haonan Sun, and Chengqian Zhang

2.1 Introduction

A maglev train (Fig. 2.1) will be the first thing come up to a man's imagine when he hears "magnetic levitation". For it is well known that magnets will be repel each other when their same poles getting close. However, it is impossible to use a single magnet to levitate another magnet. This phenomenon was firstly proved by Earnshaw in 1842 through theoretical derivation. The Earnshaw theorem pointed out that the point particle set cannot be stably maintained in a stable static mechanical equilibrium structure consisting only of electrostatic interaction of charge. Therefore, to obtain statically stable levitation between magnets, additional constraints need to be added. Usually, two or more sets of magnet pairs are used in one system, such as in some kind of maglev trains. Due to the magnetic flux intensity of an electromagnet can be directly adjusted by changing the current through the coils, precise control method can remain a dynamic stabilization between two magnets.

Conversely, diamagnetic materials can theoretically reach to stable levitation without additional restraint. However, the magnetic susceptibility of most diamagnetic materials is too weak to be observed in daily life. The magnetic susceptibility of diamagnetic materials is usually at least 3 orders of magnitude lower than that of paramagnetic materials like MnCl_2 , FeCl_2 , etc., not to mention with ferromagnetic materials. Until 1990s, Andrew Geim proposed an interesting experiment on levitating living materials in an ultra-high magnetic field generated by a superconducting electromagnet. The "flying frog" tumbling and struggling in the air without any contact [1]. This famous experiment attract the following research on how to

P. Zhao (✉) · H. Sun · C. Zhang

The State Key Laboratory of Fluid Power and Mechatronic Systems, College of Mechanical Engineering, Zhejiang University, Hangzhou, China

e-mail: pengzhao@zju.edu.cn

J. Xie

College of Mechanical Engineering, Zhejiang University of Technology, Hangzhou, China



Fig. 2.1 Maglev train in Shanghai, China

levitate common material in magnetic field. Through theoretical analysis, people notice that not only high magnetic flux intensity can levitate diamagnetic materials, but also large gradient of magnetic flux intensity with large diamagnetic susceptibility can achieve the similar effects. If the magnetic field can get changed from N pole to S pole in a very narrow space, the gradient of magnetic flux intensity could be large enough to levitate object through diamagnetic levitation. On the contrary, it is hard to find a material with very large diamagnetic susceptibility. Pyrolytic graphite is the known material that has the largest bulk diamagnetic susceptibility. Its susceptibility is still relatively too small to visibly respond to a magnetic field. The magnets arranged with alternating polarity can just lift the pyrolytic graphite sheet to a height of 2 mm.

In general, although kinds of ingenious methods were carried out to levitate diamagnetic materials, the levitating ability is still limited for heavier materials. Therefore, a novel concept called “magneto-Archimedes levitation” was applied to levitate heavier materials.

2.2 Magneto-Archimedes Levitation

The effect of gravity causes the presence of static pressure inside the liquid. As is common knowledge, this static pressure increases with the depth interior the liquid. The buoyancy of a liquid is caused by the difference in pressure between surfaces of an object in the liquid. As we now know, every substance has its own magnetism. Although the magnetism of most substances is always neglected in our daily life, they still respond in high magnetic field (such as the pyrolytic graphite and living beings introduced in previous section). Similar to the gravity, the paramagnetic fluid will

be attracted in a magnetic field, thereby generate an “extra buoyancy” to the object interior the fluid. To better distinguish it from the buoyancy caused by the gravity, “magnetic force” is used in the following article to refer to this “extra buoyancy”. When the sum of the magnetic force in vertical direction and the buoyancy is larger than the gravity, the object can be levitated.

The greater the attraction of a paramagnetic medium in a magnetic field, the greater magnetic force it produces. Therefore, there are two key factors that influence the magnetic force: the paramagnetic medium and the magnetic field.

The choice of paramagnetic medium can be pure substances or mixtures of paramagnetic and diamagnetic substances. For the oxygen molecule has a single electron in its orbitals, it exhibits paramagnetism macroscopically. Therefore, the oxygen is most common pure paramagnetic substance used as the medium. The compressibility of oxygen gas enables the enhancement of its density and magnetic susceptibility through compression, by which the levitation of heavy materials like gold and lead can be realized (Fig. 2.2a) [2]. Paramagnetic solutions are another kind of commonly used media. Some metals, like iron and manganese, are of very high magnetic susceptibility. Their soluble compounds inherited this property. For instance, MnCl_2 has the molar magnetic susceptibility of $14,350 \times 10^{-6} \text{ cm}^3/\text{mol}$, which is nearly 4 times larger than that of the oxygen [3]. Dissolve these compounds in water or other liquids, paramagnetic media that suitable for room temperature and pressure can be easily prepared.

On the other hand, adjusting the magnetic field is another way to enhance the levitation effect of magneto-Archimedes levitation. Intuitively, we can improve the strength of the magnetic field to enhance the levitation effect. In fact, using very-high-intensity magnetic field ($\sim 10 \text{ T}$) is the very effective way to levitate substances with large densities. The levitation of gold and lead was achieved under this condition. Accordingly, the high-intensity magnetic field requires superconducting electromagnets, which raises the threshold to achieve the magneto-Archimedes levitation. As can be noticed, changing the gradient of magnetic flux intensity can also adjust the levitation effects. Similar to the diamagnetic levitation of pyrolytic graphite, the levitation through permanent magnets can be realized using magnets in special arrangements, such as alternating polarity arrangement and Halbach arrays. The use of permanent magnet with magnetic flux intensity of $\sim 0.4 \text{ T}$ can easily levitate polymers and biomaterials. For instance, researchers levitated different seeds in the field generated by the magnets in alternating polarity arrangement [4]. However, there is a mutual restriction between the levitation ability and the levitation space. Large gradient of magnetic flux intensity can only be achieved in a narrow space. Hence, the levitation through permanent magnets can only deal with feeble objects.

Fig. 2.2 Levitation of metals using superconducting electromagnet. Top to bottom: a silicon crystal, a gallium arsenide crystal, a £1 coin, a piece of lead and a gold coin. The max magnetic flux intensity is up to 2.0 T. Reproduced with permission from Ref. [2]. Copyright 2003 Springer Nature



2.3 Applications of Magneto-Archimedes Levitation

2.3.1 Separation and Detection

The concept of magneto-Archimedes levitation is inspired by the buoyancy of liquids. However, magneto-Archimedes levitation has its unique character: the direction and magnitude of extra buoyancy generated by the magnetic field (“magnetic force” is used in the following article to refer to this extra buoyancy) vary with the position of the sample. On contrast, buoyancy generated by the gravity is uniform interior the medium. Therefore, buoyancy caused by the gravity will levitate a sample *on* a uniform medium, while the magneto-Archimedes levitation can levitate objects *in* the paramagnetic medium. It is easy to predict that different object will be levitated at different position in magneto-Archimedes. Similar to Archimedes principle, the key character to distinguish different object in magneto-Archimedes is the density of the object. Hence, the idea that separate different materials by the differences in densities came to researchers’ mind. To separate materials with different densities, different structures of magnets are used to generate magnetic field gradient.

The first structure is two electro magnets with N pole faces to S pole, as shown in Fig. 2.3a [5]. This structure is usually used to generate uniform magnetic field between the magnets, which is widely used in magnetic oscillation devices. However, along the direction that is vertical to the axis between two magnets, the magnetic field changes rapidly, which could generate a proper magnetic field gradient to levitate materials. This idea was directly used to separate polymer materials. The trials on separating polystyrene (PS), poly(ethylene terephthalate) (PET), poly(methyl methacrylate) (PMMA), syndiotactic polypropylene (sPP), and styrene-butadiene block copolymer (SB) was achieved in this structure with the max magnetic field flux intensity of 2.0 T, as shown in Fig. 2.3b. The effect of the magnetic field gradient is similar to the density gradient, but has an advantage that the gradient of magnetic flux intensity can be easily controlled in a flexible manner than the density gradient. A continuous flow would be a promising way in designing a more practical separation process. However, even the different polymer pellets can be obviously separated, this structure of magnets has its disadvantages. The space between the two magnetic poles is too narrow to permit large containers. Hence, the separation can only take place in several pellets, which is not suitable for polymers of large amount or large sizes.

The second way is the sole magnet that commonly used. As introduced in previous section, electro magnet can levitate materials from small density, such as polymers and biomaterials, to large density, such as metals and their compounds. Hence, it is easy to extend the levitation to the application of separation and purification, as long as the paramagnetic medium is chosen properly. For instance, the paramagnetic solutions were widely used in the separation, for the preparation process is brief and the solvents are usually market available, such as MnCl_2 and FeCl_2 . With the aid of this kind of paramagnetic medium, the separation of polymers and biomaterials were carried out. These studies showed that magneto-Archimedes levitation has the great advantage in extracting or separating target material(s) from a mixture of multiple substances in a non-contact manner during a short period of time. For some soluble materials, pressed oxygen is another common choice of paramagnetic medium. For

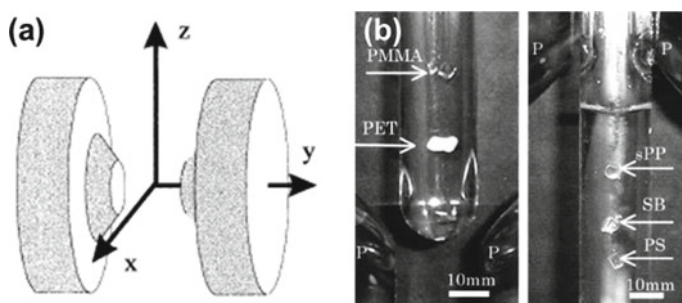


Fig. 2.3 a Structure of electromagnets. b Levitation of different polymers in MnCl_2 aqueous solution. Reproduced with permission from Ref. [5]. Copyright 2000 The Chemical Society of Japan

instance, the use of pressed oxygen well solved the problem that some collagens have good solubility and has the ability to bind ions, such as different types of collagens [6, 7]. In addition, the electromagnets also have the ability to adjust the magnetic flux intensity to obtain different levitation abilities. This ability allows the separation of each individual material from a mixture step by step through increasing the magnetic field gradually.

However, although the advantage of the ability to adjust the magnetic flux intensity makes the levitation through electro magnets has the ability to fit different requirements, the cost of the device limits its broad use in practical occasions. As discussed in previous section, the levitation through permanent magnets has been proved to have the capacity to levitate materials like polymers and biomaterials. In fact, as long as the gradient of magnetic flux intensity is large enough, the levitation of heavy materials, such as metals, through permanent magnets came to reality. For example, a practice for recycling heavy metals from waste electrical and electronic equipment (WEEE) has used bar magnet array in alternating polarity arrangement for the levitation, as shown in Fig. 2.4 [8]. The bar magnet has a small width of 10 mm. Therefore, the change of magnetic field between adjacent magnets is large enough to generate a large gradient of magnetic flux intensity. Benefit from the large gradient of magnetic flux intensity, the heavy metals with densities greater than 5.00 g cm^{-3} can be slightly levitated at a height of 3 mm (in 5 mol/L MnCl_2 aqueous solution). Although the levitation effect of the metals is not evident, it is enough to extract the metal powders from other material powders. This configuration of magnets successfully extracted indium-tin oxide (ITO) from ITO-glass powder mixtures. The recovery rates of indium exceed 95% (up to 100%) and the indium concentrations in the processed glass sheds are doubled (from 912.0 to 1873.1 ppm). Even the outcomes and throughput of this kind of separation requires further attention, it provided a practical way for recycling tiny amounts of precious metals from WEEE.

Admittedly, use magnetic force generated by permanent magnets to resist gravity can hardly create space for separation of multiple materials in a large density range. But in the mean time, it is worth noticing that the direction of magnetic force can be easily adjusted by changing the pole direction of magnets. Hence, a separation method use magnetic force as a driven force to “project” materials to different distance, thereby to achieve the separation of the materials (Fig. 2.5) [9, 10]. The square magnets, square or ring, are set horizontally. Object interior the paramagnetic medium can be horizontally pushed away from the surface of the magnet. The gravity and buoyancy will lead the object to the bottom of the container or the surface of the medium. Depending on the object’s density, the he final position of the object will have a certain distance from the magnet. Therefore, separating materials with different densities can be achieved through their projecting distance. The advantages of the magnetic projection method are two folds: (i) The method can separate multiple materials simultaneously in just one process. (ii) The materials’ densities can be in a large range. Typically, the range can cover materials from 0.8 to 3.0 g/cm^{-3} . An interesting phenomenon should be noticed that according to the typical distribution of magnetic field, there is a magnetic potential well near the pole center of the

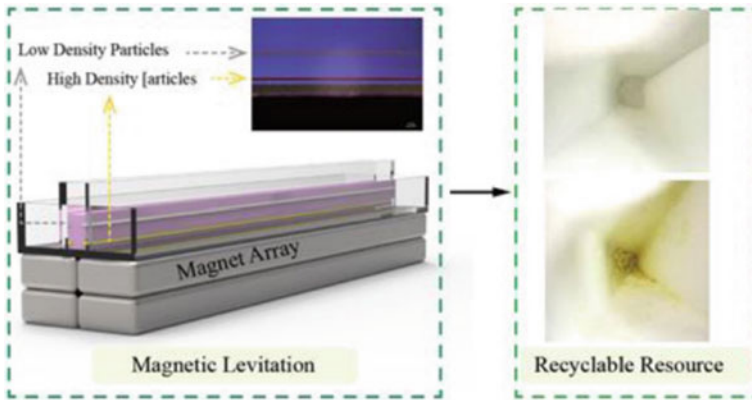


Fig. 2.4 The recycling of heavy metals using magneto-Archimedes levitation. Special arranged bar magnets are used to generate high-gradient magnetic field. Reproduced with permission from Ref. [8]. Copyright 2021 Elsevier

magnet. The material with density near the medium would be possibly trapped in the area. Therefore, the preparation of the medium should avoid getting similar density with the materials. Otherwise, an initial velocity should be given to the materials to escape the well. Benefit from the accurate simulation of finite element software, the final position of the materials in different occasions can be precisely predicted. The demonstration of total separation of 6 waste plastics or 4 construction and demolition wastes in one process was carried out. The recovery rate of each material can achieve to above 95 wt%. Because the dynamic process of material separation is considered, the automatic separation of materials can be easily achieved by a simple design of the device, which showed its ability to deal with large amounts of wastes.

The separation methods introduced above have a similar character that they all mainly consider the magnetic force perpendicular to the surface of the magnet. This is because the force parallel to the surface is relatively too weak. However, due to the horizontal direction only has the magnetic force (when the poles of the magnet point to the same direction as the gravity), the force can push an object away from the magnetic field even the object cannot be levitated. This effect can extract diamagnetic metals and their compounds from paramagnetic mixtures. In addition, although the parallel force will not affect the final levitation position, it surely has effect on the motion during levitation. Typically in the levitation using single square magnet, an object with smaller density could be fast levitated and slowly pushed away with an oscillation in levitation height. If the object has a certain density that could lead to a slight levitation above the magnet, it will reach to an equilibrium position along the centreline of the magnet. Of course, objects with very large density will surely not be levitated. Inspired by this phenomenon, an automatic separation device was designed, as shown in Fig. 2.6 [11]. The device uses an N45 magnet square magnet with the size of 50.8 mm × 25.4 mm × 25.4 mm. Collectors are set at different heights to collect the separated materials. Materials that could be levitated above

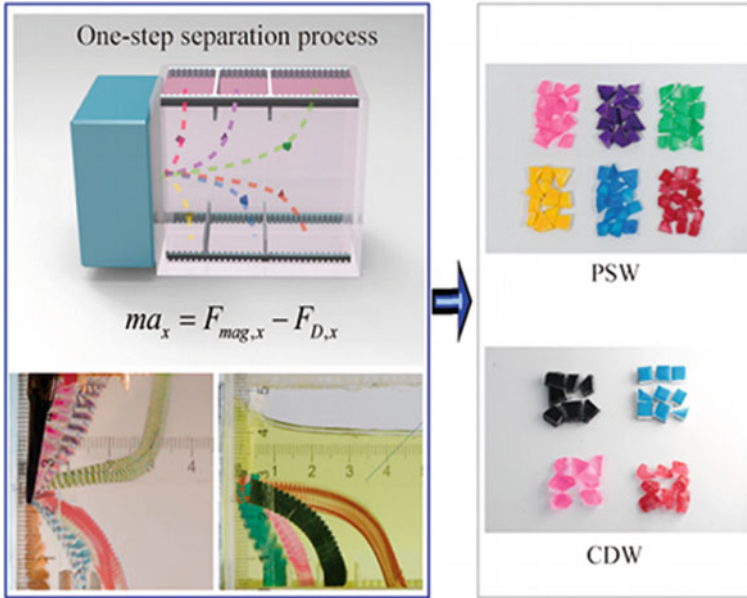


Fig. 2.5 Magnetic projection for the one-step separation of multiple wasted materials. Reproduced with permission from Ref. [10]. Copyright 2020 American Chemical Society

8 mm will be collected within the boundary of the collector above the outlet port I. Other materials can be collected under outlet port II. In the experiment, a mixture of waste plastics was levitated and automatically separated and collected at different heights. The area above the magnet can also be automatically cleaned at the end of each separation process. The purity of each target materials can reach to above 96.2%.

In general, the magneto-Archimedes levitation could theoretically separate materials as long as their densities are different. It has a predominant advantage over common separation method that it can simultaneously separate multiple materials in one or just few trials, which evidently increases the efficient in separating, purifying or recycling solid materials. However, it may still need additional steps to deal materials with very similar densities or with a very large density gap. The applications in practical occasions should also be further studied.

2.3.2 Manipulation

As discussed in previous sections, it is known that magneto-Archimedes effect can generate a force that can affect the state of objects without direct touch. Hence, the magneto-Archimedes levitation also can be a significant method for the manipulation and accumulation of cells [12–14]. The magnetic forces, in fact, are in proportion

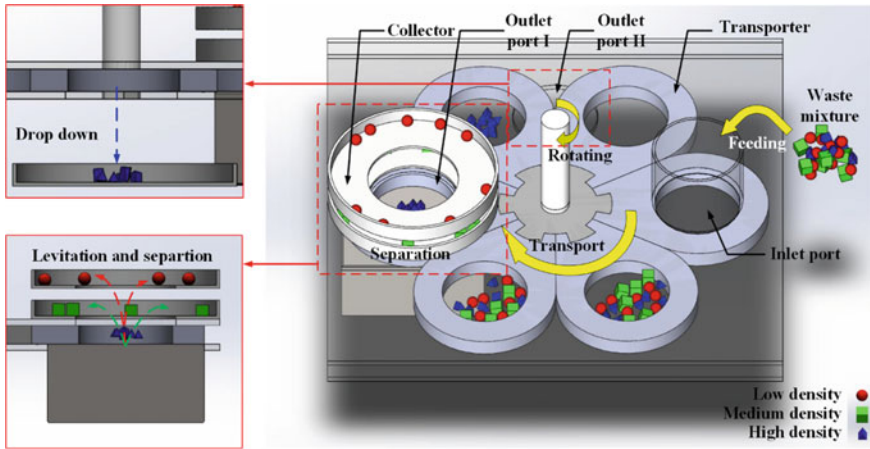


Fig. 2.6 Automatic separation device using permanent square magnet and its operation principle. Reproduced with permission from Ref. [11]. Copyright 2022 Elsevier

to the magnetic susceptibility of the material and the product of the field and its gradient. Thus, by designing the gradient direction of the magnetic field, the action of the sample, such as motion and aggregation, can be performed as expected.

A simple 3D cellular assembling method uses a simple magnet matrix of 2×2 to trap and aggregate cells at the lowest area of the magnetic field. The schematic of the method is shown in Fig. 2.7. Low concentration (34.6 mM) of Gd-DTPA is applied for low cytotoxicity. It allows the exposure of living cells for less than one day without leaving significant damage to the cells.

The distribution of the magnetic flux intensity is shown in Fig. 2.8. It is the simulation result of the magnets with the shape of 10 mm cubic. The atmosphere in the simulation is set as air. Considering the size of the magnet, the edges of the

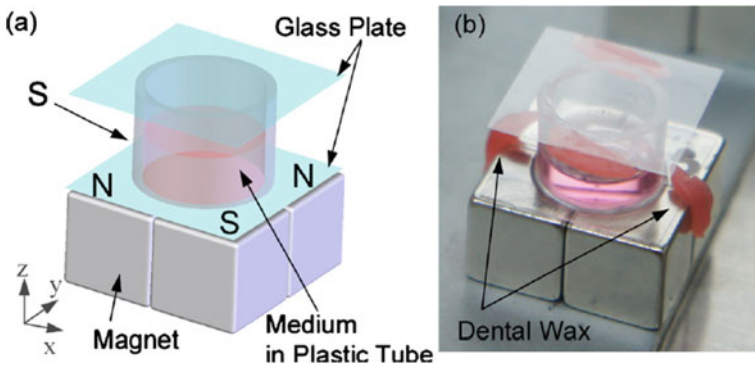


Fig. 2.7 Magneto-Archimedes levitation device for cell aggregation. **a** Schematic. **b** Photoimage. Reproduced with permission from Ref. [12]. Copyright 2011 AIP Publishing

magnet are rounded with the radius of 0.5 mm for more accurate result. The remanent flux density of the magnets was set to 1.2 T. The arrows in the figures demonstrate the direction and dimension of the magnetic forces. The dark area means there has lower magnetic flux intensity and that is where the diamagnetic particles, like cells, can be carried by the magnetic field. The magnetic susceptibility of Gd-DTPA (used as solute of paramagnetic medium) is measured by the nuclear magnetic resonance to estimate the magnetic force applied on the cells. The Gd-DTPA has the mass susceptibility of $5.406 \times 10^{-7} \text{ m}^3/\text{kg}$ and is different from the cell of 1.016×10^{-5} in volume magnetic susceptibilities. Based on these parameters, the magnetic force on the $z = 0.5 \text{ mm}$ plane (the thickness of the bottom of the container is considered) can be up to 12 pN, which is comparable to that of an optical trap [12].

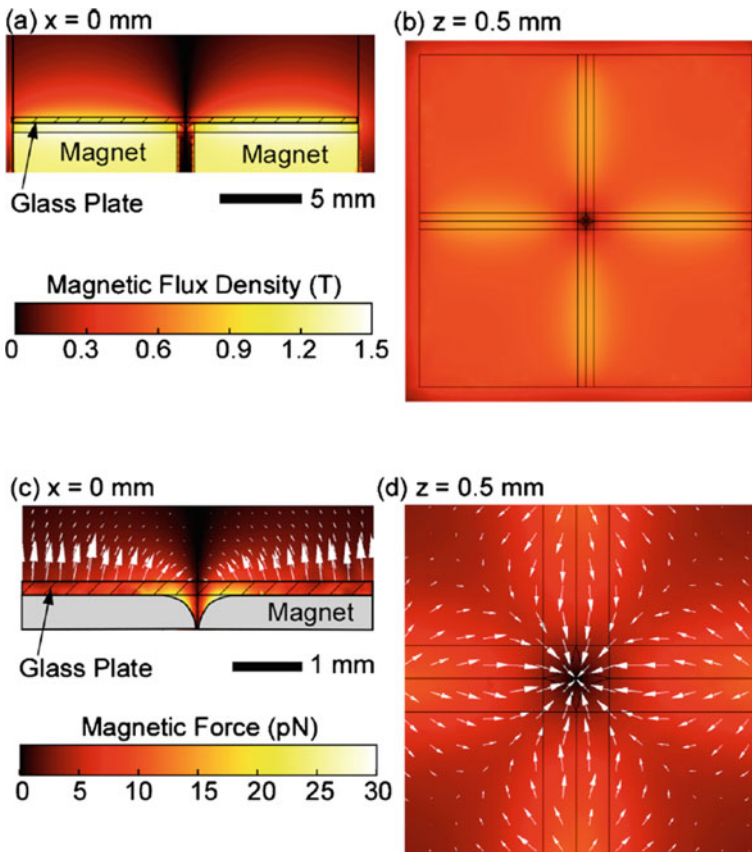


Fig. 2.8 **a** Magnetic flux density distribution on the plane at $x = 0$. **b** Magnetic flux density distribution on the plane at $z = 0.5 \text{ mm}$. **c** Vector and contour plots of the magnetic force applied on the cells on the plane at $x = 0$. **d** Vector and contour plots of the magnetic force applied on the cells on the plane at $z = 0.5 \text{ mm}$. Reproduced with permission from Ref. [12]. Copyright 2011 AIP Publishing

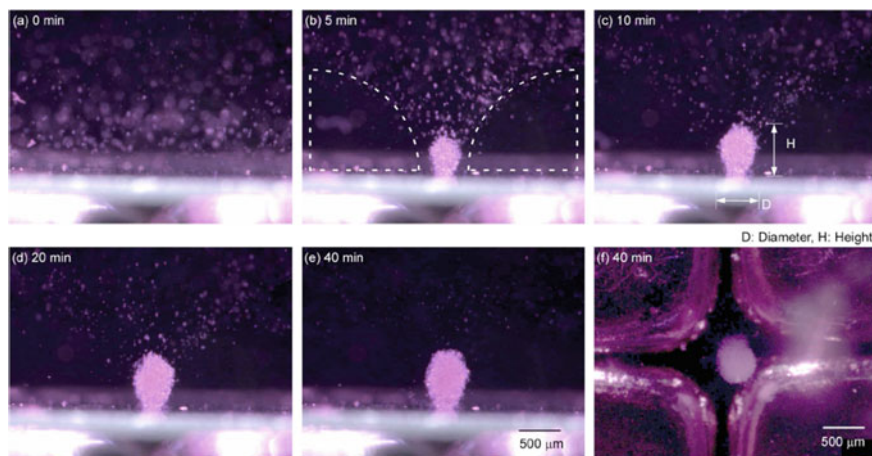


Fig. 2.9 The aggregation of cells in 40 min. **a** The initial image of cells when put into the magnetic field. The cells floating near the bottom and cells lying on the bottom went upward as they were repelled by the magnetic field. **b** The cells moved to the center area in the following several minutes. **c** An egg-shaped cell aggregate was formed at approx. 10 min ($\sim 470 \mu\text{m}$ diameter; $600 \mu\text{m}$ height). **d** At 20 min, most of the cells are aggregated at the center in an egg shape with $510 \mu\text{m}$ diameter and $690 \mu\text{m}$ height. **e** The size of the aggregated cells is almost the same in the following 20 min. **f** Top view of the aggregation after 40 min. Reproduced with permission from Ref. [12]. Copyright 2011 AIP Publishing

The cell in the container will be dragged up from the bottom by the magnetic force and pushed to the area above the center of the magnet matrix (Fig. 2.9). The cells become an egg-shaped aggregate after a ~ 20 min levitation. It is interesting that there are few cells in the sector areas near the center (as shown in Fig. 2.9b, the area surrounded by dotted lines). The result well matches the simulation results: the magnetic force in the light area pushed the cells to the dark area and cause the aggregation in the dark area.

Taking the xy component into concern, the moving velocity of a cell near the aggregation area (0.2 mm away, on the bottom of the container) is measured as $5 \mu\text{m/s}$. Accordingly, the magnetic force at this area is calculated as 1.4 pN . Thus the velocity is estimated as $8.3 \mu\text{m/s}$ according to Stokes' law. Considering the dragging force of the medium, the calculated results is in agreement with the actual value. It is also worth noticing that after 1 day aggregation (before the toxicity of Gd-DTPA cause vital damage to the cells), the cells contact closely to each other and formed a firm egg-like structure. The repetition of the magnet matrix can form a large area that can trap cell in a spheroid array formation [14]. These results proves that the prediction of the aggregation of the cells through simulation is reliable, and it is possible to fabricate arbitrarily shaped tissues by designing a suitable magnetic field. Furthermore, the method can be potentially applied to fabricate bio-actuators, such as a micropump and micropillars, by the self-assembly of the cells. The magneto-Archimedes effect become more conspicuous in much smaller scale, for the gradient

of magnetic flux intensity can reach to a relatively high level. It is an effective method to manipulate and arrange micro particles [16]. The manipulation can be carried out on nickel grids of the desired geometry and typical periodicity L , 1–10 μm . The grids are embedded in a 300 nm thick layer of polydimethylsiloxane (PDMS) and placed on a permanent magnet with magnetic flux intensity of 0.442 T. The Ni/PDMS composite structure can concentrate and modulate the uniform field of the magnet. The finite element calculation shown in Fig. 2.10a illustrates how the forces acting on the colloidal particles and drive them to specific positions. The fluorescently labelled colloidal particles are flowed with the paramagnetic medium (0.2–0.4 M $\text{Ho}(\text{NO}_3)_3$ in $\text{DMSO}/\text{H}_2\text{O}$) over the grid at $106 \mu\text{l s}^{-1} \text{cm}^{-2}$. As expected, magnetic particles locate on the nickel islands (Fig. 2.10b), while diamagnetic particles land above the grid voids (Fig. 2.10c). By simultaneously treating the magnetic and diamagnetic colloids, they can create multi-component arrays. For instance, the assembly of magnetic and diamagnetic particles of similar size on a square grid can form the shape of AB lattice, as shown in Fig. 2.10d. Spatial effects become important when particle sizes vary widely, as demonstrated by the AB2 structure in Fig. 2.10e. Smaller magnetic particles only fit into the threefold junctions of the honeycomb grid instead of the edges between adjacent larger particles (Fig. 2.10f).

In fact, the island larger than particles can aggregate several particles in particular configurations, which depend on the shape of islands and their relative dimensions to particles. The assembly of the particles in the islands is also known as colloidal ‘molecules’. The large-area confocal image reveals the accumulation four diamagnetic particles in each island, as shown in Fig. 2.10g. These tetramers are attached to the substrate with carbamide bonds and become permanent structure by silica deposition (Fig. 2.10h). The released tetramers in solutions can well maintain their structures. Similarly, hexamers can be prepared in triangular voids (Fig. 2.10i). The method can also afford the assembly of different particles. The AB dimer in Fig. 2.10j illustrates the assembly of multicomponent colloidal molecules. For the size of the egg-shaped voids can only afford the aggregation of one large particle (1.2 μm) and a small particle (0.8 μm), the dimer formed AB structure. By controlling the size of the island, AB2, AB3, and A2B2 clusters can be realized (Fig. 2.10k–m).

Except for the magnetic force, the interaction between magnetic dipoles is also effective for manipulating particles under ultra-high magnetic field (above 4 T). The interactions among magnetic dipoles can be divided into two categories depending on the directions of the dipoles and their configurations: attractive or repulsive. Specifically, a two-dimensional crystallization of particles is formed when repulsive interactions are applied to a system contains non-magnetic particles, such as gold. The gold spheres with diameters of 1.0 μm can form a triangular lattice in the plane perpendicular to the magnetic fields in the magneto-Archimedes levitation. Because the similarity to the Wigner crystals, it is called “magneto-Wigner crystal” [16].

When the magnetic field was applied, magnetic dipoles directed opposite to the field were induced in the gold spheres, and repulsive interactions among the spheres appeared in the horizontal direction. Figure 2.11a shows the formation of the magneto-Wigner crystal realized under the magnetic flux intensity of 4.87 T. Accordingly, the product of the field and the vertical field gradient BdB/dz reaches to

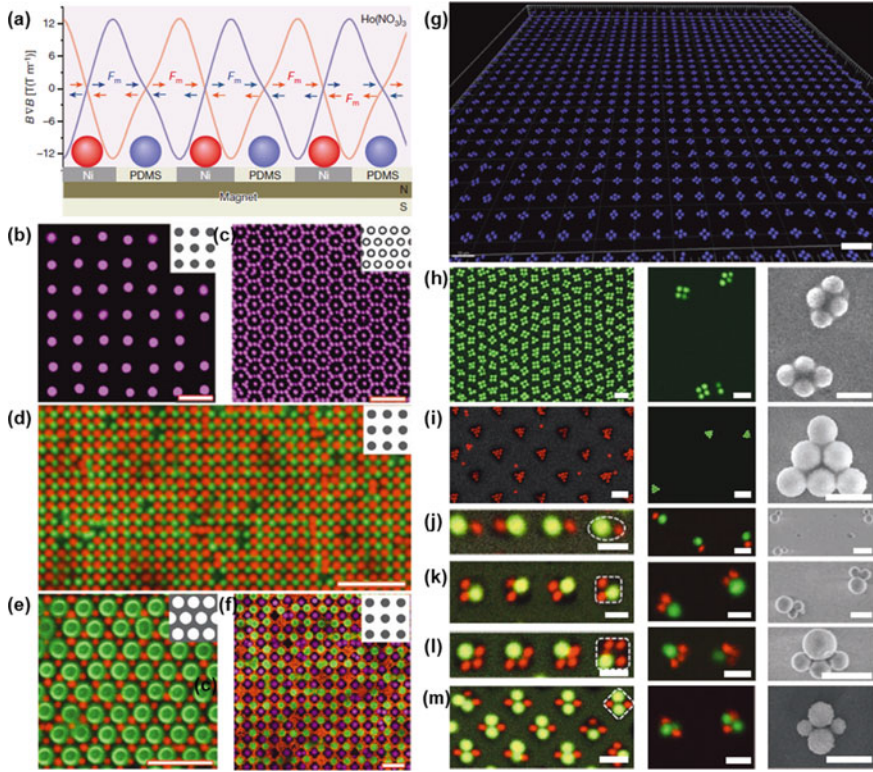


Fig. 2.10 Manipulation of micro particles above magnet matrix. **a** Structure of magnet matrix and simulation of magnetic forces. **b** Paramagnetic particles locate on the nickel islands. **c** Diamagnetic particles locate on the grid voids. **d** Magnetic and diamagnetic particles with similar sizes form the shape of AB lattice. **e** Magnetic and diamagnetic particles with different sizes form the shape of AB₂ structure. **f** Smaller magnetic particles fit into the threefold junctions of the honeycomb grid. **g** Large-area confocal image of the accumulation of four diamagnetic particles. **h** Particles of A₄ structure. **i** Particles of A₆ structure. **j** Particles of AB structure. **k** Particles of AB₂ structure. **l** Particles of AB₃ structure. **m** Particles of A₂B₂ structure. Reproduced with permission from Ref. [15]. Copyright 2013 Springer Nature

$\sim 265 \text{ T}^2/\text{m}$. It can be seen that the spheres away from the center presents larger interval, while the spheres near the center arranged closer. The main cause of the phenomenon is the magnetic dipoles. By adding the spheres gradually to the magnetic, the process of the formation of the magneto-Wigner crystal is demonstrated. At first, the single sphere is driven by the magnetic force and settled in the middle of the bore where has the minimal magnetic energy. The second sphere added to the container is also pulled to the middle of the bore. However, the repulsive interaction between each magnetic dipole prevents the spheres adjacent to each other. In this experiment, the spheres were further apart than in previous experiments. This seems to indicate that there are no other spheres around in the outer region, and that these

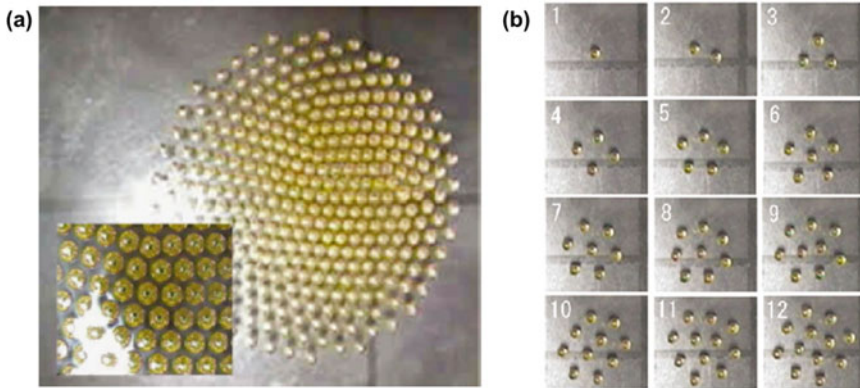


Fig. 2.11 Magneto-Wigner crystal formed by magneto-Archimedes levitation. **a** Magneto-Wigner crystal observed in a system of gold spheres with diameters of 1.0 mm **b** Magneto-Wigner crystals in a case with a small number of gold spheres. Reproduced with permission from Ref. [16]. Copyright 2005 AIP Publishing

spheres will provide repulsive forces towards the center of the hole, so that in this case the total cohesion acting on the sphere is less than in Fig. 2.11a. Similar results repeat after sequentially adding spheres. In the delicate balance of magnetic energy and dipole interactions, the spheres restructure their spatial distribution to minimize potential energy in the system as a whole. Finally, the spheres form various polygonal structures, as shown in Fig. 2.11b. The generation of magneto-Wigner crystal can be obviously observed in the figure, which can be used as a model for crystal growth process.

2.3.3 Auxiliary Method

The non-contact levitation brings benefits that it can isolate the target sample from unnecessary influences. An interesting trial based on the method is to apply the magneto-Archimedes levitation to the crystallization/polymerization process. The levitation of the product can be free from adverse influences of the container walls.

Using GdCl_3 instead of NaCl , which is common crystallizing agent for lysozyme, allows the crystallization processed during levitation in the magnetic field with the flux intensity of 3.8 T [17]. It requires approximately 3 days for the total growth of the crystal. The obtained crystal in levitation is shown in Fig. 2.12a, b. On contrary, the crystal generated from the boundary of the container is shown as Fig. 2.12c, d. For comparison, the crystal grown without applying the magnetic field is also shown in Fig. 2.12e, f. It is obvious that the crystals grow in levitation have the typical tetragonal habit and much fewer macroscopic flaws than that of other results, which indicates the method is effective to obtain high-quality crystals.

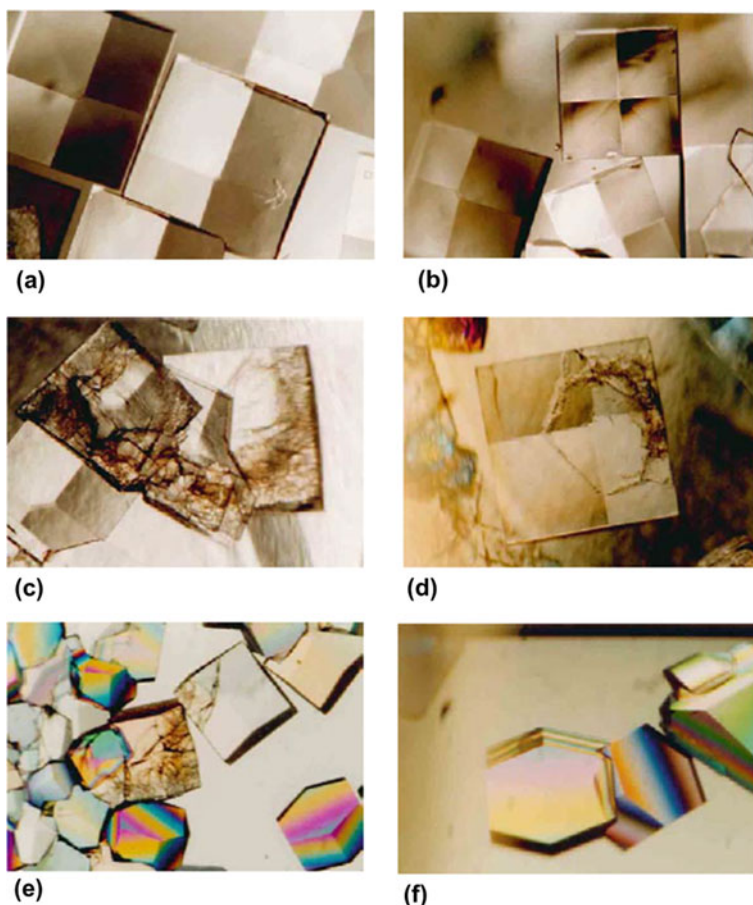


Fig. 2.12 Photographs of the lysozyme crystals after 3 days crystallization. **a, b** The levitated crystals at $z = \pm 40$ mm and 3.8 T. **c, d** The sinking crystals at $z = \pm 40$ mm and 3.8 T. **e, f** The crystals grown without applying the magnetic field. Reproduced with permission from Ref. [17]. Copyright 2004 Elsevier

References

1. Berry MV, Geim AK. Of flying frogs and levitrons. *Eur J Phys.* 1997;18(4):307.
2. Catherall AT, Eaves L, King PJ, et al. Floating gold in cryogenic oxygen. *Nature.* 2003;422(6932):579–79.
3. CRC handbook of chemistry and physics. CRC Press; 2004.
4. Maki S, Ataka M. Magnetic levitation with permanent magnet: application to three types of plant seed. *Jpn J Appl Phys.* 2007;46(5R):2910.
5. Kimura T, Mamada S, Yamato M. Separation of solid polymers by magneto-Archimedes levitation. *Chem Lett.* 2000;29(11):1294–5.
6. Hirota N, Kurashige M, Iwasaka M, et al. Magneto-Archimedes separation and its application to the separation of biological materials. *Physica B.* 2004;346:267–71.

7. Yokoyama K, Hirota N, Iwasaka M. Separation of collagen by magneto-Archimedes levitation. *IEEE Trans Appl Supercond.* 2007;17(2):2181–4.
8. Zhang C, Daofan T, Mingyi CAO, et al. A novel MagLev-based separation approach for heavy metal recycling. *Resour Conserv Recycl.* 2021;174:105769.
9. Zhang X, Gu F, Xie J, et al. Magnetic projection: a novel separation method and its first application on separating mixed plastics. *Waste Manage.* 2019;87:805–13.
10. Zhao P, Zhang X, Gu F, et al. Bidirectional magnetic projection: one-step separation for recycling mixed wastes. *ACS Sustain Chem Eng.* 2020;8(29):10774–85.
11. Xie J, Zhang C, Jia Y, et al. Automatic and continuous separation of mixed waste plastics via magneto-Archimedes levitation. *Sep Purif Technol.* 2022;287(34): 120537.
12. Akiyama Y, Morishima K. Label-free cell aggregate formation based on the magneto-Archimedes effect. *Appl Phys Lett.* 2011;98(16): 183702.
13. Akiyama Y, Morishima K. Label-free ultrarapid spheroid formation in microfluidic chip using magneto-archimedes effect. In: 2012 IEEE 25th international conference on micro electro mechanical systems (MEMS). IEEE; 2012, p. 116–19.
14. Akiyama Y, Morishima K. Spheroid array formation by non-label cell manipulation using magneto-archimedes effect. In: 2011 international symposium on micro-nanomechanics and human science. IEEE; 2011, p. 45–50.
15. Demirörs AF, Pillai PP, Kowalczyk B, et al. Colloidal assembly directed by virtual magnetic moulds. *Nature.* 2013;503(7474):99–103.
16. Takayama T, Ikezoe Y, Uetake H, et al. Self-organization of nonmagnetic spheres by magnetic field. *Appl Phys Lett.* 2005;86(23):234103.
17. Maki S, Oda Y, Ataka M. High-quality crystallization of lysozyme by magneto-Archimedes levitation in a superconducting magnet. *J Cryst Growth.* 2004;261(4):557–65.

Chapter 3

Magnetic Forces



Chengqian Zhang, Zhezai Hu, Huangzhe Dai, and Peng Zhao

3.1 Introduction

In the study of electromagnetic phenomena, this chapter delves into the domain of magnetic forces, shedding light on the intricate relationship between electric charges, currents, and fields. Central to this exploration are Maxwell's Equations [1, 2], which stand as a cornerstone of modern physics, elegantly describing the behavior of electric and magnetic fields. These equations provide a framework for comprehending how charges and currents give rise to the complex interplay of fields that encompass space.

As the exploration progresses, attention shifts to magnetic materials [3–6], each revealing distinct aspects of magnetism. Ferromagnetic materials display strong magnetic properties when subjected to an external magnetic field. Paramagnetic materials yield more subtly to the magnetic allure, while diamagnetic materials, such as water and copper, gently repel magnetic fields, exposing the fundamental nature of their properties.

In the realm of magnetic interactions, ferromagnetic materials exhibit strong magnetic properties. Under the influence of an external magnetic field, these materials demonstrate powerful magnetism. The expectation of equilibrium is disrupted within a magnetic field, as magnetic forces exert torque and translational forces on the materials. Earnshaw's theorem highlights the complexity of achieving stable equilibrium in static magnetic fields [7, 8]. However, innovation transcends these limitations by harnessing the interplay of gravity and magnetic forces to achieve stable levitation, thereby paving the way for magnetic separation and particle manipulation.

Overall, Chapter 3 provides a comprehensive examination of magnetic forces, revealing the intricate relationship between electric and magnetic fields as elucidated by Maxwell's Equations. This realm encompasses the magnetization of magnetic

C. Zhang (✉) · Z. Hu · H. Dai · P. Zhao

The State Key Laboratory of Fluid Power and Mechatronic Systems, College of Mechanical Engineering, Zhejiang University, Hangzhou, China

e-mail: zhangcq@zju.edu.cn

materials and the complex interplay of forces and torques that govern the movement of particles. Furthermore, this understanding of magnetism not only advances our knowledge of electromagnetism but also holds immense potential for transformative technological applications.

3.2 Maxwell's Equations

Maxwell's equations are a set of four equations that describe the behavior of electric and magnetic fields in space. They were developed by James Clerk Maxwell in the 1860s and played a crucial role in the development of modern physics. The equations relate electric and magnetic fields to their sources, which are electric charges and currents. The first of Maxwell's equations, Gauss's law for electric fields, is a fundamental law of electromagnetism. It states that the electric flux through any closed surface is proportional to the electric charge enclosed by the surface. Mathematically, this can be written as:

$$\nabla \cdot E = \rho/\epsilon_0 \quad (3.1)$$

where ∇ is the divergence operator. This equation relates the electric field E to the charge density ρ . The left-hand side of the equation describes the divergence of the electric field, which represents the flow of electric field lines into or out of a point in space. The right-hand side of the equation represents the charge density, which is the amount of electric charge per unit volume. The constant ϵ_0 is the permittivity of free space. This equation delineates the relationship between electric charges and the resulting electric fields that propagate throughout space. It also illustrates that the electric field is a vector field, possessing both magnitude and direction. Additionally, it follows the principle of superposition, whereby the total electric field at a given point is the sum of the individual fields produced by nearby charges. It serves as the foundation for comprehending the other three Maxwell's equations.

The second of Maxwell's equations, Gauss's law for magnetic fields, is another fundamental law of electromagnetism. It states that the magnetic flux through any closed surface is always zero. Mathematically, this can be written as:

$$\nabla \cdot B = 0 \quad (3.2)$$

where B is the magnetic field. This means that magnetic field lines never start or end, but always form closed loops. This equation shows that magnetic monopoles, which would be the magnetic analogs of electric charges, do not exist in nature.

The third of Maxwell's equations, Faraday's law of induction, is a key principle behind the operation of many electrical devices, such as generators and transformers. It states that a changing magnetic field generates an electric field. Mathematically, this can be written as:

$$\nabla \times E = -\partial B/\partial t \quad (3.3)$$

The equation presented describes the relationship between the electric field E , and the changing magnetic field B . On the left-hand side of the equation, it depicts the curl of the electric field, which signifies the tendency of electric field lines to form closed loops around a particular point in space. On the right-hand side, it represents the rate of change of the magnetic field with respect to time. It is a fundamental principle in electromagnetism and is used to explain various phenomena, such as the generation of electricity in generators and the operation of transformers.

The fourth of Maxwell's equations, Ampere's law with Maxwell's correction, relates the magnetic field to the electric current that produces it. It describes how a current flowing in a wire creates a magnetic field that circles around the wire. Mathematically, Ampere's law can be written as:

$$\nabla \times B = \mu_0 j + \mu_0 \epsilon_0 \partial E/\partial t \quad (3.4)$$

where μ_0 is the magnetic constant, j is the current density. The first term on the right-hand side of the equation represents the magnetic field produced by the current, while the second term represents the magnetic field produced by a changing electric field. This correction term was added by Maxwell to account for the fact that electric currents can also create magnetic fields, as shown by the third of Maxwell's equations. It is a fundamental equation in electromagnetism that relates the curl of the magnetic field (B) to the current density (j) and the rate of change of the electric field (E) with respect to time. This equation, along with the other three Maxwell's equations, forms the foundation of classical electromagnetic theory.

One of the key contributions of Maxwell's equations to our understanding of magnetic fields is the concept of magnetic flux. Magnetic flux is a measure of the number of magnetic field lines passing through a given area. The lines form closed loops, which means that magnetic flux is conserved. This conservation law is a consequence of Gauss's law for magnetic fields, which states that the magnetic flux through any closed surface is always zero.

The concept of magnetic flux has important applications in electromagnetism, such as in the design of magnetic circuits and the calculation of magnetic forces. For example, the force exerted on a current-carrying wire in a magnetic field is given by the formula $F = IlB \sin(\theta)$, where F is the force, I is the current, l is the length of the wire, B is the magnetic field, and θ is the angle between the wire and the magnetic field. Another important contribution of Maxwell's equations to our understanding of magnetic fields is the relationship between electric currents and magnetic fields. According to Ampere's law, a current flowing in a wire creates a magnetic field that circles around the wire. The strength of the magnetic field is proportional to the current and inversely proportional to the distance from the wire. In addition, the changing electric field associated with a current can also create a magnetic field, according to Faraday's law. This is the principle behind the operation of transformers, which use a changing magnetic field to induce a voltage in a secondary coil.

In summary, Maxwell’s equations provide a deep understanding of the behavior of magnetic fields and their relation to electric charges and currents. They are fundamental to the study of electromagnetism and have numerous practical applications in modern technology.

3.3 Magnetization and Magnetic Materials

Magnetization is the transformative process through which a material obtains magnetism in the presence of a magnetic field. This remarkable phenomenon can manifest across a vast array of materials. Magnetism, as one of the fundamental enduring attributes of matter, has captivated humanity for millennia, serving as a wellspring of exploration and advancement. Its historic influence encompasses the invention of the compass, lauded as one of the “Four Great Inventions” from ancient China, and its omnipresence in the constituent components of contemporary information and communication devices further attests to the pervasive and extensive integration of magnetism in materials.

Materials can be categorized into three simple types based on their magnetic susceptibility χ : ferromagnetic ($\chi \gg 1$), paramagnetic ($\chi > 0$), and diamagnetic ($\chi < 0$). The materials that are widely used in various applications are all ferromagnetic materials ($\chi \gg 1$), which exhibit noticeable magnetism under external magnetic fields. However, for the vast majority of materials, their magnetism is very weak (magnetic susceptibility $|\chi| < 10^{-5}$), making it difficult for them to exhibit significant magnetic response under external magnetic fields. Magnetism arises from the motion of charged particles, such as electrons, in a material. When electrons move in a certain direction, they generate a magnetic field. In a magnetized material, the magnetic moments of the electrons are aligned in the same direction, creating a net magnetic moment for the material. The strength of the magnetization is proportional to the number of magnetic moments per unit volume and their degree of alignment. The values of magnetic susceptibility for typical materials are shown in Fig. 3.1 [9]. Most matter exhibit weakly magnetic properties ($|\chi| < 10^{-5}$) and are usually considered as non-magnetic materials.

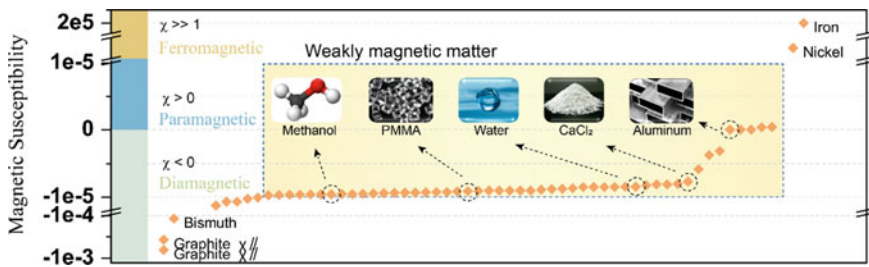


Fig. 3.1 Magnetic susceptibilities of common substances

3.3.1 Ferromagnetic Materials

Ferromagnetic materials are materials that exhibit strong magnetization even in the absence of an external magnetic field. They have a high degree of electron spin alignment, which leads to the spontaneous alignment of magnetic moments in the same direction. The magnetic behavior of ferromagnetic materials is described by the magnetization M and the magnetic field strength H . According to the coercivity (H_c), ferromagnetic materials can be divided into hard magnetic materials ($H_c > 1000$ A/m) and soft magnetic materials ($H_c \leq 1000$ A/m) [10]. Generally, once magnetized (after being exposed to a strong external magnetic field and then removed), hard magnetic materials like Alnico, SmCo alloys, and NdFeB alloys exhibit high remanence (represented by high B_r), which allows them to retain strong magnetism. Furthermore, their high coercivity (represented by high H_c) enables them to maintain a high residual magnetic flux density even when subjected to applied magnetic fields below their coercive field strength. In contrast, soft magnetic materials retain weak magnetism and are easily demagnetized.

Hard magnetic materials, also known as permanent magnets, are ferromagnetic materials with a high coercivity (H_c) and a high remanence (B_r). Coercivity is the measure of a material's resistance to becoming demagnetized, while remanence is the measure of the magnetic field strength that remains in a material after the external magnetic field is removed. Hard magnetic materials are used in applications where a strong and permanent magnetic field is required, such as in motors, generators, and magnetic storage devices. Examples of hard magnetic materials include alloys of rare earth metals such as neodymium-iron-boron (NdFeB) and samarium-cobalt (SmCo).

Soft magnetic materials, on the other hand, have a low coercivity and a low remanence, which means they can be easily magnetized and demagnetized. They are used in applications where a magnetic field needs to be rapidly and repeatedly switched on and off, such as in transformers, inductors, and electric motors. Examples of soft magnetic materials include iron-silicon alloys (e.g., silicon steel) and nickel-iron alloys (e.g., permalloy).

The magnetic properties of ferromagnetic materials can be described by the magnetization curve, which shows the relationship between the magnetic field strength H and the magnetization M . The magnetization curve is characterized by the saturation magnetization, which is the maximum magnetization that can be achieved in a material, and the magnetic susceptibility χ , which is the measure of the material's ability to become magnetized in response to an external magnetic field. All these parameters can be extracted from the magnetization curve shown in Fig. 3.2.

In summary, ferromagnetic materials are widely used in various applications due to their strong magnetization. Hard magnetic materials are used in applications where a strong and permanent magnetic field is required, while soft magnetic materials are used in applications where a magnetic field needs to be rapidly and repeatedly switched on and off. The magnetic properties of ferromagnetic materials can

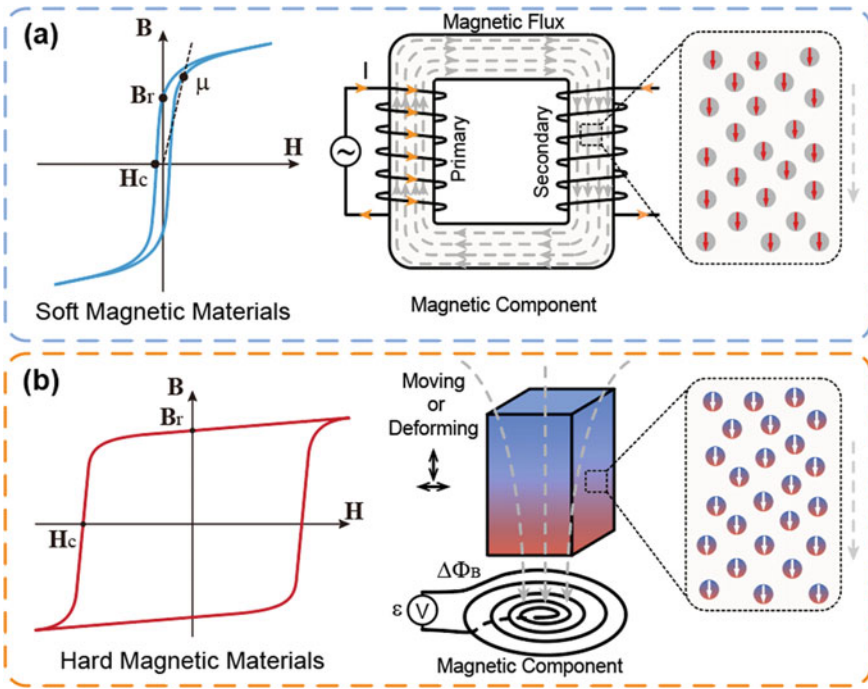


Fig. 3.2 Schematic of typical magnetization and working mechanism of **a** soft and **b** hard magnetic materials and electronics components. Reproduced with permission from Ref. [11]. Copyright 2021 Wiley

be described by the magnetization curve, which is characterized by the saturation magnetization and the magnetic susceptibility.

3.3.2 Paramagnetic Materials

Paramagnetic materials are a class of materials that exhibit weak magnetization, meaning that they do not have any permanent magnetic moment in the absence of an external magnetic field. However, when subjected to an external magnetic field, they acquire a magnetic moment proportional to the applied field. This is due to the presence of unpaired electrons in their atomic or molecular orbitals, which have intrinsic magnetic moments that can align themselves with the external magnetic field. The degree of magnetization in paramagnetic materials is proportional to the strength of the applied magnetic field, and it disappears as soon as the external field is removed.

The magnetic susceptibility of paramagnetic materials is positive and proportional to the applied magnetic field, as described by Curie's law. According to this law, the

magnetic susceptibility is given by $\chi = C/T$, where C is the Curie constant, and T is the absolute temperature (K) [12]. The Curie constant is a material-dependent constant that characterizes the strength of the magnetic response to an applied field. Typically, the magnetic susceptibility of paramagnetic materials is on the order of 10^{-6} to 10^{-3} , which is much weaker than that of ferromagnetic materials.

One important application of paramagnetic materials is magnetic resonance imaging (MRI), which uses the interaction between the magnetic moments of protons in the human body and a strong external magnetic field to generate high-resolution images of the body's interior. Gadolinium and dysprosium are often used as contrast agents in MRI due to their strong magnetic moments and good biocompatibility. Another application is in magnetic separation, where paramagnetic particles are separated from non-magnetic particles using an external magnetic field.

In conclusion, paramagnetic materials are an important class of magnetic materials that exhibit weak magnetization that can be aligned with an external magnetic field. Their magnetic properties are characterized by the magnetic susceptibility, which is generally small and proportional to the applied magnetic field. The applications of paramagnetic materials include MRI and magnetic separation, and their typical examples include gadolinium, dysprosium, europium, and neodymium.

3.3.3 Diamagnetic Materials

Diamagnetic materials, also commonly treated as non-magnetic materials, have a very weak magnetization that opposes the applied magnetic field ($\chi < 0$). Unlike ferromagnetic and paramagnetic materials, diamagnetic materials have completely filled electron shells, and there are no unpaired electrons to produce a magnetic moment. When subjected to a magnetic field, the electrons in the material are slightly displaced and produce a magnetic field opposite to the applied field, leading to a repulsive force between the material and the magnet.

Diamagnetism is a universal property of all materials, including non-magnetic substances such as copper, silver, gold, and even water. However, diamagnetism is a very weak effect, and its magnitude is typically several orders of magnitude smaller than the other two magnetic effects. For example, the magnetic susceptibility of copper is -1.1×10^{-5} , which is more than 100 times smaller than that of aluminum, a weak paramagnetic material with a susceptibility of 2.2×10^{-3} .

Mathematically, the magnetic susceptibility of diamagnetic materials is negative and very small, typically in the range of -10^{-6} to -10^{-8} . This value is independent of the applied magnetic field and temperature. The magnetic response of diamagnetic materials is characterized by the Larmor diamagnetic susceptibility, which is given by:

$$\chi_d = -(\mu_0 n e^2 \tau) / (6m) \quad (3.5)$$

where χ_d is the diamagnetic susceptibility, μ_0 is the magnetic constant, n is the number density of electrons, e is the charge of an electron, τ is the relaxation time of the electrons, and m is the mass of an electron.

Diamagnetic materials are generally weakly repelled by a magnetic field and exhibit a negative susceptibility that is independent of the magnetic field. They do not retain any magnetization when the magnetic field is removed. Some examples of diamagnetic materials include copper, silver, gold, bismuth, and graphite. Among these materials, Bismuth is one of the most diamagnetic elements, with a susceptibility of -1.6×10^{-4} , and is often used as a standard reference material for measuring the magnetic susceptibility of other materials.

Superconductors, which exhibit zero resistance to the flow of electric current, are a special class of diamagnetic materials. When a superconductor is cooled below its critical temperature, it expels all magnetic flux from its interior, a phenomenon known as the Meissner effect. This behavior is due to the formation of Cooper pairs, which are pairs of electrons that are bound together and behave as a single entity. Superconductors have a wide range of applications in fields such as power generation and transmission, magnetic levitation, and medical imaging. The development of high-temperature superconductors in the 1980s has made these materials more practical and economical for various applications.

In summary, diamagnetic materials are non-magnetic materials that exhibit weak repulsion in the presence of a magnetic field. Their magnetic susceptibility is negative and independent of the magnetic field. Superconductors, which are a special class of diamagnetic materials, exhibit zero resistance to electric current and expel magnetic fields from their interior. Despite their weak magnetic properties, diamagnetic materials have a wide range of applications in various fields, including biology, materials science, and physics.

3.4 Force on Magnetic Materials

3.4.1 Magnetic Force

When a material is placed in a magnetic field, it experiences a force known as the magnetic force. The magnitude and direction of this force depend on the magnetic field strength, the magnetic moment of the material, and the angle between the field and the moment. The magnetic force can be divided into two components: (i) the torque or moment, which tends to align the magnetic moment of the material with the field, and (ii) the translation force, which tends to move the material in a direction perpendicular to the field.

The torque or moment on a magnetic dipole in a magnetic field is given by the expression:

$$\boldsymbol{\tau} = \boldsymbol{\mu} \times \boldsymbol{B} \quad (3.6)$$

where $\boldsymbol{\tau}$ is the torque or moment, $\boldsymbol{\mu}$ is the magnetic moment of the dipole, and \mathbf{B} is the magnetic field. The cross product symbol \times indicates that the torque is perpendicular to both the magnetic moment and the magnetic field. The torque tends to align the magnetic moment of the dipole with the field, causing the dipole to rotate until it is aligned with the field.

The translation force on a magnetic dipole in a magnetic field is given by the expression:

$$\mathbf{F} = (\nabla(\boldsymbol{\mu} \cdot \mathbf{B}))/\mu_0 \quad (3.7)$$

where \mathbf{F} is the translation force, μ_0 is the magnetic constant, and ∇ represents the gradient operator. The translation force is perpendicular to both the magnetic moment and the magnetic field, and its direction depends on the gradient of the field. In regions of high field gradient, the translation force is strong and can cause the dipole to move rapidly in a direction perpendicular to the field.

In addition to the magnetic force on individual dipoles, there is also a force on a bulk sample of magnetic material, known as the magnetic force. The magnetic force on a material can be described mathematically using the following equation:

$$\mathbf{F} = \nabla(\mathbf{m} \cdot \mathbf{B}) \quad (3.8)$$

where \mathbf{m} is the magnetic moment of the magnetic material. The dot product (\cdot) between \mathbf{m} and \mathbf{B} indicates the projection of the magnetic moment along the direction of the magnetic field.

In general, the magnetic force on a material can be broken down into three components: (i) the torque due to the misalignment between magnetic moment and external magnetic field; (ii) the force due to the external magnetic field gradient. The torque/force due to the magnetic field gradient is the dominant effect for materials under a static or quasi-static magnetic field. It is important to note that even non-magnetic materials experience forces or torques when exposed to a varying magnetic field, as a result of the phenomenon of eddy currents. Eddy currents are a significant phenomenon that occurs in electrically conductive materials when subjected to changing magnetic fields. These currents circulate within the material, creating their own magnetic fields, which in turn induce additional electrical currents. This interplay between the original magnetic field and the induced currents results in the generation of forces and torques, which can be utilized to manipulate non-magnetic but conductive objects [13]. An interesting observation is that non-contact dexterous manipulation can be achieved on objects that contain electrically conductive material but not necessarily a significant amount of ferromagnetic material. This is possible due to the generation of eddy currents in the conductive material when exposed to time-varying magnetic fields. The interaction between these eddy currents and the magnetic field creates forces and torques that can be utilized for manipulation. Previous studies have used this phenomenon to induce drag on objects passing through a static magnetic field or to exert force on an object in a specific direction using a dynamic field. However, the application of this principle for dexterous manipulation of conductive

objects was not explored until 2021. Researchers presented a novel application where multiple rotating magnetic dipole fields are utilized to enable six degrees of freedom manipulation of conductive objects. Through dimensional analysis, along with multi-physics numerical simulations and experimental verification, the forces and torques on a conductive sphere within a rotating magnetic dipole field are characterized [13].

For a uniform magnetic field, the magnetic force on a material is zero, since there is no magnetic field gradient. However, in a non-uniform magnetic field, the force can be significant and can be used to manipulate and control the motion of magnetic materials. One important consequence of the magnetic force on materials is Earnshaw's theorem, which states that it is impossible to achieve stable equilibrium of a collection of point magnetic dipoles in a static magnetic field, using only permanent magnets. This theorem is important in the design of magnetic levitation systems, as it implies that additional control mechanisms, such as feedback control or electromagnets, are necessary to achieve stable levitation.

It is important to note that the magnetic force on a material is dependent on the magnetic properties of the material. Diamagnetic materials, which have a negative magnetic susceptibility, experience a weak repulsive force in a magnetic field. Paramagnetic materials, which have a positive magnetic susceptibility, experience a weak attractive force in a magnetic field. Ferromagnetic materials, which have a large positive magnetic susceptibility, experience a strong magnetic force that can result in magnetization and magnetic hysteresis.

3.4.2 Diamagnetic Force

When a diamagnetic material is placed in an external magnetic field, the magnetic moments of its atoms will experience a torque that tends to align them antiparallel to the applied field. This alignment results in a small negative magnetization of the material that opposes the applied field. In contrast to paramagnetic and ferromagnetic materials, the magnetic susceptibility of diamagnetic materials is independent of temperature and is typically several orders of magnitude smaller in magnitude. The diamagnetic susceptibility of a material is a universal property that arises from the response of its electron cloud to the applied magnetic field.

The force exerted on a diamagnetic material by a magnetic field can be calculated using the magnetic energy density U of the material in the field. The magnetic energy density is defined as the energy per unit volume required to create the magnetic field. In terms of the magnetic field strength H and the magnetic induction B , the magnetic energy density is given by:

$$U = 1/2\mu_0(H \cdot B) \quad (3.9)$$

where μ_0 is the magnetic constant, which has a value of $4\pi \times 10^{-7}$ T m/A. The force F on a small volume element δV of a diamagnetic material is given by the negative gradient of the magnetic energy density:

$$\mathbf{F} = -\nabla U = -\mu_0(\nabla \mathbf{H}) \cdot \mathbf{B} \quad (3.10)$$

where ∇ is the gradient operator. This equation shows that the force on a diamagnetic material is proportional to the gradient of the magnetic field, and is thus strongest in regions of high field curvature.

In 1842, Earnshaw conclusively demonstrated that a collection of point particles cannot be maintained in a stable equilibrium solely through the interaction forces governed by the classical inverse square law. This principle, commonly referred to as Earnshaw's theorem, affirms that a mechanical equilibrium structure composed exclusively of gravitational, electrostatic, and static magnetic forces is incapable of achieving stable suspension. Earnshaw's theorem states that a stable equilibrium cannot be attained by relying solely on electric and magnetic forces. Specifically, it asserts that it is impossible to hold a system of charged particles or magnets in stable equilibrium through any combination of electric and magnetic fields. This theorem also carries the implication that levitating a diamagnetic material using solely magnetic fields is unachievable due to the persistent destabilizing force acting on the material.

Nonetheless, it is feasible to levitate a diamagnetic material by harnessing a combination of magnetic and gravitational forces. In 1939, German physicist Braunbeck achieved stable levitation in a static magnetic field by utilizing diamagnetic materials possessing a negative magnetic susceptibility. This breakthrough supplemented Earnshaw's theorem and paved the way for the advancement of levitation technology using diamagnetic materials. Subsequently, researchers have been diligently working on constructing magnetic fields with more substantial gradients, ranging from 15 to 30 T, in order to achieve stable suspension for an expanded range of materials. These materials include metallic antimony, water, and even organic life forms. By meticulously arranging a system of permanent magnets and diamagnetic materials, it becomes possible to establish a stable levitation configuration wherein the diamagnetic material is suspended within the magnetic field.

3.5 Magnetic Buoyant Force

The potential energy of a material in a magnetic field is shown in Eq. 3.11:

$$E = -\frac{1}{\mu_0} \vec{m} \cdot \vec{B} = -\frac{\chi_s - \chi_m}{2\mu_0} B^2 V \quad (3.11)$$

where χ_s and χ_m are the magnetic susceptibilities of the material and the surrounding medium, respectively. $\mu_0 = 4\pi \times 10^{-7} \text{ N/A}^2$ is the vacuum permeability, B is the external magnetic field strength at the location, and V is the sample volume. From this, it can be seen that to achieve a stable suspension state, the magnetic potential energy must have a minimum value. The stable position must satisfy the condition:

$$\nabla^2 E = -\frac{\chi_s - \chi_m}{2\mu_0} \nabla^2 B^2 > 0 \quad (3.12)$$

Since $\nabla^2 B^2 \geq 0$ has been proven, the above equation can be simplified to:

$$\chi_s - \chi_m < 0 \quad (3.13)$$

It can be seen from this that a sample with a magnetic susceptibility less than that of the surrounding medium can achieve stable suspension under the action of magnetic forces. Professor Ikezoe achieved stable levitation of water droplets using a 60-fold compressed air, which increased the ratio of the magnetic susceptibilities of water droplets and air from ~ 0.042 to ~ 2.5 [14]. As a result, the required magnetic field strength and gradient for stable levitation were greatly reduced to $BdB/dz = 420 \text{ T}^2/\text{m}$. This allows the magnetic levitation method to no longer be limited to the use of super-strong magnetic field devices or materials with high diamagnetic susceptibility, laying a solid foundation for its widespread applications.

The magnetic buoyant force is a type of magnetic force that arises when a magnetic field is applied to a fluid containing magnetic particles/ions. This force is due to the interaction between the magnetic field and the medium surrounding sample, which can cause them to move or be suspended in the medium. The magnetic buoyant force has been studied in the context of magnetic separation and particle manipulation.

References

1. De la Barriere O, Hlioui S, Ahmed HB, et al. 3-D formal resolution of Maxwell equations for the computation of the no-load flux in an axial flux permanent-magnet synchronous machine. *IEEE Trans Magn.* 2011;48(1):128–36.
2. Ward AJ, Pendry JB. Refraction and geometry in Maxwell's equations. *J Mod Opt.* 1996;43(4):773–93.
3. Coey JMD. Hard magnetic materials: a perspective. *IEEE Trans Magn.* 2011;47(12):4671–81.
4. Jiles DC. Recent advances and future directions in magnetic materials. *Acta Mater.* 2003;51(19):5907–39.
5. Coey JMD. Magnetic materials. *J Alloy Compd.* 2001;326(1–2):2–6.
6. Buschow KHJ. New developments in hard magnetic materials. *Rep Prog Phys.* 1991;54(9):1123.
7. Simon MD, Heflinger LO, Geim AK. Diamagnetically stabilized magnet levitation. *Am J Phys.* 2001;69(6):702–13.
8. Geim AK, Simon MD, Boamfa MI, et al. Magnet levitation at your fingertips. *Nature.* 1999;400(6742):323–4.
9. CRC handbook of chemistry and physics. CRC Press; 2014.
10. Perigo EA, Weidenfeller B, Kollár P, et al. Past, present, and future of soft magnetic composites. *Appl Phys Rev.* 2018;5(3):031301.
11. Zhang C, Li X, Jiang L, et al. 3D printing of functional magnetic materials: from design to applications. *Adv Func Mater.* 2021;31(34):2102777.
12. Hatscher S, Schilder H, Lueken H, et al. Practical guide to measurement and interpretation of magnetic properties (IUPAC technical report). *Pure Appl Chem.* 2005;77(2):497–511.

13. Pham LN, Tabor GF, Pourkand A, et al. Dexterous magnetic manipulation of conductive non-magnetic objects. *Nature*. 2021;598(7881):439–43.
14. Ikezoe Y, Hirota N, Nakagawa J, et al. Making water levitate. *Nature*. 1998;393(6687):749–50.

Chapter 4

Stable Levitation



Chengqian Zhang, Zhezai Hu, Jun Xie, and Peng Zhao

4.1 Introduction

Earnshaw's Theorem, formulated by Samuel Earnshaw, serves as a foundational principle within classical mechanics [1, 2], positing the impossibility of point particles achieving stable equilibrium solely under classical inverse square law forces. This theorem resonates throughout the realms of physics, rendering stable suspension unattainable through gravity, electrostatics, and static magnetism. At its core lies the interplay of electric field line divergence and Gauss's law, resulting in the absence of stable equilibria in open spaces. The electric force derived from potential adheres mathematically to Laplace's equation, a perpetually divergence-free framework.

The theorem's significance reverberates in multi-particle scenarios, precluding stable configurations. Demonstrated by contradiction, equilibrium configurations teeter into instability due to potential energy extremities. Its implications span domains such as electric dipole orbits, and it curtails applications of static magnetic fields for levitation due to the inverse cube relationship.

A pivotal moment transpired in 1939 when German physicist Braunbeck defied this constraint, achieving stable levitation using diamagnetic materials. This breakthrough laid the foundation for the emergence of Magneto-Archimedes levitation, introduced by Yasuhiro Ikezoe in 1998 [3]. This technique amplifies buoyancy and magnetic forces by manipulating paramagnetic medium pressure, favoring permanent magnets over electromagnets. This chapter probes the equilibrium interplay, ranging from diamagnetic achievements to the technological leaps of Magneto-Archimedes levitation [4, 5].

C. Zhang (✉) · Z. Hu · P. Zhao

The State Key Laboratory of Fluid Power and Mechatronic Systems, College of Mechanical Engineering, Zhejiang University, Hangzhou, China
e-mail: zhangcq@zju.edu.cn

J. Xie

College of Mechanical Engineering, Zhejiang University of Technology, Hangzhou, China

The Magneto-Archimedes levitation method, an extraordinary feat within magnetic levitation, offers precise manipulation and analysis of objects suspended within paramagnetic mediums. Orchestrating magnetic buoyancy and gravitational forces, this method presents a captivating means of suspending and positioning objects without physical touch. This paper delves into the nuanced intricacies of the Levitation Feature, delving into vital aspects like Levitation Height [6, 7] and Levitation Posture. Furthermore, it introduces the groundbreaking concept of Circular Levitation, expanding stability beyond the central axis. This innovation holds promise across diverse applications, encompassing density measurements, defect detection, and beyond.

4.2 Earnshaw's Theorem

Earnshaw's theorem, named after Samuel Earnshaw, is a fundamental theorem in classical mechanics that states that a collection of point particles cannot be maintained in a stable equilibrium solely by the interaction forces governed by the classical inverse square law, i.e., a mechanical equilibrium structure composed solely of gravitational, electrostatic, and static magnetic forces cannot achieve stable suspension. The theorem states that there is no configuration of the particles that results in a stable equilibrium, i.e., a configuration where the forces on each particle sum to zero.

The behavior of a point charge in a static electric field can be explained by considering Gauss's law. In order for a particle to be in a stable equilibrium, small disturbances or "pushes" in any direction should not disrupt the equilibrium; the particle should return to its original position. This implies that the electric field lines surrounding the equilibrium position of the particle should all point inward, towards that position. If all the field lines around the equilibrium point converge towards it, then the divergence of the field at that point must be negative, indicating that it acts as a sink.

However, Gauss's law dictates that the divergence of any electric field in free space is zero. Therefore, in mathematical terms, any electrical force (\mathbf{F}) resulting from a potential (U) will always satisfy Laplace's equation, guaranteeing that it is divergenceless.

$$\nabla \cdot \mathbf{F} = -\nabla^2 U = 0 \quad (4.1)$$

In free space, the absence of local minima or maxima in the field potential is due to the fact that there are only saddle points. This implies that a stable equilibrium for a particle cannot exist, and there must be an instability in at least one direction. However, it is important to note that this argument may not be sufficient if all the second derivatives of the potential function, denoted as U , are null. In such cases, additional considerations are required to determine the stability of the system.

To comprehend Earnshaw's theorem, it is beneficial to examine a system comprising two charged particles. The interactions between these particles adhere to

Coulomb's law, which asserts that the force between two charged particles is directly proportional to the product of their charges and inversely proportional to the square of the distance separating them. When the two particles possess identical charges, they will repel each other. Conversely, if they bear opposite charges, they will attract each other. Upon attempting to establish a state of equilibrium by countering the forces between the particles, we discover that a stable equilibrium is unattainable.

Earnshaw's theorem was proven using the method of contradiction. Assume that a stable equilibrium configuration exists for a collection of point particles. By definition, the equilibrium configuration is one where the forces on each particle sum to zero. If we consider the second derivative of the potential energy with respect to the position of each particle, Earnshaw showed that this equilibrium configuration is necessarily a local maximum or a local minimum of the potential energy, but not a stable equilibrium. In other words, any small perturbation from the equilibrium configuration will result in the particles moving away from the equilibrium position, and the system will be unstable. Earnshaw's theorem has important implications in various areas of physics. For example, it has been used to prove that there can be no stable orbits of charged particles around a static electric dipole. This is because the forces between the charged particles fall off as the inverse square of the distance, which violates the conditions for stable equilibrium. The theorem also places a fundamental limitation on the use of static magnetic fields for levitation. This is because, as stated earlier, the forces between magnetic dipoles fall off as the inverse cube of the distance, which violates the conditions for stable equilibrium.

An intriguing implication of Earnshaw's theorem is its essential restriction on the practical application of static magnetic fields for levitation purposes. As previously mentioned, the forces between magnetic dipoles decline in proportion to the inverse cube of the distance, thereby contradicting the conditions required for stable equilibrium. However, in 1939, German physicist Braunbeck managed to achieve stable levitation within a static magnetic field by utilizing diamagnetic materials with negative magnetic susceptibility. This breakthrough not only provided a supplementation to Earnshaw's theorem but also paved the way for the advancement of diamagnetic levitation technology.

Diamagnetic levitation relies on the fact that the magnetic susceptibility of diamagnetic materials is negative, which means that they are repelled by magnetic fields. This repulsion results in a force that can balance the force of gravity, allowing the diamagnetic material to levitate stably in a magnetic field. The force of the magnetic field on a diamagnetic material is given by:

$$F = -\chi V \nabla B^2 / (2\mu_0) \quad (4.2)$$

where χ is the magnetic susceptibility of the material, V is the volume of the material, B is the magnetic field, and μ_0 is the permeability of free space.

To achieve stable levitation, the potential energy of the diamagnetic material in the magnetic field must have a minimum, which means that the magnetic susceptibility of the material and its surrounding medium must satisfy the condition:

$$\chi_s - \chi_m < 0 \quad (4.3)$$

where χ_s is the magnetic susceptibility of the surrounding medium. This condition ensures that the potential energy of the diamagnetic material in the magnetic field is minimized at the center of the field, where the force of the magnetic field is balanced by the force of gravity.

4.3 Magneto-Archimedes Levitation

4.3.1 Principle

As we discussed before, samples can be levitated stably using magnetic field when $\chi_s - \chi_m < 0$. Thus, the study of weakly magnetic samples ($|\chi| \leq 10^{-5}$), which are typically considered “non-magnetic”, suspended in paramagnetic environments has become increasingly widespread. This technology utilizing the magnetic buoyant force to stable the sample and the buoyant force from surrounding medium to provide the enormous force to against gravity, is widely called “Magneto-Archimedes levitation”. The concept “Magneto-Archimedes levitation” was firstly proposed by Yasuhiro Ikezoe in 1998 [3]. They utilized the gravitational and magnetically induced buoyancy forces in the host paramagnetic atmosphere (i.e., pressurized oxygen) to balance the gravitational force on the levitating object. By increasing the pressure of the gaseous paramagnetic medium, there are two main benefits: (i) the buoyant force is increased due to the density increasement of the surrounding medium; and (ii) the magnetic susceptibility of the paramagnetic atmosphere is significantly strengthened, since there is more paramagnetic oxygen gas molecule in a unit volume, i.e., the ratio of magnetic susceptibility between medium and object (water) was boosted from ~ 0.042 to ~ 2.5 at 60 atm. Through this method with both buoyancy force and magnetic force enhanced, the requirement to the magnetic field, i.e., magnetic source, can be enormously reduced, resulting in the wide application of permanent magnet instead of superconducting electromagnet (Fig. 4.1).

The magnetic force F_m and Archimedes buoyant force F_b acting on the object surrounded by paramagnetic medium can be given by:

$$\vec{F}_m + \vec{F}_b = \frac{\chi_s - \chi_m}{\mu_0} V_s (\vec{B} \cdot \nabla) \vec{B} + (\rho_s - \rho_m) V_s \vec{g} \quad (4.4)$$

where subscript s and m represent the object and paramagnetic medium, χ is the magnetic susceptibility, ρ is the density, V_s is the volume of object, \vec{B} is the magnetic field, and \vec{g} is the gravitational acceleration. Based on this equation, Magneto-Archimedes levitation can be realized using a magnetic field source to produce magnetic field strength and gradient $(\vec{B} \cdot \nabla) \vec{B}$ once the magnetic susceptibility and density of the surrounding paramagnetic medium is sufficient to satisfy $\vec{F}_m + \vec{F}_b = 0$.

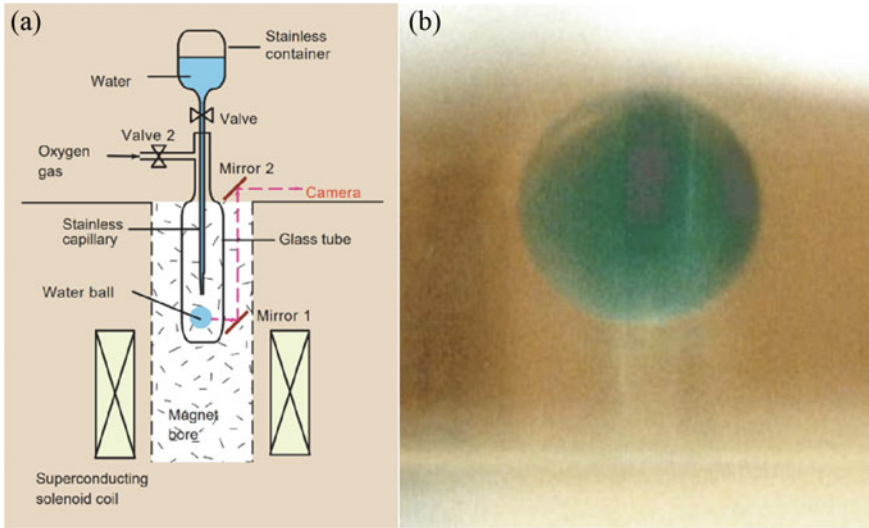


Fig. 4.1 **a** Schematic and **b** picture of levitating water in a superconducting solenoid. Reproduced with permission from Ref. [3]. Copyright 1998 Springer Nature

Before Magneto-Archimedes levitation is proposed, scientists always utilized strong magnetic field source, i.e., superconducting electromagnet, to produce extremely high magnetic field (>10 T) to achieve diamagnetic levitation. With the help of paramagnetic medium, the requirement for magnetic source is significantly reduced and permanent magnets is able to levitate weakly magnetic objects.

4.3.2 Paramagnetic Medium

The utilization of denser solutions has been discovered to enhance the buoyancy experienced by the sample, thus partially counteracting the force of gravity. Moreover, the use of a paramagnetic medium with higher magnetic susceptibility can amplify the magnetic force acting on the sample under similar circumstances. Common paramagnetic media with elevated magnetic susceptibilities include metal salt solutions containing ions such as Mn^{2+} , Gd^{3+} , and Dy^{3+} [8]. These paramagnetic solutions are easily prepared and stored, possess stable chemical properties, and are suitable for diverse applications. As a result, the development of new paramagnetic solutions has reduced the reliance on magnetic suspension systems that necessitate high field strength and gradient, enabling the employment of low-strength electromagnets or even permanent magnets in Magneto-Archimedes levitation technology.

The research implications of this advancement primarily include density measurements of weakly magnetic materials and non-contact magnetic manipulation of

suspended samples. For instance, in 2002, Yamato et al. employed a < 10 T superconducting electromagnet alongside a high-concentration MnCl_2 aqueous solution at 70°C under atmospheric pressure to achieve real-time observation of the polymerization process of benzyl methacrylate, a high polymer. The stable position of the material in the magnetic field changed due to variations in properties, particularly density and magnetic susceptibility, during the polymerization process. This study also demonstrated the potential of magnetic control to alter the position of suspended samples by adjusting the magnetic field strength [9]. In 2004, Maki et al. used a 3.8 T electromagnet and GdCl_3 to achieve high-quality lysozyme crystallization, as depicted in Fig. 4.2, where crystals grown in the suspended state exhibited improved orientation and fewer macroscopic defects [10]. Furthermore, in 2005, Yakayama et al. employed a 4.87 T magnetic field and a 40 wt% MnCl_2 solution to suspend and self-assemble gold particles, observing a phenomenon similar to crystallization by introducing a paramagnetic medium to amplify the magnetic force between particles [11]. In 2004, Winkleman et al. constructed a magnetic suspension device with a substantial magnetic field gradient using a permanent magnet magnetic tip [12] and combined it with a low-concentration $\text{Gd}\cdot\text{DTPA}$ solution to create a biocompatible paramagnetic medium for capturing and manipulating cell particles. This demonstrates the gradual shift in the composition of magnetic suspension systems from superconducting electromagnets to permanent magnets, significantly reducing the requirements for employing Magneto-Archimedes levitation technology. The combination of permanent magnets and paramagnetic solutions has expanded the range of applications for magnetic suspension technology.

The initial magnetic susceptibility of paramagnetic solution is given by:

$$\chi_m = \frac{\mu_0 n m_{\text{eff}}^2}{3k_B T} + \chi_{\text{solvent}} \quad (4.5)$$

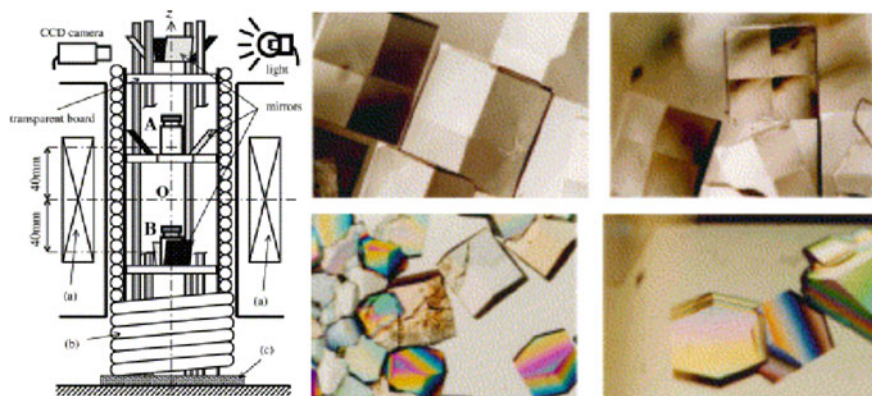


Fig. 4.2 Early applications of magnetic levitation technology: high-quality crystal growth in an electromagnetic coil device. Reproduced with permission from Ref. [10]. Copyright 2004 Elsevier

Table 4.1 Effective magnetic moment of different ions [13]

Ion	Number of unpaired electrons	m_{eff}/μ_B
Ti ³⁺	1	1.73
Ni ²⁺	2	2.8–3.5
Cr ³⁺	3	3.70–3.90
Fe ²⁺	4	5.1–5.7
Mn ²⁺	5	5.65–6.10
Fe ³⁺	5	5.7–6.0
Ga ³⁺	7	8.9
Dy ³⁺	5	10.6

where n is the number density of the ions or particles, m_{eff} is the effective magnetic moment of the paramagnetic salt ion, k_B is Boltzmann constant, T is temperature, χ_{solvent} is the bulk magnetic susceptibility of the solvent. For paramagnetic salts, m_{eff} is usually expressed in multiples of Bohr magnetons, $\mu_B \approx 9.27 \times 10^{-24} \text{ J/T}$, which is used to describe the magnetic properties of electrons in atoms and molecules, particularly their interaction with external magnetic fields. Typical metal ions and their effective magnetic moments are listed in Table 4.1. There are two drawbacks when employing paramagnetic salt solution as medium: (i) the highest concentrations attainable of these ions are typically less than 5 mol/L, corresponding to magnetic susceptibility of e.g., $\chi_m = 1.77 \times 10^{-3} - 9 \times 10^{-6} \approx 1.77 \times 10^{-3}$ for 3 M Dy³⁺ solution at room temperature ($T = 300 \text{ K}$); (ii) highly concentrated paramagnetic salt solutions are toxic for living matter, such as cells and tissues, limiting their applicability in biological levitation.

Magnetic nanoparticle dispersions, i.e., magnetic fluid or ferrofluid, containing superparamagnetic nanoparticles (NPs) provide an intriguing alternative due to their considerably high magnetic moment and capacity for tailoring surface chemistries in order to achieve compatibility with living cells. Specifically, an iron oxide nanoparticle with an effective diameter of 5 nm shows effective magnetic moment of ca. 3400 μ_B . These high values suggest that a much lower concentration of NPs can be used to achieve the same level of susceptibility as paramagnetic salt solutions. However, it is important to note that superparamagnetic nanoparticles saturate at much lower fields compared to ionic solutions. In an ideal scenario, there are no intermolecular interactions, such as dipole–dipole interactions or van der Waals forces, between the magnetic nanoparticles in a magnetic fluid, i.e., there is no aggregation observed among these nanoparticles. In this ideal case, the magnetic fluid can be considered as a single system consisting only of individual particles. The magnetization intensity of the magnetic fluid can be effectively described using the Langevin function model.

$$M = nm_{\text{eff}} \left(\coth x - \frac{1}{x} \right) \quad (4.6)$$

where $x = \frac{m_{\text{eff}}\mu_0 H}{k_B T}$.

In addition, it is necessary to consider the influence of thermal fluctuations on the suspension of magnetic nanoparticles under strong field gradients, unlike paramagnetic salts which do not face this issue. A rough estimate can be obtained by comparing the magnetic energy of a fully magnetized and comparing this value to thermal energy. Gerber et al. [14] have developed the following criterion to estimate its diameter D_p :

$$|F|D_p \leq k_B T \quad (4.7)$$

where $|F|$ is the magnitude of the total force acting on the particle. For the Fe_3O_4 particles in water, the threshold diameter is $D_p = \frac{k_B T}{|F|} = 40 \text{ nm}$ [15]. Larger particles will partially migrate towards the high-field regions near magnetic sources. The manipulation of cells and other biological materials requires careful consideration of surfactants, pH value, and ionic strength when using ferrofluids to ensure biocompatibility. It is crucial to maintain a pH value of approximately 7, and the nanoparticle materials must be non-toxic to cell cultures. Additionally, it is important to maintain colloidal stability to ensure the viability of live cells. However, one limitation of ferrofluids is their opacity, which can make observation challenging unless a fluorescent dye is used.

4.3.3 Required Magnetic Field

The successful application of Magneto-Archimedes levitation heavily depends on the magnetic field. As mentioned earlier, the use of a high-density paramagnetic liquid medium significantly reduces the necessary magnetic field and field gradient to $\text{BdB/dz} = 420 \text{ T}^2/\text{m}$. This enables the levitation of samples using the magnetic field generated by permanent magnets. Nevertheless, it is crucial to carefully construct an appropriate magnetic field to achieve stable sample suspension. In a magnetic field, there must be a place satisfying $\nabla^2 B^2 \geq 0$, i.e., the stable levitation point. Before employing the Magneto-Archimedes levitation, it is necessary to find out whether the manipulation/levitation region has the stable levitation, i.e., the minimum magnetic potential value for diamagnetic object. Therefore, choosing an adequate magnetic field is the key to Magneto-Archimedes levitation.

Here, taking single rectangular magnets for example, spatial magnetic field above a series of square magnets with various length to height ratio ($alb = 0.5\text{--}2$) are simulated using COMSOL Multiphysics and shown in Fig. 4.3. The grade designation of the magnet is N52, indicating the remanence ranges from 1.42 to 1.48 T (T). From the simulation results, two points can be observed: (1) There will always be a region of minimum values on the surface of the magnet; (2) As the length/height ratio increases, the range of usable minimum value regions also increases. Certainly, for magnets with the same height, increasing the surface area of the magnet pole will lead to a decrease in the magnetic field gradient, thus reducing the strength of the magnetic field force. On the other hand, if a magnet with a smaller pole area, commonly

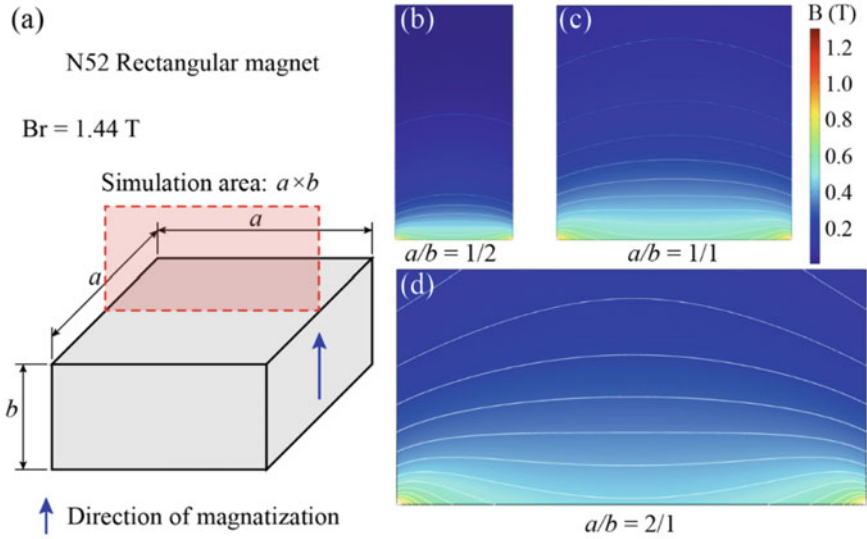


Fig. 4.3 Simulation of the magnetic field distribution above a N52 rectangular magnets. **a** Schematic of magnet, and simulation results of magnets with length/height ratio of **b** $a/b = 1/2$; **c** $a/b = 1/1$; **d** $a/b = 2/1$

known as a magnetic needle, is chosen, it can generate considerable magnetic force for particles. However, due to its limited range of effect, the overall range of stable levitation is also greatly restricted. This result provides us with some preliminary insights for designing the desired magnetic field: for magnets with the same height, a smaller pole area can generate a larger magnetic field force, but the operational area is also smaller, and vice versa.

4.4 Levitation Feature

4.4.1 Levitation Height

There are two main forces acting on the levitating object in the paramagnetic medium: Magnetic buoyant force F_m , and buoyant force F_b . The former magnet exhibits a magnetic field in all directions, while the latter magnet only exerts a force in the direction of gravity. In a Cartesian coordinate system, a suspended sample must satisfy the conditions $F_{mx} = F_{my} = 0$, and $F_{mz} = F_b$. The magnetic buoyant force varies at different positions within the magnetic field. Typically, for square magnets and circular/ring magnets, the stable suspension position is located along a vertical line passing through the center of the surface. Nevertheless, at different locations along this line, the experienced F_{mz} differs. Thus, considering Eq. 4.4, it becomes

evident that, apart from the magnetic source, factors such as solution density and the magnetization of both the solution and the sample influence the suspension height.

Here taking single ring magnet as an example, as shown in Fig. 4.4 [16]. Two kinds of ring magnet with axial magnetization are used to create the magnetic field, i.e., N35-H20 (inner radius $r_1 = 20$ mm, outer radius $r_2 = 30$ mm, height $h = 20$ mm, and surface magnetic pole density $\sigma = 1.23$ T) and N35-H10 ($r_1 = 12.5$ mm, $r_2 = 25$ mm, $h = 10$ mm, and $\sigma = 0.88$ T). Under the influence of a gradient magnetic field in the axial direction, the diamagnetic objects (e.g., cells, carbon materials, and polymers) immersed in the paramagnetic solution will be relocated at an equilibrium levitation position along the centerline of the magnet (Fig. 4.4a). The transparent paramagnetic solutions allow a good visualization of the submerged objects.

The magnetic force that is applied on a diamagnetic object around the N35-H20 ring magnet (provided by Jiuci Magnets, Inc., Beijing, China) can be calculated. In the blue region in Fig. 4.4a, the diamagnetic object in the tube is forced to move away from the centerline of the magnet, while the object is forced to move along with the

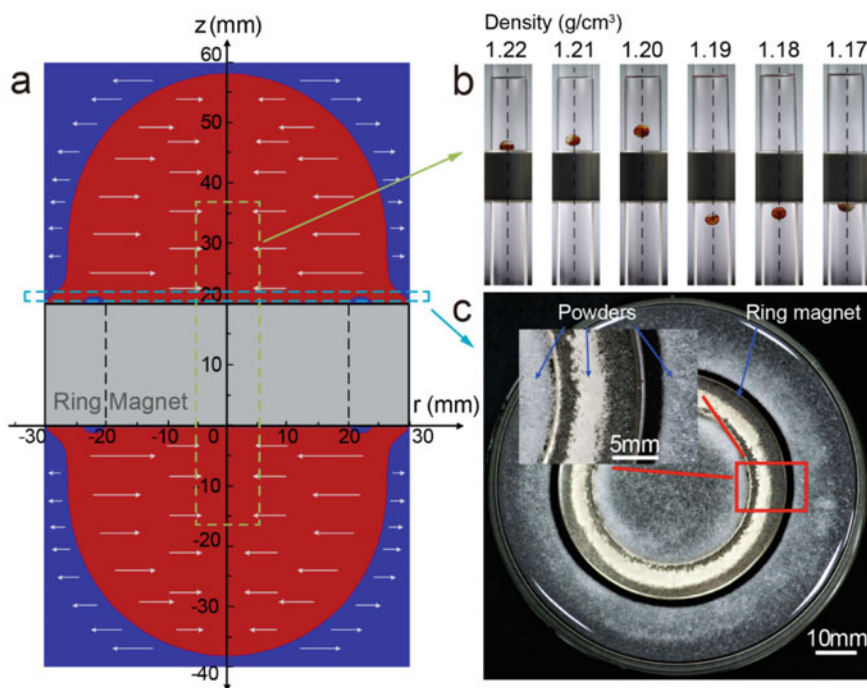


Fig. 4.4 Magnetic force acting on a diamagnetic object around the ring magnet. **a** Plot illustrating the direction of the horizontal force in the r - z plane surrounding the N35-H20 ring magnet. The red region indicates the horizontal force directed towards the centerline, while the blue region represents the reverse direction. **b** Plot of levitating object ($\rho_s = 1.1700$ – 1.2200 g/cm³) along the centerline in 2.0 M MnCl₂ aqueous solution. **c** Plot of distribution of highly dense powders (microcrystalline cellulose, diameters ~ 80 μ m) at a distance of 1 mm from the upper surface of the ring magnet. Reproduced with permission from Ref. [16]. Copyright 2022 American Chemical Society

centerline in the red region. This finding explains the phenomenon that the object assembles along the centerline, see in Fig. 4.4b. As shown in Fig. 4.4a, a unique pattern of the magnetic force that applied on the surface of the ring magnet can be found: the force drives the object to move away from the centerline in the semi-circular blue region, while the object is forced towards the centerline in the red region. Microcrystalline cellulose powders (purchased from Sinopharm Chemical Reagent Co., Ltd, Beijing, China) are used to verify this phenomenon. The microcrystalline cellulose powders are of higher density ($\rho_s = 1.605 \text{ g/cm}^3$), and consequently, they subside on the upper surface of the ring magnet. The ring magnet configuration exhibited that high-density powders can be dispersed around the inner and outer rings of the magnet, as shown in Fig. 4.4c. This distribution of the powders is consistent with the pattern of the magnetic force distribution (see Fig. 4.4a). The proposed mathematic model improves the understanding of the single ring Magneto-Archimedes levitation. In Fig. 4.4b, standard density beads with different densities ($\rho_s = 1.1700 - 1.2200 \text{ g/cm}^3$) are levitated along the centerline in 2.0 M MnCl_2 aqueous solution. The levitation height varies with the bead's density. The experiment results are consistent with the calculation results. According to Eq. 4.4, once the magnetic field and paramagnetic medium are established, the levitation height is primarily influenced by the magnetic susceptibility and density of the object. However, it is worth noting that the density plays a more prominent role due to the minimal variations in magnetic susceptibility among different materials.

Glass beads of standardized densities ($1.1200 - 1.3500 \pm 0.0002 \text{ g/cm}^3$, purchased from American Density Materials, Inc., Staunton, VA, USA) are tested using different solutions and magnets, and the experiments are performed at an ambient temperature of 23 °C. Figure 4.5 shows the actual density values (dots) and calculated results (lines) under two different magnets (N35-H20 and N35-H10) using 1.5 M, 2.0 M, 2.5 M and 3.0 M MnCl_2 aqueous solutions. From Fig. 4.5, it can be seen that the calculated curves show a good agreement with the actual values of these standardized density glass beads. These results confirm the effectiveness of the derived density measurement equation under different magnets and different paramagnetic solutions. The ring magnets in Fig. 4.5a, b were N35-H20 and N35-H10, respectively. A unified mathematic model is necessary to precisely correlate the density, magnetic field and levitation height. The proposed configuration can be used with ring magnets of any size. Aside from changing magnets, it can also be found that changing solutions could alter the ranges and sensitivity of density measurement of the configuration. As shown in Fig. 4.5a, choosing paramagnetic solutions with higher concentrations will yield a higher measurement range; $\rho_s = 1.1258 - 1.1706 \text{ g/cm}^3$ in 1.5 M solution, while $\rho_s = 1.2461 - 1.3379 \text{ g/cm}^3$ in 3.0 M solution. Similarly, a higher sensitivity can be achieved using paramagnetic solutions of lower concentrations. In sum, through changing solutions or magnets, the proposed configuration can be employed in various scenarios where a wider density measuring range or a higher sensitivity is required.

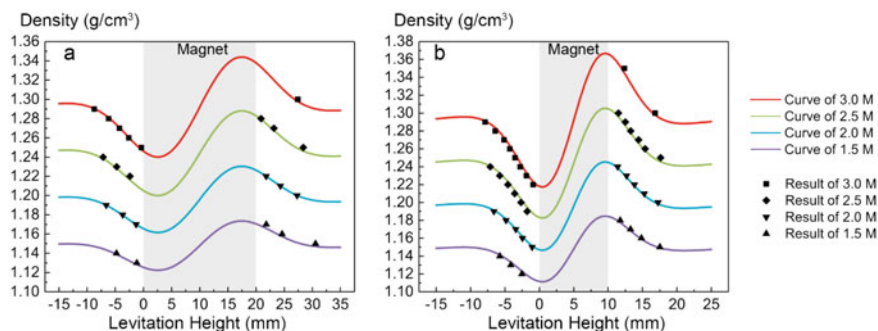


Fig. 4.5 The experimental results and actual densities in 1.5 M, 2.0 M, 2.5 M and 3.0 M MnCl_2 aqueous solutions. **a** The measurements of different standard density glass beads using the N35-H20 ring magnet. The view of the gray region is blocked by the ring magnet. **b** The measurements of different standard density glass beads using the N35-H10 ring magnet

4.4.2 Levitation Posture

Magneto-Archimedes levitation is capable of suspending, localizing, and orienting an object without the need for contact with a solid surface, such as a gripper or solid wall, by carefully balancing gravitational and magnetic forces. When subjected to an applied magnetic field, it has the ability to levitate various diamagnetic materials in a paramagnetic medium. This method is widely available and offers high density resolution and portability. Numerous studies have demonstrated the effectiveness of Magneto-Archimedes levitation in analyzing forensic evidence, food, minerals, and other substances [17–19]. Furthermore, the principles of Magneto-Archimedes levitation have been applied to various fields, including 3D cell culture [20], separation of mixed waste [21], and self-assembly [22]. In addition to using the levitation height of an object for density measurement, the levitation posture can also be utilized for defect detection within the object. It is important to consider the object's shape rather than simplifying it as a particle when employing the levitation posture for detection. The imbalance between magnetic force and buoyancy can result in a non-horizontal levitation posture due to variations in density among different parts of an axisymmetric object. By combining the theoretical model for spatial magnetic field distribution with the levitation posture, internal defects can be detected using the Magneto-Archimedes levitation method in a matter of seconds.

Xie et al. [23] established a theoretical model to demonstrate the influence of different distances between the two magnets on the linear relationship of the device. The model explains the phenomenon of samples assembling along the centerline. In another study, Xia et al. [24] utilized the Magneto-Archimedes levitation method to diagnose internal voids in 3D printed parts, highlighting its potential for non-destructive product testing. Gao et al. [25] proposed a dynamically rotating MagLev method to amplify the interior differences in objects of different density distribution, and characterizes the spatial density heterogeneity of the levitation objects.

The use of the rotating-mode density measurement method with magnetic levitation shows promise for offering a straightforward operational approach to separate and perform quality control on objects with varying shapes in materials science and industrial applications. Tang et al. [26] proposed a non-destructive measurement based on the Magneto-Archimedes levitation method for analyzing internal defects in plastic gears by its levitation posture. The experimental results demonstrate that the calculated porosity level has an average relative error of less than 7%. Additionally, the theoretical model for the distribution of shrinkage voids aligns well with the results obtained through CT detections, with a correlation coefficient of up to 99.8%. These findings indicate that the proposed method holds immense potential for mass detection of plastic gears.

For instance, the presence of shrinkage voids in plastic gears leads to density variations; higher numbers of shrinkage voids correlate with lower densities compared to samples with fewer voids. In general, when the mass of plastic gears remains constant, there is a linear relationship between the porosity levels and the reciprocal of the sample density, as outlined by Eq. 4.8:

$$\eta = f(\rho_s) = k \frac{1}{\rho_s} + b \quad (4.8)$$

where η is the porosity level of the sample, k and b are the coefficients that are determined by the chosen samples with the maximum and minimum porosity levels. Through Eq. 4.8, the porosity levels of defective samples in a certain interval can be measured through the Magneto-Archimedes levitation method without CT detection.

To establish the relationship between levitating posture and the distribution of shrinkage voids in plastic gears, the principle of minimum potential energy [27]. Equation 4.9 represents the total energy of a sample levitating in a magnetic field, where $\mathbf{r}_{cm} = (i_{cm}, j_{cm}, k_{cm})$ represents the center of mass, which may deviate from the centroid of the sample due to the presence of non-uniform shrinkage voids. Additionally, \vec{e}_z denotes the unit vector along the z-axis. When the sample achieves an equilibrium state with a specific posture, the total energy should be minimized. Equation 4.10 illustrates the energy associated with different sample postures, where θ is the tilt angle of the sample, and λ_l denotes the lengths of principal axes calculated by $\lambda_l^2 = \frac{1}{V} \int_V I^2 dV$ for $l \in \{i, j, k\}$. These principal axes affect the final posture of the sample in the magnetic field. Given the plastic gear's symmetrical nature, resembling a hollow cylinder, it is practical to select the principal axes wherein the center of mass \mathbf{r}_{cm} always lies on the i-axis, as $(i_{cm}, 0, 0)$.

$$U = U_{mag} + U_{grav} = - \int_V \left(\frac{\Delta\chi}{2\mu_0} \vec{B} \cdot \vec{B} + \Delta\rho g \mathbf{r}_{cm} \cdot \vec{e}_z \right) dV \quad (4.9)$$

$$U(\theta) = - \frac{2B_0^2 \Delta\chi V}{\mu_0 d^2} (\lambda_i^2 - \lambda_k^2) \cos^2 \theta - \rho_s V g i_{cm} \cos \theta \quad (4.10)$$

The random nature of the distribution of shrinkage voids within the plastic gear makes it challenging to determine the position and volume of each void. To quantify the distribution of shrinkage voids, a new variable called the moment of volume M_v is introduced, which is analogous to the moment of force in mechanics. Previous research [22] has shown that larger volumes of voids and greater distances from the centroid of the sample both contribute to an increased tilt angle of the sample. Equation 4.11 illustrates the relationship between the tilt angle θ and the moment of volume M_v for the deflection of the plastic gears.

$$M_v = V_{total}L_i = -\frac{4B_0^2\Delta\chi V(\lambda_i^2 - \lambda_k^2)}{\mu_0gd^2(\rho_r - \rho_v)} \sin\theta \quad (4.11)$$

where V_{total} represents the total volume of shrinkage voids, and L_i represents the distance between the centroid of shrinkage voids and the central point of the sample, which is situated along the body-fixed i-axis to facilitate computation. ρ_v and ρ_r are the density of shrinkage voids and parts without shrinkage voids of sample, respectively. From Eq. 4.11, the distribution of the shrinkage voids can be quantified.

4.5 Axial Levitation

The current applications of Magneto-Archimedes levitation method are briefly discussed in the above sections, and they primarily utilize the principle of levitation along the centerline, i.e., axial levitation. However, how can we determine whether the sample in the device is effectively suspended along the center line based on the magnetic field?

When a sample is placed in a paramagnetic medium within a Magneto-Archimedes levitation device, its vertical motion is influenced not only by the magnetic force but also by the differences in gravitational and buoyant forces experienced by different samples. Therefore, it is necessary to conduct stability analysis in the horizontal direction first in order to determine the stable region of horizontal movement. This analysis involves examining the horizontal movement trend of the sample under the influence of the horizontal magnetic field force. Once the stable region in the horizontal direction has been identified, the vertical magnetic force within that region is analyzed to determine the conditions for stable levitation and to identify the stable levitation position for different samples within the circular magnet device.

Here, taking axial levitation in a two-ring-magnet configuration as an example (Fig. 4.6a). When a sample is placed in the Magneto-Archimedes levitation device, it is subject to magnetic field forces in both horizontal and gravitational direction. When the sample is stably levitated, the horizontal magnetic force becomes 0 and the gravitational magnetic force is equal to the gravitational and buoyant forces. Therefore, for a sample to be stably levitated, the magnetic force it experiences in the horizontal direction must be equal to zero, as shown in Eq. 4.12. However, this is not

enough; in addition to a zero magnetic field force, the sample also needs the ability to resist disturbances to achieve stable levitation. The direction of the horizontal component of the magnetic force should point towards the stable point on both sides of the stable region, as shown in Fig. 4.6b. The figure presents a two-color plot of the horizontal component of the magnetic force on a single ring magnet. The red color indicates that the force points in the negative direction of the r-axis, while the blue color indicates that the force points in the positive direction of the r-axis. The yellow line in the figure represents the region where the magnetic force is zero. A horizontal line segment is selected near the surface of the magnet ($z = 21$ mm) and away from the surface of the magnet ($z = 30$ mm) for analysis. The five points (numbered in the figure) where the line segment intersects with the yellow line are the points where the magnetic force is zero on the line segment. Based on the analysis of the plot, it can be determined that points #1, #3, and #5 have their horizontal component of the magnetic force pointing towards the respective points. This indicates that the sample can be in a stable state in the horizontal direction when located at these three points. From a numerical analysis perspective, for stable levitation in the horizontal direction, the magnetic force on both sides of the stable point should point towards the stable point, i.e., the horizontal component of the magnetic force should satisfy Eq. 4.13. Therefore, combining Eq. 4.12, it can be seen that all values inside the magnetic force formula, except for the magnetic field intensity, are constant. Furthermore, since the magnetic susceptibility of paramagnetic media is always greater than that of the sample, i.e., $\chi_s - \chi_m < 0$, it is sufficient to satisfy Eq. 4.14 for the horizontal component of $(\vec{B} \cdot \vec{\nabla})\vec{B}$ to find the stable region of the sample in the Magneto-Archimedes levitation device.

As shown in Fig. 4.6c, d, numerical calculations were performed on the selected line segment's $B_r(\partial B_r/\partial r) + B_z(\partial B_r/\partial z)$ (red line) and its derivative (blue line). The five selected points were also marked in the figure. For points #2 and #4, although they satisfy $B_r(\partial B_r/\partial r) + B_z(\partial B_r/\partial z) = 0$, their corresponding derivatives are both less than zero. This indicates that these two points do not satisfy the condition of Eq. 4.14 and therefore cannot achieve stability in the horizontal direction. In contrast, points #1, #3, and #5 satisfy Eq. 4.14 and can achieve stability. This is consistent with the results from the analysis of the plot, demonstrating the importance of the mathematical model in Magneto-Archimedes levitation theory.

$$F_{\text{mag},r} = \frac{\chi_s - \chi_m}{\mu_0} V \left(B_r \frac{\partial B_r}{\partial r} + B_z \frac{\partial B_r}{\partial z} \right) = 0 \quad (4.12)$$

$$\frac{dF_{\text{mag},r}}{dr} < 0 \quad (4.13)$$

$$B_r \frac{\partial B_r}{\partial r} + B_z \frac{\partial B_r}{\partial z} = 0 \quad \text{and} \quad d \left(B_r \frac{\partial B_r}{\partial r} + B_z \frac{\partial B_r}{\partial z} \right) / dr > 0 \quad (4.14)$$

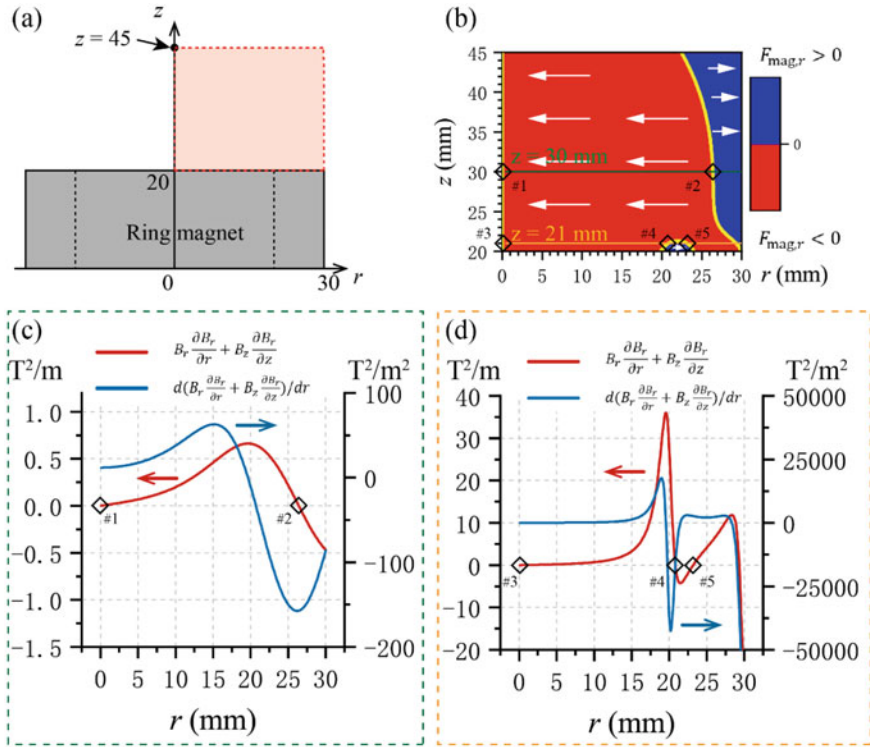


Fig. 4.6 Calculation of horizontal stability in the levitation condition **a** schematic of the analysis region **b** two-dimensional graph of the horizontal component of magnetic force **c** numerical analysis of the horizontal stability state at $z = 30$ mm **d** numerical analysis of the horizontal stability state at $z = 21$ mm

4.6 Circular Levitation

The ability to detect small differences in density is crucial for achieving precise measurements of the shape and properties of precision products. The ring magnet device offers various advantages in density measurement, including high accuracy, a large operational and observation space, low cost, and rapid measurement. Similarly, the two-magnet device allows for high sensitivity measurements by adjusting the spacing between the magnets. However, a limitation shared with the rectangular opposing magnet configuration [28] is that increasing the spacing between the magnets causes the sample to be suspended unstably and pushed away from the centerline. This constraint restricts traditional magnetic levitation devices when attempting to achieve high sensitivity density measurement through increased spacing between magnets. Existing high-sensitivity density measurement methods also fail to ensure a comprehensive density measurement range. Furthermore, in current magnetic levitation methods, stable sample suspension can only be achieved

within a one-dimensional linear structure along the centerline. This constraint leads to mutual compression among samples with small density differences during density measurement or sample separation, thereby affecting the suspension effect. As a result, the axial levitation method often faces limitations when conducting batch density characterization.

Here, taking magneto-levitation device consisting of two H2O magnets with same poles facing each other as an example. The two-ring-magnet device can achieve axial levitation when the spacing is small ($d < 32$ mm). The measurement sensitivity can vary depending on the spacing, reaching its maximum at $d = 32$ mm. However, when the spacing is greater than 32 mm, due to the presence of a non-zero horizontal component of the magnetic force on the sample, with the magnetic force pointing towards the outer region, the sample cannot stably levitate along the center line. Consequently, the device loses its capability for axial levitation, similar to rectangular magnet devices [23]. However, the ring magnet device differs in that, after analyzing the magnetic field and its distribution, it is observed that the stable levitation region is not limited to the center line but rather forms a stable circular levitation region. Taking the dual-block H2O magnet device as an example with a spacing of $d = 33$ mm, the calculated results are shown in Fig. 4.7. Considering the green line segment ($z = 28$ mm) as an example, horizontal force analysis of the non-axial levitation region in the figure reveals the presence of points where stable levitation can still be achieved in the outer region, such as point #1. This indicates that stable levitation can be realized along the yellow segment in Fig. 4.7a. Moreover, an analysis of the vertical stability conditions for this region shows compliance with the conditions, as shown in Fig. 4.7b. Hence, it can be concluded that although increasing the spacing in the device prevents continuous axial levitation of the internal sample, it allows for stable levitation in the corresponding circular region. Additionally, due to the axial symmetry of the magnetic field generated by the ring magnet, it can be inferred that this stable levitation region forms a circular levitation structure, which is different from any existing magnetic levitation structures. This method breaks the requirement of “axial levitation” in existing magnetic levitation techniques and achieves stable sample levitation in cases where the spacing is large, constructing a stable circular levitation region. This also enhances the research value and application prospects of ring magnet devices in the field of magnetic levitation.

To utilize the ring magnetic levitation method for density measurement, it is important to consider the operational procedure of the magnetic levitation method. In this procedure, the sample to be measured is placed in a container aligned coaxially with the ring magnet. The sample is positioned slightly below the lower surface of the upper magnet. As a result, under the influence of magnetic field forces, the sample will automatically find its balance at the corresponding levitation point. It is important to note that the annular levitation region exists in the middle part of the device (between the two yellow regions), rather than being comprised solely of the two separate regions shown in Fig. 4.7a. In density measurement using the dual ring magnet setup, which follows the “up small and down large” measurement range, we further increase the spacing to $d = 40$ mm, as shown in Fig. 4.8 [28]. For ease of comparison, the “red-blue gradient” color map is changed to a “green-brown

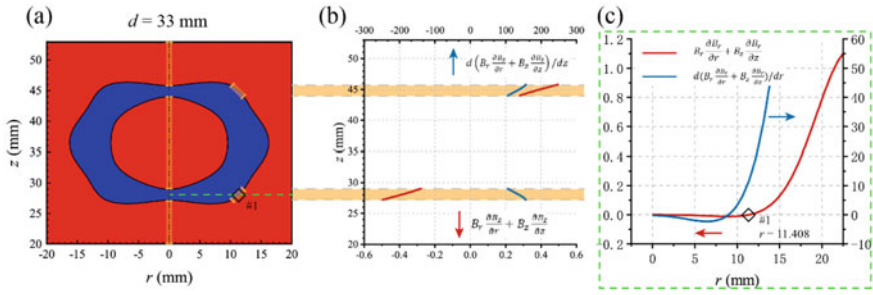


Fig. 4.7 Analysis of stable levitation of the two-ring-magnet device with a large distance ($d = 33$ mm). **a** Contour plot of the horizontal component of the magnetic force. **b** Analysis of vertical stability within the region. **c** Analysis of horizontal stability within the region

gradient". When the sample is levitated in a lower region (IV or V region), it will inevitably traverse through an outward horizontal force region (II region) within the vertical force effect during the balancing process. The magnitude of the magnetic force is linearly correlated with $(\vec{B} \cdot \vec{\nabla})\vec{B}$, considering a specific sample and solution. Therefore, as the sample passes through the II region, where the horizontal outward force is relatively large, it will be pushed towards a stable region outside the centerline. This is indicated by the outer black dashed line in Fig. 4.8a. If the levitation height of the sample corresponds to the IV region, its stable point will still align with the black dashed line. On the other hand, if the sample's levitation region is in the V region, after descending to the corresponding height, it will experience an inward horizontal component of magnetic force in that region. As a result, the sample will continue to levitate along the center line. In the case of the III region, despite the existence of stable conditions for axial levitation in that region, the operational procedure for sample density measurement involves balancing from top to bottom. Therefore, the horizontal component of magnetic force exerted on the sample in the II region is relatively substantial. Consequently, the stable levitation region at the corresponding height in the III region will still be defined by the outer dashed line. Based on the aforementioned analysis, it can be inferred that in an annular levitation setup with a large spacing, the stable region for sample levitation will inevitably be defined by the red dashed line in the upper right corner of Fig. 4.8a. This implies axial levitation on both the upper and lower sides (I and V regions), while the middle section remains stably levitated beyond the center line. The axial symmetry of the ring magnet setup results in a corresponding axial symmetry in the stable region outside the center line. Consequently, samples of the same density exhibit a ring-shaped levitation structure during the levitation process, as depicted in Fig. 4.8b. This figure illustrates the schematic diagram of batch sample levitation in a ring magnet setup with a spacing of 40 mm. It is evident that the levitated samples, influenced by the horizontal component of the magnetic field force, are pushed beyond the center line, forming an annular levitation structure. In the stable levitation state, the sample only possesses a vertical component that balances gravity and buoyancy.

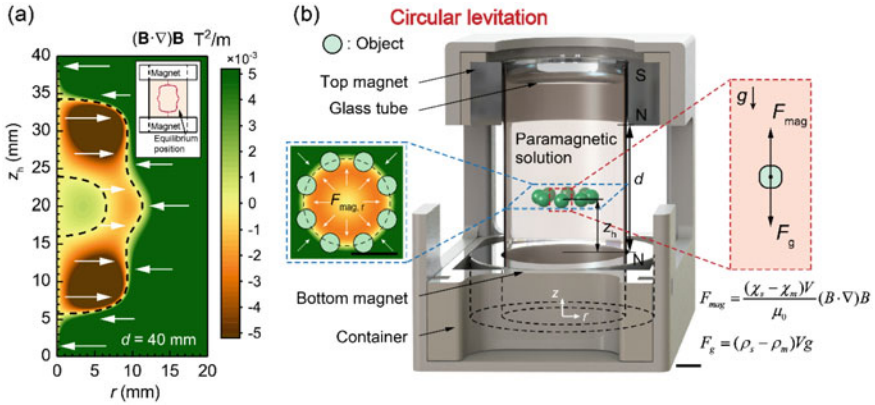


Fig. 4.8 Circular levitation structure in the two-ring-magnet device at $d = 40$ mm **a** contour plot of the horizontal component of the magnetic force. **b** Schematic diagram of the device. Reproduced with permission from Ref. [29]. Copyright 2020 American Chemical Society

In order to accurately determine the levitation position (r, z) for samples levitating in the circular region, the observed data of the sample’s levitation height z from a frontal view is necessary. This is because the levitation position directly affects the calculation of the vertical component of the magnetic force acting on the sample. When samples levitate along the center line, the levitation position can be easily confirmed as $r = 0$. However, for samples levitating in the circular region, the horizontal position r cannot be determined solely through observation. Therefore, it is essential to compute the point that satisfies the horizontal stability condition mentioned in Eq. 4.14 at the given height z in order to determine the horizontal position r . Then the density of levitating sample can be calculated accurately.

References

1. Simon MD, Heflinger LO, Geim AK. Diamagnetically stabilized magnet levitation. *Am J Phys.* 2001;69(6):702–13.
2. Geim AK, Simon MD, Boamfa MI, et al. Magnet levitation at your fingertips. *Nature.* 1999;400(6742):323–4.
3. Ikezoe Y, Hirota N, Nakagawa J, et al. Making water levitate. *Nature.* 1998;393(6687):749–50.
4. Ikezoe Y, Kaihatsu T, Sakae S, et al. Separation of feeble magnetic particles with magneto-Archimedes levitation. *Energy Convers Manage.* 2002;43(3):417–25.
5. Hirota N, Kurashige M, Iwasaka M, et al. Magneto-Archimedes separation and its application to the separation of biological materials. *Physica B.* 2004;346:267–71.
6. Liu J, Ding A, Cao Q. Magnetic levitation with cylindrical magnets for density-based measurement. *IEEE Trans Instrument Measur.* 2021.
7. Miura O, Yamagishi K, Yamamoto D. Magneto-Archimedes levitation of precious metals under a high magnetic field gradient. *J Phys Conf Ser.* 2018;1054(1): 012086.
8. CRC handbook of chemistry and physics. CRC Press; 2014.

9. Yamato M, Nakazawa H, Kimura T. Levitation polymerization to fabricate a large polymer sphere. *Langmuir*. 2002;18(24):9609–10.
10. Maki S, Oda Y, Ataka M. High-quality crystallization of lysozyme by magneto-Archimedes levitation in a superconducting magnet. *J Cryst Growth*. 2004;261(4):557–65.
11. Takayama T, Ikezoe Y, Uetake H, et al. Self-organization of nonmagnetic spheres by magnetic field. *Appl Phys Lett*. 2005;86(23):234103.
12. Winkleman A, Gudiksen KL, Ryan D, et al. A magnetic trap for living cells suspended in a paramagnetic buffer. *Appl Phys Lett*. 2004;85(12):2411–3.
13. Wikipedia contributors. 2023, March 24. Magnetochemistry. In: Wikipedia, the free encyclopedia. Retrieved 07:17, August 25, 2023, from <https://en.wikipedia.org/w/index.php?title=Magnetochemistry&oldid=1146373329>.
14. Gerber R, Takayasu M, Friedlaender F. Generalization of HGMS theory: the capture of ultra-fine particles. *IEEE Trans Magn*. 1983;19(5):2115–7.
15. Furlani EP. Analysis of particle transport in a magnetophoretic microsystem. *J Appl Phys*. 2006;99(2):024912.
16. Zhang C, Zhao P, Gu F, et al. Single-ring magnetic levitation configuration for object manipulation and density-based measurement. *Anal Chem*. 2018;90(15):9226–33.
17. Bøyum A, Brincker Fjerdingstad H, Martinsen I, et al. Separation of human lymphocytes from citrated blood by density gradient (Nycoprep) centrifugation: monocyte depletion depending upon activation of membrane potassium channels. *Scand J Immunol*. 2002;56(1):76–84.
18. Xie J, Zhao P, Zhang C, et al. A feasible, portable and convenient density measurement method for minerals via magnetic levitation. *Measurement*. 2019;136:564–72.
19. Lockett MR, Mirica KA, Mace CR, et al. Analyzing forensic evidence based on density with magnetic levitation. *J Forensic Sci*. 2013;58(1):40–5.
20. Souza GR, Molina JR, Raphael RM, et al. Three-dimensional tissue culture based on magnetic cell levitation. *Nat Nanotechnol*. 2010;5(4):291–6.
21. Zhang X, Gu F, Xie J, et al. Magnetic projection: a novel separation method and its first application on separating mixed plastics. *Waste Manage*. 2019;87:805–13.
22. Mirica KA, Ilijevski F, Ellerbee AK, et al. Using magnetic levitation for three dimensional self-assembly. *Adv Mater*. 2011;23(36):4134–40.
23. Xie J, Zhang C, Gu F, et al. An accurate and versatile density measurement device: magnetic levitation. *Sens Actuators B Chem*. 2019;295:204–14.
24. Xia N, Zhao P, Xie J, et al. Non-destructive measurement of three-dimensional polymeric parts by magneto-Archimedes levitation. *Polym Testing*. 2018;66:32–40.
25. Gao QH, Zhang WM, Zou HX, et al. Tunable rotating-mode density measurement using magnetic levitation. *Appl Phys Lett*. 2018;112(14):142408.
26. Tang D, Zhao P, Shen Y, et al. Detecting shrinkage voids in plastic gears using magnetic levitation. *Polym Testing*. 2020;91:106820.
27. Subramaniam AB, Yang D, Yu HD, et al. Noncontact orientation of objects in three-dimensional space using magnetic levitation. *Proc Natl Acad Sci*. 2014;111(36):12980–5.
28. Mirica KA, Shevkoplyas SS, Phillips ST, et al. Measuring densities of solids and liquids using magnetic levitation: fundamentals. *J Am Chem Soc*. 2009;131(29):10049–58.
29. Zhang C, Zhao P, Gu F, et al. Axial-circular magnetic levitation: a three-dimensional density measurement and manipulation approach. *Anal Chem*. 2020;92(10):6925–31.

Chapter 5

Standard MagLev Testing Method



Jun Xie, Yifeng Pan, Hao Chen, and Peng Zhao

5.1 Introduction

As introduced in previous sections, magneto-Archimedes levitation is one of the few methods that can levitate and control objects without direct touch. In addition, it has been theoretically proved that stable levitation can be achieved solely in a stable magnet field instead of using accurate control or other methods, which means it is possible to stably levitate object using permanent magnets. This special character allows the magneto-Archimedes levitation to be applied in the field of separation and control of diamagnetic materials.

However, in the theory analysis showed that the areas of single magnets for stable levitation are too narrow to afford the levitation of objects except for very small particles. Researchers tried to combine several magnets in different arrangements to generate a large area to levitate objects, and finally a special structure was proposed by Whitesides' research group that reached this goal. The method is named as magnetic levitation method, which is abbreviated as "MagLev" [1]. Benefit from the stable levitation of object in a relatively large area, the method has a basic function of density measurement. As can be easily predicted, due to the limitation of the magnetic field generated by permanent magnets, the levitation capacity of the method can only handle objects with density similar to the paramagnetic medium. On the contrary, the method thus achieves higher accuracy. This allows the MagLev to be broadly used as a density-based method in the fields of materials science, chemistry and bioengineering, etc. This section will mainly introduce the original MagLev method and device.

J. Xie (✉)

College of Mechanical Engineering, Zhejiang University of Technology, Hangzhou, China
e-mail: jxie93@zjut.edu.cn

Y. Pan · H. Chen · P. Zhao

The State Key Laboratory of Fluid Power and Mechatronic Systems, College of Mechanical Engineering, Zhejiang University, Hangzhou, China

5.2 Structure of MagLev Device

In the retrospect of previous sections, it can be found that permanent magnets have an area near the surface of a pole that can stably levitate object. For instance, this area of the square magnet with the size of $50 \times 50 \times 25$ (mm) are dome-shaped with the peak of 9 mm. In fact, enhance the magnetic flux intensity can surely enhance the levitation capacity of the magnet, the shape of the area will not be affected by this change. To increase this area, the magnets that generate the magnetic field need to be reshaped. Scaling up the magnet is a certain way that can enlarge the area. However, the method is hard to be implemented, for the manufacturing of large magnets cannot guarantee the accurate sizes and magnetism. Therefore, using multiple magnets to construct a proper distribution of magnetic field was chosen to solve the problem.

Generally, the devices with two magnets with like poles facing each other at a certain distance are classified as “MagLev device”, as shown in Fig. 5.1. This kind of devices has the space between the two magnets, in which the objects can reach to stable levitation along the centerline. Typically, the device using square magnets with size of $2 \times 2 \times 1$ (in.) or $50 \times 50 \times 25$ (mm), and has the distance between the two magnets of 45 mm, is called “standard MagLev device”. In this device, the relationship between the density and the levitation heights of the objects can be approximately assumed as linear.

5.3 Stable Levitation Along the Centerline

As introduced in Chap. 4, what is desired to know is the distribution of $(\vec{B} \cdot \vec{\nabla})\vec{B}$ between the two magnets, which is presented as Eq. 5.1. The initial study is the analysis of a single square magnet. Although the results look a kind of sophisticated, they only contains basic formulas. Hence, the Numerical solution of the distribution can be easily obtained with the help of computer software, such as Mathematica and Matlab [2].

$$(\vec{B} \cdot \vec{\nabla})\vec{B} = \begin{bmatrix} B_x \frac{\partial B_x}{\partial x} + B_y \frac{\partial B_x}{\partial y} + B_z \frac{\partial B_x}{\partial z} \\ B_x \frac{\partial B_y}{\partial x} + B_y \frac{\partial B_y}{\partial y} + B_z \frac{\partial B_y}{\partial z} \\ B_x \frac{\partial B_z}{\partial x} + B_y \frac{\partial B_z}{\partial y} + B_z \frac{\partial B_z}{\partial z} \end{bmatrix} \quad (5.1)$$

The stable levitation of object along the centreline in standard MagLev device means there exists an area covers the entire centreline, in which the force acting on the object is aiming towards the centreline. It is easy to obtain the model for standard MagLev by combining the distribution of the magnetic field of two magnets. Based on the model, the stable levitation and the its influencing factors can be explained and analysed.

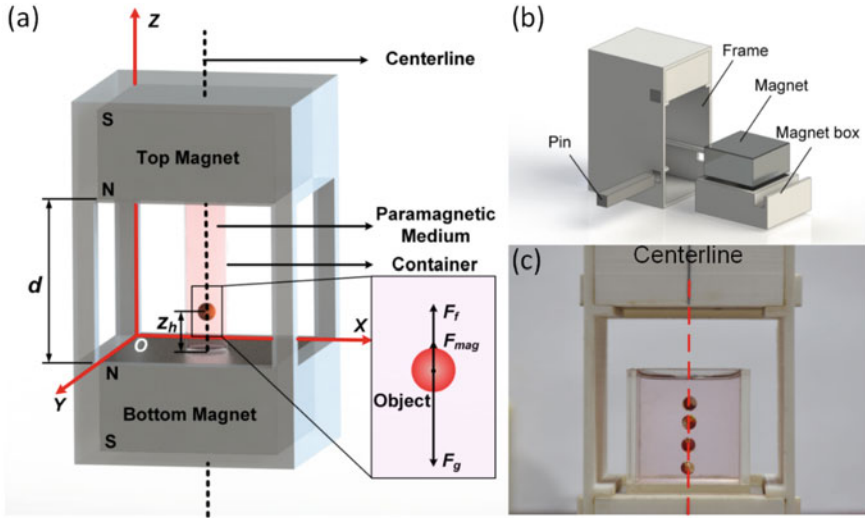


Fig. 5.1 The configuration that based on magnetic levitation used in this study. **a** The principle of magnetic levitation and its Cartesian coordinates. Two square magnets with the like-poles facing each other at a distance d can make the object levitated in paramagnetic solution at an equilibrium position along the centerline. The origin point of the coordinates is set at a corner of the bottom magnet on its top surface. **b** The structure of the measuring device. **c** Glass beads of standard densities that levitated in the medium of the device. Reproduced with permission from Ref. [2]. Copyright 2019 Elsevier

To better explain the stable levitation, the $(\vec{B} \cdot \vec{\nabla})\vec{B}$ can be divided into two parts: the vertical component and the horizontal component. The vertical component affects the final levitation heights of the object. The horizontal component determines whether the object can be stably levitated along the centreline or not. Take the $(\vec{B} \cdot \vec{\nabla})\vec{B}$ along x-axis of a standard MagLev device for example, Fig. 5.2 show its distributions on the planes parallel to xOz plane with the interval of 5 mm between the planes.

The warm colour means the value of $(\vec{B} \cdot \vec{\nabla})\vec{B}$ along x-axis is larger than 0, while the cold colour has the opposite meaning. Go back to the equation of \vec{F}_{mag} , it can be found that the $\vec{F}_{mag_{||}}$ acting on the object heads left and right in the warm area and cold area respectively. On account of the symmetry of the device, the distribution of $(\vec{B} \cdot \vec{\nabla})\vec{B}$ along y-axis is the same. Hence, it can be concluded that, the force acting on the object $\vec{F}_{mag_{||}}$ is aiming towards the centreline in most area between two magnets. This suggests that the object can will be pushed to the centreline at any position in the area. In addition, this magnetic field distribution can bring the sample back to the center line when it is disturbed away from it. Thereby, the object can be stably maintained along the centreline.

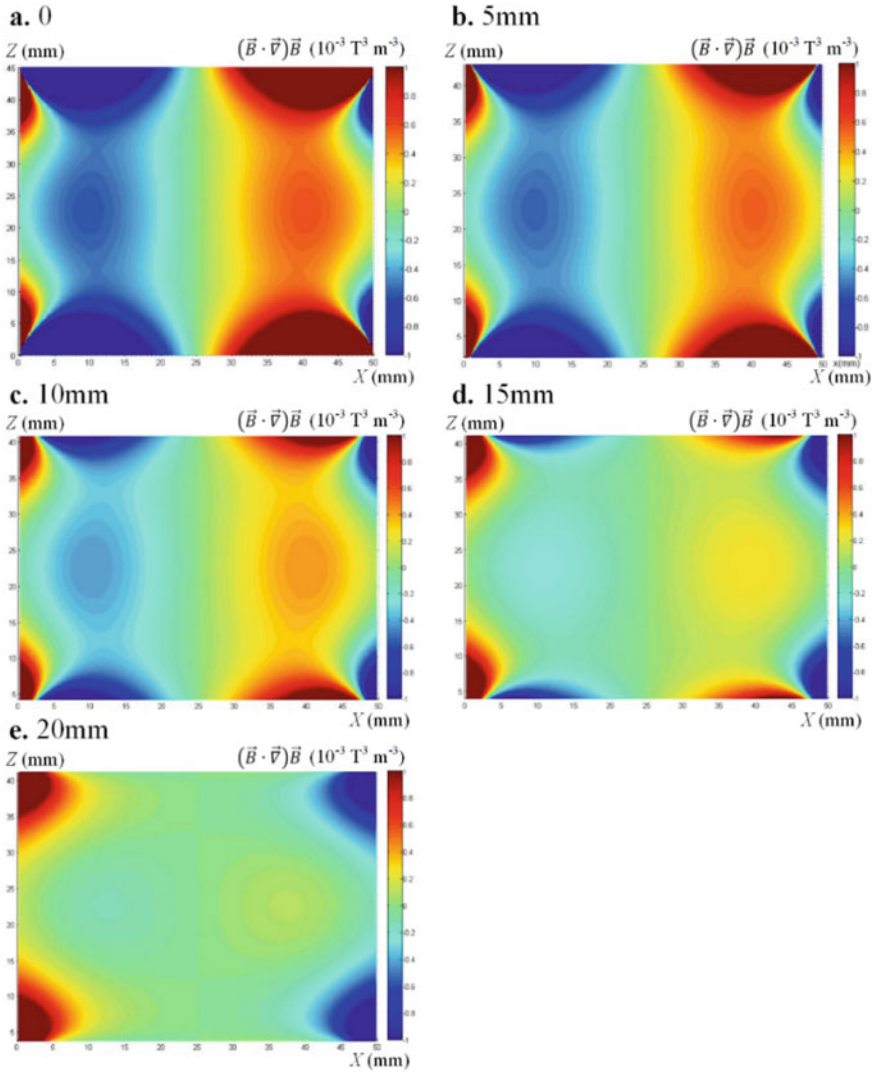


Fig. 5.2 The distributions of $(\vec{B} \cdot \vec{\nabla})\vec{B}$ along x -axis in the area between the two magnets with $d = 45$ mm. The figures are the distributions on the planes parallel to xOz plane. From **a–e**, the interval of the figures is 5 mm. It can be concluded from the figures that, in most area between two magnets, the force acting on object \vec{F}_{mag} is aiming at the centreline. The object can be maintained along the centreline. Reproduced with permission from Ref. [2]. Copyright 2019 Elsevier

According to the $\vec{F}_{mag_||}$ acting on the object, the space between two magnets can be defined as two areas (Fig. 5.3a, b): (I) the direction of the extra buoyancy is aiming towards the centreline; (II) the direction of the extra buoyancy is aiming away from the centreline. Thus, objects in the area (I) will be pushed to the centreline, but will be pushed away in area (II). The shapes of the areas are significantly affected by the structure of the device. In other word, the shape of the magnets and the distance between the magnets play very important roles in stably levitating the objects.

For instance, with the increasing of d , the area (I) shrinks and finally reaches to a limitation (Fig. 5.3a–c). Above this limitation, area (II) reaches to the centreline (Fig. 5.3d). Under this condition, the samples cannot get balanced along the centreline in area (II). Based on the theoretical analysis, we find the phenomenon occurs when

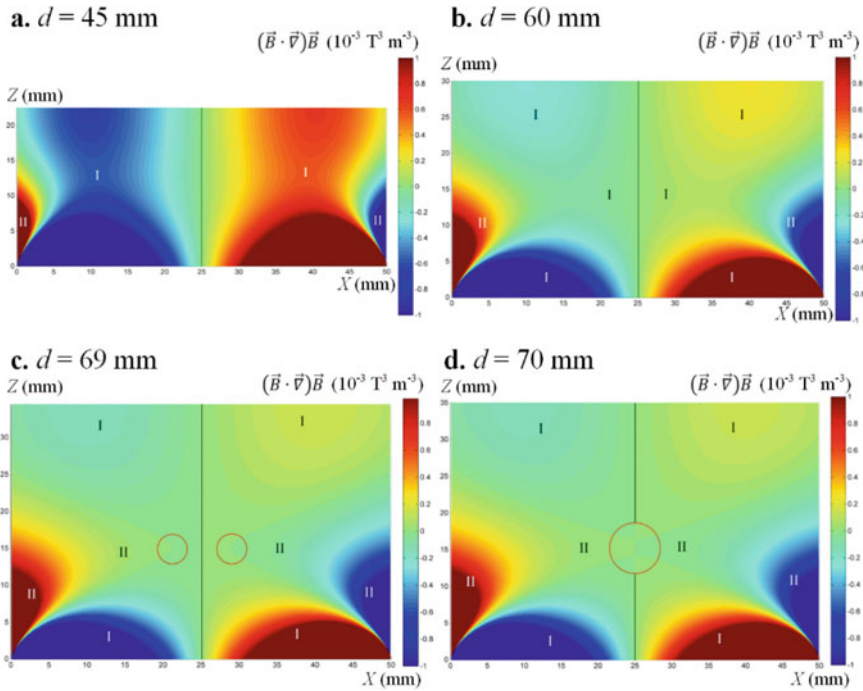


Fig. 5.3 The distribution of $(\vec{B} \cdot \vec{\nabla})\vec{B}$ along x -axis under different d . The two magnets are the same and at precise alignment, so half of the figure can express the distribution, for the other half is a mirror image. From **a–d**, the distance of the two magnets are 45 mm, 60 mm, 69 mm and 70 mm desperately. According to the extra buoyancy acting on the object, the distribution contains two area: (I) the extra buoyancy is aiming at the centreline; (II) the extra buoyancy is aiming away from the centreline. From the clouds we can find the area (I) is shrinking with the increase of d (**a**, **b**), and finally approach to a limitation that area (II) reaches to the centreline (red circle in **c**, **d**). The breakage of area (I) appears at about $z = 14$ mm along the centreline and remain enlarging when d is continually increasing. The objects in this area cannot be steadily levitated alone the centreline. Reproduced with permission from Ref. [2]. Copyright 2019 Elsevier

$d > 69$ mm using $50 \text{ mm} \times 50 \text{ mm} \times 25 \text{ mm}$ N45 magnets (Sect. 5.2 in SI). In addition, changing magnets can change the limitation of d .

Nevertheless, solely scaling up the value of the magnetic flux intensity will do no effect on changing the areas. From the calculation results of $(\vec{B} \cdot \vec{\nabla})\vec{B}$ distribution in open space, we can find that these equations are all constituted by two parts: (i) the quadratic coefficient $J^2/16\pi^2$ and (ii) a function that is dependent on the size parameter of magnet. Noticing that $J^2/16\pi^2$ is always greater than 0, therefore, two observations can be found: (i) for the magnets with the same size, the change of \vec{B}_0 does not affect the direction of F_m ; (ii) the direction of F_m is affected by the shape of the magnets.

Simulation and experiments on standard density glass beads are employed for verifying the cause behinds the phenomena.

Using the N45 magnets with size of $50 \text{ mm} \times 50 \text{ mm} \times 25 \text{ mm}$ at $d = 70$ mm, the calculation results and experimental results are plotted in Fig. 5.4c. Due to the symmetry of the device, the distribution of $(\vec{B} \cdot \vec{\nabla})\vec{B}$ along x -axis between the two magnets are calculated for the bottom half. And the calculation results were shown as the dual-colour figures and were adjusted and set as the background of the experimental results. The experimental results agree with the analysis. It can be found that glass beads (1.20 and 1.22 g cm^{-3}) cannot be steadily levitated along the centreline. Comparing with double-colour figure at background, the behaviour of the glass beads is as same as the analysis predicted. As discussed above, the restriction of d is not affected by \vec{B}_0 , but affected by the shape of the magnets. This phenomenon can be observed in Fig. 5.4a, b. In these experiments, the magnets changed from N45 magnets (Fig. 5.4a) to N35 magnets (Fig. 5.4b). Despite the sizes of the magnets were the same, the \vec{B}_0 of each magnet changed ($\vec{B}_0 = 0.425 \text{ T}$ for the N45 magnets and $\vec{B}_0 = 0.335 \text{ T}$ for the N35 magnets). This change only decreases the measurement range of the device, but does not change the shape of the areas (I) and (II).

As shown in the figures, this change of \vec{B}_0 does not influence the shape of the areas, however, the levitating ability of the device decreases with the decrease of \vec{B}_0 . On the other hand, the changes in the side length and height of the magnets would result in variations in the areas (Fig. 5.4c, d). The limitation of d increases with the decrease of the height of magnets or increase of the side length of magnets. It is worth noting that the volume and the density distribution of the standard density glass beads are not uniform, these beads cannot easily be assumed as mass points. Thus, the areas II observed in experiments seem to be larger than the analytical results.

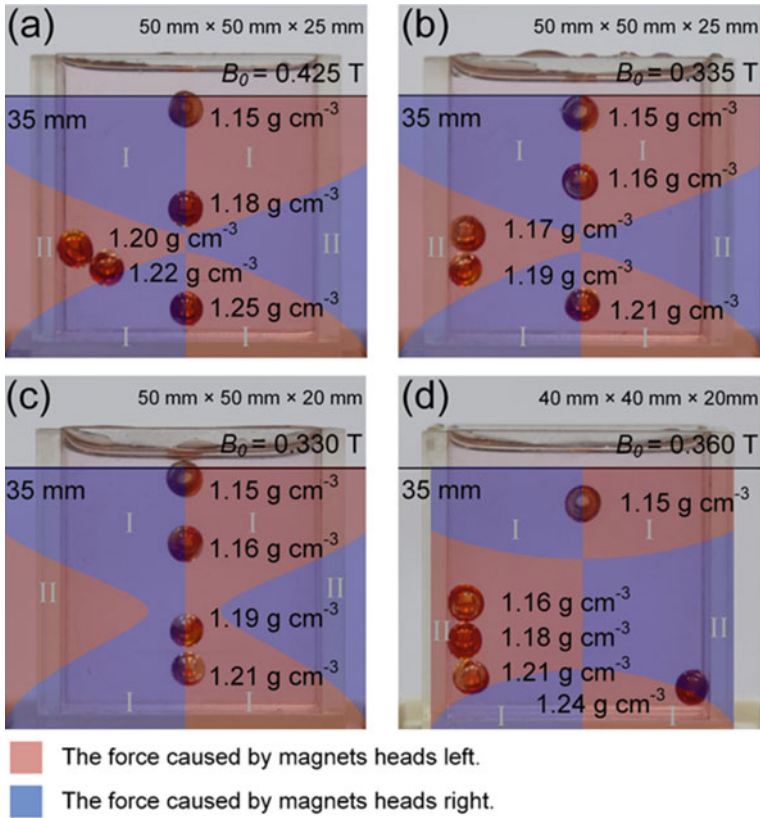


Fig. 5.4 Calculation results and experimental results of misalignment. **a–d** Experimental results under $d = 70$ mm with the calculation results as background using magnets of different sizes. From **a–d**, the magnets used in device are N45 of $50 \text{ mm} \times 50 \text{ mm} \times 25 \text{ mm}$, N35 of $50 \text{ mm} \times 50 \text{ mm} \times 25 \text{ mm}$, N35 of $50 \text{ mm} \times 50 \text{ mm} \times 20 \text{ mm}$ and N35 of $40 \text{ mm} \times 40 \text{ mm} \times 20 \text{ mm}$. Reproduced with permission from Ref. [2]. Copyright 2019 Elsevier

5.4 Theory for Density Measurement

5.4.1 Density Calculation Formula

As long as the stable levitation can be achieved, the density measurement of the object can be easily realized. The forces acting on the object are gravity \vec{F}_G , the buoyancy \vec{F}_f and the extra buoyancy force imparted by the magnetic field acting on the solution (refer to “magnetic force” in the following parts) \vec{F}_{mag} , as expressed as Eqs. 5.2–5.4 [1].

$$\vec{F}_G = \rho_s \vec{g} V \tag{5.2}$$

$$\vec{F}_f = -\rho_m \vec{g} V \quad (5.3)$$

$$\vec{F}_{mag} = \frac{\chi_s - \chi_m}{\mu_0} V (\vec{B} \cdot \vec{\nabla}) \vec{B} \quad (5.4)$$

where ρ_s and ρ_m (g cm^{-3}) denotes density of the object and the medium, χ_s and χ_m (unitless) represents susceptibilities of the object and the medium. Parameter \vec{g} (m s^{-2}) is the acceleration of gravity, \vec{B} (T) is the magnetic flux intensity, V (m^3) is the volume of the object, and $\mu_0 = 4\pi \times 10^{-7}$ (N A^{-2}) is the permeability of a vacuum.

When the object reaches its equilibrium position, the sum of these forces meets Eq. 5.5. Noticing that \vec{F}_G and \vec{F}_f are on the contrary directions, only the directions of the forces are along the same line can the sample be levitated at an equilibrium position. Therefore, the density of the sample can be obtained by Eq. 5.6, where $g(z_h)$ denotes the distribution of $(\vec{B} \cdot \vec{\nabla}) \vec{B}$ on the direction of z -axis.

$$\vec{F}_G + \vec{F}_f + \vec{F}_{mag} = 0 \quad (5.5)$$

$$\rho_s = \frac{\chi_s - \chi_m}{\mu_0 g} g(z_h) + \rho_m \quad (5.6)$$

Noticing that the equilibrium position of the object must be along the centerline, where the $(\vec{B} \cdot \vec{\nabla}) \vec{B}$ along centerline only contains the z -axis component. Hence, the components B_x , B_y , $\frac{\partial B_x}{\partial z}$, and $\frac{\partial B_y}{\partial z}$ are 0, and the equation of $(\vec{B} \cdot \vec{\nabla}) \vec{B}$ along the centerline can be simplified as Eq. 5.7. In this equation, a series of substitutions can be made: $A_1 = z_h$, $A_2 = z_h + h$, $D_1 = d - z_h$, $D_2 = d + h - z_h$, $F_1(A, D) = 1/\left[(a^2 + 4A^2)\sqrt{a^2 + 2D^2}\right]$, and $F_2(A, D) = \arctan\left(A/\sqrt{a^2/2 + D^2}\right)$, where a and h denote the side length and height of the magnet, respectively, J (A m) is the surface current density of the magnet that can be calculated using the surface magnetic flux intensity \vec{B}_0 of the magnet. Only positional information needed in Eq. 5.6 is the levitation height z_h . Combining Eqs. 5.5 and 5.6, the density of object can be accurately obtained through acquiring its levitation height precisely.

$$\begin{aligned} g(z_h) &= B_z \frac{\partial B_z}{\partial z} \\ &= -64\sqrt{2} \left(\frac{\mu_0 J}{4\pi} a \right)^2 (F_1(A_1, A_1) + F_1(D_1, D_1) - F_1(A_2, A_2) - F_1(D_2, D_2)) \\ &\quad \times (F_2(A_2, A_2) + F_2(D_1, D_1) - F_2(A_1, A_1) - F_2(D_2, D_2)) \end{aligned} \quad (5.7)$$

Additionally, in the standard MagLev device, B_z varies virtually linearly ($R^2 = 0.9999$) with z , from a maximum of $+B_0$ (at the upper surface of the bottom magnet

(z)) to a minimum of $-B_0$ (at the lower surface of the top magnet (z)). Because of this linearity, the magnetic flux intensity along the centreline can be approximated as:

$$B_z = -\frac{2B_0}{d}z + B_0 \quad (5.8)$$

Therefore, Eq. 5.6 can be rewritten as Eq. 5.9

$$\rho_s = \alpha h + \beta \quad (5.9)$$

where

$$\alpha = \frac{4(\chi_s - \chi_m)B_0^2}{g\mu_0 d^2} \quad (5.10)$$

$$\beta = \rho_m - \frac{2(\chi_s - \chi_m)B_0^2}{g\mu_0 d} \quad (5.11)$$

The approximate linearity makes can simplify the calculation procedure without significant influence on accuracy. There are two methods to use Eq. 5.9: knowing the parameters of Eqs. 5.10 and 5.11, and calibration.

- (a) **Direct Measurements of Density with Knowing Parameters.** This method requires the accurate knowledge of the parameters of the system, including ρ_m , h , d , χ_s , χ_m , and B_0 . The influences of environment on these parameters should also be clarified, such as the temperature and humidity during the test. In fact, these influences will affect of the values of parameters ρ_m , and χ_m , etc. Therefore, the measurement should be carried out in a stable environment, which may limit its applications in outdoor occasions. Except these potential influences, Eq. 5.9 provides easy access to routine density measurements using magnetic levitation with very high accuracy.
- (b) **Measurements of Density with Calibrated Standards.** Another simple way to measure unknown densities by magnetic levitation is to first calibrate Eq. 5.9 by levitating objects with known densities. Theoretically, two knowing object can determine the parameter α and β . Then, use Eq. 5.9 can calculate the unknown density from the levitation heights of a levitated object. The most outstanding advantage of this method is that it does not require an accurate knowledge of each individual parameter in Eqs. 5.10 and 5.11, nor the detailed understanding of the physics of magnetic levitation.

5.4.2 Preparation of Paramagnetic Medium

The most common medium used in MagLev is the paramagnetic aqueous solutions. This kind of media has the advantages of easily to prepare and commercially available. The solutions also do not need strict environments. The paramagnetic salts are all very stable under room temperature. However, water-based and alcohol-based solvents are not applicable to soluble salts.

Replacing solutions of paramagnetic salts with paramagnetic ionic liquids (PILs) circumvents some of the limitations imposed by water (or organic fluids), often used as solvents in MagLev [3]. The chemical and physical properties of PILs can be tuned by changing the anion–cation pair, by which the PILs can be either hydrophilic or hydrophobic. The magnetic susceptibility thereby can also be adjusted. For the PILs themselves are paramagnetic, thus they can be directly used as paramagnetic media. The low vapour pressures make the PILs stable at room temperature and atmospheric pressure. Accordingly, the water-based and alcohol-based media may get concentrated with the vaporization of the solvent, which may cause large errors in long time testing. However, the measuring range using PILs may be very narrow (1.0–1.5 g/cm³). This shortage can be overcome by employ aqueous paramagnetic salt solutions without cosolute additives. Figure 5.5 shows the synthesis of some typical PILs.

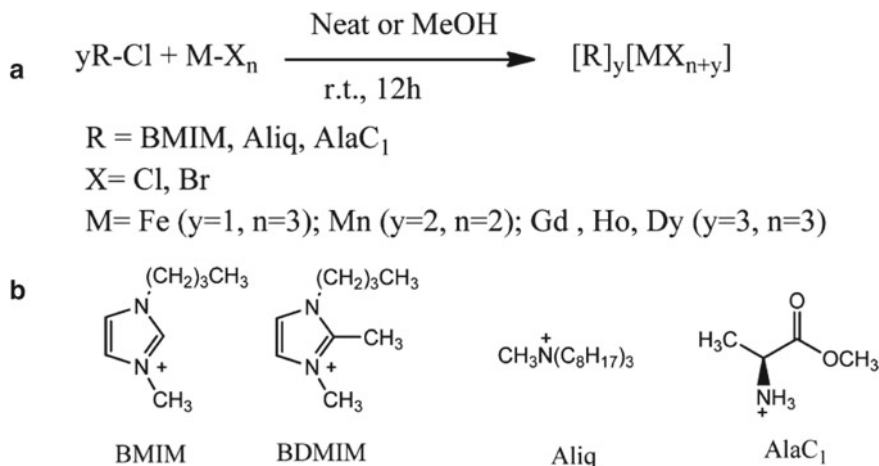


Fig. 5.5 Synthesis of some typical PILs. Reproduced with permission from Ref. [3]. Copyright 2013 American Chemical Society

5.4.3 Determine of the Levitation Height

The most intuitive way to determine the levitation height is using a ruler to measure the distance between the equilibrium position and the upper surface of the bottom magnet. However, the accuracy of a ruler can only be 0.5 mm, for it is impossible to use more accurate tools, such as vernier caliper, and micrometer caliper. In addition, it is also hard to put the ruler beneath the levitated object. Hence, the angle of vision and the lensing effect of the container will also affect the measuring result.

In some research, the experimental research was recorded by a digital camera. And the levitation height is calculated by counting the pixels in the picture. The camera is set horizontally in front of the device. A line of reference parallel to the camera lens was made through the centre of each magnet. The pictures of the experimental results were taken after the samples reach the equilibrium positions (the smaller the sample is, the more time was needed). The distance between two magnets is converted into number of pixels N_d in the figure, which is the pixels between the lines of reference of two magnets. Then the number of pixels N_s between the object and the bottom magnet can be obtained by the same method. Thereby, the height of the object can be calculated by Eq. 5.12. In this method, the tolerance of z can reach to ± 0.3 mm.

$$z_h = \frac{N_s}{N_d}d \quad (5.12)$$

5.4.4 Assumptions

In theory of density measurement through MagLev method, six assumptions and approximations are made. (i) The theory of the distribution of \vec{B} is based on the molecules circulation hypothesis of magnetic medium. This hypothesis assumed that at macro level, the magnet only contains surface current. The internal molecular currents counteract each other that have no expression at macro level. (ii) Assuming the two magnets are at precise alignment. (iii) Ignoring the effect caused by the size of the sample in x -axis and y -axis directions. (iv) Assuming the bulk magnetic susceptibilities of medium solutions and samples are uniform and homogenous. (v) Assuming the distribution of the density of medium solution is homogenous that it is not effected by magnetic field. (vi) Assuming the pair of magnets used in one device are exactly the same.

5.4.5 Minimum Size of the Object

For particles with sizes that are visible to the naked eyes, the effect of thermal motion on their macroscopic behaviour can be negligible. It means the derivation of Eq. 5.9 only need to focus on the gravity and magnetic force. However, for sufficiently small particles (e.g., molecules), this assumption is no longer correct. In order to estimate the limitation of the size of an object for stable levitation and avoid the errors due to the relatively large thermal motion, it is necessary to compare the gravitational potential energy U_g and the magnetic potential energy U_m interactions with thermal energy E_T in MagLev system. Assuming that the shape of the object is spherical, the lower limit for the radius of the object can be estimated by solving the inequality in Eq. 5.13 [1]. Generally, when U_g and U_m satisfy the condition that $U_g + U_m \geq 10k_B T$, the effect of the thermal motion can be neglect. Therefore, the radius of the object can be expressed as the inequality in Eq. 5.14. In practice, it is estimated that $R > \sim 2 \mu\text{m}$ is necessary for a reliable correlation of levitation height with density.

$$U_g + U_m = (\rho_s + \rho_m)Vgz - \frac{(\chi_s - \chi_m)V}{\mu_0}(\vec{B} \cdot \vec{B}) \gg k_B T = E_T \quad (5.13)$$

$$R \gg \left(\frac{k_B T}{\frac{4\pi}{3} \left((\rho_s + \rho_m)gz - \frac{(\chi_s - \chi_m)}{\mu_0} \left(-\frac{2B_0}{d}z + B_0 \right)^2 \right)} \right)^{1/3} = E_T \quad (5.14)$$

5.5 Error Analysis

As mentioned in paper, ρ_m and χ_m can be computed by T and c . The density of the medium solution ρ_m can be calculated by Eq. 5.15. In this equation, $W_0 = 999.65$, $W_1 = 2.0438 \times 10^{-1}$ and $W_2 = -6.1744 \times 10^{-2}$ are the parameters of the pure water. For example, the paramagnetic medium that most commonly used in the works, MnCl_2 , has the parameters of $A = 1.022 \times 10^2$, $B = 4.966 \times 10^{-1}$, $C = -1.307 \times 10^{-2}$, $D = -3.659$, $E = -1.631 \times 10^{-2}$, and $F = -4.774 \times 10^{-3}$ [4]. The susceptibility χ_m fit Curie–Weiss theorem (Eq. 5.16), where C_{cw} is the curie constant ($\text{m}^3 \text{K mol}^{-1}$) and θ is Weiss constant ($^\circ\text{K}$) of the paramagnetic salt. The value -9×10^{-6} is the bulk magnetic susceptibility of pure water and we assume the influence of T on it can be negligible.

$$\rho_m = W_0 + W_1 T + W_2 T^{3/2} + Ac + BcT + CcT^2 + Dc^{3/2} + Ec^{3/2} + Fc^{3/2}T^2 \quad (5.15)$$

$$\chi_m = \frac{C_{cw}}{T - \theta} c - 9 \times 10^{-6} \quad (5.16)$$

If the levitation height of an object is obtained by the camera recording, the levitation height z_h of the object should be obtained by Eq. 5.12. Thereby, the error of z_h can be calculated as Eq. 5.17.

$$\delta z_h = \sqrt{\left(\frac{\partial z_h}{\partial N_s} \delta N_s\right)^2 + \left(\frac{\partial z_h}{\partial N_d} N_d\right)^2} \quad (5.17)$$

All the parameters for calculating density of the object are independent (notice that ρ_m and χ_m can be computed by T and c). The error can be estimated by Eq. 5.18. An example of measuring 1.0600 g cm^{-3} standard density glass bead using $d = 60 \text{ mm}$ device with the aid of 0.5 M MnCl_2 aqueous solution is provided below (Table 5.1)

$$\delta \rho_s = \sqrt{\begin{aligned} &\left(\frac{\partial \rho_s}{\partial a} \delta a\right)^2 + \left(\frac{\partial \rho_s}{\partial d} \delta d\right)^2 + \left(\frac{\partial \rho_s}{\partial h} \delta h\right)^2 + \left(\frac{\partial \rho_s}{\partial T} \delta T\right)^2 \\ &+ \left(\frac{\partial \rho_s}{\partial \chi_s} \delta \chi_s\right)^2 + \left(\frac{\partial \rho_s}{\partial T} \delta T\right)^2 + \left(\frac{\partial \rho_s}{\partial c} \delta c\right)^2 + \left(\frac{\partial \rho_s}{\partial z} \delta z\right)^2 \end{aligned}} \quad (5.18)$$

According to the error analysis, the dependence of error in ρ_s on each parameters using media with high and low concentrations were shown in Figs. 5.6 and 5.7 respectively. It is obvious that χ_s all have relatively important effect on the total uncertainty. This is because the susceptibility of the sample is usually an unknown value, and its uncertainty is assumed as $\pm 10 \times 10^{-6}$ (unitless).

Actually, this estimation of χ_s may be more accurate if the objects to be tested are in some certain categories, such as common polymers, organics without paramagnetic ion group. The effect of z_h tolerance on the density measurement accuracy becomes larger when using high concentration solution (maximum to 0.0043 g cm^{-3} when using 3.0 M MnCl_2 solution vs maximum to 0.0001 g cm^{-3} when using 0.1 M MnCl_2 solution). An accurate method for detecting the levitation would further improve the accuracy in density measurement. In the meantime, the accuracy of the value ρ_m plays an important role in the test in medium with lower concentration. Fortunately, the accuracy in measuring density of medium with large volume using common methods (e.g. pycnometer method) can be very high.

Similar to Eq. 5.18, the total uncertainty of simplified method using standard MagLev device is given as Eq. 5.19. Accordingly, the conclusion for the dependence of error in ρ_s on each parameters is the same as the discussion above. In addition, the equation for simplified method is a linear relationship by fitting. Hence, system error still exists, especially in the area that near the surfaces of two magnets. This phenomenon can be noticed in the density measurement of density standards.

Table 5.1 Summary of the experimental parameters, and their associated uncertainties for a specific measured sample

Parameter	Description	Typical magnitude of P^a	δP^b	$\delta \rho_s(P)$ (g cm^{-3}) ^c
B_0	Strength of magnetic field at the surface of one magnet (T)	0.425	± 0.003	$\pm 9 \times 10^{-5}$
d	Distance between magnets (mm)	45	± 0.1	$\pm 2 \times 10^{-5}$
a	Length of magnet (mm)	50	± 0.01	$\pm 7 \times 10^{-7}$
b	Width of magnet (mm)	50	± 0.01	$\pm 7 \times 10^{-7}$
h	Height of magnet (mm)	25	± 0.01	$\pm 6 \times 10^{-5}$
ρ_m	Density of the paramagnetic solution (g cm^{-3})	1.0492	$\pm 5 \times 10^{-4}$	$\pm 5 \times 10^{-4}$
χ_m	Bulk magnetic susceptibility of paramagnetic solution	8.27×10^{-5}	$\pm 1 \times 10^{-6}$	$\pm 7 \times 10^{-5}$
χ_s	Bulk magnetic susceptibility of the sample	-5×10^{-6}	$\pm 10 \times 10^{-6}$	$\pm 7 \times 10^{-4}$
z_h	Levitation height (mm)	17.9	± 0.3	$\pm 3 \times 10^{-4}$
ρ_s	Density of the sample (g cm^{-3})	1.0600		± 0.0009

Reproduced with permission from Ref. [1]. Copyright 2009 American Chemical Society

^aWe give the values because the uncertainty in ρ_s depends on the value of specific experimental parameters used for a specific measurement. The solution is 0.5 M MnCl_2 aqueous solution

^bMagnitude of uncertainty in P

^cMagnitude of uncertainty in ρ_s as a function of each individual P

$$\delta \rho_s = \sqrt{\left(\frac{\partial \rho_s}{\partial d} \delta d\right)^2 + \left(\frac{\partial \rho_s}{\partial z_h} \delta z_h\right)^2 + \left(\frac{\partial \rho_s}{\partial \chi_s} \delta \chi_s\right)^2 + \left(\frac{\partial \rho_s}{\partial T} \delta T\right)^2 + \left(\frac{\partial \rho_s}{\partial c} \delta c\right)^2 + \left(\frac{\partial \rho_s}{\partial B_0} \delta B_0\right)^2} \quad (5.19)$$

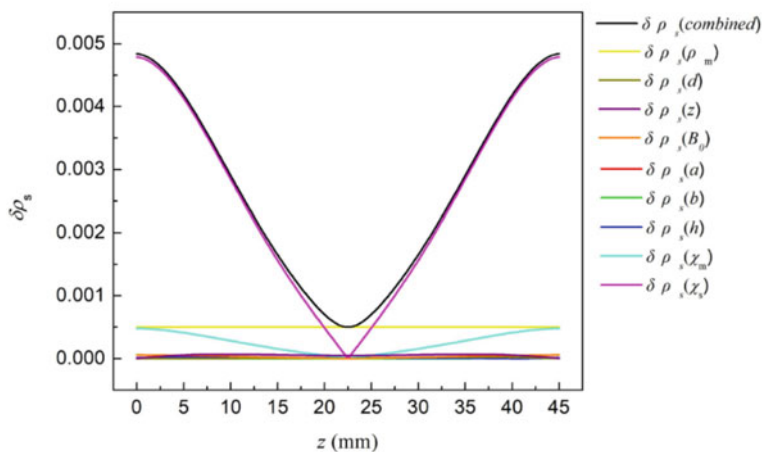
0.1 M MnCl_2 

Fig. 5.6 Plots showing the dependence of error in ρ_s on various experimental parameters when using 0.1 M MnCl_2 aqueous solution at 23 °C. Reproduced with permission from Ref. [2]. Copyright 2019 Elsevier

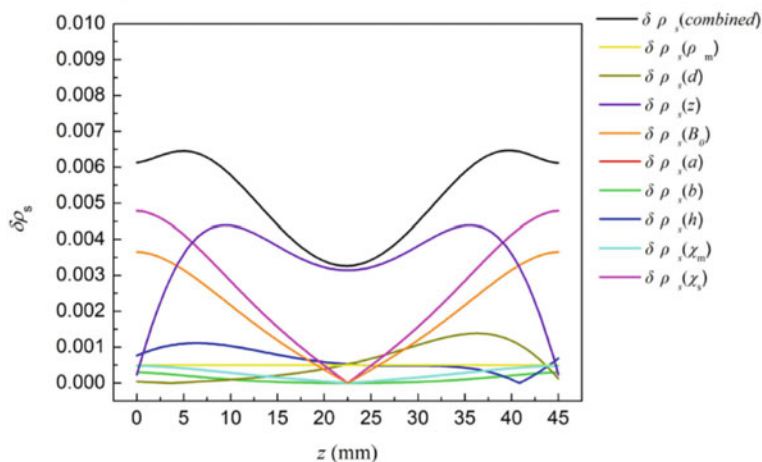
3.0 M MnCl_2 

Fig. 5.7 Plots showing the dependence of error in ρ_s on various experimental parameters when using 3.0 M MnCl_2 aqueous solution at 23 °C. Reproduced with permission from Ref. [2]. Copyright 2019 Elsevier

5.6 Density Measurement for Objects

5.6.1 Density Measurement of Standards

The high accuracy in density measurement is the most attracting character of MagLev testing method. The most intuitive way to show this advantage is using the method to measure density of standards. In the initiate research on standard MagLev, the standards were not only used to calibrate the equation, but also used to verify the accuracy in density measurement [1]. In the study, a set of glass beads of standardized, precisely known densities (0.0002 g/cm^3) were applied to the levitation in several aqueous solutions with different concentrations of MnCl_2 (0.100, and 0.500–3.000 M with interval of 0.500 M) at 23°C . The plot of the levitation results were recorded in Fig. 5.8, in which the linear relationship between the height and density of the beads can be clearly observed. The lines fitted by these results were also showed in the same figure. To evaluated the accuracy of the method, standard glass beads with three typical densities were measured by calibrated lines and the results are shown in Table 5.2. The error associated with each measurement are also given adhere to the results. Densities measured using this method correlated with the values provided by the vendors of the samples and with values obtained using a helium pycnometer within the 95% confidence interval (Table 5.2).

In fact, it can be noticed from the results above that the plots are not totally linear and has the max deviation near $\frac{1}{4}d$ and $\frac{3}{4}d$, which is the cause of the systemic error. The density measurement using Eqs. 5.6 and 5.7, on the other hand, has no problem on it. The results for calibrating Eq. 5.9 was applied to verify the accuracy of Eqs. 5.6 and 5.7. The plots show well coincidence with the curve of Eq. 5.6, as shown in Fig. 5.9. This indicate the measurement using Eqs. 5.6 and 5.7 will have

Fig. 5.8 Calibration of the magnetic levitation device with standard density beads. Reproduced with permission from Ref. [1]. Copyright 2009 American Chemical Society

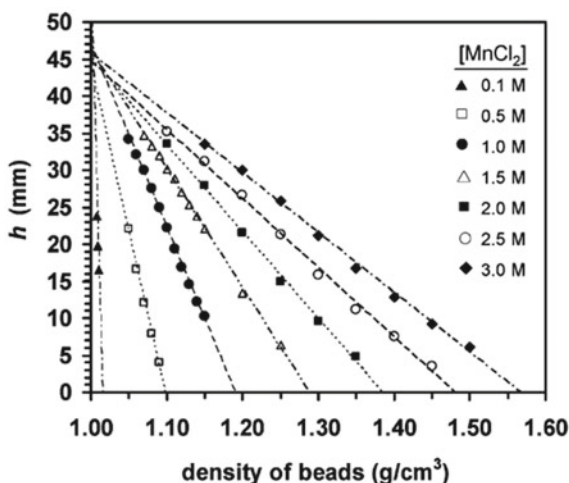
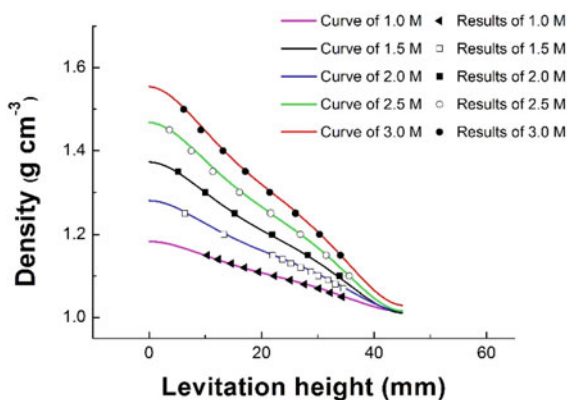


Table 5.2 Measurement results on standard density beads via multiple methods

Sample	Density (g/cm^3)			
	Obtained from vendor	Obtained from calibration curves in MnCl_2	Obtained using Eq. 5.10 in MnCl_2	Obtained using Eq. 5.10 in GdCl_3
1.0100	1.0100 ± 0.0002	1.0099 ± 0.0002	1.010 ± 0.001	1.009 ± 0.001
1.1000	1.1000 ± 0.0002	1.101 ± 0.002	1.101 ± 0.002	1.102 ± 0.002
1.1500	1.1500 ± 0.0002	1.152 ± 0.003	1.152 ± 0.003	1.152 ± 0.003

Reproduced with permission from Ref. [1]. Copyright 2009 American Chemical Society

Fig. 5.9 Density measurement of standard density beads using Eqs. 5.6 and 5.7. Reproduced with permission from Ref. [2]. Copyright 2019 Elsevier



higher accuracy in the whole measuring range. However, the introduction of more parameters may lead to a more complex effect on the error of the results.

5.6.2 Measuring Samples of Different States

As long as the object are not soluble in the medium, the objects with densities within the measuring range are suitable for MagLev. Generally, the medium using water or ethanol/methanol can measure solid particles (except for soluble salt) and oily liquid, the medium using ionic liquid is suitable for aqueous solutions and water soluble substances.

A comparison between MagLev and pycnometer shows the advantage of MagLev in testing samples of different states. The materials used are particles, powders, and oils, whose testing results are shown in Table 5.3. For comparison, every kind of sample is also measured by a 25 mL pycnometer (kuihuap®). The result and the error bar is taken from three repeated tests. The magnetic levitation shows much higher consistency than that of pycnometer method. As shown in Table 5.3, the standard deviation in the experiments by a pycnometer is 10 times larger when measuring

solid (0.05% vs. 0.5%) and 2 times larger when measuring liquid (1.1% vs. 2.1%). In general, the common density measuring methods usually can handle only one state of substances.

For example, the hydrometer method is only for measuring liquid, and the density-gradient column can only deal with particles. In these experiments, MagLev method shows its high applicability for both solid and liquid substances. In addition, although pycnometer method can also handle both solid and liquid samples, the volume required for MagLev is much less. Each test requires only one particle or droplet (0.1–20 μL), while the pycnometer usually requires a certain amount of sample (usually more than 5 g) for obtaining such accuracy. Particularly for liquid sample, it needs to full-fill the pycnometer for the test. The pycnometer method cannot measure density of single droplet with volume less than 1 ml. Besides, the solvent and the solute for preparing the medium of MagLev method are commercially available. The measuring process is also more convenient than that of helium pycnometer and hydrometer.

For water soluble samples, the PILs are proved to be adequate. Research has shown that PILs can correlate the density of a known mixture of $\text{D}_2\text{O}/\text{H}_2\text{O}$ mixture (Fig. 5.10a). Experiments on differences of five percent in composition shows

Table 5.3 Experiments of materials in different states

Sample	Medium	Density (g cm^{-3})	
		Pycnometer	Magnetic levitation
Polylactic acid (PLA) (~4 mm)	3.0 M MnCl_2 solution	1.255 ± 0.008	1.2577 ± 0.0006
polycaprolactone (PCL) (~4 mm)	1.0 M MnCl_2 solution	1.142 ± 0.008	1.1420 ± 0.0003
Thermoplastic polyurethanes (TPU) (~4 mm)		1.114 ± 0.006	1.1124 ± 0.0001
Polypropylene (PP) (~4 mm)	1.0 M MnCl_2 solution	0.904 ± 0.005	0.9038 ± 0.0001
High density polyethylene (HDPE) (~4 mm)		0.939 ± 0.005	0.9437 ± 0.0004
Peanut oil	1.0 M MnCl_2 methanol-solution	0.912 ± 0.002	0.9125 ± 0.0010
Soybean oil		0.921 ± 0.002	0.9179 ± 0.0005
Corn oil		0.920 ± 0.002	0.9169 ± 0.0004
Microcrystalline cellulose (< 100 μm)	4.0 M MnCl_2 solution	1.574 ± 0.002	1.6049 ± 0.0006
Recycled PP (< 500 μm)	1.0 M MnCl_2 solution	0.902 ± 0.007	0.9004 ± 0.0009

Reproduced with permission from Ref. [2]. Copyright 2019 Elsevier

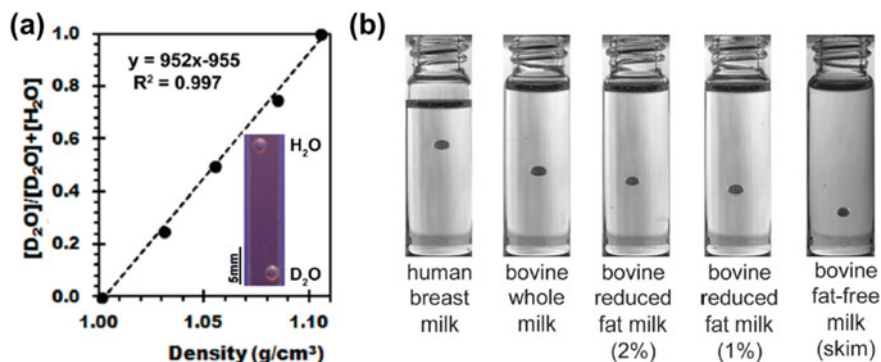


Fig. 5.10 Density measurement of water soluble materials. **a** Density measurement of isotope (D_2O/H_2O) mixture (medium: $[Aliq]_3[HoCl_6]$ PIL). **b** Density measurement of different milks (medium: 40 mM $Gd(DTAD)$ dissolved in 84:16 2-fluorotoluene/chlorobenzene. Reproduced with permission from Ref. [3]. Copyright 2013 American Chemical Society and Ref. [5]. Copyright 2010 American Chemical Society

its ability in monitoring isotope enrichment in mixtures [3]. Other trials successfully distinguished the differences between whole milk and adulterated (e.g., with melamine or water) whole milk [5].

5.6.3 Measuring Samples of Different Volumes

According to theory analysis, the method can obtain density without knowing the volume of the object exactly. Thus the method is theoretically suitable for extremely tiny samples.

A series of experimental results are shown in Fig. 5.11. The samples in these experiments were three types of materials (PCL, corn oil, and microcrystalline cellulose) of different forms (particles, liquid droplets, and powders). Each form has three experiments for different volumes. The time for each object to be levitated in a stable position is also recorded. Three PCL particles with different particle sizes $d_1 < 3$ mm, $d_2 < 1$ mm, and $d_3 < 0.5$ mm. The equilibrium time for each particles are 5 s, 10 s, and 17 s. The volumes of corn oil droplets are 5 μL , 2 μL , and 0.5 μL with the equilibrium durations of 6 s, 10 s, and 22 s, respectively. Microcrystalline cellulose is measured in forms of three heaps of powder. The three heaps contain 1 mg, 0.7 mg, and 0.5 mg microcrystalline cellulose powders respectively. The equilibrium duration for each heap is almost the same. It takes about 2 min for every heap to assemble at the stable position. Figure 5.11 shows that the same materials with different sizes were levitated at exactly the same levitation height regardless their sizes or shapes, which means the calculation results via Eq. 5.7 for their densities are the same. The minimum size of the sample in these experiments is around 0.5 μL (Fig. 5.11b).

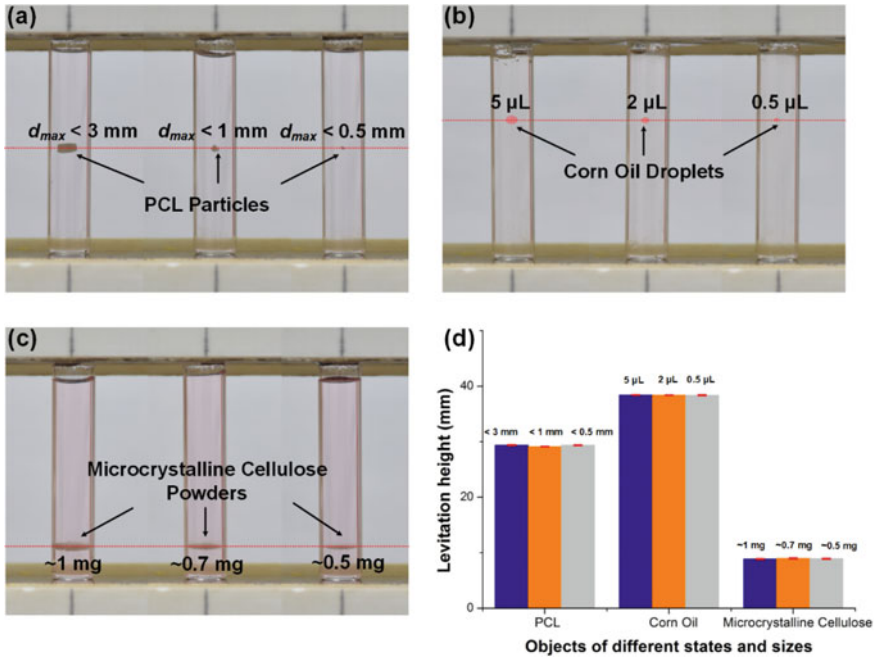


Fig. 5.11 Experiments for different materials with different scales. **a** Experiments for PCL particles. **b** Experiments for corn oil droplets (post-processing is applied to enhance the contrast ratio). **c** Experiments for microcrystalline cellulose powders. Materials of same densities but of different volumes have been levitated at the same levitation height (along the red line). **d** Figure of statistics for the three groups of experiments. The minimum size in these experiments reached to 5 μL . Reproduced with permission from Ref. [2]. Copyright 2019 Elsevier

Theoretically, tiny sample can be measured by the method provided the sample is visible, since the levitation height of a sample is irrelevant to its volume.

As mentioned above, most of existing density measuring methods require quantity of sample (usually less than 5 ml) to achieve such a high measuring accuracy, while other methods such as micro-channel resonator can only measure extremely tiny particles or droplets (~1 pL). In certain fields such as biological research, electronics and functional materials [6], a method for some tiny single particle is highly required, since the samples used in the research on these fields always have tiny volumes (< 1 μL) [6–9]. The experimental results have proved that the proposed MagLev method can deal with samples between 0.5 and 500 μL . Therefore, the method has great potential of being applied on these fields. Obviously, the existing density measuring methods are not applicable in these fields, since they require samples with volumes larger than 1 mL or smaller than 10 pL. We confirm that numerous potential applications based on measurements of density would require (or benefit from) the proposed magnetic levitation configuration, which is simple, portable, inexpensive, without external energy supply and capable of measuring density values accurately for small-sized samples.

5.7 Comprehensive Comparison

Several methods are commercially used to measuring density with very high accuracy, but require strict constraints. For comparison, Table 5.4 lists the characters of each method. Details were obtained by vendors or related organizations. All the methods' accuracy can reach 0.001 g cm^{-3} or even higher. But most of devices for these methods are complicated and require energy supply. Other than the MagLev method, the only method requires no external energy or material supply is density-gradient columns, however, preparation of density-gradient and benchmarking process are laborious [10].

Amongst the density measurements, MagLev method is the most inexpensive one that reaches such accuracy. The other advantage of MagLev method is owing to the versatility of this configuration. In some studies, such as photocuring process [11], density measurement is required for both liquid and solid samples. This method is suitable for measuring both solid and liquid samples, especially for tiny single parts and powders, while other methods often specialize in one state or scale [12, 13].

Table 5.4 Comparison of magneto-Archimedes levitation method and common methods

Method/Device ^α	Cost (RMB) ^β	Accuracy (g cm^{-3}) ^β	Versatility ^β	Quantity ^β	Portability ^β	None energy requirement ^β
Hydrometer [14]	200k	0.0001	Liquid	> 1 mL	N	N
Densitometer [15]	4k	0.001	Solid particles and powders	> 10 mL	N	N
Pycnometer [14]	4k	0.001	Liquid, solid particles and powders	> 5 ml (solid) > 20 mL (liquid)	Y	N
Helium pycnometer [1]	70k	0.001	Solid particles and powders	> 5 mL	N	N
Density-gradient column [10]	15k	0.001	Solid particles	> 1 mL	N	Y
Suspended microchannel resonator [16, 17]	100k	0.001	Nano single particle	~1 pL	N	N
Magneto-Archimedes [2]	500	0.001	Liquid, solid particles and powders	0.5 μL –1 mL	Y	Y

^αThe devices are commercially accessible from vendor or related laboratory

^βThe parameters are obtained from vendor or manual of the device

For other methods, the mass and volume of a sample are both needed and measured separately. It is extremely difficult to measure the volume accurately, particularly that of small sample. Certain quantity of sample is needed for reducing measuring error. As shown in the theoretical analysis, MagLev method avoid measuring the volume of a sample, a good applicability for different scales is thereby guaranteed, e.g. the separation of different powder, and the measurement for biomaterials such as cells and collagen. In addition, MagLev method also have advantages of portability and non-energy requirement. The basic part of a device is only two permanent magnets, which makes device have a portable size of no more than $100\text{ mm} \times 100\text{ mm} \times 200\text{ mm}$. This allows MagLev method have quick response (no need of finding power support) or apply in outdoors or resource-limited occasions. However, admittedly, the proposed MagLev method has three limitations. (i) The size range of the samples for the MagLev method is constrained (eg. limits to $\sim 2\ \mu\text{m}$ in the device with $d = 45\text{ mm}$ [1]). (ii) Like other density measurements, measuring range and sensitivity are still two competing characteristics of the MagLev method; it is difficult to enlarge measurement range and sensitivity simultaneously. (iii) The accuracy of measurement for the levitation height of the sample could have significant effect on the accuracy in measuring density when high concentration solution (maximum to 0.0043 g cm^{-3} when using 3.0 M MnCl_2 solution) is used.

References

1. Mirica KA, Shevkopyas SS, Phillips ST, et al. Measuring densities of solids and liquids using magnetic levitation: fundamentals. *J Am Chem Soc.* 2009;131(29):10049–58.
2. Xie J, Zhang C, Gu F, et al. An accurate and versatile density measurement device: magnetic levitation. *Sens Actuators B Chem.* 2019;295:204–14.
3. Bwambok DK, Thuo MM, Atkinson MJB, et al. Paramagnetic ionic liquids for measurements of density using magnetic levitation. *Anal Chem.* 2013;85(17):8442–7.
4. Sohnel O, Novotny P, Solc Z. Densities of aqueous solutions of 18 inorganic substances. *J Chem Eng Data.* 1984;29(4):379–82.
5. Mirica KA, Phillips ST, Mace CR, et al. Magnetic levitation in the analysis of foods and water. *J Agric Food Chem.* 2010;58(11):6565–9.
6. Bøyum A, Brincker Fjerdingsstad H, Martinsen I, et al. Separation of human lymphocytes from citrated blood by density gradient (Nycoprep) centrifugation: monocyte depletion depending upon activation of membrane potassium channels. *Scand J Immunol.* 2002;56(1):76–84.
7. Zhao P, Peng Y, Yang W, et al. Crystallization measurements via ultrasonic velocity: study of poly (lactic acid) parts. *J Polym Sci Part B Polym Phys.* 2015;53(10):700–8.
8. Juopperi TA, Schuler W, Yuan X, et al. Isolation of bone marrow-derived stem cells using density-gradient separation. *Exp Hematol.* 2007;35(2):335–41.
9. Feng Y, Miyata Y, Matsushita K, et al. High-efficiency separation of single-wall carbon nanotubes by self-generated density gradient ultracentrifugation. *J Phys Chem C.* 2011;115(5):1752–6.
10. Davidson S, Perkin M. An investigation of density determination methods for porous materials, small samples and particulates. *Measurement.* 2013;46(5):1766–70.
11. Dewaele M, Truffier-Boutry D, Devaux J, et al. Volume contraction in photocured dental resins: the shrinkage-conversion relationship revisited. *Dent Mater.* 2006;22(4):359–65.
12. Stange U, Scherf-Clavel M, Gieseler H. Application of gas pycnometry for the density measurement of freeze-dried products. *J Pharm Sci.* 2013;102(11):4087–99.

13. Kikuchi T, Wang B, Pikal MJ. High-precision absolute (true) density measurements on hygroscopic powders by gas pycnometry: application to determining effects of formulation and process on free volume of lyophilized products. *J Pharm Sci.* 2011;100(7):2945–51.
14. Webster JG. *The measurement, instrumentation and sensors handbook.* CRC Press; 1998.
15. Xie J, Zhao P, Zhang C, et al. Measuring densities of polymers by magneto-archimedes levitation. *Polym Testing.* 2016;56:308–13.
16. Khan MF, Schmid S, Larsen PE, et al. Online measurement of mass density and viscosity of pL fluid samples with suspended microchannel resonator. *Sens Actuators B Chem.* 2013;185:456–61.
17. Bircher BA, Krenger R, Braun T. Automated high-throughput viscosity and density sensor using nanomechanical resonators. *Sens Actuators B Chem.* 2016;223:784–90.

Chapter 6

Optimization of MagLev



Jun Xie, Zhengchuan Guo, Chengqian Zhang, and Peng Zhao

6.1 Introduction

The invention of magnetic levitation detection method brings us a potential density measurement and density-based analysis method. The advantages of standard MagLev device have been proved to be (i) of high accuracy, (ii) of high sensitivity, (iii) applicable to smaller objects, such as droplets and powders, (iv) convenient, and (v) low cost.

However, restrictions of standard MagLev still remain. Along with the advantage of low cost brought by the use of permanent magnets comes the restriction of the ability for denser materials. The permanent magnets used in the standard MagLev device can only provide the maximum magnetic flux intensity of 0.475 T at the center on one poles surface. Meanwhile, the maximum concentration of MnCl_2 aqueous solution is approximately 5.0 M. Both of the reasons lead to a main restriction that the measurement range of standard MagLev device can be only 0.8–3.0 g/cm^3 . Practically, densities of most of the common materials, such as metals, oxides, and salts, are beyond this range.

Therefore, trials on overcoming the problems were carried out by optimizing the MagLev method. This details of the optimizations will be introduced in this chapter.

J. Xie (✉)

College of Mechanical Engineering, Zhejiang University of Technology, Hangzhou, China
e-mail: jxie93@zjut.edu.cn

Z. Guo · C. Zhang · P. Zhao

The State Key Laboratory of Fluid Power and Mechatronic Systems, College of Mechanical Engineering, Zhejiang University, Hangzhou, China

6.2 Enlarging the Measurement Range

Along with the advantage of low cost brought by the use of permanent magnets comes the restriction of the ability for denser materials. The permanent magnets used in the standard MagLev device can only provide the maximum magnetic flux intensity of 0.475 T at the center on one poles surface. Meanwhile, the maximum concentration of MnCl_2 aqueous solution is approximately 5.0 M. Both of the reasons lead to a main restriction that the measurement range of standard MagLev device can be only 0.8–3.0 g/cm^3 . Practically, densities of most of the common materials, such as metals, oxides, and salts, are beyond this range.

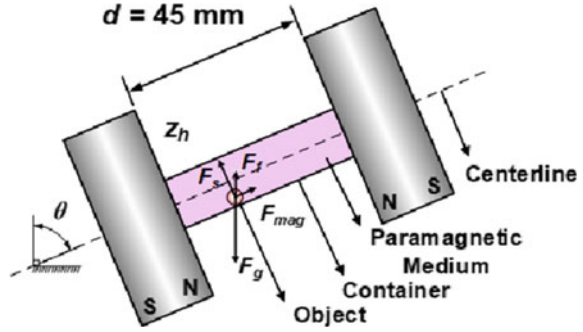
Similar to the effect of the slope in lifting heavy object, the introduction of additional constraint can levitate materials with higher densities with small magnetic force. It is still possible to measure the density of an object by the geometric relationship between the magnetic force and gravity. Two methods are reported to enlarge the measurement range according to this concept.

6.2.1 Tilting the MagLev Device

Tilting the device is the earliest configuration for enlarging the measurement range of MagLev method without increasing the magnetic flux intensity of the magnets [1]. The configuration is based on the standard MagLev device, which has two identical square magnets ($2' \times 2' \times 1'$) with like poles facing each other at a distance of 45 mm. The container filled with paramagnetic solution (typically aqueous MnCl_2 or GdCl_3) are set vertically to the surface of the magnet. It is easy to predict that a dense object cannot be levitated in standard MagLev device. Hence, when the device is tilted with a certain angle, the dense object would rest at the boundary of the container. In this case, the forces acting on the object are gravity \vec{F}_g , buoyancy \vec{F}_f , magnetic force \vec{F}_{mag} , and the holding force caused by the boundary \vec{F}_s . When the tilting angle is large enough, the most of the gravity would be balanced by the vertical component of \vec{F}_s . Thereby, the object could be pushed away from the bottom of the container by the \vec{F}_{mag} , and reached to an equilibrium position based on its density, as shown in Fig. 6.1. Similarly, the same method can be applied to an object that is much less dense than the solution, which would floats to the top of the container rather than sinking to the bottom. The figure also defines the coordinates for the MagLev frame of reference and laboratory frame of reference. The x - and z -axis are defined as fixed with the device and rotate with the angle θ ; the x' - and z' -axis are fixed to the laboratory frame of reference, and do not rotate.

Unlike standard MagLev device, the equilibrium position of the object in tilted device is no longer along with the centerline. Along with the phenomenon is a question: is the equation for \vec{F}_{mag} along the centerline available or not? To figure out the question, a theoretical analysis was carried out. Previous sections have given the

Fig. 6.1 Schematic of tilted MagLev device. Reproduced with permission from Ref. [3]. Copyright 2021 Elsevier

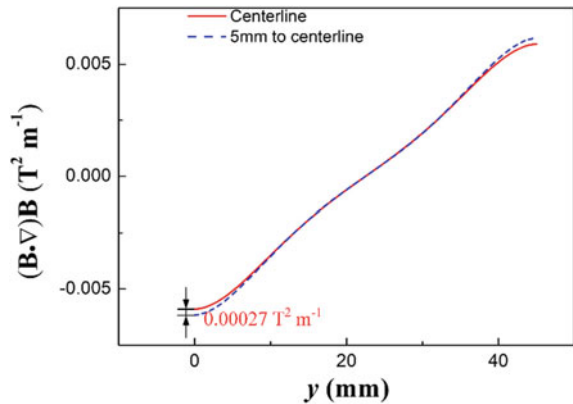


total distribution of the magnetic flux intensity of a standard MagLev device. Based on this distribution, the vertical component (in coordinate for the MagLev frame of reference) $(\vec{B} \cdot \vec{\nabla})\vec{B}$ along the centerline and 5 mm away from the centerline is calculated and drawn as curves in Fig. 6.2. It is obvious that the two curves are coincide with each other in the most area. The biggest difference occurs at the surfaces of the two magnets, which is only $0.00027 \text{ T}^2 \text{ m}^{-1}$ (4.3%). Meanwhile, the previous section also proved that the horizontal component of $(\vec{B} \cdot \vec{\nabla})\vec{B}$ can be neglected for it is much smaller than the vertical component. Therefore, the equation for \vec{F}_{mag} at the boundary 5 mm away from the centerline can be approximately replaced by that along the centerline, which can be expressed as:

$$\vec{F}_{mag} = \frac{4\Delta\chi B_0^2 V}{\mu_0 d^2} \left(\frac{d}{2} - z \right) \hat{z} \tag{6.1}$$

where, $\Delta\chi = \chi_s - \chi_m$ (unitless) is the difference between the magnetic susceptibilities of object and the medium; \hat{z} is the unit vector of the z -axis; B_0 (T) is the magnetic flux intensity at the surface center of the magnet pole; $\mu_0 = 4\pi \times 10^{-7} \text{ (N/$

Fig. 6.2 The $(\vec{B} \cdot \vec{\nabla})\vec{B}$ along the centerline and 5 mm away from the centerline. Reproduced with permission from Ref. [2]. Copyright 2021 Elsevier



A^2) is the permeability of the free space, and $d = 45$ (mm) is the distance between the two magnets.

In ideal conditions, the sample can be stably held at a position under the balance between the forces \vec{F}_g , \vec{F}_f , \vec{F}_{mag} , and \vec{F}_{bdy} ,

$$\vec{F}_g + \vec{F}_f + \vec{F}_{mag} + \vec{F}_{bdy} = 0 \quad (6.2)$$

that is,

$$(F_g - F_f) \cos \theta = F_{mag} \quad (6.3)$$

According to the expression for each force, the density of the sample ρ_s can be expressed as,

$$\rho_s = \frac{4\Delta\chi B_0^2 V}{\mu_0 g d^2 \cos \theta} \left(\frac{d}{2} - z_h \right) + \rho_m \quad (6.4)$$

where, ρ_m is the density of the medium and z_h is the distance from the sample to the bottom magnet.

Compare Eq. 6.3 with Eq. 5.5, the additional component of the equation is the $\cos \theta$. For the $\cos \theta$ is always less than 1, it is easy to conclude that the measuring range of the device can be directly enlarged. Furthermore, the adjustment of tilting angle θ would result in the change of the measuring range. Theoretically, the measuring range can be infinitely enlarged, as long as the θ is close to 90° enough. In other word, the tilted device has potential to cover the density measurement for all nonmagnetic materials.

However, the ideal condition has a premise that the friction is ignored. In actual environment, the friction plays a very important role in holding the sample stably during the spontaneous levitation of the sample. Therefore, additional processes are considered to avoid the influence of the friction.

Spherical Samples. The rotation of spherical samples can greatly reduce the effect of friction. The friction can be directly ignored under this occasion. During measurement, if the spherical object does not reach to equilibrium position, it would roll and settle at another position (after agitation). If the sphere remained at the same position, regardless of manual agitation, it can be assumed that the sphere reached its equilibrium position. Once this condition was met, the density of the object can be measured using Eq. 6.4. Accordingly, the medium with low viscosity is highly preferred.

Nonspherical Samples. The friction would even prevent a nonspherical object from leaving its initial position. An additional procedure was carried out reduce the effect of the friction: after rotating the container by 180° and then stopping, the sample fell gradually back to the bottom surface of the container. Repeat this procedure several times until the bottom position along the z-axis would no longer change, the state of

the object can be assumed as equilibrated along the z axis. To achieve the overturn of the object's position, high viscosity medium is applied. For instance, 3.00 M MnCl_2 solution with aqueous dextran of 35% by weight has the viscosity of approx. 10 Pa s (similar as honey). The highly viscous medium can "carry" the object rotating with the container. Without a viscous liquid, it is hard to overturn the object with the rotation of the container. The object may continue to stay at the bottom regardless of the rate of rotation about the z -axis.

Powders. Similar to nonspherical samples, powders also need to rotate the sample with the container. However, at the scale of powder, fluid resistance increases times larger than that of bulk objects. Therefore, medium with low viscosity is capable for "carry" the powders. On the contrary, highly viscous medium will greatly enlarge the falling time of the powder, which is a waste of time. Unlike single particles, the powders tended to disperse throughout the container during the initial rotations. But the powder will finally converge into a narrow band after enough times of rotation. Additionally, it is also found that rotate the container at a relatively small angle (e.g. rotating 90° instead of 180°), the powder will slide along the surface of the container instead of falling down through the medium. This approach can prevent the dispersion of the particles throughout the container and enable the powder reach to equilibrium position in much less rotations.

The measurement on denser spheres obviously showed the effect on enlarging measurement range, as shown in Fig. 6.3. The materials with large densities, such as Teflon and aluminum (whose densities cannot be measured using the same medium in standard MagLev device), were successfully levitated at their equilibrium positions. Their densities were measured by knowing the z_h and θ . In practical, materials with densities from 0 to over 20 g/cm^3 could all be measured by the method. Table 6.1 showed the results of these materials [1]. The results are in close agreement with those reported by the manufacturer or from other sources. The measurement of same materials in different states (particle and powder) were also well coincidence with each other. In addition, the air was also measured in the tilted device, although the device cannot afford the accurate density measurement of materials with such low density. This indicates that the enlargement of the measurement range is at a large expense of accuracy. The accuracy of the method is two orders of magnitude lower than that of the standard MagLev.

6.2.2 *Horizontally Setting the MagLev Device*

Horizontally setting the device is another concept to enlarge the measurement range of the device [2]. Similar to tilting the device, this concept introduces an addition constraint to balance a large part of an object's gravity. This constraint is coming from a string attached to the object. The other side of the string is fitted at a certain height. The length of the string L can be adjusted for different occasions. The surface center of the left magnet is set as the origin of coordinates, as shown in Fig. 6.4.

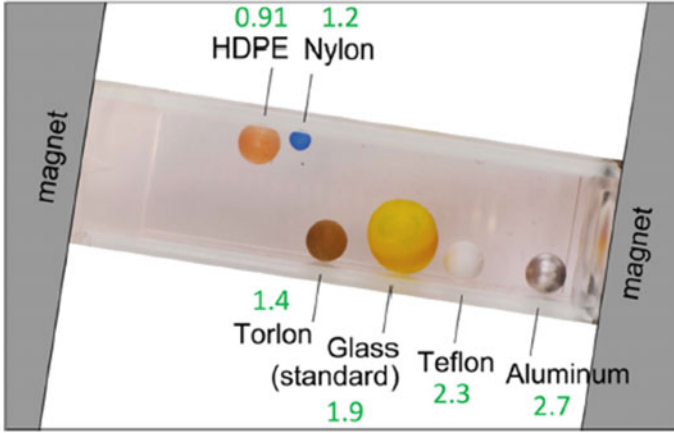


Fig. 6.3 Levitation of denser materials using tilted MagLev device. Reproduced with permission from Ref. [1]. Copyright 2021 American Chemical Society

When the sample is emerged in the paramagnetic medium, it can be pushed away from the surface of the magnet. The three forces the gravity \vec{F}_g , the buoyancy \vec{F}_b , the magnetic buoyancy caused by the magnetic field \vec{F}_{mag} will get balanced with the additional pulling force from the string \vec{F}_t ,

$$\vec{F}_g + \vec{F}_b + \vec{F}_{mag} + \vec{F}_t = 0 \tag{6.5}$$

As discussed in previous section, it can be noticed that the $(\vec{B} \cdot \vec{\nabla})\vec{B}$ can be assumed as linear, by which the density of the sample can be obtained as Eq. 6.6:

$$\rho_s = \frac{\sqrt{L^2 - d_p^2}}{d_p} \cdot \frac{\Delta\chi}{\mu_0 g} \left(\frac{4B_0^2}{d^2} \cdot d_p - \frac{2B_0^2}{d} \right) + \rho_m \tag{6.6}$$

where L is length of the nylon string. Due to the setting of the coordinates, the distance between the object and the magnet is denoted as d_p instead of z_h .

Several assumptions are made when using this method to measuring density of the denser objects. (i) In this method, the string is assumed as rigid, which means the string will not be stretched or bent during the measuring process. (ii) The $\Delta\chi$ can be approximately replaced by $-\chi_m$, for the magnetic susceptibilities of nonmagnetic materials are always much smaller than that of the medium. (iii) The measuring characteristic along the centerline can be used to measure density throughout the measuring process. It can be noticed that the biggest difference between the $(\vec{B} \cdot \vec{\nabla})\vec{B}$ along the centerline and 5 mm away from the centerline occurs at the surface of the two magnet. In addition, the object will derive from the centerline only when it is pushed away from the surface of the magnet. The effect caused by the derivation can

Table 6.1 Densities measurement results of different materials in different states [1]

Material	State	Density (g/cm ³)	
		Known	Measured
High-density polyethylene (HDPE)	Solid (spherical)	0.941	0.95 ± 0.05
Polytetrafluoroethylene (teflon)	Solid (spherical)	2.21	2.2 ± 0.04
Polytetrafluoroethylene (teflon)	Solid (non-spherical)	2.21	2.2 ± 0.05
Glass	Solid (spherical)	2.4–2.8	2.4 ± 0.04
Glass	Powder	2.4–2.8	2.4 ± 0.04
Aluminum	Solid (spherical)	2.7	2.7 ± 0.1
Aluminum	Powder	2.7	2.7 ± 0.04
Silicon nitride	Solid (spherical)	3.32	3.3 ± 0.05
Aluminum oxide	Solid (spherical)	3.88	3.9 ± 0.06
Aluminum oxide	Solid (non-spherical)	3.88	3.9 ± 0.06
Brass	Solid (spherical)	8.53	8.5 ± 0.5
Copper	Solid (non-spherical)	8.96	9.0 ± 0.6
Copper	Powder	8.92	8.8 ± 0.3
Lead	Solid (spherical)	11.2–11.3	11 ± 0.6
Lead	Solid (non-spherical)	11.2–11.3	11 ± 0.6
Mercury	Liquid	13.55	13 ± 0.9
Silicon	Solid (non-spherical)	2.33	2.4 ± 0.04
Diamond	Solid (non-spherical)	3.51	3.6 ± 0.09
Stibnite (Sb ₂ S ₃ , mineral)	Solid (non-spherical)	3.88	3.9 ± 0.06
Cerussite (PbCO ₃ , mineral)	Solid (non-spherical)	4.52–4.62	4.5 ± 0.1
Indium	Solid (non-spherical)	7.31	7.3 ± 0.2
Silver	Solid (non-spherical)	10.5	11 ± 0.1
Gold	Solid (non-spherical)	19.3	20 ± 1
Gold	Powder	19.3	19 ± 1
Osmium	Solid (non-spherical)	22.59	23 ± 2
Air	Gas	0.001	0.0 ± 0.04

Reproduced with permission from Ref. [1]. Copyright 2021 American Chemical Society

also be neglected. For example, if the length of the string is 200 mm, the maximum deviation would be less than 1.27 mm, which is much smaller than 5 mm. Therefore, the $(\vec{B} \cdot \vec{\nabla})\vec{B}$ along the centerline can be used for density measurements throughout the measuring process.

Practically, the sample cannot be simply considered as a mass point. Thus, the initial position of the sample's centroid cannot coincide with the center of the surface of the magnet. The volume of the sample will affect the measurement range of the device. For instance, assuming that the diameter of the sample is 10 mm and set the L

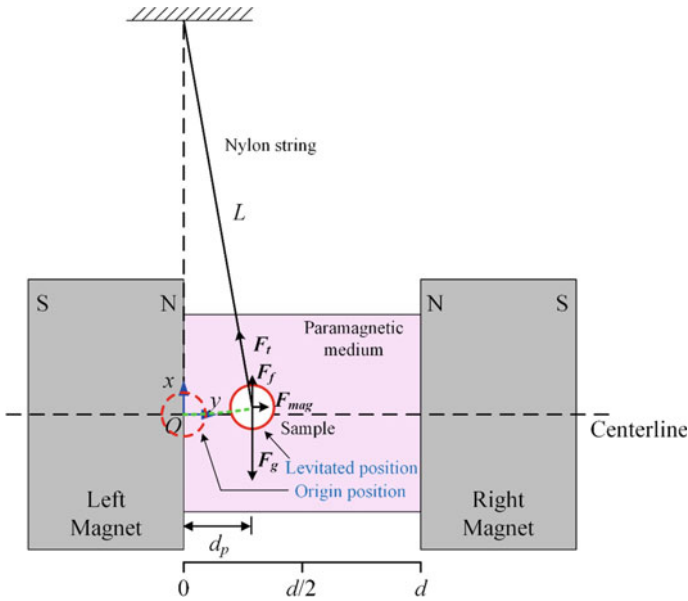


Fig. 6.4 Schematic of horizontally settled MagLev device. Reproduced with permission from Ref. [2]. Copyright 2021 Elsevier

as 200 mm, the measurement range of the device using common solutions are listed in Table 6.2.

Verifications by measuring glass, aluminum, and brass beads, lead to the conclusion that this method has a high accuracy in measuring samples with larger densities, as shown in Fig. 6.5. The measuring results well coincided with the nominal values.

In addition, this method also inherits the advantage of the standard MagLev method that it can measure density without knowing the volume of the sample precisely. This advantage allows the method to quickly obtain the density of samples under some harsh conditions. For instance, the field exploration usually need to know the density of some minerals. Common methods, such as pycnometer and densitometer need the high precision electronic balance, which can only work well

Table 6.2 Parameters for measurement and the measuring range ($L = 200$ mm)

Standard concentration solutions	Measuring range (g cm^{-3})
1.0 M MnCl_2	[1.094, 3.890]
1.5 M MnCl_2	[1.148, 5.413]
2.0 M MnCl_2	[1.197, 6.931]
2.5 M MnCl_2	[1.242, 8.730]
3.0 M MnCl_2	[1.292, 9.949]

Reproduced with permission from Ref. [2]. Copyright 2021 Elsevier

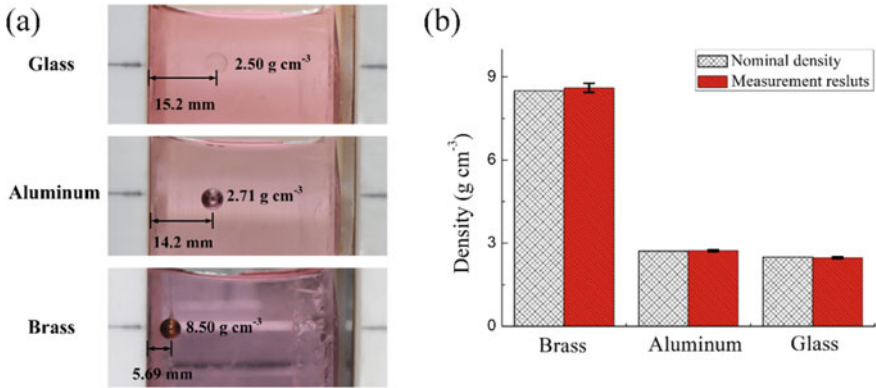


Fig. 6.5 Verifications by measuring density of glass, aluminum, and brass beads. **a** Levitation results in horizontally settled device. **b** The calculated results of glass, aluminum, and brass beads. Reproduced with permission from Ref. [2]. Copyright 2021 Elsevier

in laboratory conditions. The MagLev method provides a potential solution for rapid measurement of mineral particles in outdoor occasions.

Trials on different minerals were carried out (Fig. 6.6). Their measurement results are listed in Table 6.3. It can be noticed that the MagLev method is capable for substituting the common methods. The advantage of portability and energy-free additionally make the method be more suitable for outdoors' occasions over common methods.

However, this method also has relatively more restrictions compared with tilted MagLev device. The most important difference is that the device can only measure solid particles. The measuring process need to adhere the sample with the string.

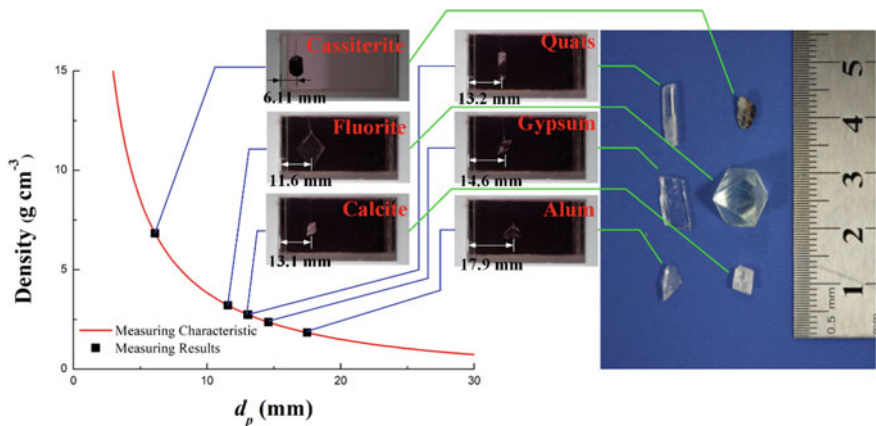


Fig. 6.6 Density measurement of different mineral particles. Reproduced with permission from Ref. [2]. Copyright 2021 Elsevier

Table 6.3 Density measurement results of different minerals [2]

Single particle		Multiple particles						
Minerals	Levitation height (mm)	Calculated results (g cm^{-3})	Average results (g cm^{-3})	Mean square error (g cm^{-3})	Pycnometer results (g cm^{-3})	Densitometer results (g cm^{-3})	Pycnometer results (g cm^{-3})	Densitometer results (g cm^{-3})
Alum	17.6	1.818	1.828	0.011	1.655 \pm 0.151	1.858	1.826 \pm 0.006	1.829
	17.4	1.839						
	17.4	1.837						
	17.5	1.830						
	17.6	1.816						
Gypsum	14.5	2.369	2.347	0.025	2.102 \pm 0.076	2.386	2.324 \pm 0.012	2.351
	14.7	2.334						
	14.7	2.322						
	14.5	2.377						
	14.7	2.331						
Quartz	13.7	2.560	2.573	0.031	2.499 \pm 0.136	2.598	2.578 \pm 0.012	2.580
	13.5	2.609						
	13.6	2.584						
	13.6	2.584						
	13.8	2.528						
Calcite	13.1	2.702	2.727	0.029	2.428 \pm 0.292	2.673	2.722 \pm 0.014	2.744
	13.0	2.735						
	12.9	2.774						
	13.1	2.707						
	13.1	2.717						

(continued)

Table 6.3 (continued)

Single particle		Multiple particles						
Minerals	Levitation height (mm)	Calculated results (g cm^{-3})	Average results (g cm^{-3})	Mean square error (g cm^{-3})	Pycnometer results (g cm^{-3})	Densitometer results (g cm^{-3})	Pycnometer results (g cm^{-3})	Densitometer results (g cm^{-3})
Fluorite	11.5	3.187	3.182	0.012	3.161 ± 0.132	3.192	3.180 ± 0.008	3.197
	11.6	3.174						
	11.6	3.166						
	11.5	3.188						
	11.5	3.195						
Barite	8.9	4.380	4.317	0.073	4.412 ± 0.238	4.381	4.310 ± 0.023	4.342
	9.0	4.320						
	9.2	4.193						
	8.9	4.354						
	9.0	4.337						
Cassiterite	6.2	6.650	6.742	0.072	6.790 ± 0.331	7.009	6.754 ± 0.011	6.747
	6.1	6.776						
	6.1	6.754						
	6.1	6.695						
	6.0	6.836						

Reproduced with permission from Ref. [2]. Copyright 2021 Elsevier

Thus, this device is not capable for gas, powder, and liquid samples. In addition, the constraint from the string can only prevent the sample from sinking to the bottom of the container. This means the horizontally set device also cannot measure the sample with density lower than the medium.

6.3 Improving the Sensitivity

Equation 5.6 was deduced to measure the density of an object levitated along the centerline of a MagLev device. Higher sensitivity of a MagLev device means it can distinguish small differences in ρ_s by an obvious change of z_h . Thus, the sensitivity of a device can be defined as its ability to distinguish the difference in density $\Delta\rho_s$ caused by the change in levitation Δz_h . It is known that $\Delta\rho_s = f'(z_h)\Delta z_h$. Then we defined the sensitivity using Eq. 6.7.

$$S(z_h) = \left| \frac{1}{f'(z_h)} \right| \quad (6.7)$$

Here, $S(z_h)$ denotes the sensitivity of the device. Larger $S(z_h)$ equals higher sensitivity. Note that $S(z_h)$ could be influenced by χ_m , the structure of the device (d), the magnets used in the device, and the position of the sample (z_h). This study emphasised the influence of d . The comparisons in each section were conducted using a medium with the same MnCl_2 concentrations. The magnets were the same in all of the experiments.

6.3.1 Enlarging the Distance Between the Magnets

Although standard MagLev device has high accuracy and sensitivity in measuring density, it still has place to be improved. It can be easily predicted that enlarging the distance between the magnets is a potential way to enlarge the sensitivity of the device. However, the relationship between the density and levitation height become no longer linear. Hence, further theoretical analysis should be discussed.

For the improvement is based on the standard MagLev device, the magnets are chosen as N45 magnets with the size of 50 mm \times 50 mm \times 25 mm. Based on the magnets, the performance of the device under different d is further plotted in Fig. 6.7 [3]. As mentioned above, the stable levitation along the centreline is required to guarantee the accurate measurement. According to the performance of the device, although the calculation curve of device with $d = 70$ mm shows the highest sensitivity above the other two curves (Fig. 6.7d), it cannot ensure levitating the sample steadily along the centreline (Fig. 6.7c). The device with $d = 60$ mm has a relatively higher sensitivity and a larger manipulation space than those of the standard MagLev device (Fig. 6.7b, d).

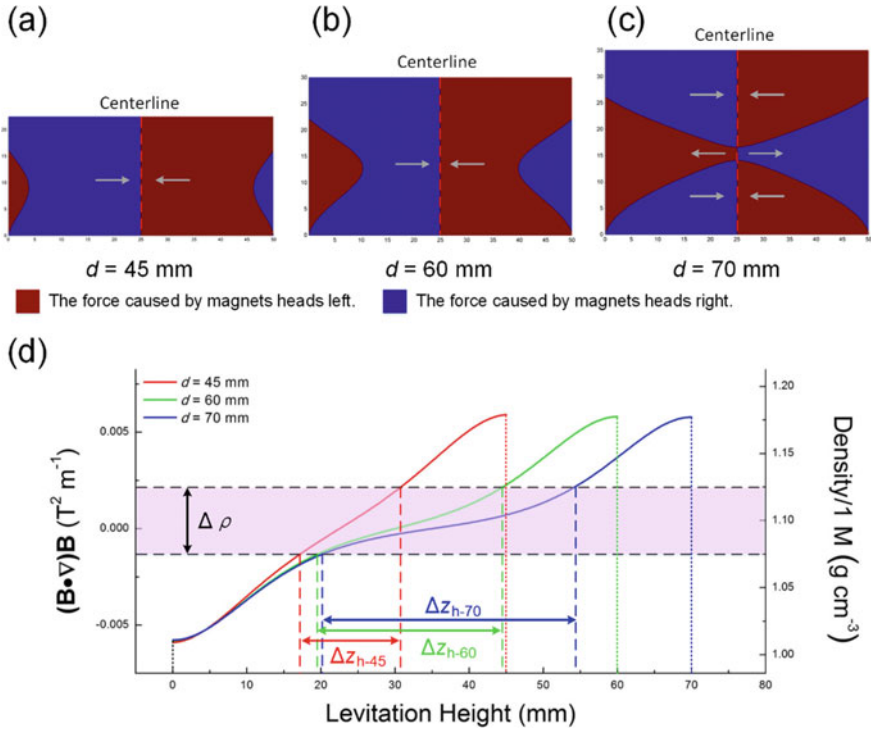


Fig. 6.7 a–c Calculation results of device with $d = 45$ mm, $d = 60$ mm, and $d = 70$ mm, respectively. The magnets are set as the same in these calculations. The magnets are N45 of $50 \text{ mm} \times 50 \text{ mm} \times 25 \text{ mm}$. For the symmetry of the device, each figure only shows bottom half of the calculation in the space between two magnets. **d** Calculation results of $(\vec{B} \cdot \vec{\nabla})\vec{B}$ along the centreline under different d . Reproduced with permission from Ref. [3]. Copyright 2021 Elsevier

According to the aforementioned density measurement calculation, the expression for the standard MagLev device is a first-order expression. Therefore, for a given paramagnetic medium, $S(z_h)$ of the standard MagLev device is a constant value. On the other hand, $S(z_h)$ of the device with $d = 60$ mm can be obtained as a second-order expression (Eq. 6.8) [4]. For the same paramagnetic medium (2.0 M MnCl_2 aqueous solution, for example), $S(z_h)_{60}$ (from $z_h = 12.71$ to 47.29 mm) is larger than $S(z_h)_{45}$ in most areas. It can be easily observed in Fig. 6.7, for the slope of the expression of the device with $d = 60$ mm is obviously smaller than that of the device with $d = 45$ mm.

$$\Delta \rho_s = (-50.055 + 2.748x - 4.602 \times 10^{-2}x^2)\chi_m \cdot \Delta z_h = \frac{1}{S(z_h)_{60}} \Delta z_h \quad (6.8)$$

A series of experiments on standard density beads can reveal the effect of high sensitivity. The five beads with densities of 1.1000, 1.1500, 1.2000, 1.2500 g cm^{-3} ,

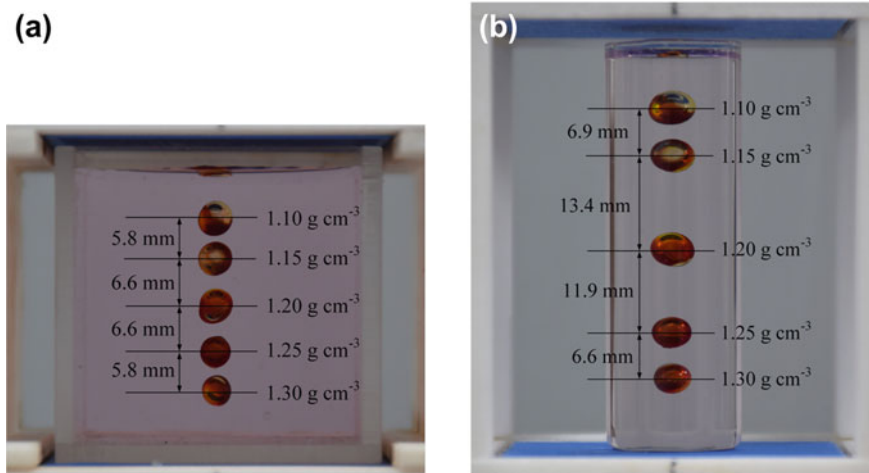


Fig. 6.8 Levitation of standard density beads in **a** standard MagLev device, and **b** high-sensitivity MagLev device device. Reproduced with permission from Ref. [4]. Copyright 2018 Elsevier

and 1.3000 g cm^{-3} were levitated simultaneously, as shown in Fig. 6.8. The gap of z_h between the adjacent beads in the device with $d = 60 \text{ mm}$ was larger than in the standard MagLev Device. Moreover, in the device with $d = 60 \text{ mm}$, the levitations near the middle plate between the magnets have larger gap than in other areas. This area (Fig. 6.8b, z_h from 20 to 40 mm) is called a high sensitivity area. The $S(z_h)_{60}$ in this area reached 204 and $305 \text{ mm cm}^3 \text{ g}^{-1}$, which is 1.67–2.50 times larger than that of the standard MagLev device.

High sensitivity enabled the devices to tolerate larger disturbances in z_h caused by environmental or other random factors. Small differences in z_h did not cause distinct deviation in measuring ρ_s . The devices were also better at measuring samples whose force centres were difficult to determine. Thus, enhancing sensitivity provided higher accuracy. Moreover, devices with higher sensitivity can distinguish miniscule differences in densities. Thus, such devices can be used to separate objects with similar densities.

For example, thermoplastic urethane (TPU, BASF 1190A) and polylactic acid (PLA, NatureWorks 3001D) have very similar densities (1.112 g cm^{-3} vs. 1.242 g cm^{-3}). Although single particles can be distinguished by the standard MagLev device (by a 7.54 mm interval between their levitation heights), the device is insufficient to separate multiple particles, as shown in Fig. 6.9a, b. It can be observed that the clusters of two materials had an obvious interference (red circle in Fig. 6.9b) that the two materials were not completely separated. Changing the device of high sensitivity, the mixed particles were separated again in the same medium (Fig. 6.9c). As predicted above, the interval between their respective levitation heights increased 70% (12.09 mm). $S(z_h)_{60}$ in this interval ranged from 293 to $304 \text{ mm cm}^3 \text{ g}^{-1}$, which

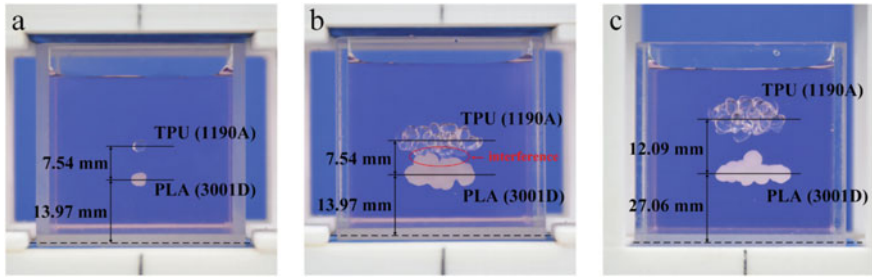


Fig. 6.9 Separating experiments involving TPU (1190A) and PLA (3001D). **a** Separation of two single particles. **b** Separation of two masses of samples in the device with $d = 45$ mm. **c** Separation of two masses of samples in the device with $d = 60$ mm. Reproduced with permission from Ref. [4]. Copyright 2021 Elsevier

is much larger than $S(z_h)_{45}$ ($122 \text{ mm cm}^3 \text{ g}^{-1}$). The two materials become no longer adhere to each other. Hence, the two materials were completely separated.

In addition, high sensitivity not only means the MagLev device can distinguish minute differences among varying samples, but also suggests it is sensitive to defective parts. The defect interior a part will cause the misalignment of the centre of mass and the geometric centroid. When the difference between the moments caused by the magnetic force and the gravity balances each other, the sample reaches its equilibrium position. Higher sensitivity means the magnetic force changes more slowly in the vertical direction. Thus, the sample's equilibrium position deflects a larger angle from the horizontal position. The effect of high sensitivity can be revealed in the test of polycarbonate (PC) washers as shown in Fig. 6.10. For the washers have the symmetrical structure, the levitation position of the homogeneous washer should be horizontal (Fig. 6.10d, g). On the contrary, the defective washers would deflect from the horizontal position. Results in standard MagLev device verified the prediction, as shown in Fig. 6.10d–f: The heterogeneous washer was levitated horizontally. The angle of the washer with small interior bubbles was 6.9° . The washer with larger interior bubbles deflected a larger angle of 27.1° .

Remain the experimental condition unchanged, the washers were levitated in high sensitivity device. Coincidentally, the levitation heights of the washers were in the range of the high sensitivity area (from 32.29 to 32.60 mm). $S(z_h)_{60}$ at this height was 2.4 times greater than $S(z_h)_{45}$. Due to the substantial increase in $S(z_h)$, the defective washers all deflected larger angles (15.0° vs. 6.9° and 27.1° vs. 64.8° , see Fig. 6.10h, i). The results indicate that: (i) the levitation position of defective samples deflected from that of the homogeneous sample and (ii) enhancing the device's sensitivity increases the deflect angle of the defective sample. Therefore, the device with higher sensitivity is more appropriate for samples with minute defects.

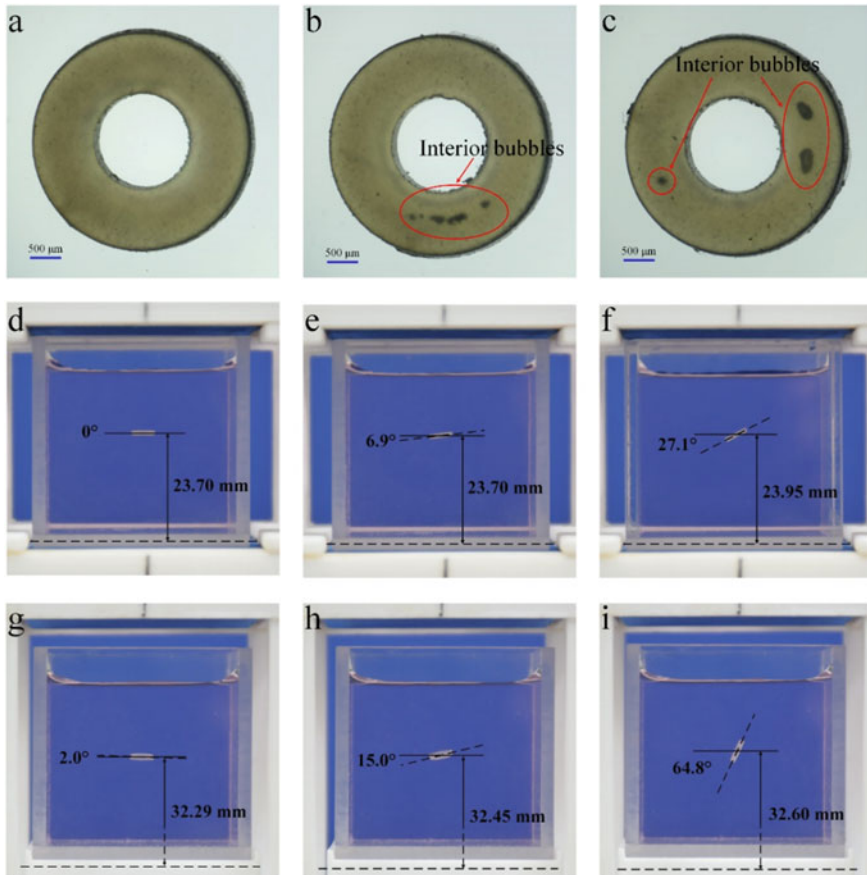


Fig. 6.10 **a** Micrographs of the homogeneous washer. **b** Micrographs of the washer with small interior bubbles. **c** Micrographs of the washer with large interior bubbles. **d–f** Levitation positions of the washers in the device with $d = 45$ mm. **g–i** Levitation positions of the washers in the device with $d = 60$ mm. Reproduced with permission from Ref. [4]. Copyright 2021 Elsevier

6.3.2 Enhancing Sensitivity by Introducing Additional Centrifugal

In standard MagLev device, the objects are levitated along the centerline, which is vertical to the ground. Some researchers conceived a rotating method, which can levitate objects along an oblique line without tilting the device [5]. The testing platform is designed as Fig. 6.11a. Two additional magnets were added to the MagLev device for balancing the centrifugal force. Each pair of magnets were arranged with like poles facing each other. Objects with close densities may cluster in the levitation for the lack of sensitivity, as shown in Fig. 6.11b. The rotation of the platform gives the sample an additional centrifugal force, which pushes the sample away from the

centerline of the MagLev device. The magnetic force generated by the horizontal pair of magnets will prevent the sample from leaving the centerline. When the two forces on horizontal direction meet the balance, the sample reaches to a new equilibrium position. For the centrifugal force can be expressed as Eq. 6.9, the equilibrium conditions of the sample can be updated as Eqs. 6.10 and 6.11.

$$F_c = m_s \omega^2 (d_e - x) = \rho_s V \omega^2 (d_e - x) \tag{6.9}$$

$$F_x = \frac{\Delta\chi}{\mu_0} \left| \left(\vec{B} \cdot \vec{\nabla} \right) \vec{B} \right|_x V - (\rho_s - \rho_m) \omega^2 (d_e - x) V = 0 \tag{6.10}$$

$$F_z = \frac{\Delta\chi}{\mu_0} \left| \left(\vec{B} \cdot \vec{\nabla} \right) \vec{B} \right|_z V - (\rho_s - \rho_m) g V = 0 \tag{6.11}$$

where, ω is the rotating speed of the plate and d_e is the eccentric distance (as shown in Fig. 6.11a).

As can be easily noticed, the density of the object can not only be calculated by its levitation height, but also can be a function of d_x :

$$\rho_s = \frac{\Delta\chi}{\mu_0 \omega^2 (d_e - x)} \left(\vec{B} \cdot \vec{\nabla} \right) B_x + \rho_m \tag{6.12}$$

The slice of the distribution of magnetic field in the x - z plane on the centerline is shown in Fig. 6.12. The changes of B_x and $\left(\vec{B} \cdot \vec{\nabla} \right) B_x$ for varying x and z are shown in Fig. 6.12b, c. It can be observed that in certain areas ($x \in [-10.0 \text{ mm}, 10.0 \text{ mm}]$ and $z \in [-10.0 \text{ mm}, 10.0 \text{ mm}]$), these two values vary linearly with x , which means

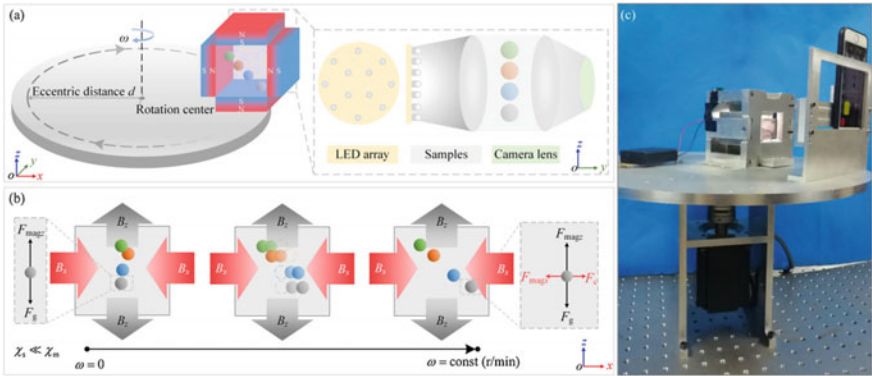


Fig. 6.11 The centrifugal magnetic levitation approach for density measurement. **a** Schematic of the measurement system. **b** Illustration of the dynamic migration process of the levitation positions under the combined effect of magnetic forces, gravity and centrifugal force. **c** Prototype platform for the density measurement using the centrifugal magnetic levitation approach. Reproduced with permission from Ref. [5]. Copyright 2021 Elsevier

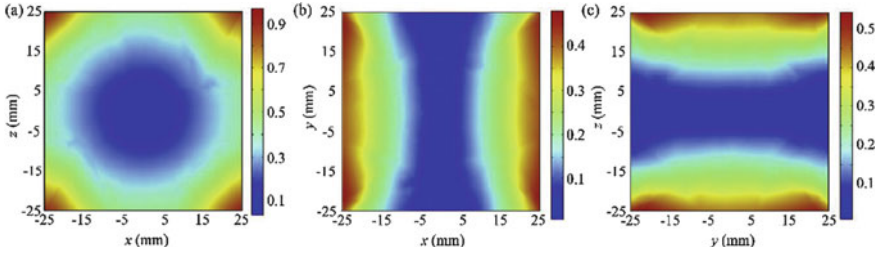


Fig. 6.12 3D simulation model of the magnetic field distribution. **a** The x - z section at $y = 0$. **b** The x - y section at $z = 0$. **c** The y - z section at $x = 0$. The magnetic field is symmetric with the center at the plane of x - z , x - y and y - z . Reproduced with permission from Ref. [5]. Copyright 2021 Elsevier

the relationship between ρ_s and x can also be approximately expressed as a linear function:

$$\rho_s = \frac{\Delta\chi}{\mu_0\omega^2} \frac{x}{(d_e - x)} B_x^2 + \rho_m \quad (6.13)$$

According to the function, a larger eccentric distance d_e and a higher rotation rate ω will provide larger centrifugal force. This can result in a larger deviation of an object from centerline of the device. Under this condition, objects with similar densities will have larger intervals between each other. In other words, the measurement has a larger sensitivity.

The series of experiments on standard density beads validates the conclusion, as shown in Fig. 6.13. In the figure, the grey curves in Fig. 6.13 are positions of each constant ρ_s vary with the change of ω , while the blue curves represent levitation position as a function of density ρ_s under constant rotation speed. The beads with the density of 1.06, 1.09, and 1.11 g/cm^3 were levitated in the 0.8 M MnCl_2 aqueous solution. The device was driven to rotate at the d_e of 30 mm and 60 mm. The rotation speeds are ranging from 50 to 160 r/min with the interval of 5 r/min. The points of the results well landed on their theoretical curves. As the result, the beads spread apart more obviously with larger eccentric distance and higher rotation speed. The highest resolution of minute differences in density was calculated to be 0.003 g/cm^3 in these results. In fact, continue to increase the eccentric distance and rotation speed within a reasonable can further increase the sensitivity during measurement.

As discussed above, the most direct effect of high sensitivity is that the device can separate objects with similar densities more obviously. The example given in the research of the rotating device fully demonstrated this effect. The experiment is a levitation of PMMA particles with different interior bubbles. These interior bubbles cause the differences of densities among the particles (Fig. 6.14a). For the lack of sensitivity, the little differences can not lead to the total separation of each particle in static device (Fig. 6.14b). When rotating the device at a speed of 140 r/min, the particles arranged on a sloping curve, as shown in Fig. 6.14c. Therefore, the particles got obviously separated. It is also worth noting that, the sensitivity of the rotating

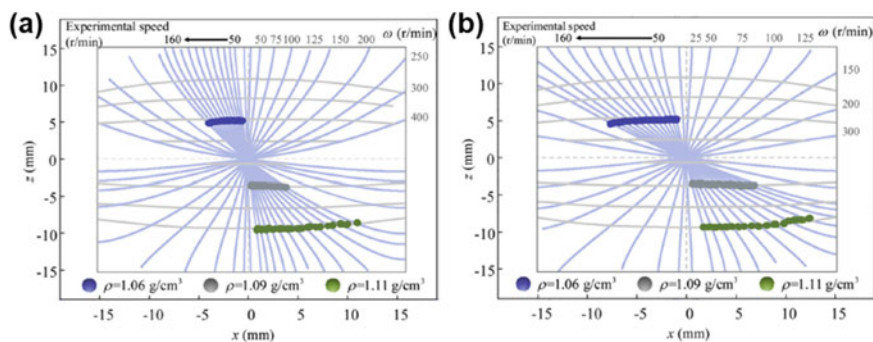


Fig. 6.13 Effect of the eccentric distance on the spatial levitation positions as a function of rotating speeds. Three standardized beads with densities of 1.06 g/cm^3 (blue), 1.09 g/cm^3 (grey) and 1.11 g/cm^3 (green) were levitated in a 0.8 M MnCl_2 aqueous solution with different eccentric distances: **a** $d = 30 \text{ mm}$. **b** $d = 60 \text{ mm}$. Reproduced with permission from Ref. [5]. Copyright 2021 Elsevier

device does not remain a constant value. It reaches approximate two times larger than that of the static device when levitating denser objects.

In general, the MagLev device has a potential structure that simple improvement can improve its sensitivity without sacrificing the measuring range. The improvement of sensitivity is a promising method for distinguishing and separating similar densities.

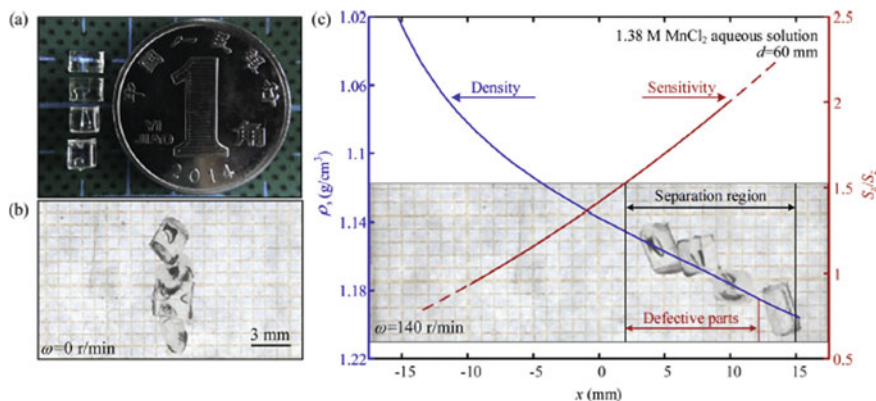


Fig. 6.14 Separation of PMMA particles with internal defects. **a** Image of four small transparent PMMA particles (millimeter-sized) and one coin with a diameter of 19 mm . **b** Image of the clustered particles along the centerline of the device in an aqueous solution of 1.38 M MnCl_2 when the MagLev device was static. The scale bar is 3 mm . **c** Separation of particles in the same batch when the rotating speed was 140 r/min with the eccentric distance of 60 mm . Reproduced with permission from Ref. [5]. Copyright 2021 Elsevier

6.4 Changing the Magnets

Changing magnets is a way that researchers tried to meet the requirements of different fields. The research have proved that except for the squared magnets, magnets with other shapes can also achieve stable levitation of object, as long as the magnets have same poles facing each other. The following parts will introduce the achievements on MagLev device using magnets with different shapes in specific application scenarios.

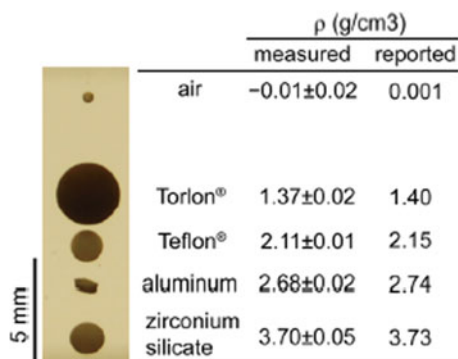
6.4.1 Using Ring Magnets

As we can find in common markets, round magnets are good substitutes for the square magnets. In fact, using round magnets is similar as using square magnets. Therefore, almost no research focused on these devices. However, using ring magnets brought many interesting characters into the MagLev Device.

The improvement began with the direct change of the square magnets, which is given a name of “axial MagLev device” [6]. All the characteristics that standard MagLev device has can be observed in the axial MagLev device: (i) the diamagnetic object can be stably levitated on the centerline; (ii) the distribution of magnetic field is approximately linear along the centerline. Of course, these characteristics also require the certain distance between the magnets. For instance, the inner diameter (r)/outer diameter (R)/height (h)/distance between magnets (d) = 1:3:1:0.6 can fully satisfies the condition. Equations 5.8–5.11 can be copied for the axial MagLev device. Clearly, the hole of the ring magnet has significant effect on the distribution of the magnetic field, as well as the B_0 . Hence, to maintain the linear distribution of magnetic field, the distance between the magnets is much smaller than that of the comparable standard MagLev device (16 mm vs. 45 mm). Instead, the narrow space between magnets multiplies the gradient of the magnetic field (see Eqs. 5.10 and 5.11). Consequently, the measuring range gets enlarged that it can measure lighter/denser materials. As shown in Fig. 6.15, air bubble (0.001 g/cm^3) and zirconium silicate (3.73 g/cm^3) can be levitated and measured, which is impossible for standard MagLev device (measuring range from 0.8 to 3.0 g/cm^3).

Accordingly, enlarging the distance between the magnets makes the distribution of magnetic field along the centerline no longer linear. The phenomenon is also related to the shape of the ring magnets (e.g. inner diameter/outer diameter and the height of the magnet). This change can be modeled by the theoretical analysis. According to the model, the density measurement can be achieved by the device using any kind of ring magnets. Two pairs of magnets (H20 magnets: $r \times R \times h = 20 \times 30 \times 20 \text{ mm}$, $B_0 = 1.23 \text{ T}$; H10 magnets: $r \times R \times h = 12.5 \times 25 \times 10 \text{ mm}$, $B_0 = 0.88 \text{ T}$) are calculated as examples as shown in Fig. 6.16. When the distance between the magnets remains 20 mm, the two pairs of magnets can both stably levitate the objects. The relationships between the density and levitation height are monotonical, although the relationship for H20 magnets is much more linear. This means the density can

Fig. 6.15 Levitation and density measurement of objects using axial MagLev device. Reproduced with permission from Ref. [6]. Copyright 2021 American Chemical Society



be obtained directly by knowing the levitation height of an object. With the increase of the distance between the H2O magnets, the linearity between the density and the levitation height no longer exists. Similar to the enhancement of the sensitivity of standard MagLev device, the curvature of the relationship curve becomes larger, which brings higher sensitivity and an area of ultra-high sensitivity.

An interesting phenomenon occurs along with the continuous increase of the distance between the magnets. As mentioned in previous sections, the MagLev device using square magnets cannot levitate objects stably with a large distance between the magnets. Enlarging the distance between the magnets in Axial MagLev device leads to a total different result [7]. Yet the equilibrium position for a levitated object is no longer along the centerline, a bell-shaped area for stable levitation is generated, as shown in Fig. 6.17. The three dimensional levitation is also an approach to obtain higher sensitivity. Particularly, the bell-shaped area allows the objects have choice for different equilibrium positions. Hence, the hamper from each other can be drastically reduced, which is an advantage in measuring multiple samples. In fact, the increase of the sensitivity is not the most valuable contribution of bell-shaped area. Reasonable

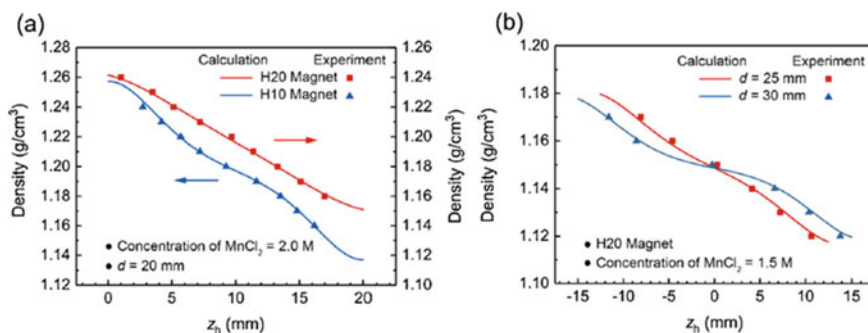


Fig. 6.16 Relationship between density and levitation height using different pair of magnets. Reproduced with permission from Ref. [8]. Copyright 2021 Elsevier

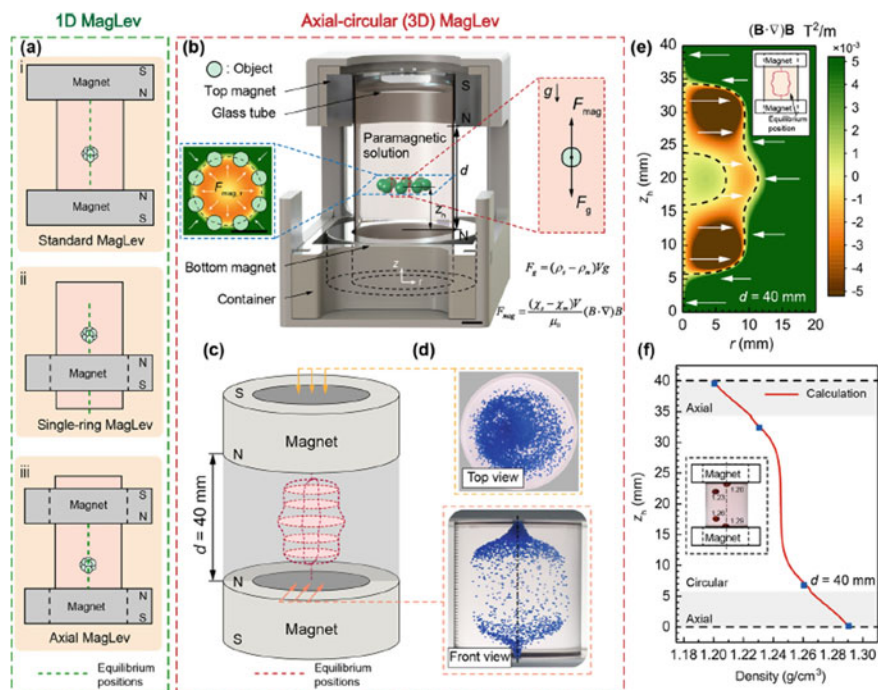


Fig. 6.17 Three dimensional (3D) levitation using ring magnets. **a** Schematic of 1D MagLev. **b** Schematic of 3D MagLev. **c** Bell shape area for stable levitation. **d** The levitation of particles spread over the bell shape area. **e** Theoretical calculation of magnetic force near the bell shape area. **f** Relationship between levitation height and density. Reproduced with permission from Ref. [7]. Copyright 2021 American Chemical Society

use of this area can further realize the manipulation of particles. This approach will be introduced in the following parts.

Beyond common prediction, further increase the distance between the ring magnets is still meaningful. The equilibrium positions of the objects come back to the centerline when the d reaches to 105 mm. Under this condition, the sensitivity of the device reach to a very high level (140 times larger). It is not a good choice to use the device to measure density of a sample, for the preparation of the medium should be more precise. The parameters, such as density and magnetic susceptibility, are required to be obtained accurately. This will make the MagLev lose its advantage of convenience. However, the high sensitivity is very useful for separation of sample with very similar densities, or the distinguish of unknown substances.

The device also has advantages over standard MagLev device of the ability to manipulate and observe the sample from top side [8]. A schematic of the combination of MagLev and ultrasonic is shown in Fig. 6.18. The levitation of object not only can measure the density and evaluate the quality of the sample, but also acts as a fixture. Therefore, the sample can be further detected by the ultrasonic with a certain

posture. For example, the levitation postures of the plates shown in Fig. 6.18b can be easily predicted as horizontal. Therefore, it is easy for ultrasonic to measure the height of the plates. In fact, the MagLev is a kind of non-contact levitation. Thus, it can prevent some disturbance from fixture, which makes the additional testing techniques test samples with complex structures. However, the levitation posture for a certain sample is determined. The sample may also rotate during the levitation. These may affect the testing results.

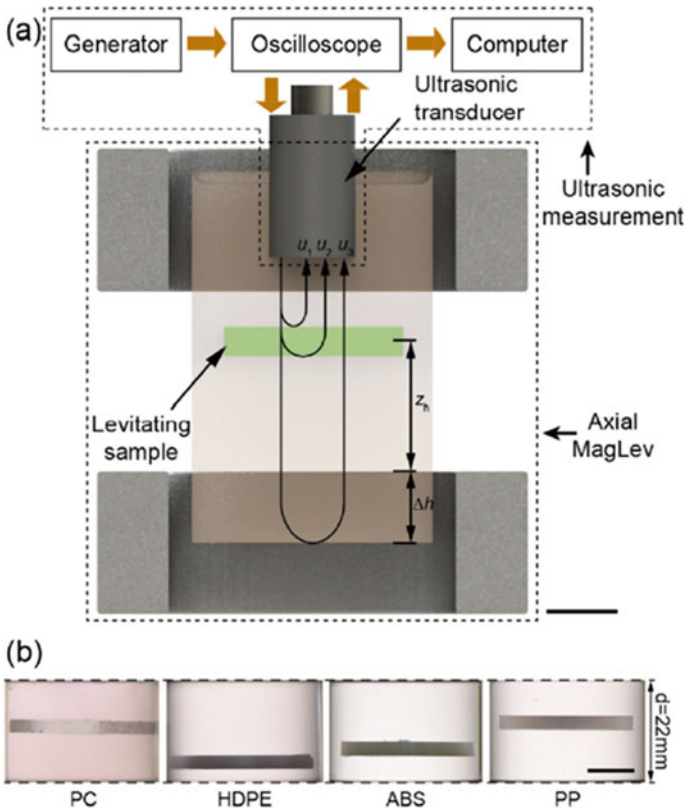


Fig. 6.18 The scheme of method combining the axial MagLev and the ultrasonic measurement. **a** A schematic representation of the measurement device. The ultrasonic transducer is fixed coaxially with the ring magnets. **b** Experimental photographs for various materials using device with $d = 22$ mm. The scale bars are 10 mm in length. Reproduced with permission from Ref. [8]. Copyright 2021 Elsevier

6.4.2 Using Magnet Arrays

One of the most prominent advantages of MagLev device is its portability. It is benefited from the market-available permanent magnets. In addition, the price of the magnets is relatively cheaper. Usually, the magnets used in standard MagLev device have the size of $2'' \times 2'' \times 1''$, which cost approximately \$15 per piece. This kind of NdFeB magnets can generate a magnetic field has the maximum $B_0 = 0.475\text{T}$, which can afford the levitation of common materials, as introduced in previous sections. However, it disadvantage is also obvious that the size of magnet limits the maximum size of the sample: the standard MagLev can levitate sample with the diameter of 10 mm, while can only measure sample with maximum thickness of only 3–4 mm. Although using large magnets is a possible way, it lack the feasibility for the following two reasons. (i) The cost of the mold for manufacturing larges size magnets is too large. Meanwhile, the market of the large magnets cannot make manufacturers profitable. Thus, the manufacturer tend not to provide the large magnets. (ii) The magnetization direction cannot be ensured when magnetizing large magnets. This will cause the magnetic field of MagLev device is different from the prediction and then affect the levitation.

Therefore, special arrangements of a group of magnets is a possible way to solve the problem. Halbach Array is a near-ideal structure that can generate the strongest magnetic field with the least amount of magnets. It is conceived by Klaus Halbach in 1979, when he was experimenting with electron acceleration. However, the distribution of Halbach array is a bit more complex. Although it can generate a large magnetic field with a large gradient, it requires in depth analysis to figure out a proper structure for stable magnetic levitation.

In fact, that if we arrange magnets close together with the same direction of the poles, the magnet array can be assumed as a whole magnet. According to the Ampere molecular circulation hypothesis, the surface equivalent current of each magnet can be counteracted by their near neighbor magnets. Hence, the equivalent current of outermost surface of the magnet arrays is connected in series, which is the same as a whole magnet. Predictably, this arrangement of the magnets definitely causes large repulsive force from adjacent magnets. This requires additional structure to constrain the magnets. For small magnets, an iron plate with special fixtures can achieve the purpose. When facing the large magnets, the fix with bolts is highly required.

It has been proved that using magnet arrays to construct MagLev devices is feasible [9]. Eight identical N35 magnets with the size of $20 * 20 * 10$ mm are used to replace the integrated N35 magnets with the size of $40 * 40 * 20$ mm. The simulations of the magnetic fields are shown in Fig. 6.19. Obviously, the results are almost the same. This directly results in the similarity of MagLev devices using magnet arrays and integrated magnets. In Fig. 6.19c, d, the simulation of $(\vec{B} \cdot \vec{\nabla})\vec{B}$ on horizontal direction indicates the device can afford the stable levitation along the centerline (similar results were discussed in Chap. 5. Thus, the basic function, density measurement, can be realized.

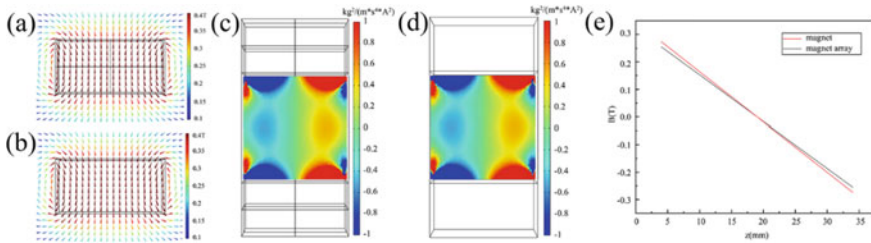


Fig. 6.19 Schematic diagram of the equivalent currents of the magnets. **a** The distribution of magnetic flux intensity of magnet array. **b** The distribution of magnetic flux intensity of single square magnet. **c** The distribution of the gradient magnetic flux intensity of standard MagLev device using magnet array. **d** The distribution of the gradient magnetic flux intensity of standard MagLev device using single square magnets. **e** Correction of magnetic field of magnet array. Reproduced with permission from Ref. [9]. Copyright 2021 Elsevier

In this series of analysis, the design of the device ensures the linear relationship between the levitation height and the density. The device uses magnet arrays should be the same as the device constructed with integrated magnets. However, there is a minute difference of $B_z \frac{\partial B_z}{\partial z}$ between the two devices. The chamfers on each small magnet may be the cause of the result. These structures lead to the uneven upper surface of the array, which surely affect the distribution of the magnetic field. Figure 6.19e exhibits the calculation of the magnetic flux intensity along the centerline, by which the minute difference can be revealed. The experiments on standard density glass beads verify the accuracy of the device, as shown in Fig. 6.20.

As expected, the levitation heights were proportional to the density of the beads. The levitation results shows good agreement with the simulation results. For comparison, same experiments were carried out in device using the integrated magnets. The slight difference mentioned above can be observed in these experiments: the levitation of the same bead has a little difference between the two devices. Furthermore, the levitations using different media suggests similar results that the levitation height linearly relates to the density. Concluded from the experiments, the following points can be drawn: (i) the two devices have similar levitation abilities, which indicates the device using magnet arrays can afford the density measurement as well as the device using square magnets; (ii) the simulation can well reveal the $B_z \frac{\partial B_z}{\partial z}$ along the centerline, which could provide an accurate calculation method for density measurement with devices using different magnet arrays.

Take steps along the idea, a magnified MagLev device is constructed. The magnet array consists of 9 identical magnets with the arrangement of $3 * 3 * 1$. The size of the magnet is $50 * 50 * 50$ mm. To adjust the different occasions, the distance between the magnet arrays can be changed by a ball screw. As predicted, the repulsive force causes difficulties in arranging the magnet. Therefore, bolts are used to fix the magnets on the iron base board. But this brings another problem that the through-hole may greatly changes the magnetic field of the magnet. Fortunately, this structure of the magnet only has obvious effect near its surface, but will not significantly affect the higher area. In addition, magnify the device will also result in a reduction of

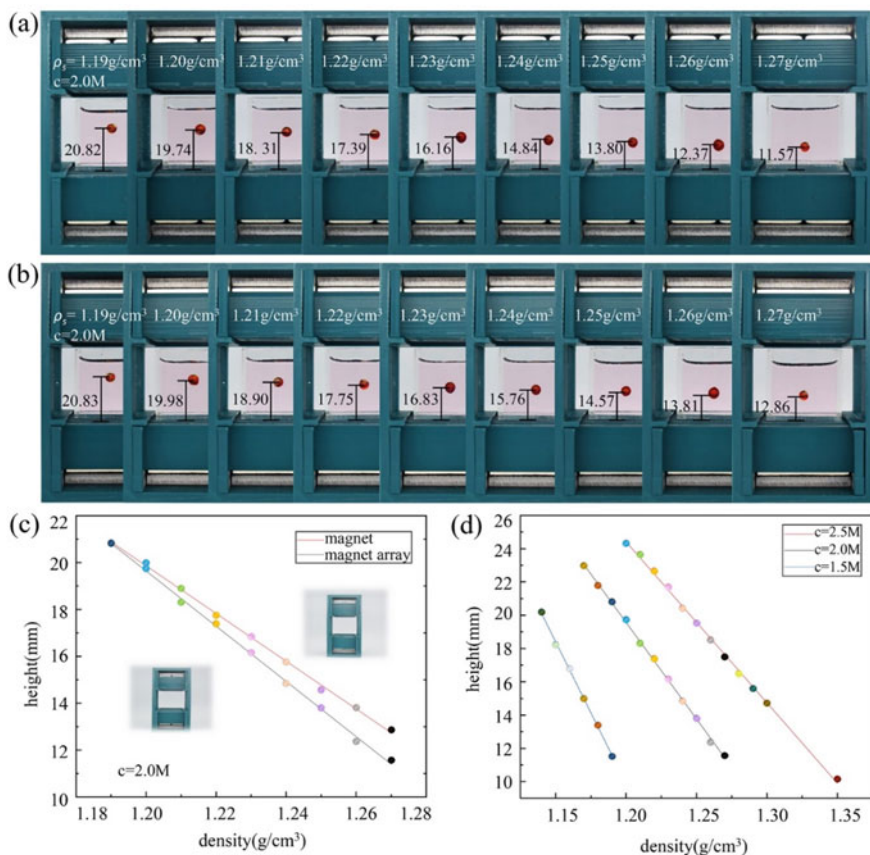


Fig. 6.20 Feasibility verification experiments using standard density beads. **a** Results obtained with the magnet array. **b** Results obtained with the square magnets. **c** Comparison of the results obtained from different devices. **d** Measurement results using media with different concentrations. Reproduced with permission from Ref. [9]. Copyright 2021 Elsevier

measurement range and enhance the sensitivity of the device. This is because the magnify of the magnet ensures the same surface magnetic flux intensity. However, the magnify of the device makes the distance of the magnets times larger than the standard MagLev device. While the larger distance causes less gradient of magnetic field. Finally, according to Eq. 5.7, the device cannot levitate denser materials as the standard MagLev device can, but will be sensitive to the minute density differences.

The above discussion can all be revealed in the experiments on standard density beads. As shown in Fig. 6.21, the measurement range is obviously smaller than the standard MagLev device. The difference of 0.01 g/cm^3 leads to a much larger difference in levitation height using the same medium. For instance, the levitation height intercept between 1.26 and 1.25 g/cm^3 in 2.5 M MnCl_2 aqueous solution is

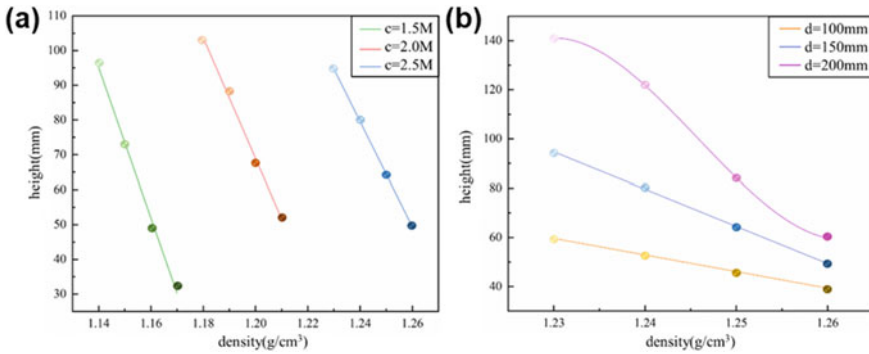


Fig. 6.21 Density measurement results using magnified MagLev device. **a** Measurement results using media with different concentrations. **b** Measurement results under different distance between the magnet arrays

2.6 mm using standard MagLev device. It comes to 24.42 mm when using magnet array device.

The high sensitivity and large operation area guarantee the detection of large objects. For instance, a trial on measuring carbon fiber reinforced polymer tensile bar is shown in Fig. 6.22. The bar has the width of 76 mm, which is definitely impossible for standard MagLev device to test. The density of the bar is measured as 1.502 g/cm³. Compared with the results from common method (nominal density of 1.501 g/cm³), the result has a high accuracy.

The most advantageous character of the device is the ability to test large polymer parts. For standard MagLev device, the maximum diameter of the part is restricted to 30 mm, not to mention the thickness should be much smaller (several millimeters). Moreover, the less sensitivity of the standard MagLev device cannot measure the density of thick parts precisely. This is also a disturbance in testing tiny defects of the part. While, these problems are all fixed in MagLev device with magnet array. A typical sample is the detection of the polyetherimide (PEI) base of aerospace craft

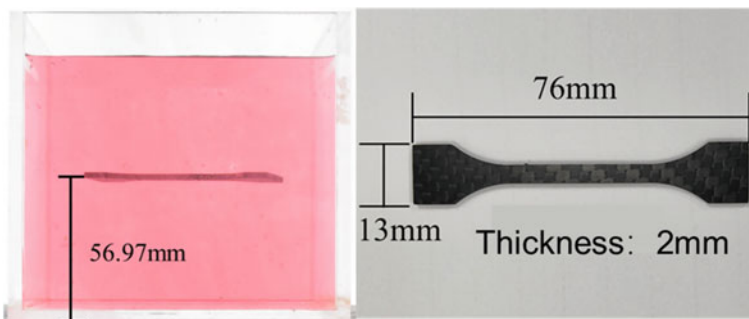


Fig. 6.22 Levitation of carbon fiber reinforced polymer tensile bar

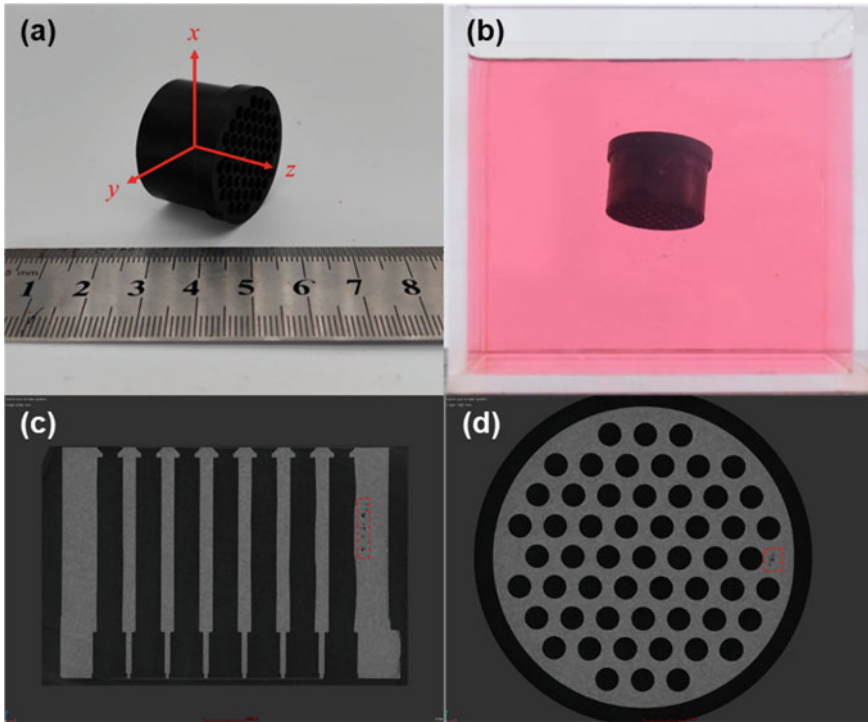


Fig. 6.23 Defect detection of PEI base of aerospace craft electric coupler. **a** Scale of the coupler. **b** Levitation result. **c, d** SEM test of the coupler

electric coupler, as shown in Fig. 6.23. The tilted levitation posture indicates the part has interior voids on upper direction. The SEM test verifies the MagLev testing result (Fig. 6.23c, d). Slight voids locates at the relatively thicker structure of the part, which cause an obvious incline of the part during levitation.

In general, although difficulties and disadvantages still occur along with predominant advantages of large operation area, higher sensitivity, and high accuracy, the magnify of the MagLev device by using magnet array is a promising for MagLev testing method to deal with large and complex parts with the mean density in the range from 0.8 to 2.0 g/cm³.

6.4.3 Using Bar Magnets

The magnetic levitation can also be achieved by the bar magnets. A high throughput configuration was carried out by utilizing a re-engineered device based on bar magnets (Fig. 6.24a). The long levitation area is divided into several wells to separately handle very small amount of target materials in each wells. In practice, the

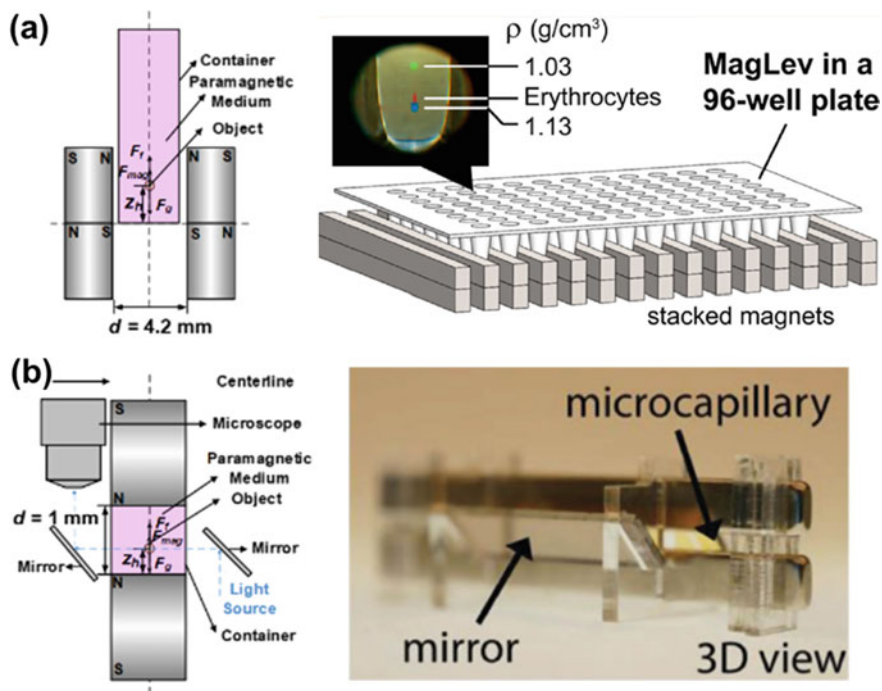


Fig. 6.24 MagLev using bar magnets. **a** High throughput configuration. **b** Configuration combines magnetic focusing and fluorescence microscopy. Reproduced with permission from the article “Current state of magnetic levitation and its applications in polymers: A review.” Copyright 2021 Elsevier

device could measure 96 wells at the same time and still have potential to handle more wells. This configuration has promising applications in the field of materials chemistry, forensic evidence and analytical science.

Different from the levitation by square magnets, the MagLev device with bar magnets can also generate a long area between the magnets, which can concentrate small particles on a line. Combined with microfluidics, it opens up a novel direction in the application of MagLev in biology and medicine. This configuration combines magnetic focusing and fluorescence microscopy (Fig. 6.24b). The magnetic field would drive the particles to a line where the forces acting on the particle reaches a balance when they are passing through the channel between the two magnets in paramagnetic medium. For instance, polymeric microspheres (5–10 μm) could be concentrated and measured via the improved MagLev device within 120 s [10]. Considering the detectable size of the particle, it is especially suitable for focusing and detecting micro scale particles, such as polymer microspheres and cells [11–13]. Benefit from the stable levitation and concentration of cells inside the device, the self assembled 3D cell cultures [14] and weightlessness culture of mesenchymal stem cells [15] can be easily achieved. Noticing the device occupies much less space

than standard MagLev device and the operation space is relatively narrow, the smart phone can be employed to enhanced its ability of real-time monitoring, sorting and digital quantification of particles [10, 16–18].

Among the applications using this configuration, the detection of sickle cell is a typical case of successful application of the device. It indicates that the configuration could become a useful point of care diagnosis tool. Followed by the change of ion permeability, the shape of red blood cell become a sickle. The average density of red blood cells also increased with these changes. Finally, the red blood cells lose their function and finally result in the sickle cell disease (Fig. 6.25a). Cells through the tube between the two bar magnets could be focused and separated. The density differences between normal and sickle red blood cells could cause the deviation between their levitation heights (Fig. 6.25a). Additionally, it also can be noticed that the density distribution of normal red blood cells is uniform, while sickle red blood cells have a wide density distribution. These phenomena can be used to the rapid screening diagnosis of sickle cell disease. Benefit from the portability of MagLev device, handheld magnetic platform was developed for convenient and low cost self-testing [18–21].

This improved MagLev device was also successfully applied in the detection of cell membrane-bound and antigen–antibody bindings [22]. Ligand-coated microbeads can capture soluble antigens or bind to the antigens on the surface of the cell. The bindings would result in a density change on the beads and cause a physical aggregation of two types of particles, (Fig. 6.25b) which enables the detection of the bindings and enumeration for quantification. Another work proposed a magnetic susceptibility-based method to detect protein [23]. The target protein could be captured by a polymer microsphere. Another magnetic nanoparticle was then attached onto the captured protein. Thus, the polymer microspheres attached

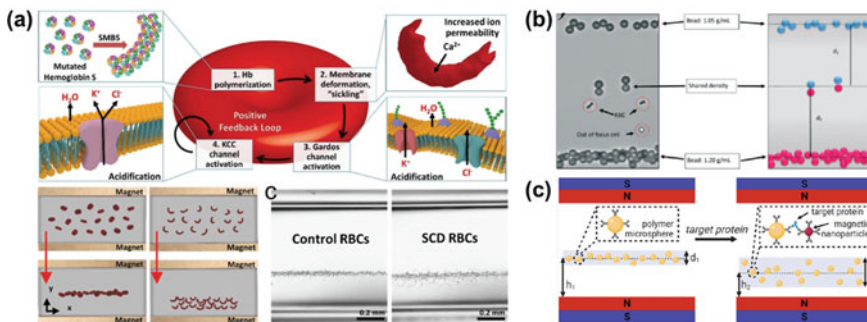


Fig. 6.25 Bio-applications of MagLev using bar magnets. **a** Diagnosis of sickle cell disease. **b** Detection of ligand-coated microbeads capture or bind to the antigens. **c** Detection of polymer microspheres attached with target protein and magnetic nanoparticles. Reproduced with permission from the article “Current state of magnetic levitation and its applications in polymers: A review.” Copyright 2021 Elsevier

with target protein and magnetic nanoparticles would have different magnetic susceptibilities compared with those without protein, which finally reflects in the different levitation heights of the microspheres (Fig. 6.25c).

References

1. Nemiroski A, Soh S, Kwok SW, et al. Tilted magnetic levitation enables measurement of the complete range of densities of materials with low magnetic permeability. *J Am Chem Soc.* 2016;138(4):1252–7.
2. Xie J, Zhao P, Zhang C, et al. A feasible, portable and convenient density measurement method for minerals via magnetic levitation. *Measurement.* 2019;136:564–72.
3. Xie J, Zhang C, Gu F, et al. An accurate and versatile density measurement device: magnetic levitation. *Sens Actuators B Chem.* 2019;295:204–14.
4. Xie J, Zhao P, Jing Z, et al. Research on the sensitivity of magnetic levitation (MagLev) devices. *J Magn Magn Mater.* 2018;468:100–4.
5. Gao QH, Li WB, Zou HX, et al. A centrifugal magnetic levitation approach for high-reliability density measurement. *Sens Actuators B Chem.* 2019;287:64–70.
6. Ge S, Whitesides GM. “Axial” magnetic levitation using ring magnets enables simple density-based analysis, separation, and manipulation. *Anal Chem.* 2018;90(20):12239–45.
7. Zhang C, Zhao P, Gu F, et al. Axial-circular magnetic levitation: a three-dimensional density measurement and manipulation approach. *Anal Chem.* 2020;92(10):6925–31.
8. Zhang C, Zhao P, Tang D, et al. Axial magnetic levitation: a high-sensitive and maneuverable density-based analysis device. *Sens Actuators B Chem.* 2020;304: 127362.
9. Zhao P, Jia Y, Xie J, et al. Magnetic levitation for polymer testing using magnet array. *Polym Testing.* 2021;103: 107361.
10. Knowlton S, Yu CH, Jain N, et al. Smart-phone based magnetic levitation for measuring densities. *PLoS ONE.* 2015;10(8): e0134400.
11. Ge S, Wang Y, Deshler NJ, et al. High-throughput density measurement using magnetic levitation. *J Am Chem Soc.* 2018;140(24):7510–8.
12. Durmus NG, Tekin HC, Guven S, et al. Magnetic levitation of single cells. *Proc Natl Acad Sci.* 2015;112(28):3661–8.
13. Tasoglu S, Khoory JA, Tekin HC, et al. Levitational image cytometry with temporal resolution. *Adv Mater.* 2015;27(26):3901–8.
14. Anil-Inevi M, Yaman S, Yildiz AA, et al. Biofabrication of in situ self assembled 3D cell cultures in a weightlessness environment generated using magnetic levitation. *Sci Rep.* 2018;8(1):7239.
15. Anil-Inevi M, Yilmaz E, Sarigil O, et al. Single cell densitometry and weightlessness culture of mesenchymal stem cells using magnetic levitation. *Stem Cell Nanotechnol Methods Protocols.* 2020:15–25.
16. Amin R, Knowlton S, Yenilmez B, et al. Smart-phone attachable, flow-assisted magnetic focusing device. *RSC Adv.* 2016;6(96):93922–31.
17. Knowlton SM, Sencan I, Aytar Y, et al. Sick cell detection using a smartphone. *Sci Rep.* 2015;5(1):15022.
18. Knowlton S, Joshi A, Syrrist P, et al. 3D-printed smartphone-based point of care tool for fluorescence-and magnetophoresis-based cytometry. *Lab Chip.* 2017;17(16):2839–51.
19. Yenilmez B, Knowlton S, Tasoglu S. Self-contained handheld magnetic platform for point of care cytometry in biological samples. *Adv Mater Technol.* 2016;1(9):1600144.
20. Yenilmez B, Knowlton S, Yu CH, et al. Label-free sickle cell disease diagnosis using a low-cost, handheld platform. *Adv Mater Technol.* 2016;1(5):1600100.
21. Subramaniam AB, Gonidec M, Shapiro ND, et al. Metal-amplified density assays (MADAs), including a density-linked immunosorbent assay (DeLISA). *Lab Chip.* 2015;15(4):1009–22.

22. Andersen MS, Howard E, Lu S, et al. Detection of membrane-bound and soluble antigens by magnetic levitation. *Lab Chip*. 2017;17(20):3462–73.
23. Yaman S, Tekin HC. Magnetic susceptibility-based protein detection using magnetic levitation. *Anal Chem*. 2020;92(18):12556–63.

Chapter 7

Magnetic Levitation in Mechanical Engineering



Jun Xie, Ruoxiang Gao, Daofan Tang, and Peng Zhao

7.1 Introduction

Novel testing method is an important research direction in the field of mechanical engineering. Magnetic levitation testing method has proved its advantages of high accuracy and sensitivity in density-based analysis. Therefore, trials in testing materials and products for materials processing using magnetic levitation have achieved series of progress.

7.1.1 Testing for Materials

The consistency is a very important character of materials, which significantly affects the quality of the products in manufacturing. The problem of how to determine the ideal material is particularly acute in polymer processing, for the polymers consist large collections of different materials for different applications. For instance, the grades of thermoplastic polyurethane (TPU), related to their different mechanical properties, are determined by their different components. The glass fiber reinforced polymers exhibit different mechanical and forming properties according to their adding percentages [1]. The unique properties of the materials are utilized to produce parts for different occasions. The misuse of the materials would result in unqualified products or even accidents. Thus, the importance of distinguishing the ideal material for manufacturing from a larger group of confusable materials is self-evident.

J. Xie (✉)

College of Mechanical Engineering, Zhejiang University of Technology, Hangzhou, China

e-mail: jxie93@zjut.edu.cn

R. Gao · D. Tang · P. Zhao

The State Key Laboratory of Fluid Power and Mechatronic Systems, College of Mechanical Engineering, Zhejiang University, Hangzhou, China

There are a number of testing methods to test the properties of polymer materials. X-ray diffraction (XRD) and nuclear magnetic resonance spectroscopy (NMR) can detect the microstructure of a polymer [2]. Differential scanning calorimetry (DSC) and thermo gravimetric analysis (TGA) are widely used in characterizing thermal characteristics of polymers [3]. Rheological property of a melt polymer can be measured by the capillary rheometry [4]. However, it is worth noticing that some characters of the material are not highly required in manufacturing. On the contrary, the engineers prefer to judge the consistency of the feedstock materials with a simple method. Knowing the exact property of the material becomes relatively insignificant. However, some disadvantages, such as time-consuming, high cost, and difficult to use, hinder the widespread applications of these common methods in practical manufacturing. Thus, a convenient, cost effective, and reliable method for characterizing polymer materials is highly required.

7.1.2 Testing for Products

Injection molding, which is arguably the primary approach for producing polymer products, contributes approximately 80% of polymer merchandises in modern society. However, the existence of unexpected defects is one of the main factors that affect the passing rate of polymer products [5]. The defects usually occur with improper settings or the fluctuation of molding parameters. For example, improper packing and cooling is one of the main causes of interior voids in the parts [6]. Low packing pressure will lead to short shot of the products [7]. An improper design of the cavity would result in weld lines in pipe fittings and couplings [8], which would weaken the mechanical property of the polymer parts [9].

There are techniques for evaluating the quality of polymer parts. Microscopy is the most commonly used in factories [10]. However, this method is not capable for internal defects of non-transparent parts. It has been proved that industrial computed tomography (ICT) can afford the non-destructive testing (NDT) of injection molded products with high accuracy and efficiency [11]. However, this method cannot test large amounts of samples for its considerably expensive device, time-consuming process, and harmfulness to humans. In addition, ultrasonic is another possible method for testing polymer injection molded parts [12]. However, ultrasonic lacks the accuracy in testing defects. Its procedure is also relatively complex for the large amounts of samples. Thus, it remains beneficial to further develop a quality control method that is convenient and low-cost for testing polymer products.

Density is an important index of polymer feedstocks and products. Commonly, the density distribution of a qualified polymer product should be uniform. Evidently, defects, such as voids, weld lines, and impurities would have different densities from those of other areas. Therefore, the density distribution of defective parts would not be uniform. It can be inferred from this conclusion that the density-based testing methods have potential in evaluating the quality of injection molded polymer parts.

In the following several sections, the applications of MagLev to NDT of polymer parts are introduced.

7.2 Testing of Consistency for Raw Materials

7.2.1 Method

According to the theoretical analysis in *Section III*, the MagLev testing method could afford accurate density measurement of diamagnetic samples. Noticing that most polymers are diamagnetic, it is possible to identify materials through MagLev. In practice, two approaches for characterizing materials using the MagLev testing method are applied.

The first approach is measuring the exact density of the material. Benefiting from its high accuracy and sensitivity, the density of a polymer material can be easily obtained through the measurement of few pellets using MagLev testing method. By comparing the obtained density with the standard density, whether the material is qualified could be determined. In addition, another advantage of this approach is that it can also calculate the characteristics directly from the density.

The other approach is comparing the levitation height of the material with the standard height. Generally, this standard height could be selected from an ideal process. The difference between the levitation height of the material and the standard height can be directly observed. In practical production, this approach has the outstanding advantages of convenience and directness.

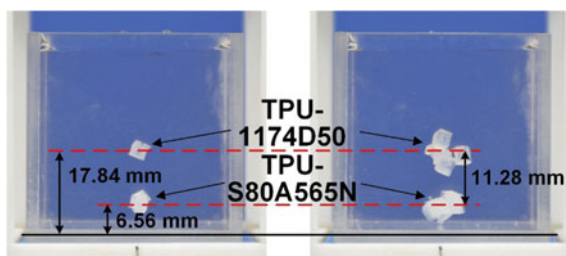
7.2.2 Characterization of Polymers

7.2.2.1 Different Grades of TPU

TPU is a large collection of rubbers that contains different grades with different characteristics. Some of them have a very similar appearance that would cause misuse. For instance, the two grades, 1174D50 and S80A565N, having the confusable appearances of being semi-transparent with little bubble inside, are applicable for totally different occasions due to different characteristics. 1174D50 has a shore hardness of 73D and is usually used in producing electric wire. Meanwhile, the shore hardness of S80A565N is 85A. This grade of TPU also has advantages of high mechanical performance, high wearing resistance, and high oil resistance. Hence, to distinguish different grades of polymers before processing, a fast and convenient testing method is needed.

The MagLev testing method is a potential method that meets this requirement, and was employed to distinguish the different grades of TPU [13]. The paramagnetic

Fig. 7.1 The levitation results of different grades of TPU. Reproduced with permission from Ref. [13]. Copyright 2020 Springer Nature

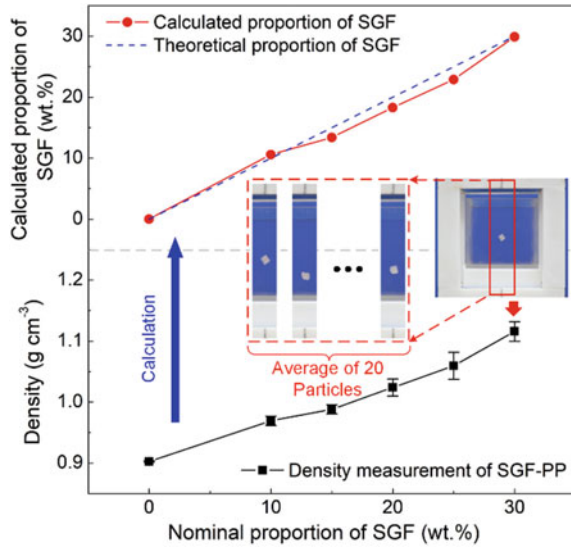


medium is a 0.5 M MnCl_2 aqueous solution with an additive of 1.4 M CaCl_2 . The solution has a $\rho_m = 1.1609 \text{ g/cm}^3$ and $\chi_m = 8.4 \times 10^{-5}$ (unitless). Levitation results are shown in Fig. 7.1. Apparently, the two materials are levitated in different heights. The gap between the two materials is 11.28 mm, which means the density of the materials have a difference of 0.0226 g cm^{-3} . In addition, it is also worth noticing that the calculated densities of the two materials are highly consistent with their nominal parameter. Each test would consume no more than 20 s. Hence, the grade of the material can be determined by comparing the density obtained from MagLev testing with the nominal parameter. More conveniently, two or more materials can be distinguished by directly comparing their levitation heights using MagLev testing. Along with its advantages, the MagLev method is a promising method to avoid the misuse of inappropriate materials with confusable appearances.

7.2.2.2 Different Proportions of SGF-PP

By adding reinforcement components, such as glass fiber and carbon fiber, polymers can obtain superior mechanical properties. For polymers with different adding proportions, MagLev testing method can easily distinguish them with a series of simple experiments. In this case, the short glass fiber reinforced polypropylene (SGF-PP) with different adding percentages were tested. The nominal adding percentages of the SGF-PPs were 10, 15, 20, 25, and 30 wt%. The test of pure PP was also carried out for comparison. In the experiments, same kind of SGF-PP pellets showed large differences in the levitation. This is because the uniformity of the pellets cannot be ensured during the mixing process. Hence, the characterization for each material was carried out by testing 20 random pellets, as shown in Fig. 7.2. It is found that the differences in density of different SGF-PPs are relatively large, which means one paramagnetic medium alone cannot test all these SGF-PPs. Therefore, four kinds of MnCl_2 solutions were employed in the tests. The four solutions, all containing 1.0 M MnCl_2 , had the same magnetic susceptibilities of 1.77×10^{-4} (unitless). The solvents were the mixture of pure water and ethanol. The volume percentages of pure water were 100%, 70 vol.%, 30 vol.%, and 0%, respectively, which resulted in the densities of the solutions being 1.0985, 1.0472, 0.9825, and 0.9230 g/cm^3 . The average densities of the materials are shown as the black line in Fig. 7.2. As

Fig. 7.2 Experimental results of SGF-PPs. The figures are typical results for SGF-PP particles with an added percentage of 30 wt% glass fibers. Each density result was obtained by averaging the results of 20 individual pellets. The calculated percentage of SGF was calculated by the density results. Reproduced with permission from Ref. [13]. Copyright 2020 Springer Nature



predicted, the densities of SGF-PPs increased with the rise of the adding proportions of short glass fibers.

Furthermore, the adding proportion of short glass fibers could be calculated according to the density of the sample. Assuming that the volumes of the components in SGF-PP are linearly superimposed, the added proportion p thereby can be calculated through Eq. 7.1.

$$p = \frac{\rho_{SGF}(\rho_{PP} - \rho)}{\rho(\rho_{PP} - \rho_{SGF})} \tag{7.1}$$

The calculated results of p are also shown in Fig. 7.2 as the red line. The results are highly consistent with the values provided by the vendor. The little differences between the results and the nominal values may be caused by: (i) the adding proportions of the pellets were not uniform; (ii) tiny cracks/bubbles that may exist between the SGF and PP. The results illustrate that the MagLev testing method could distinguish different fiber reinforced polymers precisely through accurate density measurement. The densities obtained by MagLev can also afford the further determination of the adding proportions of short glass fibers.

7.2.2.3 True and Substandard PC

The use of substandard materials will almost certainly lead to the unqualified products. This is mainly because the performance of the substandard feedstock cannot meet the requirements. Usually, substandard materials have similar appearances as true materials, which may confuse the manufacturer. For instance, Fig. 7.3b shows

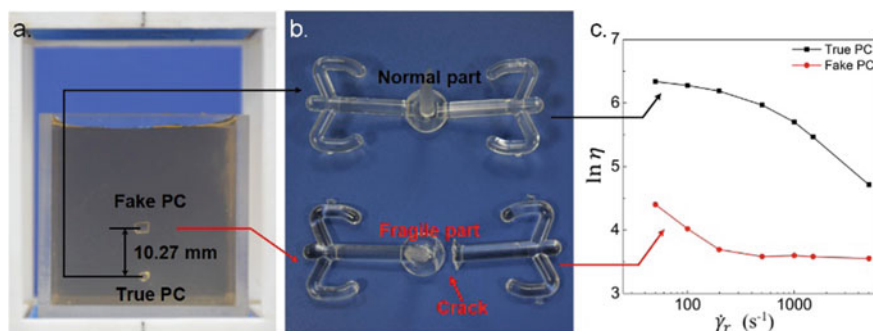


Fig. 7.3 Parts and experimental results of different batches of PC. **a** Levitation results of true and substandard PC. **b** Injection molded parts of true and substandard PC. **c** The rheological test results of the different PC materials. Reproduced with permission from Ref. [13]. Copyright 2020 Springer Nature

the injection-molded parts produced by true and substandard polycarbonate (PC) under the same process parameters. The upper part in Fig. 7.3b was the product of true PC, while the other one was produced by the substandard material. It was found the product produced by the substandard PC was more fragile than that of true PC. As the processing conditions were the same, it can be speculated that differences in the performance of the final parts was caused by the different materials. In order to acquire high sensitivity, the medium with $\chi_m = 1.89 \times 10^{-5}$ (unitless) and $\rho_m = 1.1852 \text{ g/cm}^3$ was prepared. The medium contained 0.15 M MnCl_2 to obtain low magnetic susceptibility, and 2.1 M CaCl_2 to adjust the density. Random pellets were chosen as the samples in the experiment. Their levitation result is shown in Fig. 7.3a. Apparently, the two samples were levitated at different heights. Further analysis determined that the materials differ from each other by a minute difference in density of 0.0045 g/cm^3 . The levitation results amply proved that MagLev testing method is capable for distinguishing the true and substandard materials through density-based analysis.

Furthermore, a capillary rheometer (R10, Malvern, Britain) was employed to figure out the reason why substandard PC caused the product to become brittle. The results are recorded in Fig. 7.3c. The experiment on substandard PC showed an abnormal curve on the natural log of viscosity versus shearing rate. The curve is also significantly lower than that of the true PC. The lower viscosity means the material has a shorter chain length, which finally results in the fragility of the product. The difference in the viscosity was reflected in the tiny density changes of the materials, which can be directly observed in the levitation.

In practice, the levitation height of a known true material could be recorded as the standard. Larger difference in levitation height means higher possibility that the sample is a kind of substandard material. Comparing with the common methods mentioned in the introduction of this section, the MagLev testing method has the superior advantages of high efficiency, convenience, and low cost. And the MagLev

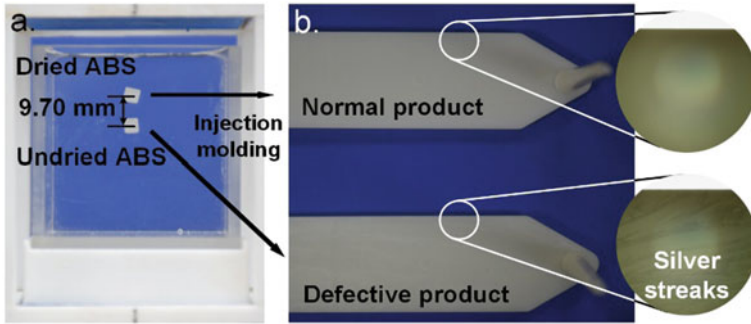


Fig. 7.4 The performances of ABS with and without adequate drying (dried ABS and undried ABS for short) in polymer processing using MagLev testing. **a** Levitation results of dried and undried ABS. **b** Injection molded parts produced by the ABS. The inadequate drying of ABS caused silver streaks. Reproduced with permission from Ref. [13]. Copyright 2020 Springer Nature

testing method has great potential in distinguishing true and substandard materials in polymer processing.

7.2.2.4 ABS with and Without Adequate Drying

Adequate drying before injection molding is a significant process for qualified products. Materials with inadequate dried is one of the main causes of interior voids or silver streaks. Acrylonitrile butadiene styrene (ABS) is a typical material that may cause silver streaks if the material is not adequately dried (Fig. 7.4b). ABS has a high hydroscopicity of 0.8%, for its polypropylene nitrile can absorb water. The swelling of the undried ABS is too small to cause apparent change on volume of the material. Thus, the density of ABS without adequate drying should be larger than that of the dried ABS. However, this difference is so small that it generally gets ignored.

Benefitting from the high sensitivity, minute differences in densities can be detected by MagLev testing method. The paramagnetic medium is chosen as an aqueous solution with 0.2 M MnCl_2 and 0.35 M CaCl_2 . The magnetic susceptibility and density of this solution were 2.82×10^{-5} (unitless) and 1.0471 g/cm^3 . Results in Fig. 7.4a are the ABS pellets with and without adequate drying in the same MagLev process. Obviously, undried sample is levitated at a lower position due to its higher density. Further calculation showed that the difference in density is 0.0041 g/cm^3 , which reflect a gap of 9.70 mm between the two pellets. Consequently, the dried and undried ABS can be easily distinguished.

7.3 Non-destructive Testing of Polymer Parts

7.3.1 Levitation Posture of Defective Samples in MagLev

For density measurement, theoretical analysis in previous chapters indicates that $(\vec{B} \cdot \vec{\nabla})\vec{B}$ becomes linear under a proper distance between two magnets. Therefore, F_{mag} can be rewritten as Eq. 7.2:

$$F_{mag} = \frac{\Delta\chi}{\mu_0} V \left(\frac{4B_0^2}{d^2} \cdot z_h - \frac{2B_0^2}{d} \right) \quad (7.2)$$

where B_0 is the value of the magnetic flux intensity at the center on the magnet surface, d is the distance between the two magnets (typically 45 mm for standard MagLev device), and z_h is the levitation height of the sample [14].

As mentioned in previous chapters, the density of a sample levitated in MagLev device can be calculated by Eq. 7.3:

$$\rho_s = \frac{\Delta\chi}{\mu_0 g} \left(\frac{4B_0^2}{d^2} \cdot z_h - \frac{2B_0^2}{d} \right) + \rho_m \quad (7.3)$$

The equilibrium process of the levitation of a sample follows the principle of minimum potential energy. Take the center on the top surface of the bottom magnet as the origin, the coordinate system is shown as Fig. 7.5. The total potential energy U consists of two parts, U_{mag} and U_{grav} , which respectively denote potential energies of the magnetic field and the gravity, as expressed in Eq. 7.4:

$$U = U_{mag} + U_{grav} = - \int_V \frac{\Delta\chi}{2\mu_0} \mathbf{B} \cdot \mathbf{B} dV - \int_V \Delta\rho \mathbf{g} \cdot \vec{z}_h dV \quad (7.4)$$

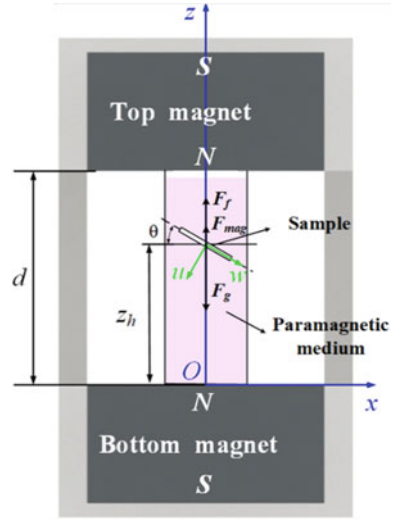
where $\Delta\rho = \rho_s - \rho_m$ is the difference of the densities between the polymer and the paramagnetic medium; parameter \vec{z}_h is vector of the levitation position of the sample.

The levitating process of a sample can be regarded as a combination of rotation and translation, which can be expressed as Eqs. 7.5 and 7.6:

$$z = \vec{r}^{\rightarrow} \cdot \mathbf{R} \cdot \mathbf{k} + z_h \quad (7.5)$$

$$\mathbf{R} = \begin{bmatrix} \cos(\vec{x}, \vec{u}) & \cos(\vec{y}, \vec{u}) & \cos(\vec{z}, \vec{u}) \\ \cos(\vec{x}, \vec{v}) & \cos(\vec{y}, \vec{v}) & \cos(\vec{z}, \vec{v}) \\ \cos(\vec{x}, \vec{w}) & \cos(\vec{y}, \vec{w}) & \cos(\vec{z}, \vec{w}) \end{bmatrix} \quad (7.6)$$

Fig. 7.5 Schematic of sample levitated in MagLev device. Reproduced with permission from Ref. [14]. Copyright 2019 Wiley



where $\mathbf{k} = (0, 0, 1)^T$, and $\vec{\mathbf{r}}' = (u, v, w)$ defines reference frame that moves along with the sample. The origin of the reference frame is set at the centroid of the sample. $\mathbf{X} = (\cos(\vec{z}, \vec{u}), \cos(\vec{z}, \vec{v}), \cos(\vec{z}, \vec{w}))$ is used to describe the levitation posture of the sample. Noticing that \mathbf{X} is a unit vector, z can thereby be expressed as Eq. 7.7:

$$z = u \cdot \cos(\vec{z}, \vec{u}) + v \cdot \cos(\vec{z}, \vec{v}) + w \cdot \cos(\vec{z}, \vec{w}) + z_h = \vec{\mathbf{r}}' \cdot \mathbf{X}^T + z_h \quad (7.7)$$

Combining Eqs. 7.4 and 7.7, the relationship between U , z_h , and \mathbf{X} of a sample can be expressed asy Eqs. 7.8–7.10:

$$U = -\mathbf{X} \cdot \mathbf{C} \cdot \mathbf{X}^T + \mathbf{X} \cdot \mathbf{b} - \frac{\Delta\chi B_0^2 V}{2\mu_0} \left(1 + \frac{4z_0^2}{d^2} - \frac{4z_0}{d} \right) + \Delta\rho g z_h V \quad (7.8)$$

$$\mathbf{C} = \frac{2\Delta\chi B_0^2 V}{\mu_0 d^2} \begin{bmatrix} \lambda_{uu} & \lambda_{vu} & \lambda_{wu} \\ \lambda_{uv} & \lambda_{vv} & \lambda_{wv} \\ \lambda_{uw} & \lambda_{vw} & \lambda_{ww} \end{bmatrix} = \beta \mathbf{A} \quad (7.9)$$

$$\mathbf{b} = \bar{\rho}_s g V (u_{cm}, v_{cm}, w_{cm})^T \quad (7.10)$$

In these equations, $\lambda_{mn} = \frac{1}{V} \int_V m n dV$, where $m, n \in \{u, v, w\}$, $\beta = \frac{2\Delta\chi B_0^2 V}{\mu_0 d^2}$; The shape and dimensions of the sample can be described by the matrix \mathbf{A} ; $\bar{\rho}_s = \frac{1}{V} \int_V \rho_s dV$ is the average density of the molded part; the coordinates $u_{cm} = \frac{\int_V \rho_s u dV}{\int_V \rho_s dV}$, $v_{cm} = \frac{\int_V \rho_s v dV}{\int_V \rho_s dV}$, and $w_{cm} = \frac{\int_V \rho_s w dV}{\int_V \rho_s dV}$ are used to describe the position of the center of gravity of the sample in the reference frame.

A series of extreme value problems is employed to determine the equilibrium posture of a sample:

$$\min U(X, z_h) \quad (7.11)$$

$$\begin{aligned} \text{s.t. } & X \cdot X \\ & z_h \in [0, d] \end{aligned}$$

In Eq. 7.11, no coupling exists between $X_{equilibrium}$ and z_h . The Lagrange multiplier method is applied to solve the problem:

$$L = U + \xi(X \cdot X^T - 1) \quad (7.12)$$

where ξ is a Lagrange multiplier.

When the sample reaches to equilibrium position, the $\frac{\partial L}{\partial X}$ should be 0. Therefore, the equilibrium posture can be obtained by Eq. 7.13.

$$(\xi E - C) \cdot X^T = \frac{-1}{2} b \quad (7.13)$$

where E is a unit matrix.

For example, the total energy of a cylinder levitated in MagLev differs from its levitation posture [15]. The cylinder with $R < 1$ will have axial direction perpendicular to the horizontal plane when it reaches to the equilibrium posture. While the axial direction is parallel to the horizontal plane for the cylinder with $R > 1$.

In summary, the shape and the density distribution would affect the equilibrium posture of a sample levitated in MagLev. Thus, a defective sample, whose defect would change its density distribution (apparently), would have different equilibrium posture from a qualified sample. The non-destructive testing of defective samples therefore could be realized based on levitation result.

7.3.2 Evaluation of Injection Molded Parts

Whether a sample has defects can be distinguished through its levitation posture. A group of experiments on polycarbonate (PC) washers proved this prediction [16]. PC washers were chosen for the two advantage: (i) PC washers are transparent, which allow direct observation of the defects. (ii) The symmetrical shape of PC washer means the levitation posture of qualified washer is horizontal. On the contrary, the defective washer would deflect from the horizontal position. Washers and their levitations are shown in Fig. 7.6. A qualified washer and two defective washers with different volumes of void were employed in the experiment (Fig. 7.7a–c). The paramagnetic medium was a 1.5 M $MnCl_2$ aqueous solution, whose $\chi_m = 2.70 \times$

10^{-4} (unitless) and $\rho_m = 1.148 \text{ g cm}^{-3}$. Using standard MagLev device (Fig. 7.7d–f), the qualified washer was horizontally levitated at a height of 23.70 mm. The defective washer deflected at an angle of 6.9° and 27.1° from the horizontal. As predicted, the larger voids caused larger deflection angle. Additionally, the voids also caused a change on the average density of the washer, resulting in a minute difference of 0.25 mm between their levitation heights. Sensitivity of the device also affect the levitation results. In the device with $d = 60 \text{ mm}$, defective washers have larger deflection angles (15.0° vs. 6.9° and 27.1° vs. 64.8° , as shown in Fig. 7.7h, i). The sensitivity $S(z_h)$ under this condition reaches to $400 \text{ mm cm}^3 \text{ g}^{-1}$, 2.4 times greater than that of standard MagLev device. In addition, the deflection of the qualified washer indicates that there might be tiny invisible defects that was undetected by the standard MagLev device. Therefore, evaluating polymer samples using MagLev can be realized through the observation of their levitation posture. High sensitivity of MagLev will guarantee the validity of the evaluation.

Applications were carried out on the evaluation of injection molded lenses. Voids and impurities are common defects for polymer parts, which significantly influence the quality of the products. Three types of defective lenses were obtained in injection molding process and tested by MagLev: voids, PP impurities, and brass scraps impurities (see Figs. 7.8a, 7.9a, and 7.10a). The lenses with voids may be produced by the PC without adequate drying. PP impurities are the residuals in the barrel after washing the screw. Brass brushes and blocks for cleaning the mold may leave powders in the environment and may accidentally fall in the cavity of the mold. As predicted, the defective lenses exhibited deflection during MagLev.

The levitation results of the defective lenses are shown as Figs. 7.8b, 7.9b, and 7.10b. For comparison, the levitation for qualified lens was also carried out and is shown in Fig. 7.7. The lenses with different defects all exhibited deflections at different levitation heights.

Among the four lenses, the lens with brass scraps has the highest density and the lowest levitation height of 15.20 mm. This is because brass scraps have a large density (6.9 g cm^{-3}) that affects the average density of the lens significantly. Due to the densities of the PP (0.96 g cm^{-3}) and voids (~ 0) being lower than PC (1.2 g cm^{-3}), the other two defective lenses have densities lower than that of the qualified lens. The levitation heights of these defective lenses are also higher. In particular, the voids affect the average density of the lens more significantly and caused a higher levitation height than that of the lens with the PP impurities (20.37 mm vs. 18.60 mm).

7.3.3 Moment of Volume Evaluation Method for Defects

Distinguishing defective parts can be easily realized through the levitation posture and heights. Trails on the quantitative analysis of the defects were then carried out. Some commonly used polymer parts, such as lenses, washers and gears, have strictly centrosymmetric structures. The levitation postures of their qualified products should

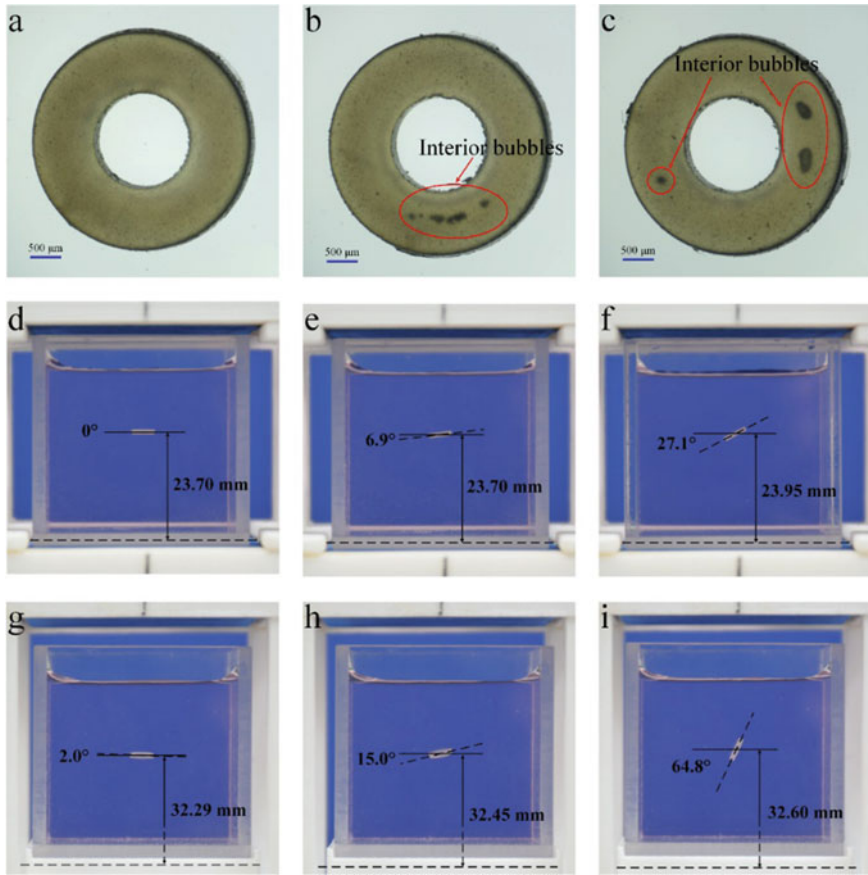


Fig. 7.6 **a** Micrographs of the homogeneous washer. **b** Micrographs of the washer with small interior bubbles. **c** Micrographs of the washer with large interior bubbles. **d–f** Levitation positions of the washers in the device with $d = 45$ mm. **g–i** Levitation positions of the washers in the device with $d = 60$ mm. Reproduced with permission from Ref. [16]. Copyright 2018 Elsevier

Fig. 7.7 MagLev testing results of acceptable lens. **a** Configuration of lens. **b** Levitation posture of lens. Reproduced with permission from Ref. [14]. Copyright 2019 Wiley

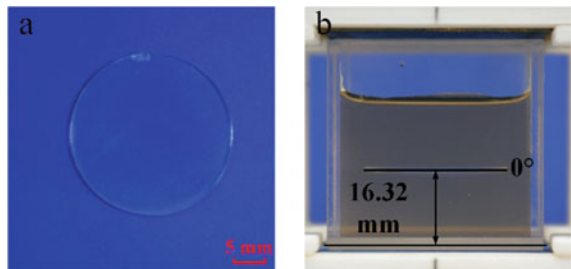


Fig. 7.8 MagLev testing results of lens with void defects. **a** Configuration of lens. **b** Levitation posture of lens. Reproduced with permission from Ref. [14]. Copyright 2019 Wiley

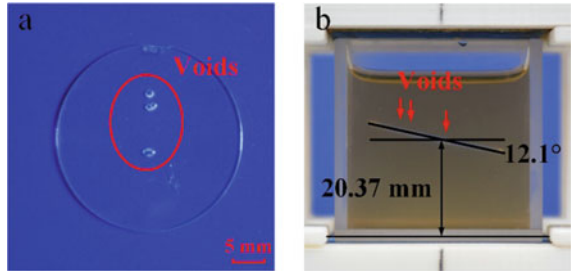


Fig. 7.9 MagLev testing results of lens with PP impurities. **a** Configuration of lens. **b** Levitation posture of lens. Reproduced with permission from Ref. [14]. Copyright 2019 Wiley

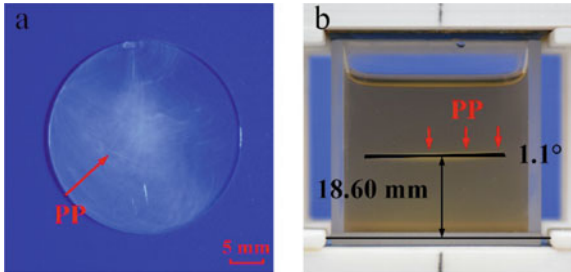
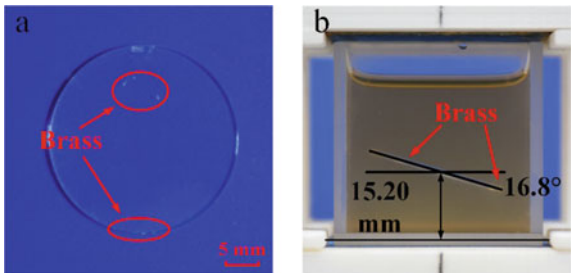


Fig. 7.10 MagLev testing results of lens with brass impurities. **a** Configuration of lens. **b** Levitation posture of lens. Reproduced with permission from Ref. [14]. Copyright 2019 Wiley



be horizontal, which can be easily predicted. According to this premise, a moment of volume evaluation method for the void defects was proposed [17].

According to the principle of minimum potential energy mentioned in previous sections, when a sample reaches to the equilibrium position, its total potential energy should be minimized. Considering the deflect angle of the sample, Eq. 7.4 can be rewritten as Eq. 7.14.

$$U(\theta) = -\frac{2B_0^2 \Delta \chi V}{\mu_0 d^2} (\lambda_{ii} - \lambda_{kk}) \cos^2 \theta - \rho_s V g i_{cm} \cos \theta \quad (7.14)$$

where θ is the deflect angle of the sample. The lengths of principal axes λ affect the final posture of the sample in the magnetic field. For centrosymmetric parts, the

principal axes can be easily determined, because the center of gravity r_{cm} is always located on the i -axis as $(i_{cm}, 0, 0)$.

Noticing that the voids are randomly distributed inside a part, it is impossible to determine the position and the volume of each void. To better evaluate the distribution of the voids, a new variable termed the moment of volume M_v is defined. It could be easily speculated that the deflect angle of the sample is affected by the volumes of the voids and the distances of voids from the centroid of the sample. The relationship between the θ and M_v of the polymer parts can be established by Eq. 7.15.

$$M_v = V_{total} L_i = -\frac{4B_0^2 \Delta\chi V (\lambda_{ii} - \lambda_{kk})}{\mu_0 g d^2 (\rho_v - \rho_r)} \sin \theta \quad (7.15)$$

where V_{total} is the total volume of voids, and L_i is the distance from the centroid of all voids to the centroid of the sample. For a more convenient calculation, L_i is located along the i -axis of the body-fixed frame. ρ_v and ρ_r are the density of the voids and the density of the solid part of the sample, respectively. Using Eq. 7.15, the distribution of the voids can be quantified. A series of experiments on plastic gears were carried out to verify the theoretical analysis, as shown in Fig. 7.11. Noticing different gears performed quite different levitation postures, it can be easily concluded that the posture is related to the distributions of internal voids. The perspective of the internal structures was established through CT scanning of the gears to help understanding the variation of the levitating postures.

The comparison between the MagLev and the CT results showed that the gear with voids uniformly distributed around the centroid deflected a smaller angle. On the contrary, the sample with concentrated voids deflected a larger angle. For example, the gear in Fig. 7.11a had an extremely uneven distribution of voids, with a total volume of the voids of 0.94%. Consequently, this gear deflected the angles of 28.1° in the 3.5 M MnCl₂ aqueous solution and 39.3° in the 2.5 M MnCl₂ + 1.5 M CaCl₂ aqueous solution, as shown in Fig. 7.11b, c. When the sample reaches to the equilibrium position, the region contains more voids would be at a higher position in the deflected sample. In contrast, the CT scanning images showed that the other two samples had the voids with relatively small average sizes (Fig. 7.11d, g). Moreover, the distribution of the voids is almost uniformly aggregated around the centroid. Therefore, the deflect angles of these two gears are much smaller in the same experimental condition.

To further verify the relationship between the deflect angle and the distribution of internal voids, the M_v was calculated through Eq. 7.15 and showed in Fig. 7.12a. The volumes and positions of the voids can be determined precisely by CT scanning. Therefore, the centroid of each sample was further calculated. The results of the centroid of the samples are shown in in Fig. 7.12b. The correlation coefficient between experimental results and the theoretical analysis reached 99.8%. Affected by the internal voids, the gear's center of gravity no longer overlaps with the its centroid. The larger the distance between the centroids of the gear and the voids, the larger deflect angle will the gear maintain. Therefore, utilizing moment of volume evaluation method, the distribution of internal voids can be evaluated through the analysis of the equilibrium levitation posture of centrosymmetric parts.

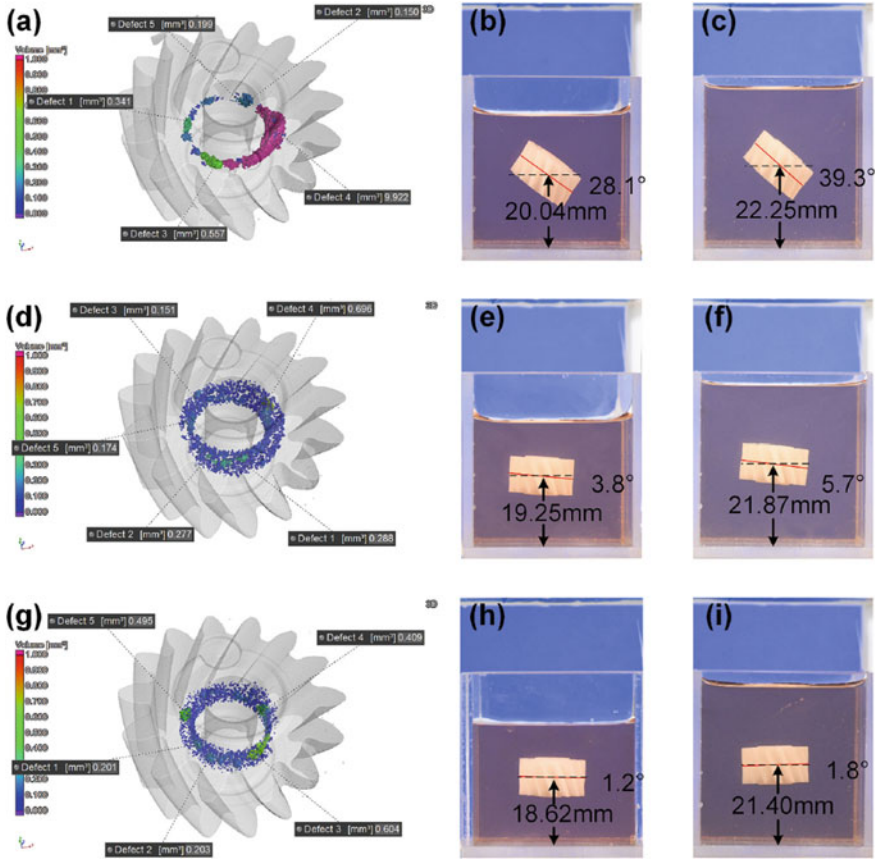


Fig. 7.11 Comparison between different samples in different solutions. **a** CT scanning image of the first sample. **b, c** Experimental results of the first sample in 3.5 M MnCl₂ and 2.5 M MnCl₂ + 1.5 M CaCl₂. **d** CT scanning image of the second sample. **e, f** Experimental results of the second sample in 3.5 M MnCl₂ and 2.5 M MnCl₂ + 1.5 M CaCl₂. **g** CT scanning image of the third sample. **h, i** Experimental results of the third sample in 3.5 M MnCl₂ and 2.5 M MnCl₂ + 1.5 M CaCl₂. Reproduced with permission from Ref. [17]. Copyright 2020 Elsevier

7.3.4 Location of Interior Defects

The levitation height and posture of the sample in different paramagnetic media can locate the defects of the sample [18]. It is assumed that there are small inclusions ρ_i and volume V_0 in the sample. Since the volume of internal defects affects the average density of defective samples, it can be calculated by the ratio of the average density of qualified samples to defective samples, as shown in Eq. 7.16:

$$V_0 = \frac{\bar{\rho}_s - \bar{\rho}_q}{\rho_i - \bar{\rho}_q} \frac{\partial L}{\partial \Theta} = 2(\eta E - C) \cdot \Theta^T + b = 0 \quad (7.16)$$

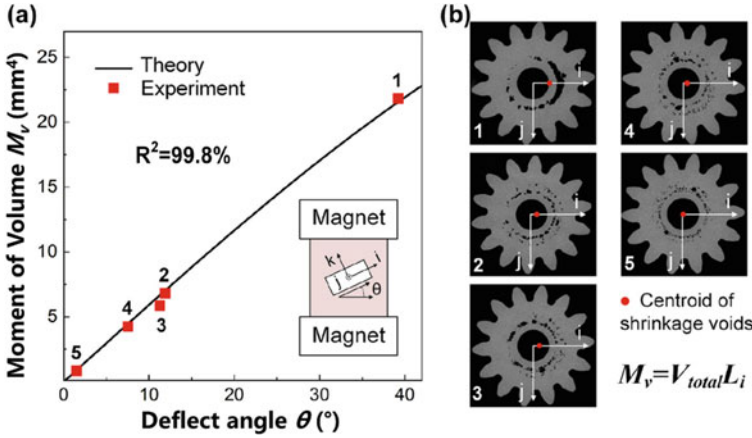


Fig. 7.12 **a** The theoretical and experimental results for the moment of volume based on the deflect angle. **b** 2-dimensional CT scanning images and centroids of shrinkage voids. Reproduced with permission from Ref. [17]. Copyright 2020 Elsevier

where, $\overline{\rho_s}$ and $\overline{\rho_q}$ are respectively the averaged densities of qualified sample and the sample to be tested. In this equation, ρ_i is a parameter known a priori, for example, the air density in a interior void defect is zero. When dealing with other types of defects, prior knowledge of the impurity material is required.

For a defective sample, its center of mass w'_{cm} along the w axis can be expressed as:

$$w'_{cm} = \frac{\int_{V_0} (\rho_i - \overline{\rho_q}) w dV}{\int_{V_0} (\rho_i - \overline{\rho_q}) dV} = \frac{\overline{\rho_s} V w_{cm}}{\int_{V_0} (\rho_i - \overline{\rho_q}) dV}. \tag{7.17}$$

In the follow-up reference frame of the sample, the coordinate of the center of the interior defect can be defined as $\vec{r}'_{cm} = (u'_{cm}, v'_{cm}, w'_{cm})$. Similar to Eq. 7.17, the relationship between the position of the interior defect and the center of mass of the sample along the u axis and the v axis can be obtained. Combine Eqs. 7.11 and 7.17, the relationship between \mathbf{b} and the interior defect can be expressed as Eq. 7.18:

$$\mathbf{b} = \int_{V_0} (\rho_i - \overline{\rho_q}) g dV (u'_{cm}, v'_{cm}, w'_{cm})^T, \tag{7.18}$$

Therefore, it is required to determine the parameters η and \mathbf{d} to locate the interior defect of the sample through Eq. 7.18. Whereas the two parameters cannot be solved only by the single levitation posture of the sample.

If the shape of the sample is simple, the sample can be reasonably simplified. For example, for a one-dimensional sample (the center line of the sample overlaps with the w axis, and the size of the w axis dimension is much larger than that of the u and

v axis dimensions), its interior defects can be considered to be located in the w axis. Hence, the parameter \mathbf{b} can be simplified as $\overline{\rho_s}gV(0, 0, w'_{cm})^T$. The parameters η and \mathbf{d} can be then calculated as:

$$\eta = \beta\lambda_{vv} + \frac{\beta\lambda_{uv} \cos(\vec{z}, \vec{v}) + \beta\lambda_{vw} \cos(\vec{z}, \vec{w})}{\cos(\vec{z}, \vec{v})}, \quad (7.19)$$

$$\mathbf{b} = \int_{V_0} (\rho_i - \overline{\rho_q})g dV (u'_{cm}, v'_{cm}, w'_{cm})^T. \quad (7.20)$$

The position of interior defect in one-dimensional samples can be calculated by measuring the posture of stable levitation of the sample and substituting it into Eqs. 7.19 and 7.20.

For irregularly shaped samples, the equation for the location of interior defects needs to be solved. As mentioned earlier, the equation has two unknowns that need to be contacted through the system of equations. By using two paramagnetic media with different magnetic susceptibility to levitate the defective sample, two different levitation postures were obtained: $\Theta_1 = (F_1, G_1, H_1)$, $\Theta_2 = (F_2, G_2, H_2)$. According to minimum energy principle, when $\partial L/\partial \Theta = 0$, the sample reaches to its equilibrium position:

$$\frac{\partial L}{\partial \Theta} = 2(\eta E - C) \cdot \Theta^T + b = 0 \quad (7.21)$$

Substitute Θ_1 and Θ_2 into Eq. 7.21, the following equations can be obtained:

$$2 \left(\eta_1 \begin{bmatrix} 1 & 0 & 0 \\ 0 & 1 & 0 \\ 0 & 0 & 1 \end{bmatrix} - \frac{2\Delta\chi_1 B_0^2 V}{\mu_0 d^2} \begin{bmatrix} \lambda_{uu} & \lambda_{uv} & \lambda_{uw} \\ \lambda_{uv} & \lambda_{vv} & \lambda_{vw} \\ \lambda_{uw} & \lambda_{vw} & \lambda_{ww} \end{bmatrix} \right) \begin{pmatrix} F_1 \\ G_1 \\ H_1 \end{pmatrix} = -\frac{1}{2}\overline{\rho_s}gV \begin{pmatrix} u_{cm} \\ v_{cm} \\ w_{cm} \end{pmatrix}, \quad (7.22)$$

$$2 \left(\eta_2 \begin{bmatrix} 1 & 0 & 0 \\ 0 & 1 & 0 \\ 0 & 0 & 1 \end{bmatrix} - \frac{2\Delta\chi_2 B_0^2 V}{\mu_0 d^2} \begin{bmatrix} \lambda_{uu} & \lambda_{uv} & \lambda_{uw} \\ \lambda_{uv} & \lambda_{vv} & \lambda_{vw} \\ \lambda_{uw} & \lambda_{vw} & \lambda_{ww} \end{bmatrix} \right) \begin{pmatrix} F_2 \\ G_2 \\ H_2 \end{pmatrix} = -\frac{1}{2}\overline{\rho_s}gV \begin{pmatrix} u_{cm} \\ v_{cm} \\ w_{cm} \end{pmatrix}. \quad (7.23)$$

Equation 7.24 can be obtained by eliminating the unknown parameters η_1 and η_2 :

$$\begin{bmatrix} -G_1 & F_1 & 0 \\ 0 & H_1 & -G_1 \\ 0 & H_2 & -G_2 \end{bmatrix} \begin{pmatrix} u_{cm} \\ v_{cm} \\ w_{cm} \end{pmatrix} = \begin{pmatrix} Q_1 \\ Q_2 \\ Q_3 \end{pmatrix} \frac{\partial L}{\partial \Theta} = 2(\eta E - C) \cdot \Theta^T + b = 0 \quad (7.24)$$

where, Q_1 , Q_2 and Q_3 are constants after subtraction, respectively:

$$Q_1 = \frac{1}{\rho_s g} \frac{2\Delta\chi_1 B_0^2}{\mu_0 d^2} (F_1 G_1 (\lambda_{vv} - \lambda_{uu}) + \lambda_{uv} (G_1^2 - F_1^2) + G_1 H_1 \lambda_{uw} - F_1 H_1 \lambda_{uv}) \quad (7.25)$$

$$Q_2 = \frac{1}{\rho_s g} \frac{2\Delta\chi_1 B_0^2}{\mu_0 d^2} (G_1 H_1 (\lambda_{vv} - \lambda_{ww}) + \lambda_{vw} (G_1^2 - H_1^2) + F_1 G_1 \lambda_{uw} - F_1 H_1 \lambda_{uv}) \quad (7.26)$$

$$Q_3 = \frac{1}{\rho_s g} \frac{2\Delta\chi_2 B_0^2}{\mu_0 d^2} (G_2 H_2 (\lambda_{vv} - \lambda_{ww}) + \lambda_{vw} (G_2^2 - H_2^2) + F_2 G_2 \lambda_{uw} - F_2 H_2 \lambda_{uv}) \quad (7.27)$$

Thus, the location of the defect can be obtained:

$$\begin{pmatrix} u_{cm} \\ v_{cm} \\ w_{cm} \end{pmatrix} = \begin{bmatrix} -G_1 & F_1 & 0 \\ 0 & H_1 & -G_1 \\ 0 & H_2 & -G_2 \end{bmatrix}^{-1} \begin{pmatrix} Q_1 \\ Q_2 \\ Q_3 \end{pmatrix} \quad (7.28)$$

To verify the theoretical analysis, a series of experiments for customized hexagon polylactic acid (PLA) bolts are carried out. The customized hexagon bolts were manufactured by melting deposition 3D printing. The dimensions are shown in Fig. 7.13a. The PLA has the density of 1.243 g/cm³. The head of the bolt have the side length of 4 mm and the thickness of 3 mm. The stud of the bolt has the diameter of 3 mm and length of 10 mm. The customized bolts include qualified bolts and bolts with interior void defects. The center of the customized bolts is calculated to be 2.85 mm away from the outer surface of the head of the centerline sentence. The inside of qualified bolts is uniform and dense. For defective bolts, there is a 1 mm × 1 mm × 2 mm void defect located at the center line of the bolt, and the distance between the defect and the outer surface of the bolt head is 1 mm and 6 mm, respectively, as shown in Fig. 7.13b, c.

The media is chosen as 2.5 mol/L MnCl₂ aqueous solution and 1.1 mol/L MnCl₂ aqueous solution with 0.88 mol/L sucrose. The function of the sucrose is changing the density of the medium without changing the susceptibility. The density of the media have the densities of 1.244 g/cm³ and 1.219 g/cm³, with the susceptibility of 4.65 × 10⁻⁴ (unitless) and 1.99 × 10⁻⁴ (unitless), separately.

The levitations of the defective bolts are shown in Figs. 7.14 and 7.15. For qualified bolt, its density is 1.243 g/cm³ (the same as the nominal density of PLA). The mass of the bolt can be measured by the electronic balance. Hence, the volume of the bolt can be determined as 195.39 mm³. For defective bolts, the voids are interior of the bolts. Therefore, the volumed of the bolts would not be affected by the defect. According to the levitation height of the defective bolts, the average density of the defective bolts is 1.230 g/cm³, thus, the volume of the void is calculated as 2.06 mm³, which coincides with the designed defect size (2 mm³). The levitations of the bolts in different media have different levitation heights z_c and levitation postures Θ . By substituting known parameters into Eq. 7.28, the location of the defects can be obtained. According to

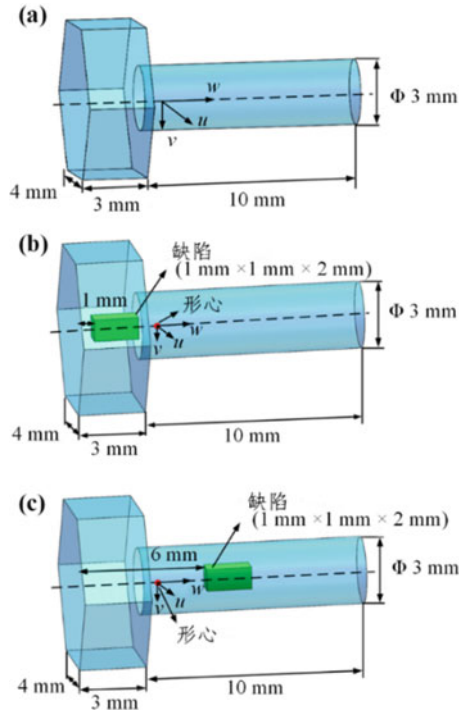


Fig. 7.13 Schematic of customized hexagon bolts. **a** Qualified bolt; **b** the defect is located in the head of the bolt; **c** the defect is located in the stud of the bolt. Reproduced with permission from Ref. [18]. Copyright 2018 Elsevier

the levitation experiments of two samples with defects located at different positions, the calculated locations of the defects are listed in Table 7.1. It can be seen that the maximum difference between the calculated results and the actual location of defects is no more than 0.2 mm, indicating that the defect inversion method based on magnetic levitation testing method proposed in this section can be used to locate and analyze the interior defects of three-dimensional samples.

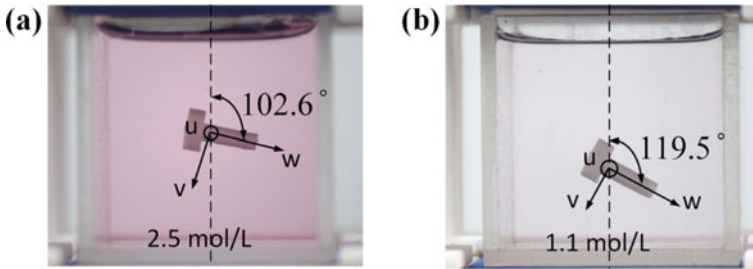


Fig. 7.14 The levitation of the bolt with defect at the head. **a** Levitation in 2.5 mol/L aqueous solution. **b** Levitation in 1.1 mol/L aqueous solution. Reproduced with permission from Ref. [18]. Copyright 2018 Elsevier

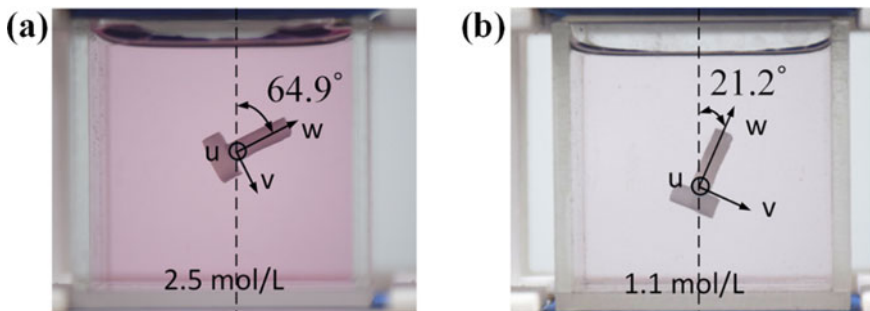


Fig. 7.15 The levitation of the bolt with defect at the stud. **a** Levitation in 2.5 mol/L aqueous solution. **b** Levitation in 1.1 mol/L aqueous solution. Reproduced with permission from Ref. [18]. Copyright 2018 Elsevier

Table 7.1 The actual location and the calculated results of the void defects

Sample	Actual location	Calculated location
Sample 1	(0, 0, -1.85 mm)	(0, -0.16 mm, -1.65 mm)
Sample 2	(0, 0, 3.15 mm)	(0, -0.09 mm, 3.18 mm)

Reproduced with permission from Ref. [18]. Copyright 2018 Elsevier

References

1. Fu SY, Lauke B, Mäder E, et al. Tensile properties of short-glass-fiber-and short-carbon-fiber-reinforced polypropylene composites. *Compos A Appl Sci Manuf.* 2000;31(10):1117–25.
2. Ha J, Chae S, Chou KW, et al. Effect of polymers on the nanostructure and on the carbonation of calcium silicate hydrates: a scanning transmission X-ray microscopy study. *J Mater Sci.* 2012;47:976–89.
3. Eyvazzadeh Kalajahi A, Rezaei M, Abbasi F. Preparation, characterization, and thermo-mechanical properties of poly (ϵ -caprolactone)-piperazine-based polyurethane-urea shape memory polymers. *J Mater Sci.* 2016;51:4379–89.

4. Hamad K, Kaseem M, Deri F. Effect of recycling on rheological and mechanical properties of poly(lactic acid)/polystyrene polymer blend. *J Mater Sci.* 2011;46:3013–9.
5. Jiang J, Wang S, Hou J, et al. Effect of injection velocity on the structure and mechanical properties of micro injection molded polycarbonate/poly(ethylene terephthalate) blends. *Mater Des.* 2018;141:132–41.
6. Ribeiro B. Support vector machines for quality monitoring in a plastic injection molding process. *IEEE Trans Syst Man Cybern Part C (Appl Rev).* 2005;35(3):401–10.
7. Sadeghi BHM. A BP-neural network predictor model for plastic injection molding process. *J Mater Process Technol.* 2000;103(3):411–6.
8. Sanschagrin B, Gauvin R, Fisa B, et al. Weldlines in injection molded polypropylene: effect of filler shape. *J Reinf Plast Compos.* 1990;9(2):194–208.
9. Merah N, Irfan-ul-Haq M, Khan Z. Temperature and weld-line effects on mechanical properties of CPVC. *J Mater Process Technol.* 2003;142(1):247–55.
10. Brunner AJ, Hack E, Neuenschwander J. Nondestructive testing of polymers and polymer-matrix composites. Wiley. 2015, p. 7–10.
11. Wismans JGF, Govaert LE, Van Dommelen JAW. X-ray computed tomography-based modeling of polymeric foams: the effect of finite element model size on the large strain response. *J Polym Sci Part B Polym Phys.* 2010;48(13):1526–34.
12. Zhao P, Zhao Y, Kharbas H, et al. In-situ ultrasonic characterization of microcellular injection molding. *J Mater Process Technol.* 2019;270:254–64.
13. Xie J, Zhao P, Zhang J, et al. Characterization of polymer materials using magnetic levitation. *J Mater Res.* 2020;35(9):1182–9.
14. Zhao P, Xie J, Zhang J, et al. Evaluation of polymer injection molded parts via density-based magnetic levitation. *J Appl Polym Sci.* 2020;137(7):48431.
15. Subramaniam AB, Yang D, Yu HD, et al. Noncontact orientation of objects in three-dimensional space using magnetic levitation. *Proc Natl Acad Sci.* 2014;111(36):12980–5.
16. Xie J, Zhao P, Jing Z, et al. Research on the sensitivity of magnetic levitation (MagLev) devices. *J Magn Magn Mater.* 2018;468:100–4.
17. Tang D, Zhao P, Shen Y, et al. Detecting shrinkage voids in plastic gears using magnetic levitation. *Polym Testing.* 2020;91:106820.
18. Xia N, Zhao P, Xie J, et al. Defect diagnosis for polymeric samples via magnetic levitation. *NDT E Int.* 2018;100:175–82.

Chapter 8

Magnetic Levitation in Chemistry



Jun Xie, Baocai Zhang, Xuemei Li, and Peng Zhao

8.1 Introduction

It is well known that the density is the basic character of a substance. Density measurement is an important characterization method for both static and dynamic analysis and for inferences of chemical composition in specific experiments. For example, the density of polymers depends not only on their chemical composition, but also on how the chains are arranged in space (i.e. crystalline or amorphous arrangements). Therefore, the minute difference in density can be used to analyze polymers with similar atomic compositions. For certain classes of polymers (formed by polymerization of small monomers, such as acrylic esters or other vinyl monomers), the kinetics of the polymerizations can be monitored through the measurement of the change in density associated with polymerization. In fact, many types of chemical/biochemical reactions, such as cycloaddition reactions (dimerization) of cyclopentadiene [1], chemical reactions (or binding) on a solid support (e.g., covalent attachments of low-molecular-weight organic molecules to 4-benzyloxybenzaldehyde polystyrene beads [2], and binding of carbonic anhydrase to porous hydrogel particles presenting aryl sulfonamides—a class of inhibitors specific to carbonic anhydrase [3]), and biochemical reactions between antigens and antibodies, can be monitored by analyze the dynamic change in density over time. The density of minerals can also be used to assess their purity, and the difference in density provides the basis for mineral separations [4]. Differently sized carbon nanotubes, coated with structure-discriminating surfactants, show different densities, and thus provide a basis for simple separation.

J. Xie (✉)

College of Mechanical Engineering, Zhejiang University of Technology, Hangzhou, China

e-mail: jxie93@zjut.edu.cn

B. Zhang · X. Li · P. Zhao

The State Key Laboratory of Fluid Power and Mechatronic Systems, College of Mechanical Engineering, Zhejiang University, Hangzhou, China

8.2 Identification of Substances

The type and composition of a matter reflect on its density. Density measurement can be used as a primary method for separating and identifying substances in specific occasions such as analyzing forensic evidence. Common contact trace objects are used in forensic investigations to establish an association (i.e., link criminals to crime scenes and to victims). The objects may be the hairs, fibers, paint chips, and fragments of broken glass that are left at the crime scene. In addition, glitter is another contact trace material that has been used as associative evidence [5]. It is worth noting that, usually, these objects are diamagnetic. The tests of these contact trace objects are sophisticated and expensive, from visual or microscopic inspection to spectroscopic analysis. As introduced above, the density of an object could in principle be used to characterize a trace object. For common density measurement methods, it requires precise determination of the volume of an irregularly shaped objects to measure the density. However, volume measurements are difficult for small objects such as glitter particles, and thus, there exists a need for a method that makes it possible to determine the density of trace objects quickly and easily. Kirk used density columns with the mixture of two organic liquids (e.g., bromoform and bromobenzene) in a specific ratio to analyze glass fragments (naming “sink/float method”) [6]. Questioned and known glass fragments are placed together in the mixture, and the ratio of the organic liquids is adjusted until the two glass fragments are separated and distinguished according to their differences in densities. Otherwise, if the glass fragments cannot be separated (sank or levitated together) in a large range of liquid ratio, it can be concluded that the fragments are originated from the same source. Predictably, this method also requires long testing process, for the adjustment of the mixture contains time consuming trials. Considering the advantages over the common methods, MagLev is applied to identify these small and irregular-shaped forensic evidences.

8.2.1 Method

The objects, such as smokeless gunpowder, glass pieces, fibers, hair, glitter, etc., commonly encountered in crime scenes are diamagnetic and are possible for MagLev. The container is chosen as glass or transparent polymer (such as PMMA) cuvettes for direct observation. Various paramagnetic solutes are available for preparing appropriate solutions (e.g., MnCl_2 , MnSO_4 , GdCl_3 , FeCl_3 , CuSO_4 , etc.). Chelated paramagnetic ions, such as $\text{Gd}(\text{DTPA})$ and $\text{Mn}(\text{EDTA})$, are other choices for aqueous and nonaqueous solvents. The samples immersed in the paramagnetic medium need pretreatment to remove the bubbles adhere to them. These bubbles will significantly influence the measuring result (the density of air is 0.00118 g/cm^3 at $25 \text{ }^\circ\text{C}$ at standard pressure). The repetitive invert of the cuvette can remove bubbles that may have formed on the samples. Washing the samples with ethanol/methanol can also greatly reduce the generation of the bubbles. However, it is not a suitable way for powders

and small particles, for these samples may bring too much ethanol/methanol to the medium, which will change the concentration of the medium and finally cause large inaccuracy in testing. Adding a small amount of detergent (e.g., Tween 20, 0.1% (vol./vol.)) to the MnCl_2 solution can lower the surface tension of the medium and reduce the interactions between hydrophobic objects, as well as their interactions with the walls of the cuvette. Combined with sonication treatment, the bubbles that form on the walls of the cuvette and on the sample itself can be removed. It has been proved that this treatment can result in the most precise measurements. For the forensic samples are in very small scales, the levitation require a much longer time (several minutes) to reach the equilibrium position.

8.2.2 Identification of Forensic Evidences

The identification of glitters with same appearance shows the advantages of MagLev method [7]. The properties of a series of glitters are shown in Table 8.1. According to their nominal densities, the medium is chosen as 3.0 M MnCl_2 aqueous solution. Figure 8.1a exhibits an example of levitating different amount of *Crystalina #321* after 6 min. Two standard density beads (1.350 and 1.450 g/cm^3) are levitated together for comparison. The densities measured through MagLev and provided by the manufacturer are listed in Fig. 8.1b. The results are obtained by the levitation of 20 pieces of each glitter. Their standard deviation of each result is $\pm 0.001 \text{ g/cm}^3$ based on $n = 7$ independent measurements.

According to the comparison between the measuring results and nominal densities provided by the manufacturer, the measured densities for the 11 glitters can be categorized into three groups. (i) High agreement: average density difference below 0.05 g/cm^3 , (ii) Moderate agreement: average density difference between 0.05 and 0.10 g/cm^3 . (iii) Low agreement: average density difference above 0.10 g/cm^3 . Most of the samples (6 in 11) are in high agreement level. Three samples are in moderate agreement. Noticing that there are two samples (Alpha Jewels I and II) differed by more than 1.0 g/cm^3 from the nominal densities. These samples may be fake or from other unknown sources.

The determination of the density of the glitters have potential to identify the samples extract from a mixture like commercial nail polish. A Sally Hansen diamond strength nail polish sample with Alpha Jewels I glitter (1.394 \pm 0.002 g/cm^3) inside was applied to demonstrate the idea. 0.5 g of the sample is in 5 mL acetone, and the glitters are then collected by straining the solution via a piece of quantitative filter. The glitters then measured by the MagLev method. Comparing the Alpha Jewels I glitter extract from the nail polish and previous levitation results, it can be found that the levitation height of the extracted glitters is within the standard deviation of the measurement. This means MagLev method is accurate in obtaining density of unknown target objects from complex cosmetic matrices.

Except for the particles, powders are another type of evidence that is always found in crime scenes. For example, smokeless gunpowder is of great vital for shooting

Table 8.1 Properties of the glitters

Sample	Thickness (μm)	Size (μm)	Shape	Character
Alpha Jewels I	25	204 \times 204	Square	Holographic glitter particles consist of micro-embossed vacuum metalized (0.5% aluminum) polyethylene terephthalate (PET)
Alpha Jewels II	25	635	Hexagonal	
Alpha Jewels Epoxy	50	635	Hexagonal	Holographic glitter particles consist of micro-embossed aluminum copolymer particles
Crystalina #321	28–36	635	Hexagonal	Iridescent glitter particles with a polyester/ acrylic optical core and a polyester outer layer
Mirror Crystalina I	28–36	635	Hexagonal	
Mirror Crystalina II	28–36	204 \times 204	Square	
Chrome Silver 1P	178	635	Hexagonal	Metallic glitter particles consist of vacuum metalized (0.5% aluminum) pigmented PET
Silver 1P Epoxy I	25	102 \times 102	Square	
Silver 1P Epoxy II	178	102 \times 102	Square	
Silver 1UP Ultrathin Polyester	13	635	Hexagonal	
Silver Plastic Jewels #21	178	380 \times 380	Square	Metallic glitter consists of a copolymer

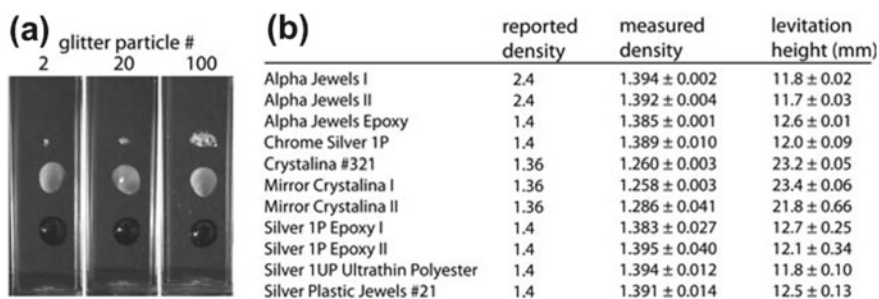


Fig. 8.1 Identification of glitters using MagLev. **a** Levitation results of different amount of Crystalina #321 (upper cluster) after 6 min. Two standards (lower spheres) are levitated together for comparison. **b** Identification results of different glitters. Reproduced with permission from Ref. [7]. Copyright 2012 Wiley

Table 8.2 Measurement results of different gun powders using MagLev

Sample	Height (mm)	Density (g/cm ³)
Hercules Red Dot	27.5 ± 0.28	1.226 ± 0.010
IMR Trail Boss	18.9 ± 0.74	1.557 ± 0.059
Hercules Bullseye Orange	15.3 ± 0.20	1.655 ± 0.023
Hercules Blue Dot	14.8 ± 0.13	1.657 ± 0.015
IMR PB	13.2 ± 0.28	1.660 ± 0.030
IMR Hi Skor 800-X	13.1 ± 0.31	1.662 ± 0.025

scene investigation. The MagLev method is applied to determine the density of six smokeless gunpowder samples. For the powders have a relatively large density range, two media, 3.0 M and 4.0 M MnCl₂ aqueous solutions, are used in the testing. The testing result of the powders are shown in Table 8.2. Normally, gunpowder is susceptible to dampness and will not be effective for ignition. The dampness may also affect the density measurement via MagLev. However, the experiments shows different conclusion. The repeated exposure and prolonged exposure to an aqueous MnCl₂ solution are considered in experiments. The Hercules Blue Dot samples immersed in a 4.0 M MnCl₂ solution for 7 days, and the density was measured every 24 h. Considering the effect on the concentration of the medium caused by the evaporation of the water, standard density beads are introduced to the levitation to calibrate the results. The result shows a maximum change of 0.012 g/cm³ on the change in the average density of the gunpowder. It is within the standard deviation of the initial measurements, which means the dampness will not affect the density of the gunpowder that it can be accurately measure via MagLev. The same conclusion can also be drawn by the experiments on Hercules Blue Dot gunpowder after repeated exposures to MnCl₂ solution. The samples are tested for 10 consecutive measurements. The gunpowder is levitated in MagLev device, then removed, rinsed by water, and dried in nitrogen atmosphere for next test. The change of the results is also within the standard deviation. In addition, the MnCl₂ solution has a pH of ~3.0. The results also proved that the density of the gunpowder will not affected by little change of the environment.

8.2.3 Identification of Drugs

Drug abuse is a major public health problem. The overdoses cause over 100,000 death around the world. In order to identify a drug according to the forensic standards of analysis, multiple analytical methods have to be used to obtain results that correspond to each other. Common analytical methods are listed in Table 8.3.

The techniques that are able to parse molecular configurations has the highest ranking for forensic analysis, such as X-ray diffractometry and IR, NMR, Raman spectrum, and mass spectrometry [8]. However, their cost and inconvenience in

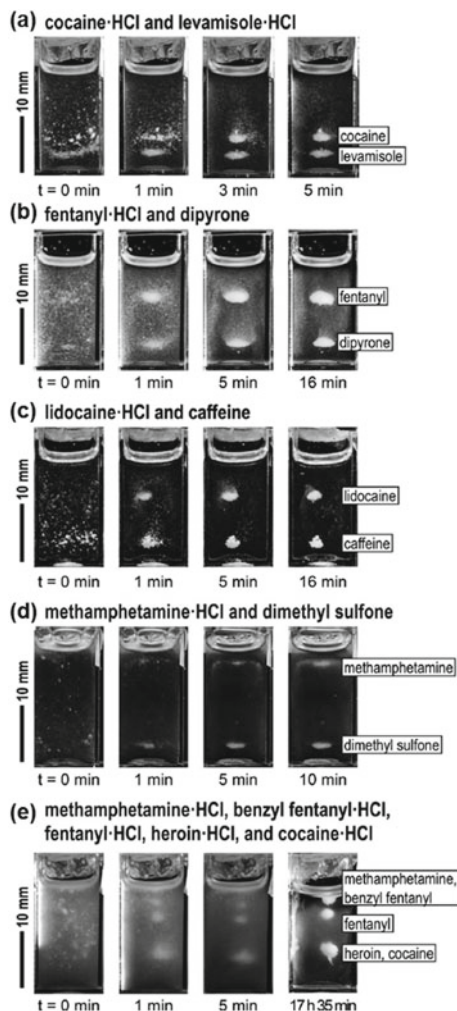
Table 8.3 Classification of common analytical method

Category A Highest selectivity for molecular structure	Infrared spectroscopy
	Mass spectrometry
	Nuclear magnetic resonance spectroscopy
	Raman spectroscopy
	X-Ray diffractometry
Category B Intermediate selectivity	Capillary electrophoresis
	Gas chromatography
	Ion-mobility spectrometry
	Liquid-chromatography
	Microcrystalline tests
	Super critical fluid chromatography
	Thin-layer chromatography
	Ultraviolet/visible spectroscopy (full spectrum)
	Macroscopic examination (cannabis only)
	Microscopic examination (cannabis only)
Category C Lowest selectivity	Color tests
	Fluorescence spectroscopy
	Immunoassay
	Melting point
	Pharmaceutical identifiers

use make these methods available only under laboratory conditions. The less-molecularly-specific separation methods are considered to be the med-level for identification. The methods that cannot or limitedly provide molecular structure information are in the lowest category. In some cases, although the lowest ranking method (e.g. immunoassays [9, 10] and colorimetric tests [11]) can only provide weak evidence of molecular information, but have advantage that they can be easily used in resource-limited circumstances. Therefore, MagLev also have the potential to be used as a presumptive identification method that based on its ability to sensitively test the compound density [12].

Mixtures of illicit drugs can contain a wide range of compounds. These compounds, including hydrochloride salts of fentanyl, acetyl fentanyl, cocaine, heroin, and methamphetamine, can be separated and measured by MagLev method. Noting that most of these compounds are water soluble, the Gd(DPM)₃TOPO (450 mM) dissolved in a mixture of 23 vol.% hexane and 77 vol.% tetrachloroethylene is use as the medium. Typical separation results are shown in Fig. 8.2. In fact, some drugs like synthetic opioids requires high dilution (~5 wt%) of the active components, and thus, makes the analysis of these opioids from small amount samples a big challenge. For example, the fentanyl may be present only as a few crystals in a 50 mg mixture.

Fig. 8.2 Separation process of mixtures of powdered illicit drugs, adulterants, and dilutants (2.5–9.5 mg of each compound) using MagLev. $\text{Gd}(\text{DPM})_3\text{TOPO}$ (450 mM) dissolved in a mixture of 23 vol.% hexane and 77 vol.% tetrachloroethylene is used as paramagnetic medium. Reproduced with permission from Ref. [12]. Copyright 2019 Wiley



A series of separation experiments of lidocaine HCl and caffeine mixture are carried out to demonstrate the advanced ability of MagLev to screen out minute amounts of target matter. The lidocaine HCl and caffeine mixed in different proportions are significantly separated in MagLev device, as shown in Fig. 8.3. It is worth noticing that very small proportion of fentanyl HCl in the mixture (e.g. 1 wt%) can not be detected by FTIR-ATR, but can be clearly identified by FTIR-ATR after separation (Fig. 8.3b). Ulteriorly, the limit of concentration of separable mixture can be even less than 1 wt%. The MagLev method can screen out as few as five 100–200 μm crystals, from 50 mg mixture that contains hundreds to thousands of particles of other compounds. The image analysis (Fig. 8.3d) also verifies that the amount of separated compounds well agrees quantitatively with the known compositions of the samples.

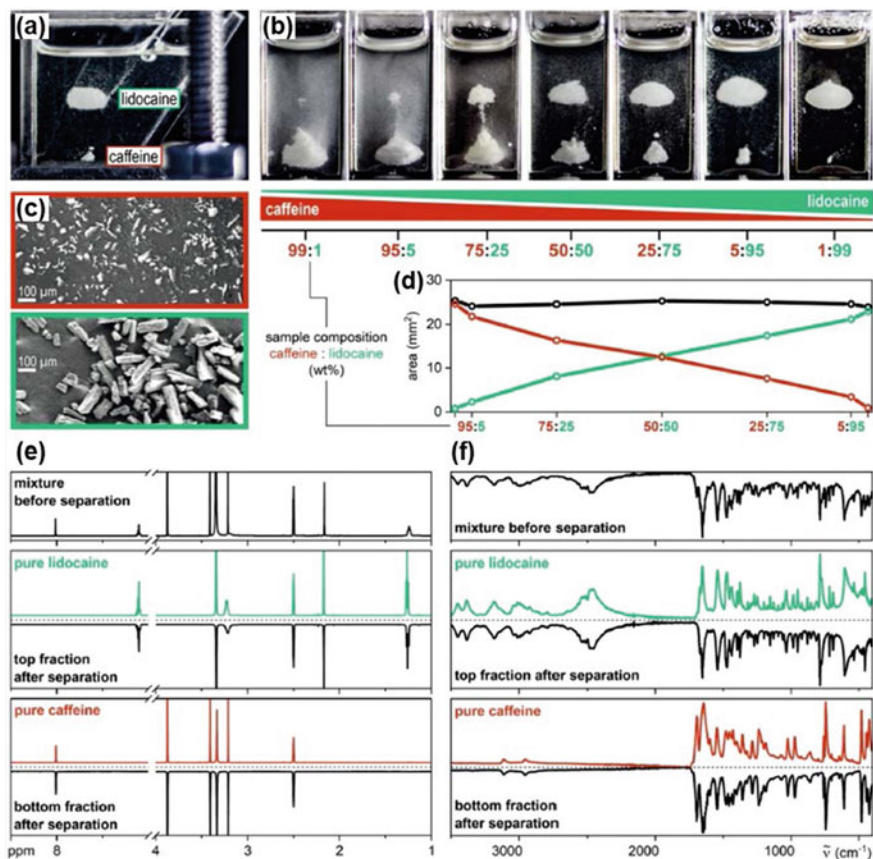


Fig. 8.3 The investigation of MagLev separation of powdered mixtures and the following characterization with spectroscopic techniques. **a** MagLev separation (30 min) of a mixture of lidocaine HCl and caffeine (95:5 wt%; 50 mg) in a cuvette filled with the paramagnetic solution, and extraction using a Pasteur pipette. **b** MagLev separation (20 min) of powdered mixtures (50 mg) of lidocaine HCl (top clouds) and caffeine (bottom clouds) in different proportions (wt%). **c** Scanning electron micrographs of crystals of lidocaine HCl and caffeine (pure compounds). **d** The projected, two-dimensional areas of the levitating fractions of lidocaine HCl (green line) and caffeine (red line), and their combined area (black line), are plotted against the chemical composition of mixtures. **e** ^1H NMR (600 MHz) characterization of a mixture (50 mg) of lidocaine HCl and caffeine (50:50 wt%) and the fractions after separation (30 min) in the MagLev. **f** FTIR-ATR characterization (normalized to highest peak) of the samples purified in **e** except that the residue was characterized as a dry powder. Reproduced with permission from Ref. [12]. Copyright 2019 Wiley

The separation after MagLev can be further characterized by high ranking method such as NMR (Fig. 8.3e) and FTIR-ATR (Fig. 8.3f). The spectra of the extracted compounds well coincided with the spectra of pure compounds, which suggests excellent separation of crystals of these two compounds using MagLev. Although there should be minute amount of crystals remaining in the medium, the separation

can be assumed as totally separated. The separation also enabled clear identification of target compound with FTIR-ATR, which cannot be identified in the mixture before separation (Fig. 8.3f).

8.3 Monitoring the Chemical Reaction

Currently, analytical techniques to monitor the chemical reaction can be classified into two categories: (i) techniques with high-end instruments, such as rheometry, calorimetry, gel-permeation chromatography, various forms of UV/vis spectroscopy, mass spectrometry, and NMR spectroscopy. These methods can provide detailed information (e.g. online monitoring of polymerization reactions [13]), but are expensive for use and maintain. (ii) Unsophisticated tools and methods such as balances, refractometers, colorimetry, and dilatometers [14, 15]. These tools are readily available in research labs and quality control stations.

The change of density can be used to characterize the reaction process. For example, solid-state support chemistry is widely used in the preparation of peptides, nucleic acids, small molecule libraries, affinity purification, and protein target identification of capture reagents [16]. However, a major disadvantage of solid phase chemistry is that there is no cheap and fast way to quantitatively monitor the reaction process on insoluble polymer carriers [17]. Colorimetric is a common method for rapid and qualitative test. Nevertheless, it is affected by artifacts from competing side effects (false positives) and incomplete reactions (false negatives) [18]. Spectroscopic instrument can provide much more information than colorimetric tests, while the method is time-consuming and require expensive instruments (>\$10,000). A favorable addition to solid-supported chemistry, especially in the developmental phase of solid-supported synthesis, would be a quick and quantitative method to track the progress of reactions without the need for specialized or expensive equipment. In fact, what is needed is the equivalent of thin layer chromatography (TLC) in solid phase chemistry.

For free-radical polymerization, density variation, which is usually measured by volume dilatometry, is a key character for characterizing the kinetics of free-radical polymerization. The method measures the volumetric shrinkage of a sample of polymer and monomer (the polymerization makes the monomer moves from the van der Waals distance in the liquid monomer to the covalent and shorter distance). It is widely applicable to the shrink (or expand) in volume of the polymer system during polymerization (e.g. bulk, suspension, emulsion polymerization with vinyl monomers). The method could also be used to study photopolymerization after proper modifications. Similarly, volume dilatometry has its shortcomings: (i) It normally requires relatively large volumes of samples (1–10 mL). Thus, it is not applicable to monomers available in limited quantities (<100 μL). (ii) The dilatometer can only monitor the polymerization in the device. It cannot be used as a stand-alone device to monitor polymerization in other reaction vessels. (iii) It is a time-limited method for monitor the early stages of the polymerization. As long as the products, or the

mixture, become thick, solidified, or stick to the boundary of the vessel along with the progress of the reaction, the error in reading the positions of the meniscus become larger.

8.3.1 Monitor Chemical Reactions on Solid Supports

It is evident that MagLev method can test minute density change through obvious change in levitation height, by which the chemical composition of polymeric beads can be detected [19]. Figure 8.4 shows a series of examples of derivatives of 4-benzyloxybenzaldehyde polystyrene (diameters from 35 to 75 μm , loading level = 3.5 mmol $-\text{CHO}/\text{g}$ resin, ~ 350 pmol $-\text{CHO}/\text{bead}$). The derivatives are prepared through reductive amination reactions.

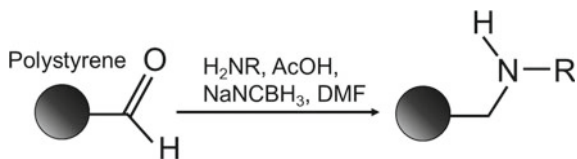
Each reaction (dissolved in 5% CH_3COOH -DMF) agitates the beads with 10 equivalent of amine and $\text{NaBH}_3(\text{CN})$ for 24 h to ensure complete conversion. The beads are sequentially washed by DMF, CH_2Cl_2 , CH_3OH , and H_2O to remove excess reagent from the polymer. The beads are stained by 2,4-dinitrophenylhydrazine to confirm that the aldehyde is completely consumed. Approximate 100 beads after each reaction are levitated by the MagLev method with the aid of 650 mM GdCl_3 . The dispersed beads in the solution become coalesced after 5 min levitation and finally get concentrated within 15 min. The height of the center point of the concentrated beads are used to calculate the average density of the beads.

Each bead contains ~ 350 pmol of small molecule. Benefit from the high sensitivity of the MagLev method, the difference in chemical composition of a single atom will lead to a distinguishable change in levitation height. For example, the b, g, and j subjects shown in Fig. 8.5b has the differences of only one fluorine atom, but reflect obvious derivations in levitation heights.

The MagLev method is then proved to be also sensitive to the change in chemical composition (through change of density) of a polymer during the course of a chemical reaction. It is demonstrated by monitoring the reaction of 2,5-diiodobenzoic acid to leucinerivatized Wang polystyrene (diameter) 75–150 μm , 1.8 mmol $-\text{NH}_2/\text{g}$ resin, ~ 1 nmol $-\text{NH}_2/\text{bead}$) at 0 $^\circ\text{C}$ using 5 equiv of O-benzotriazole-*N,N,N',N'*-tetramethyl-uronium-hexafluoro-phosphate (HBTU) and 5 equiv of diisopropylethyl amine (DIEA) in MF, as shown in Fig. 8.6.

Aliquots of beads are withdrawn from the reaction process at different times and immediately washed to eliminate the adhered reagents. About 100 beads from each aliquot are levitated by MagLev device using medium DMF with 650 mM GdCl_3

Fig. 8.4 Reductive amination reactions for preparing different series of 4-benzyloxybenzaldehyde polystyrene



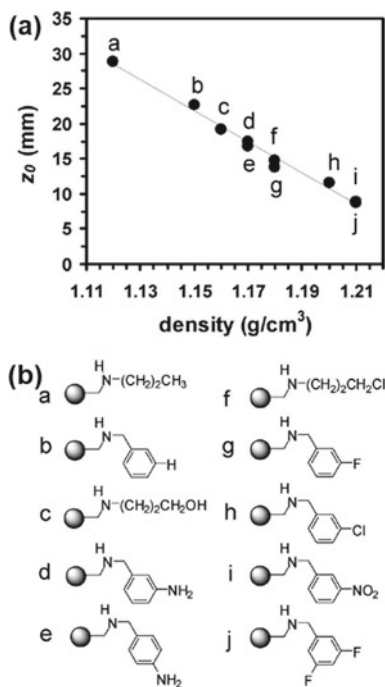


Fig. 8.5 **a** Levitation results of 10 different derivatives of the 4-benzyloxybenzaldehyde polystyrene beads in a 650 mM GdCl_3 aqueous solution. **b** Chemical structures for each derivative in (A). Reproduced with permission from Ref. [19]. Copyright 2008 American Chemical Society

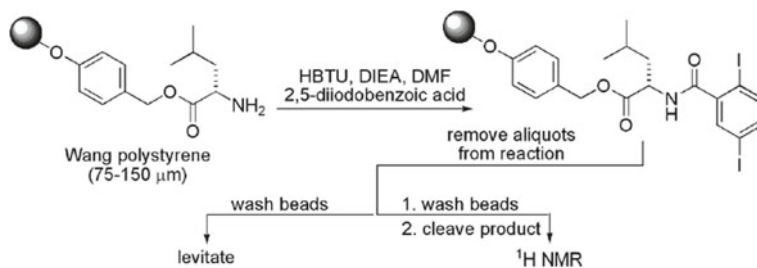


Fig. 8.6 Schematic of the process for monitoring conversion for a condensation reaction of a solid-supported amine with a carboxylic acid. Reproduced with permission from Ref. [19]. Copyright 2008 American Chemical Society

as the medium. The results are shown in Fig. 8.7. The levitation height of the beads decreases which means the average density of the beads increases as the reaction goes on. The beads form tight clusters at the beginning and end of the reaction, but their dispersity increases as the reaction approaches 50% completion. According to the theory of MagLev method, although the sizes of the beads vary from 75 to 150 μm ,

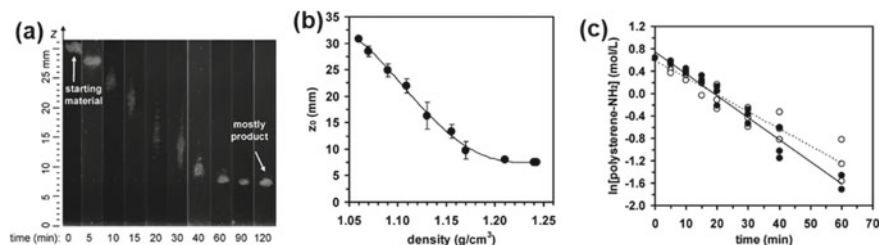


Fig. 8.7 **a** Levitation of the polymer beads cluster (leucinerivatized Wang polystyrene, ~ 100 beads/cluster) at different times throughout the course of the reaction. **b** The correlation of density of the polymer beads with their levitation height. **c** Pseudo-first-order kinetics plots for the rate of consumption of polymer-bound amine determined by ^1H NMR (solid dot) and by levitation (hollow dot) from three independent measurements. Reproduced with permission from Ref. [19]. Copyright 2008 American Chemical Society

it does not affect levitation height of the beads. Therefore, the dispersion of the beads means the incomplete reaction of the beads. This reflects in the aggregation of the beads in the MagLev experiment.

Since the amount of reagent used in the reaction is five times greater than the amount of polymer-bound $-\text{NH}_2$, the reaction follows pseudo-first-order kinetics. The verification is carried out by ^1H NMR. Figure 8.7c compares 3 independent results from ^1H NMR and MagLev. It is obvious the results of MagLev method show high coincidence with ^1H NMR results. Both MagLev method and NMR yield similar rates ($T_{1/2} = 23 \pm 4$ min (NMR) and $T_{1/2} = 18 \pm 2$ min (MagLev)) for the pseudo-first-order reaction.

8.3.2 Characterize the Kinetics of Free-Radical Polymerization

The polymerization of vinyl monomers presents an obvious change in density. For example, methyl methacrylate (MMA) and poly(methyl methacrylate) has the density of 0.936 and 1.188 g/mL, respectively, which means a 27% change in density in free-radical chain growth polymerization. The MagLev is applied to this polymerization system (through thermal polymerization and photopolymerization) to demonstrate the application to characterize the kinetics of free-radical polymerization [20].

Similar to the chemical reactions on solid supports, the change in density is primarily a direct result of the reduction in volume ΔV as the monomer covalently binds to the grown polymer chain and thus the distance between the monomers changes from the van der Waals distance to the shorter covalent distance. For polymerization of methacrylate esters, ΔV originates from the addition reaction of the double bonds. Its contribution to the reduction of the density of the product is highly correlated with its side chains. Larger side chains results in the smaller change in density

between the polymer and the monomer. Larger molecule polymer can be synthesized by the cross-linking of prepolymer. In this kind of polymerization, the prepolymer has a large volume, which lead to an inconspicuous ΔV during polymerization. Thus, the density change of the system could be approximately 0.

Thermal polymerization of MMA, hexyl methacrylate, and octadecyl methacrylate are investigated to experimentally confirmed the prediction that the density change should be smaller for monomer polymerization with larger molecular weight (or volume) but with common polymerizable groups. Small polymer beads (with diameter of ~ 1 mm) are obtained by suspension polymerization of the monomers. The densities of the monomers and polymers are determined using MagLev and listed in Table 8.4. The estimation of the density of the polymer can be calculated by Eq. 8.2,

$$\rho_m = \frac{m}{V_m} \quad (8.1)$$

$$\rho_p = \frac{m}{V_p} = \frac{m}{V_m - \Delta V} \quad (8.2)$$

where, m (kg) is the mass of a monomer molecule, V_m (m^3) is the average volume of a single molecule in a liquid monomer (including real volume a monomer and the void space averagely occupied by each monomer), V_p (m^3) is the volume that monomeric unit in the polymer occupies, and ΔV (m^3) is the difference between V_m and V_p .

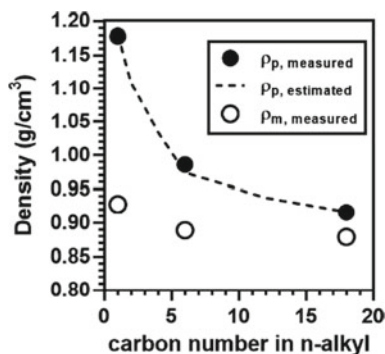
As shown in Table 8.4, the data clearly demonstrates an obvious decrease in $\frac{\rho_p}{\rho_m}$ with the increase of molecular weight.

It is known that the polymerization of n-alkyl methacrylate can maintain a reasonably consistent reduction in the molar volume consumed per vinyl methacrylate group when this series of monomers are polymerized to produce a polymer. This consistent reduction in volume results from the shared chemical moiety (i.e., vinyl group) involved in the polymerization. The densities of the monomers can be obtained from the vendors and literatures. The reduction in molar volume is reported as 22.5 mL/mol [21]. Hence, the estimation of the density of some members in this series can be calculated (Fig. 8.8). The experimental values are also listed with the estimations and show satisfactory agreement between them.

Table 8.4 Densities of methacrylate esters and their polymers

n-alkyl	ρ_m		ρ_p		$\frac{\rho_{p,set}}{\rho_{m,rep}}$	$\frac{\rho_{p,meas}}{\rho_{m,meas}}$
	Reported	Measured	Estimated	Measured		
Methyl	0.936	0.928	1.182	1.178	1.26	1.27
Hexyl	0.863	0.889	0.974	0.986	1.13	1.11
Octadecyl	0.864	0.879	0.917	0.916	1.06	1.04

Fig. 8.8 Density measurement results of methacrylate esters and their polymers via MagLev. Reproduced with permission from Ref. [20]. Copyright 2017 American Chemical Society



On the other hand, the prepolymer of vinyl-containing siloxane (for synthesizing PDMS (Dow Corning Sylgard 184)) is used to validate the prediction that the cross-linking of large “monomer” will not significantly affect the density throughout the polymerization. The Pt-catalyzed hydrosilylation (addition of Si–H bonds to olefin bonds) between vinyl-ending prepolymers and crosslinkers with Si–H groups results in the polymerization of the prepolymers and produces the final cross-linked (and cured) polymer [22].

Because the ΔV is much smaller than the volume of the prepolymers in hydrosilylation reaction ($22.5 \text{ cm}^3/\text{mol}$, under the assumption that it is the same as observed in n-alkyl methacrylate polymerization, while the molar volume is estimated to be $\sim 7300 \text{ cm}^3/\text{mol}$). Therefore, the $\frac{\rho_p}{\rho_m}$ can be calculated as 1.003. The experiment of the polymerization presents a good verification of the discussion. Although the morphological changes are obvious, the levitation height of the droplet of un-cross-linked prepolymers is the same as that of the cross-linked irregular PDMS piece.

Based on the density changes, the kinetics of the polymerization can be characterized. The radical polymerization of MMA is chosen as the standard polymer system for an example (in particular, the polymerization is thermally initiated by 2,2'-azo (isobutyronitrile) or AIBN). The pure monomer of MMA (using inhibitors of 4-methoxyphenol and O_2) and AIBN to perform the thermal polymerization. The polymerization of MMA is a first-order reaction for MMA. Its rate equation can be expressed as Eq. 8.3.

$$-\frac{dc_M}{dt} = k_P \left(\frac{fk_d c_I}{k_t} \right)^{0.5} c_M \quad (8.3)$$

where, c_M (mol/L) is the concentration of the monomer, k_P ($\text{L mol}^{-1} \text{ s}^{-1}$) is the rate constant of radical propagation, f (unitless) is the efficiency of initiation (the proportion of free radicals produced by the homolysis reaction of the initiator that successfully initiates the polymer chain), k_d (s^{-1}) is the rate constant of thermal decomposition of the initiator into radicals, c_I (mol/L) is the concentration of the initiator, and k_t ($\text{L mol}^{-1} \text{ s}^{-1}$) is the rate constant of radical termination.

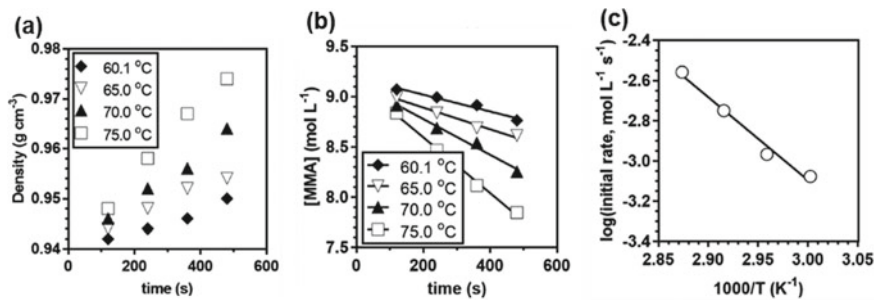


Fig. 8.9 Determination of the Arrhenius activation energy of thermally initiated polymerization of MMA using AIBN. **a** The changes in density of the polymerizing mixture (pure MMA with 1.3 wt% AIBN), over time by transferring small ($\sim 2 \mu\text{L}$), cooled aliquots of the reacting mixture to the MagLev device. **b** The changes in the concentrations of the remaining monomer in the reacting mixture. **c** The initial rates of polymerizations with respect to the temperatures. Reproduced with permission from Ref. [20]. Copyright 2017 American Chemical Society

The reactions are carried out at four temperatures. The density of the reacting mixture is measured at 2-min intervals, and convert the density to the concentration by Eq. 8.4.

$$c_M = \frac{\rho_m \rho_p}{M_w (\rho_p - \rho_m)} \left(1 - \frac{\frac{1}{\rho_p} + \frac{k_I}{\rho_I}}{\frac{1+k_I}{\rho}} \right) \quad (8.4)$$

where, M_w (g/mol) is the molecular weight of the monomer, k_I is the mass ratio of the initiator to the monomer in the mixture, ρ_I (g/cm^3) is the density of the initiator, and ρ (g/cm^3) is the density of the reacting mixture.

Utilizing MagLev method, the initial rates of polymerization over the first 10 min are determined, as shown in Fig. 8.9. The Arrhenius activation energy of this polymerization can be estimated as 79 kJ/mol, which is coincident with the reported results (range from 62.0 to 84.9 kJ/mol).

Different from the thermal polymerization, photopolymerization of MMA allows direct monitor through MagLev device by levitating a single drop of monomer mixture. The monomer contains a hydrophobic photoinitiator of 2,2-dimethoxy-2-phenylacetophenone. The photopolymerization stimulates by irradiating the drop by a 365 nm UV light. The change in density $\Delta\rho$ is measured continuously as reaction proceeded. The verification of the expected behavior of pure MMA photopolymerization is carried out by continuous or periodic UV irradiation. The measured density can be converted to the fractional conversion of the monomer x using Eq. 8.5

$$x = \frac{\rho_m \rho_p}{\rho_p - \rho_m} \left[\left(\frac{1}{\rho_m} + \frac{k_2}{\rho_2} \right) - \frac{1+k_2}{\rho} \right] \quad (8.5)$$

The continuous photopolymerization with the UV light keep irradiating is drawn as the solid black spots in Fig. 8.10a. In the first 20 min, the rate of conversion increases slowly. Then the rate starts accelerating after 30 min, and finally reaches the equilibrium statue at ~ 60 min. This autoacceleration behavior in polymerization of MMA is a well-known effect: the Trommsdorff effect, or “gel effect” in short. This is due to the slowing down of the diffusion-limiting termination rate of radical—radical binding as the viscosity of the reaction mixture increases. When irradiating the monomer periodically (the UV switch on/off every 10 min), it can be seen that the polymerization is almost halted when the UV light is off. The residual polymerization during the dark period in gel region (50–60 and 70–80 min) suggests that the free radicals persist during the reaction. When doubling the dark period (20 min), the residual polymerization can still be observed in gel region (100–120 min and 130–150 min), as shown in Fig. 8.10b.

The average rate of polymerization can be described by the theoretical model as Eq. 8.6. The model combines three key steps of radical polymerization: radical initiation, propagation, and termination. The profile of UV absorption (i.e. Beer’s Law) as light passes through the mixture (sphere droplet) is also considered in the model.

$$\begin{aligned}
 -\frac{dc_m}{dt} &= k_p c_m \left(\frac{\alpha c_A \phi 10^3 I_0}{k_t} \right)^{0.5} \times \left[\frac{3}{\alpha [A] R} \left(\frac{1}{2} + \frac{e^{-\alpha c_A R}}{\alpha c_A R} + \frac{e^{-\alpha c_A R} - 1}{(\alpha c_A R)^2} \right) \right] \\
 &= K' k_p c_m \left(\frac{\alpha c_A \phi 10^3 I_0}{k_t} \right)^{0.5}
 \end{aligned} \tag{8.6}$$

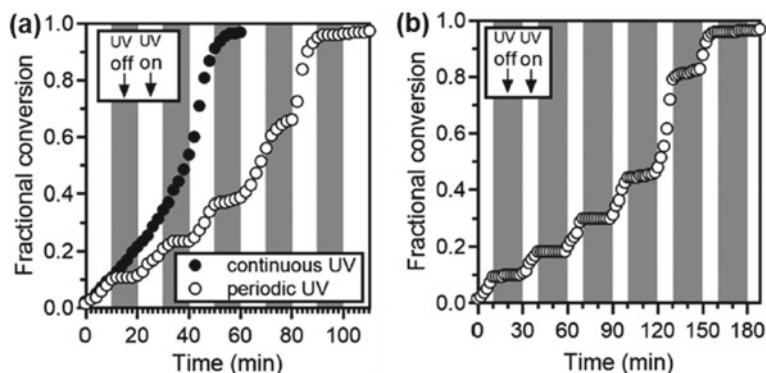


Fig. 8.10 Monitoring the progress of photopolymerization through MagLev. **a** The pure MMA with photoinitiator, 2,2-dimethoxy-2-phenylacetophenone (5 wt%) irradiated by a continuous (solid dots) or periodic (hollow dots, 10 min of dark period for every 10 min of irradiation) UV light (365 nm from a Hg lamp). **b** The photopolymerization irradiated using a periodic UV light with longer dark periods (20 min for every 10 min of irradiation). Reproduced with permission from Ref. [20]. Copyright 2017 American Chemical Society

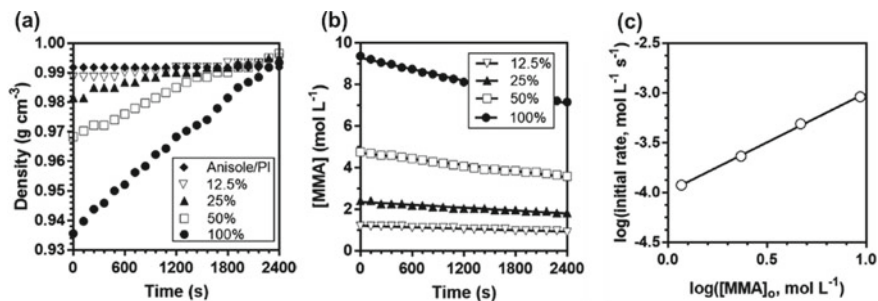


Fig. 8.11 Determination of the order of reaction for MMA in photopolymerization using MagLev. **a** The increase in the density of droplet contains MMA and photoinitiator (PI, 2,2-dimethoxy-2-phenylacetophenone, 0.27 wt%). **b** Calculated concentration of the monomer during the reaction. **c** Estimated initial rates of polymerization using the slopes of the linear fits in **(b)**. Reproduced with permission from Ref. [20]. Copyright 2017 American Chemical Society

In Eq. 8.6, k_p (L/mol s) is the rate constant for propagation, k_t (L/mol s) is the rate constant for radical termination, c_A (mol/L) is the concentration of initiator, R (m) is the radius of the mixture droplet, $\alpha = \varepsilon \ln 10$ (ε is molar absorptivity) is the absorption coefficient of A (L/mol cm), ϕ (unitless) is the quantum yield for initiation (the number of propagating chains initiated per light photon absorbed), and I_0 (mol/cm² s) is the incident light intensity at the surface of the drop. K' is the correction term that corrects the shape effect in absorbing UV light.

Under the condition of the same concentration of photoinitiator, the reaction order of monomers can be determined by measuring the initial polymerization rate of monomers with different concentration. The diluent is chosen as anisole. The density of the droplets is converted to concentrations of the monomer in the drops using Eq. 8.4. The result are plotted in Fig. 8.11. It can be observed that the monomer concentration changes with time are approximately linear in the initial 40 min. Therefore, the data in this range can be used to estimate the initial rate of polymerization. The slope of the linear fitted log–log curve of the initial rate and monomer concentration was 0.993, which indicated that the reaction order of MMA in the photopolymerization was ~ 1.0 .

References

1. Turnbull AG, Hull HS. A thermodynamic study of the dimerization of cyclopentadiene. *Aust J Chem.* 1968;21(7):1789–97.
2. Mirica KA, Shevkopyas SS, Phillips ST, et al. Measuring densities of solids and liquids using magnetic levitation: fundamentals. *J Am Chem Soc.* 2009;131(29):10049–58.
3. Shapiro ND, Mirica KA, Soh S, et al. Measuring binding of protein to gel-bound ligands using magnetic levitation. *J Am Chem Soc.* 2012;134:5637–46.
4. Koroznikova L, Klutke C, McKnight S, et al. The use of low-toxic heavy suspensions in mineral sands evaluation and zircon fractionation. *J South Afr Inst Min Metall.* 2008;108(1):25–33.

5. Grieve MC. Glitter particles—an unusual source of trace evidence? *J Forensic Sci Soc.* 1987;27(6):405–12.
6. Kirk PL. Density and refractive index. Their application in criminal identification. 1951.
7. Lockett MR, Mirica KA, Mace CR, et al. Analyzing forensic evidence based on density with magnetic levitation. *J Forensic Sci.* 2013;58(1):40–5.
8. Ash J, Hickey L, Goodpaster J. Formation and identification of novel derivatives of primary amine and zwitterionic drugs. *Forensic Chem.* 2018;10:37–47.
9. Amlani A, McKee G, Khamis N, et al. Why the FUSS (fentanyl urine screen study)? A cross-sectional survey to characterize an emerging threat to people who use drugs in British Columbia, Canada. *Harm Reduct J.* 2015;12(1):1–7.
10. Wang G, Huynh K, Barhate R, et al. Development of a homogeneous immunoassay for the detection of fentanyl in urine. *Forensic Sci Int.* 2011;206(1–3):127–31.
11. Philp M, Fu S. A review of chemical ‘spot’ tests: a presumptive illicit drug identification technique. *Drug Test Anal.* 2018;10(1):95–108.
12. Abrahamsson CK, Nagarkar A, Fink MJ, et al. Analysis of powders containing illicit drugs using magnetic levitation. *Angew Chem Int Ed.* 2020;59(2):874–81.
13. Hoogenboom R, Fijten MWM, Abeln CH, et al. High-throughput investigation of polymerization kinetics by online monitoring of GPC and GC. *Macromol Rapid Commun.* 2004;25(1):237–42.
14. Zoller P. Dilatometry. *Encyclopedia of Polymer Science and Technology*; 2002.
15. Martín O, Mendicuti F, Tarazona MP. Use of a reliable homemade dilatometer to study the kinetics of the radical chain polymerization of PMMA: an undergraduate polymer chemistry laboratory kinetics experiment. *J Chem Educ.* 1998;75(11):1479.
16. Dörwald Z. *Organic synthesis on solid phase.* Wiley VCH; 2002.
17. Cironi P, Álvarez M, Albericio F. A combination of different spectroscopic techniques to monitor the “in situ” solid-phase synthesis of organic molecules. *QSAR Comb Sci.* 2004;23(1):61–8.
18. Vazquez J, Qushair G, Albericio F. Qualitative colorimetric tests for solid phase synthesis. In: *Methods in enzymology.* Vol. 369. Academic Press; 2003, p. 21–35.
19. Mirica KA, Phillips ST, Shevkopyas SS, et al. Using magnetic levitation to distinguish atomic-level differences in chemical composition of polymers, and to monitor chemical reactions on solid supports. *J Am Chem Soc.* 2008;130(52):17678–80.
20. Ge S, Semenov SN, Nagarkar AA, et al. Magnetic levitation to characterize the kinetics of free-radical polymerization. *J Am Chem Soc.* 2017;139(51):18688–97.
21. Patel MP, Braden M, Davy KWM. Polymerization shrinkage of methacrylate esters. *Biomaterials.* 1987;8(1):53–6.
22. Lisensky GC, Campbell DJ, Beckman KJ, et al. Replication and compression of surface structures with polydimethylsiloxane elastomer. *J Chem Educ.* 1999;76(4):537.

Chapter 9

Magnetic Levitation in Medicine and Bioengineering



Chenxin Lyu, Chengqian Zhang, Daofan Tang, and Peng Zhao

9.1 Introduction

As one of the inherent characteristics of cell, density is a significant biomarker for the analysis and investigation of multiple cellular events. Density profiles of cell populations are informative data concerning physiological research such as differentiation, live-death assay, aging, immune response, or drug resistance [1]. The fast-speed, low-cost, and high-resolution measurement of single-cell level density plays a vital role in cell type recognition and detection of minute changes in cell properties, which indicates the cells' responses to the physical surroundings. Based on the density profiles of cell populations, further avalanche applications spanning over separation and sorting, manipulations, 3D cell culture, and point-of-care diagnosis are possible.

However, cell assay often faces many daunting challenges due to the low resolution, high cost, and manually intensive protocols [2]. A number of standardized methods have been developed for density measurement of cells, including ficoll gradient centrifugation [3], nanomechanical resonators [4], and dielectrophoretic field-flow fractionation [5]. These methods have certain drawbacks, like low accuracy, requiring priori knowledge of cell density, harmful to cells and time-consuming, thus hinder the development of density measurement at the single-cell level. Magnetic levitation, with its stunning advantages of high-resolution, untethered monitoring, fast-speed and low-cost as mentioned in the previous chapters, has unique potential in density-based analysis in fields of medicine and bioengineering.

C. Lyu · C. Zhang · D. Tang · P. Zhao (✉)

The State Key Laboratory of Fluid Power and Mechatronic Systems, College of Mechanical Engineering, Zhejiang University, Hangzhou, China

e-mail: pengzhao@zju.edu.cn

9.2 Single Cell Analysis

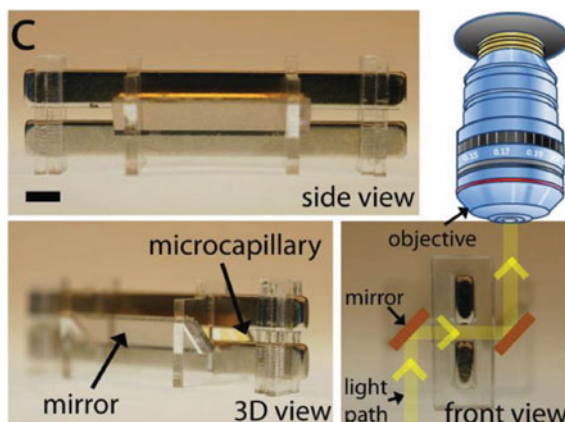
9.2.1 Design of the MagLev Platform for Density Profiling

Akin to the aforementioned macroscale diamagnetic samples in previous chapters, the millimeter-scale biological samples undergo the magnetic force (F_{mag}) and the buoyancy force (F_b), and when these two forces are equal, the measured biological samples reach the equilibrium position. In the MagLev density profiling platforms, the height of the equilibrium position can be directly measured under a microscope, and the corresponding density can be therefore calculated according to the numerical relationship between density and levitation height, regardless of the shape and size of individual cell. The measurement resolution and range can be changed by altering the concentration of the paramagnetic solution or the distance between the two magnets, while the time required for cells to reach the equilibrium position can also be affected.

Different from the density measurement of macroscale non-living samples in previous chapters, two prospects need to be considered when levitating, measuring or manipulating the microscale biological samples. The first is that due to their millimeter scale, the biological samples require stronger magnetic force to levitate compared with macroscale samples, therefore requiring higher magnetic gradient. To amplify the magnetic gradient, one solution is to scale down the macroscale MagLev configuration. The permanent magnets for microscale measurement are smaller than that for macroscale, with width and height under 10 mm, therefore maximizing the gradient they can offer [6]. Another is to reconstruct the configuration of the magnets, for example, the dual-Halbach configuration can offer stronger magnetic field and tunable sensitivity than non-Halbach configuration [7]. The second is that the paramagnetic solutions used in macroscale non-living measurement are proved toxic to living materials, as a result, the paramagnetic solutions need to be biological benign, creating a non-toxic environment conducive to the precise density measurement of living of cells and further cell culture. Common choices of biological benign paramagnetic solutions including Gd and FBS.

The most classic MagLev configuration-with two like-pole-facing cubic permanent magnets-has proved itself capable of analyzing the microscale matters by distinguishing differences in densities of polymer beads. The setup, containing two $5 \times 5 \times 2.5$ cm NdFeB magnets and a cuvette in between, was used to monitor chemical reactions on solid supports and measure changes in chemical composition of polymers [8]. Similarly, another well-established MagLev setup of macroscale density measurement and manipulation, the double ring configuration, have been altered and applied to the density measurement of cells. For example, the configuration with two N35 ring magnets of 4 mm outer radius and a glass tube through the holes was used to measure the densities of different cell clusters [6]. With two N50H ring magnets of 2.5 mm outer radius placed on both sides of a microfluidic chip, the pump-free characterization of cells' densities was realized [9]. The single ring MagLev have also been applied in density profiling of cells, where multiple cell types were levitated and transformed into 3D biological units [10].

Fig. 9.1 Design of the MagLev platform. Reproduced with permission from Ref. [11]. Copyright 2015 WILEY-VCH Verlag GmbH & Co. KGaA, Weinheim



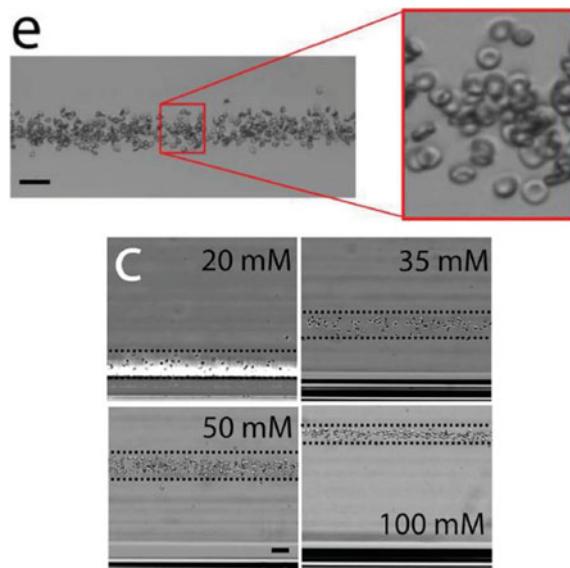
From the basic and classic configurations of magnetic levitation, the designs of biological MagLev platforms have evolved into other shapes and sizes, and in combinations with other technologies. One of the most widely applied single cell density measurement device is constructed with long bar magnets. As shown in Fig. 9.1, two rectangular like-pole-facing magnet bars fixed into a frame made of different materials, with a set or variable distance between them. A long, straight, transparent microcapillary channel, where the levitation happens, is sandwiched between the two magnets. And a pair of tilted mirrors stands beside the microcapillary channel for the observation and height measurement under a microscope. Paramagnetic solution, filled with to-be-measured biological samples, is pumped or injected through one end of the glass microcapillary.

The devices mentioned above usually need validation before measuring the actual biological samples. Off-the-shelf polyethylene beads in various sizes (from 10 to 100 μm) and densities are loaded into the device, and the levitation heights are recorded. The results can be fitted into the curve indicating the relationship between density and levitation height. The curves of different concentrations of Gd or of different distance can be the reference for calculation of the densities according to the measured levitation height. Figure 9.2 shows the image of levitating RBCs in the device, and the difference in levitation height in different concentrations of the solution.

9.2.2 Density Profiling

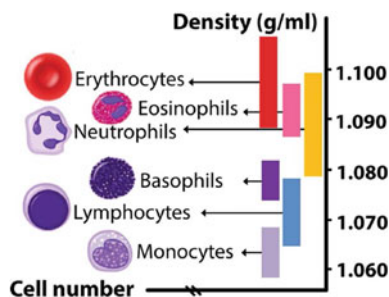
Similar to the calibration process, when the cells are loaded into the container, the individual cell reaches its stable levitation position within a few minutes. Under the microscope, it can be observed that each cell type forms a band, whose height can be directly measured. According to the difference in the height of cell bands,

Fig. 9.2 The levitation of RBCs at different Gd^{+} solution. Reproduced with permission from Ref. [11]. Copyright 2015 WILEY-VCH Verlag GmbH & Co. KGaA, Weinheim



different cell types can be therefore distinguished and separated, and the densities of each cell band can be calculated (Fig. 9.3). In Durmus's work [1], various mammalian cells including Breast adenocarcinoma (MDA-MB-231), esophageal adenocarcinoma (JHEsoAD1), colorectal adenocarcinoma (HT29), colorectal carcinoma (HCT116), and nonsmall cell lung adenocarcinoma (HCC827) cell lines and some blood cells were chosen as samples for distinguish and measurement experiment. The cells were surrounded by FBS with 30 mM paramagnetic Gd solution. In the levitated bands of cells, the densities of the cells can be measured individually, and a scatter plot describing the densities and cell size of each cell can be obtained as the density profile. Many single-cell level analyses are possible based on this density profile. In Durmus's work, the density distributions of red and white blood cells were also measured and found to be within the reported ranges in the literature, which validated the theory and experimental setup of the single cell MagLev [1]. The levitation platform used in the study was able to distinguish rare circulating tumor cells (CTCs) from whole blood, which could deepen the understanding of cancer metastasis and improve monitoring and treatment of cancer patients. The study also observed heterogeneity within seemingly homogenous cell populations, and different colorectal cancer cells from different origins had distinct density profiles, where the MDA-MB-231 cell line was found to have the most heterogeneous cancer cell population among various cancer cell populations, with a density variance of $0.0003 \text{ (g mL}^{-1}\text{)}^2$. These findings highlight the potential of using cell density measurements to characterize different cell types, including cancer cells, and to understand the heterogeneity within seemingly homogenous cell populations. Furthermore, the heterogeneity of breast cancer and how the levitation-based density profiling approach can be used to investigate multiple cell types without using any labels or external energy sources.

Fig. 9.3 The density profile of different cells. Reproduced with permission from Ref. [11]. Copyright 2015 WILEY-VCH Verlag GmbH & Co. KGaA, Weinheim



9.2.3 Real-Time Monitoring and Analysis of Cells

The MagLev platform can also be used in real-time monitoring of the cells. When the cells are exposed to harmful surroundings in a certain period of time, such as acidic conditions, the cells are possibly affected and its density information change correspondingly. Therefore, the dynamic change of the cell's density indicates the state of the cell. Due to the high resolution of the magnetic levitation, the monitoring of single cell's density is possible. One common demonstration is the live-dead assay, where the dead cells killed by the altered environmental factors become denser and are separated in height with the living ones. With the help of fluorescent markers, like calcein and propidium iodide, the real-time change of cell viability as well as the levitation height is more straightforwardly shown, where the dying cells become denser and sank to the bottom of the microtube as they turn from green to red. The MagLev platform can detect that changes in cell density preceded the onset of changes in fluorescence, and that dead cells yielded a more heterogeneous density profile than live cells.

The density profiling approach based on magnetic levitation offers a potent tool for studying the dynamic alterations in cellular levitation and density patterns amidst varying environmental conditions. This method provides valuable insights into how individual cells respond to stress and environmental changes. An intriguing application of this platform involves the swift detection of changes in levitation and density profiles of bacteria exposed to various antibiotic treatments. In Durmus's work, the authors noted that antibiotics with distinct mechanisms of action exhibited varied effects on bacterial levitation and density profiles. This correlation suggests that alterations in cellular levitation height and density might be linked to the effectiveness of drug treatments [1]. Consequently, this platform shows promise for potential use in antimicrobial susceptibility testing.

9.3 Diseases Diagnosis

Due to its unique merits of precise, fast-speed, in-real-time profiling of cells' density, magnetic levitation comes in handy with various applications further than single cell analysis. The low-cost, energy-free and easy-to-assemble MagLev configuration shows capability in detecting and separating critical biomarkers involved in disease progression from their complex environments, which has great potential in diagnostic processes. MagLev can also rapidly identify and discriminate a variety of biomolecules as they experience various physiological conditions in a biological complex and consequently change density, including drug screening in personalized medicine. MagLev can furthermore detect changes in the density of biomolecules in certain diseases, creating a point-of-care device for diagnostic purposes.

There is a growing preference for miniaturized diagnostic devices due to their rapid, cost-effective, portable, and user-friendly nature. These devices enable quick disease identification and provide people with prompt information about their health status. Conventional diagnostic tools primarily depend on immune-specific interactions to separate and capture targets from complex media, which can complicate the detection processes in terms of cost-effectiveness, durability, and analysis time [12]. MagLev has the potential to become a diagnostic tool for detecting diseases or specific biomarkers associated with certain conditions. By analyzing the density differences in biological samples, the system may be able to identify disease-specific patterns or markers that can aid in early detection and monitoring of diseases.

9.3.1 Cancer

The stiffness of the extracellular matrix (ECM) plays a significant role in influencing the malignancy and invasiveness of cancer cells [13]. The ECM is a complex network of proteins and other molecules that provide structural support to tissues and organs. Besides its structural function, the ECM also serves as a dynamic signaling platform that communicates with cells and influences their behavior, including proliferation, migration, and differentiation. Cancer cells, like normal cells, can sense and respond to these mechanical cues transmitted from the ECM, and alterations in ECM stiffness can have profound effects on cancer progression. Density, as one of the properties of cells, is also affectable by these alterations. Based on the changes of the density profiles, the cancer cells can be detected, characterized and analyzed on the MagLev platform.

In order to sort out the circulating tumor cells (CTCs) from the flow of samples, the MagLev setup serves as a label-free microfluidic sorter, where the CTCs are extracted from blood cells according to the difference in density. As CTCs are signals of secondary cancers, the MagLev platform can be applicable as risk assessment for secondary cancers [14]. MagLev has great potential in combining with other technologies in diagnosis. For example, portable devices such as smartphone can

become a helpful tool in real-time detection and image analysis, making the device more portable and easier to operate as well. A fully automated MagLev platform with Label-Free Digital Holographic Microscopy (LDIHM) was developed to separate three different cell lines (breast cancer cells MDAMB-231, bone marrow stem cells D1 and monocytes U937) from their deceased counterparts. As shown in Fig. 9.4, The imaging process utilized interferometry, where undistorted incoming light and diffracted light from the sample combined at the sensor to create an interference (hologram) pattern [15]. The results are shown in Fig. 9.5.

A more advanced smartphone-based MagLev system was designed and utilized. The system comprised a custom-designed 3D printed case to hold the smartphone, an aspheric lens with a numerical aperture of 0.64 mm and a diameter of 6.33 mm, a capillary tube, two NdFeB magnets ($50.8 \times 2 \times 5$ mm), LEDs with different colors, emission filters for dark-field and bright-field imaging modes, and electronic components for exchanging emission filters. The whole device is notably light and portable with a total weight of the system of 214 g, and only \$105.87 to construct. For evaluation purposes, microspheres with diameters ranging from 5.35 to 79 μm were

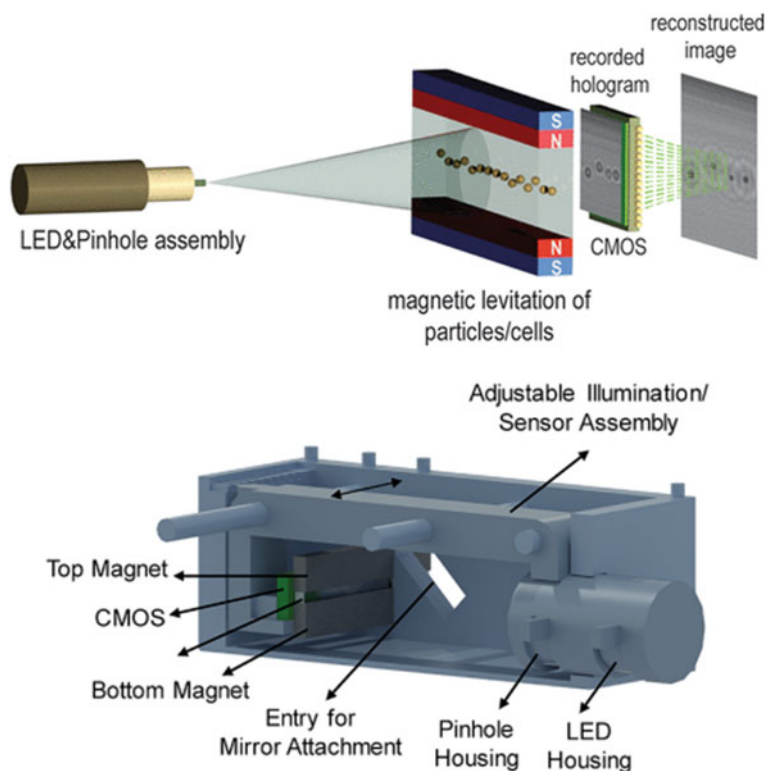
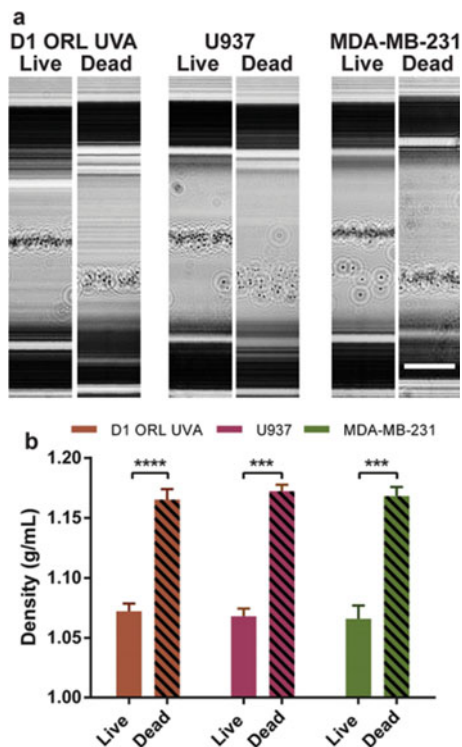


Fig. 9.4 Experimental setup. Reproduced with permission from Ref. [15]. Copyright 2021 American Chemical Society

Fig. 9.5 Live-dead assay of different cell lines.

Reproduced with permission from Ref. [15]. Copyright 2021 American Chemical Society



introduced into a 100 mM paramagnetic solution and placed in the capillary tube. The setup's performance was assessed, and it was noted that imaging the sample in both bright mode and dark mode yielded similar results, demonstrating the device's ability to capture cell-sized beads accurately. This device also achieved optimal contrast with matching colors of emission filter, RGB channel, and microspheres. Various biological applications have proved the capability of the system, including cell counting and concentration determination, using breast cancer cells cultured and stained with calcein at five different concentrations. Remarkably, the concentration of cancer cells could be accurately measured with just 10 μL of the sample, eliminating the need for large sample volumes from patients [16].

9.3.2 Sickle-Cell Disease

As mentioned before, biomolecules frequently hold vital information about pathological changes, and density variations often reflect these processes. For instance, sickle-cell disease (SCD) exhibits distinct density differences between sickled and normal erythrocytes, making the MagLev system an ideal point-of-care diagnostic

device for this condition. The 3D printed smartphone-based MagLev is useful in the diagnostic process of the sickle-cell disease, which is capable of separate the denser sickle cells from normal ones with a rather limited volume of blood sample. Analysis of smartphone images revealed that healthy (control) red blood cells (RBCs) levitated at higher heights and exhibited a narrower height distribution. On the other hand, sickle cells displayed a lower levitation height and a wider range of distribution. Microscope-acquired images further confirmed the device's efficacy in effectively sorting sickle cells [17]. The MagLev device is also an economical and rapid solution to the diagnosis of SCD. The device costs only \$100 to build, and the separation only costs 15 min. Under the different concentration of the paramagnetic medium, polystyrene microspheres and RBCs levitated at heights of 35 μm and 110 μm , respectively. This demonstrates the capability of the self-contained MagLev system to effectively levitate and analyze blood samples for diagnosing sickle cell disease (Fig. 9.6). Additionally, the study reported that using lower concentrations of the paramagnetic medium led to higher detection resolution, enabling the detection of subtle density changes more effectively [18].

9.3.3 Blood Analysis

Bounding with smart devices, magnetic levitation is a powerful weapon in analysis of blood samples. The accurate, label-free and low-cost detection of MagLev combined with extraordinary image acquisition and smart analyzation capability of smartphones, offers a novel solution to the portable, user-friendly analysis of samples and point-of-care diagnostic devices. To levitate, separate and quantify red blood cells (RBCs) and white blood cells (WBCs), a smartphone-based MagLev diagnostic system (i-LEV) was designed based on the N52 bar magnets configuration. PE beads, RBCs and WBCs were loaded between the bar magnets, where the RBCs were successfully quantified, and the trapping of single RBCs was realized. The smartphone serves as autofocus to adjust the focal plane, and as terminal to analyze or share the results [19].

Another similar MagLev system integrated with smartphone has been developed to identify both soluble and membrane-bound antigens present in blood samples. The MagLev platform has demonstrated its effectiveness in detecting a range of infectious diseases, including HBV, EBV, HIV, HAV, Dengue, Zika, and Chikungunya. Additionally, the system successfully identified specific antigens like T-cell antigen CD3, RBC antigens CD35 and RhD, eosinophil antigen Siglec-8, soluble Il6, and RBC-bound Epstein-Barr viral particles. The accuracy of this detection approach was confirmed through immunofluorescence microscopy. This smartphone-based setup exhibits capability for detection, screening, and quantification of various blood pathogens and antigens, especially in resource-constrained environments [20].

In the context of identifying sepsis patients, the utilization of MagLev technology enabled the measurement of circulating leukocytes' size, morphology, and magnetic characteristics. The findings revealed a significantly larger average cell area in pixels

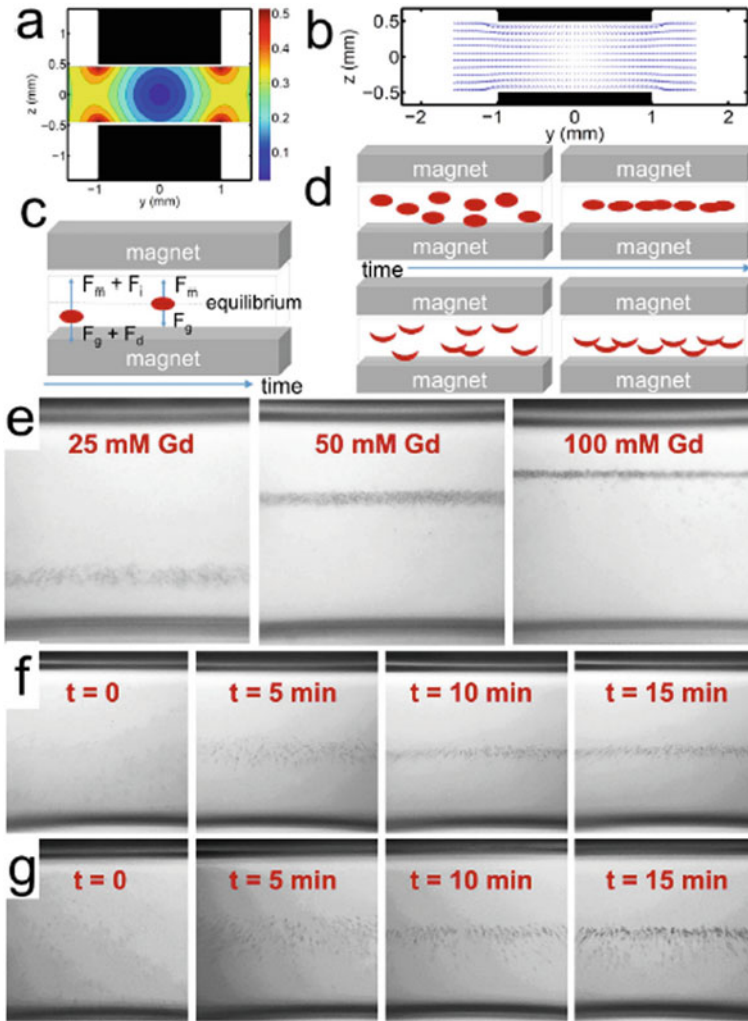


Fig. 9.6 Separation of different sickle cells. Reproduced with permission from Ref. [17]. Copyright 2015 Scientific Reports

(px) for infected individuals in comparison to non-infected controls. Specifically, the median levitation height of circulating leukocytes was assessed for 22 septic patients and 39 non-infected control patients. The results indicated that the levitation height measured 293.1 ± 61.4 px for septic patients and 288.8 ± 23.7 px for the control group. This outcome underscored the consistent and reliable classification capability of the MagLev platform [21].

9.4 3D Self-assembly

Under the effect of magnetic forces in magnetic levitation, living cells are possible to be manipulated on both the cellular and tissue levels.

Magnetic manipulation systems of varying complexity have been developed to achieve diverse biotechnological objectives, such as the spatial arrangement of cells within 2D or 3D cultures. Magnetic forces in different orientations are capable of guiding 3D self-assembly processes. Utilizing magnetic interactions for 3D self-assembly is a highly convenient method as it allows objects to be influenced by magnetic forces from a distance, eliminating the need for physical contact or marking and labeling.

Many assembly techniques rely on the use of scaffolds or support materials, which can be a limiting factor, especially in tissue engineering and regenerative medicine applications. To address this limitation, the MagLev approach encourages cells to secrete their own extracellular matrix (ECM) without the need for any additional materials, facilitating the formation of a natural and self-supported 3D structure. By eliminating the dependency on external scaffolds, this technique offers a promising solution for advancing tissue engineering and regenerative medicine approaches, providing a more authentic and physiologically relevant environment for cell growth and tissue development.

9.4.1 *Self-assembly of Multilayered Structures*

Researchers have investigated how the shape and density of PMMA templates influence the formation of complex 3D models. By designing co-levitating PMMA templates, they have ensured that spherical PMMA objects form alternative 3D lattices and structures [12]. The co-levitating templates provide a framework for the levitating objects to arrange in an ordered structure, preventing them from dispersing into disordered positions without forming clusters. Depending on the co-levitating PMMA templates used, various forms of lattices and structures can be obtained. Frames with different shapes (e.g., rectangular, triangular, and circular) but the same density as the objects enable the objects to pack into the frame in 3D fashion. Alternatively, levitating objects can encircle the surfaces or edges of the co-levitating templates. Diamagnetic objects can be guided in a magnetic field, leading to the formation of 3D assemblies depending on density differences. Magnetic levitation technology allows the formation of 3D structures by aligning, positioning, and self-assembling components without the need for physical handling. Consequently, the development of magnetic levitation and contactless manipulation contributes not only to the advancement of research in various fields but also to the progress of other areas such as tissue engineering and diagnostic tools [22].

9.4.2 3D Cell Culture

The proof-of-concept demonstrations of assembly of non-living objects can be expanded to applications to bioengineering. 3D cell cultures offer a more accurate representation of cell behavior *in vivo* compared to 2D cultures, particularly concerning drug sensitivity, signaling pathway activity, gene expression profiles, and cell–cell and cell–matrix interactions. Traditional 3D cell culturing typically follows a top-down approach, where cells are seeded into a porous scaffold to form the desired tissue. Alternatively, the bottom-up or modular approach involves assembling small modules of cells with the aid of modular scaffolds to create large tissues, overcoming limitations like low cell density, restricted diffusion, and slow vascularization.

However, the use of scaffolds in 3D cell culturing has some drawbacks, including the inhomogeneity of cells within the scaffold, the need for scaffold synthesis and sterilization, and the limited selection of biocompatible materials. Another emerging technique is 3D bioprinting, which enables the rapid prototyping of complex, perfusable 3D bioconstructs, ranging from organ-on-chip models to full-scale organs. Nevertheless, challenges remain in retaining cell viability during the bioprinting process, as high shear stress or intense light exposure can be detrimental to cell health.

The magnetic levitation (MagLev) platform was designed to facilitate scaffold-free 3D cell cultures. The setup included two $2 \times 2 \times 20$ mm magnets with approximately 0.4 T magnetic field strength, an inverted microscope, and mirrors. Instead of using magnetic nanoparticles (MNPs), the cells were magnetized using three different types of chelates of gadolinium (III) paramagnetic agents: gadobutrol, gadoteric acid, and gadodiamide. Two different cell types, NIH 3T3 mouse fibroblast cells, and HCC827 non-small cell lung cancer cells, were separately used to investigate the platform's ability to create desired 3D structures [23]. Evaluating the gadolinium (III) chelates, gadobutrol showed the highest cell viability compared to the other two chelates, mainly due to its low toxicity, which facilitated cell interactions. Additionally, the growth rate of cells (number of cells per time) in the MagLev-based culture was compared to conventional 2D culture. The results indicated an exponential growth for 3D culture and a linear growth for standard 2D culture.

In a similar setup, 3D cell cultures of bone marrow stem cells and breast cancer cells were performed using a different paramagnetic medium. It was reported that utilizing macrocyclic ligand-containing agents (Gd-BT-DO3A and Gd-DOTA) resulted in higher cell viability compared to linear ligand-containing agents [24].

9.4.3 Fabrication of 3D Cellular Structures

As shown in Fig. 9.7, Another setup was employed to investigate the effects of paramagnetic medium concentration, culture time, and cell seeding density on 3D cell culturing using mouse fibroblast cells and five different types of cancer cells (HeLa

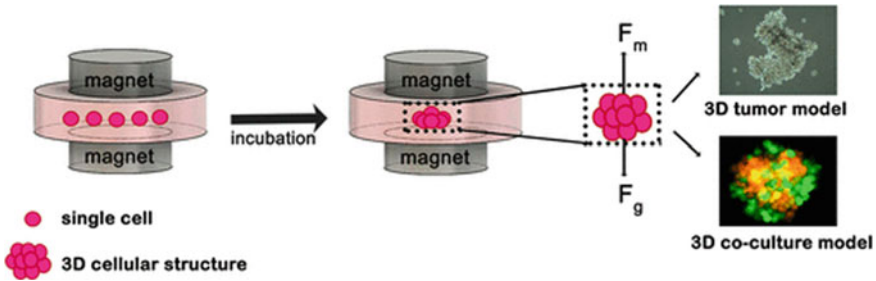


Fig. 9.7 Fabrication of 3D cellular structures via magnetic levitation guided assembly. Reproduced with permission from Ref. [25]. Copyright 2021 American Chemical Society

human epithelial cervix adenocarcinoma, PC-12 rat adrenal gland pheochromocytoma, SH-SY5Y human bone marrow neuroblastoma, MDA-MB-231 human epithelial breast adenocarcinoma, and MCF7 human epithelial breast adenocarcinoma). It was found that the circularity, area, and size of the spheroids could be controlled by manipulating cell culturing time, paramagnetic agent concentration, and cell seeding density [25]. Moreover, a higher concentration of paramagnetic medium (100 mM) led to a larger area and faster co-culture assembly. However, increasing the cell seeding density resulted in decreased cell viability below 50%. This was attributed to limited nutrient and oxygen diffusion inside the spheroid, leading to insufficient mass transport and the accumulation of metabolic waste. Despite this, the platform still provided an easy-to-use and low-cost method for forming 3D cell cultures, making it suitable for applications such as 3D bioprinting, regenerative medicine, and drug screening.

In another study, MagLev was utilized to culture a scaffold-free 3D breast cancer model *in vitro* to investigate various cell interactions and the impact of the tumor microenvironment on drug efficacy. Applying the chemotherapy drug doxorubicin (100 nM) to the coculture of cancer cells and fibroblasts resulted in an 80% and 45% decrease in the area and density of the cancer cell culture, respectively. These results closely resembled *in vivo* findings, demonstrating the suitability of MagLev cell cultures for cancer drug studies. Moreover, to study the effects of fibroblast content on drug penetration into tumors, different ratios of breast tumor cells and fibroblasts were examined, showing that a lower percentage of fibroblast cells resulted in approximately 10% higher drug penetration [26].

9.5 Tissue Engineering and Bio-fabrication

Magnetic levitation technology has been utilized to showcase its potential for culturing cells in a 3D microenvironment. While there are other approaches available, such as bioreactors, microfluidics, stereolithography, and more [12], for tissue engineering, many of these methods primarily focus on material development. In contrast,

magnetic levitation offers a unique and promising approach that enables the creation of scaffold-free 3D cell cultures, providing a more physiologically relevant environment for studying cell behavior and tissue development. In tissue engineering, the focus is shifting towards innovative methodologies that can create 3D cellular structures by mimicking the natural microenvironment rather than solely relying on developing new materials. The ultimate goal is to create functional tissues that can integrate seamlessly with the host's biological systems.

Achieving functional tissues requires not only the proper arrangement of cells but also establishing essential cell–cell and cell-ECM interactions within the 3D structure. These interactions play a crucial role in enabling tissues to function as intended. Despite considerable efforts in tissue engineering, challenges remain in guiding cells into complex 3D structures and creating the required physical force environment. Overcoming these obstacles is essential to improve the success and efficacy of tissue engineering approaches and to advance the field toward more functional and clinically relevant tissue constructs. Ongoing research and innovative technologies, such as magnetic levitation and other 3D cell culture techniques, are promising avenues to address these challenges and drive progress in tissue engineering.

9.5.1 MagLev Tissue Engineering Techniques

Recently, a magnetic tissue engineering technique called Mag-TE (Magnetic Tissue-Engineering) has been reported for the formation of artificial skeletal muscle tissue. In this approach, the generation of string or ring-shaped tissue structures mimicked the fiber bundles of skeletal muscle. Magnetite cationic liposomes (MCLs) were used as a magnetic agent, and Myoblast C2C12 cells were preloaded with MCLs before applying the magnetic force [27]. The cells were then seeded onto a magnetic concentrator where a magnet was located underneath, leading to the formation of both cell strings and cell rings through cell agglomeration without the use of any scaffold. Cell sheets and cell strings were successfully obtained in the desired shape and thickness (approximately 200 μm). However, during further culture periods for myogenic differentiation, these constructs experienced shrinkage and lost their initial shapes.

In another study, a bioinorganic hydrogel system with magnetic properties, based on M13 phages, was introduced to mimic irregular tumor formations through coculturing. This system provided a controlled approach, demonstrating the formation of 3D in vitro tumor structures with varying sizes and compositions. Not only did this model control 3D cell culture formation, but it also facilitated spheroid fusion. By magnetically guiding human glioblastoma cell spheroids and human astrocyte cell spheroids together, spheroid fusion was achieved within 12 h. This magnetic levitation system was further extended to a well-plate format, allowing for easier and more controlled tissue formation. The use of poly-l-lysine cross-linked MIO/AuNp hydrogels, termed NanoShuttle, acted as a magnetizing agent for the 3D cell culture formation. The technique was successful with various cell lines,

including human embryonic kidney cells (HEK293), mouse fibroblast cells (3T3-L1), human mammary epithelial (MDA-231), human umbilical vein endothelial cells (HUVECs), and human hepatocyte cells (HepG2). All varied cell lines formed 3D cell cultures, with some forming denser and smaller structures based on their cellular characteristics, while others produced less dense and sparse structures [12].

9.5.2 Modeling of Organs

Apart from creating 3D cultures of cells and tumors, MagLev can also be used to model body organs (Fig. 9.8). For example, an aortic valve was cultured for three days in a MagLev platform using valvular interstitial cells (VICs) and valvular endothelial cells (VECs). It was reported that the phenotype was preserved, as the aortic valve cocultures (AVCCs) stained positive for CD31 and α -smooth muscle actin (α SMA). Gene expression for collagen type I, laminin, and fibronectin proteins decreased in 3D compared to 2D, while extracellular matrix components still stained positive.

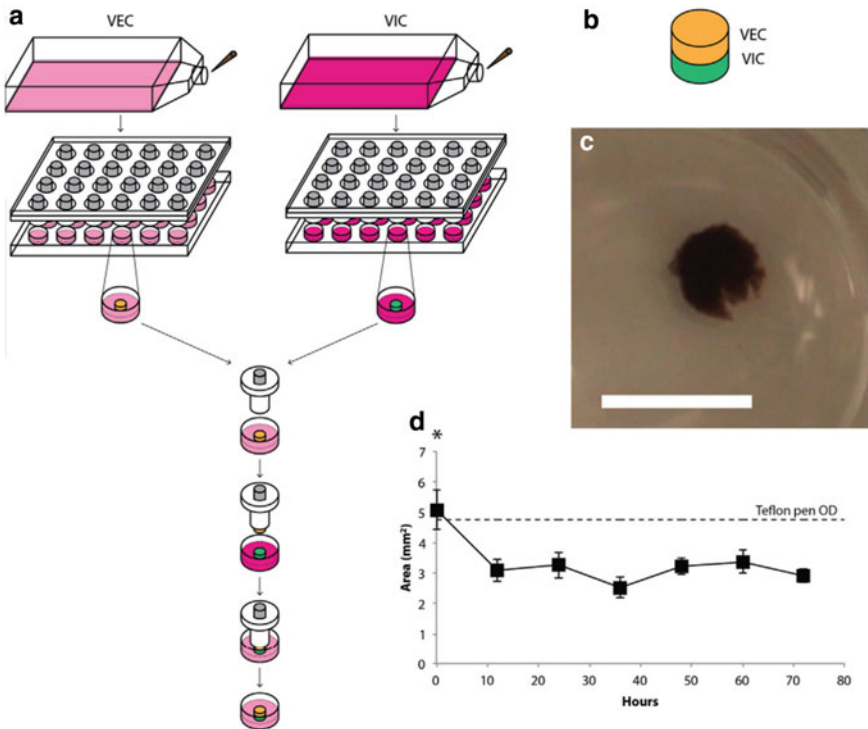


Fig. 9.8 Schematic of co-culture assembly using magnetic levitation. Reproduced with permission from Ref. [28]. Copyright 2013 Acta Materialia Inc.

The AVCCs had a thickness of approximately 500 μm after culture, suggesting their potential use in mechanobiology and the study of calcific aortic valve disease progression [28].

In conclusion, the magnetic levitation approach proves to be a versatile and valuable tool in 3D cell culture formation and various tissue engineering applications, offering a controlled and efficient approach for mimicking complex biological structures.

References

1. Durmus NG, Tekin HC, Guven S, et al. Magnetic levitation of single cells. *Proc Natl Acad Sci*. 2015;112(28):3661–8.
2. Icha J, Nedbal J, Leavesley S, et al. Phototoxicity in live fluorescence imaging understanding, quantifying and minimizing it. *Cytometry A*. 2019;95(6):634–6.
3. Grover WH, Bryan AK, Diez-Silva M, et al. Measuring single-cell density. *Proc Natl Acad Sci*. 2011;108(27):10992–6.
4. Burg TP, Godin M, Knudsen SM, et al. Weighing of biomolecules, single cells and single nanoparticles in fluid. *Nature*. 2007;446(7139):1066–69.
5. Shim S, Gascoyne P, Noshari J, et al. Dynamic physical properties of dissociated tumor cells revealed by dielectrophoretic field-flow fractionation. *Integr Biol*. 2011;3(8):850–62.
6. Lyu C, Tang D, Zhang C, et al. Magnetic levitation for non-contact manipulation and measurement of cells. *Sens Actuators B Chem*. 2023;385:133692.
7. Gao QH, Yan G, Zou HX, et al. Density-based measurement and manipulation via magnetic levitation enhanced by the dual-Halbach array. *IEEE Sens J*. 2019;20(4):1730–7.
8. Mirica KA, Phillips ST, Shevkoplyas SS, et al. Using magnetic levitation to distinguish atomic-level differences in chemical composition of polymers, and to monitor chemical reactions on solid supports. *J Am Chem Soc*. 2008;130(52):17678–80.
9. Gao QH, Wen B, Kang Y, et al. Pump-free microfluidic magnetic levitation approach for density-based cell characterization. *Biosens Bioelectron*. 2022;204:114052.
10. Anil-Inevi M, Delikoyun K, Mese G, et al. Magnetic levitation assisted biofabrication, culture, and manipulation of 3D cellular structures using a ring magnet based setup. *Biotechnol Bioeng*. 2021;118(12):4771–85.
11. Tasoglu S, Khoory JA, Tekin HC, et al. Levitational image cytometry with temporal resolution. *Adv Mater*. 2015;27(26):3901–8.
12. Turker E, Arslan-Yildiz A. Recent advances in magnetic levitation: a biological approach from diagnostics to tissue engineering. *ACS Biomater Sci Eng*. 2018;4(3):787–99.
13. Baday M, Ercal O, Sahan AZ, et al. Density based characterization of mechanical cues on cancer cells using magnetic levitation. *Adv Healthcare Mater*. 2019;8(10):1801517.
14. Ashkarran AA, Mahmoudi M. Magnetic levitation systems for disease diagnostics. *Trends Biotechnol*. 2021;39(3):311–21.
15. Delikoyun K, Yaman S, Yilmaz E, et al. HologLev: a hybrid magnetic levitation platform integrated with lensless holographic microscopy for density-based cell analysis. *Acs Sensors*. 2021;6(6):2191–201.
16. Knowlton S, Joshi A, Syrrist P, et al. 3D-printed smartphone-based point of care tool for fluorescence-and magnetophoresis-based cytometry. *Lab Chip*. 2017;17(16):2839–51.
17. Knowlton SM, Sencan I, Aytar Y, et al. Sick cell detection using a smartphone. *Sci Rep*. 2015;5(1):15022.
18. Yenilmez B, Knowlton S, Yu CH, et al. Label-free sickle cell disease diagnosis using a low-cost, handheld platform. *Adv Mater Technol*. 2016;1(5):1600100.

19. Baday M, Calamak S, Durmus NG, et al. Integrating cell phone imaging with magnetic levitation (i-LEV) for label-free blood analysis at the point-of-living. *Small*. 2016;12(9):1222–9.
20. Andersen MS, Howard E, Lu S, et al. Detection of membrane-bound and soluble antigens by magnetic levitation. *Lab Chip*. 2017;17(20):3462–73.
21. Andersen MS, Lu S, Lopez GJ, et al. A novel implementation of magnetic levitation to quantify leukocyte size, morphology, and magnetic properties to identify patients with sepsis. *Shock (Augusta, Ga.)*. 2019;51(2):147.
22. Mirica KA, Ilievski F, Ellerbee AK, et al. Using magnetic levitation for three dimensional self-assembly. *Adv Mater*. 2011;23(36):4134–40.
23. Türker E, Demirçak N, Arslan-Yildiz A. Scaffold-free three-dimensional cell culturing using magnetic levitation. *Biomater Sci*. 2018;6(7):1745–53.
24. Anil-Inevi M, Yaman S, Yildiz AA, et al. Biofabrication of in situ self assembled 3D cell cultures in a weightlessness environment generated using magnetic levitation. *Sci Rep*. 2018;8(1):7239.
25. Onbas R, Arslan YA. Fabrication of tunable 3D cellular structures in high volume using magnetic levitation guided assembly. *ACS Appl Bio Mater*. 2021;4(2):1794–802.
26. Jaganathan H, Gage J, Leonard F, et al. Three-dimensional in vitro co-culture model of breast tumor using magnetic levitation. *Sci Rep*. 2014;4(1):6468.
27. Xie J, Zhao P, Zhang C, et al. Current state of magnetic levitation and its applications in polymers: a review. *Sens Actuators B Chem*. 2021;333:129533.
28. Tseng H, Balaoing LR, Grigoryan B, et al. A three-dimensional co-culture model of the aortic valve using magnetic levitation. *Acta Biomater*. 2014;10(1):173–82.

Chapter 10

Manipulation via MagLev



Daofan Tang, Chengqian Zhang, Zhezai Hu, and Peng Zhao

10.1 Introduction

The magnetic levitation method, characterized by its simplicity, absence of sample magnetization requirements, and convenient operation, has found extensive applications not only in fields such as chemical analysis, biological measurements, and performance characterization but also in the non-contact manipulation of small-sized weakly magnetic materials. The ability to manipulate samples, whether at macroscopic, mesoscopic, or microscopic scales, forms the foundation and key to scientific research and development. In recent years, non-contact manipulation and performance characterization techniques for various materials have gained popularity due to the potential impact of physical contact-based clamping tools on the surface morphology or properties of materials. Consequently, theoretical research and technological applications related to non-contact manipulation have experienced significant advancements. Currently, several forms of non-contact manipulation techniques are available for the manipulation of small-sized samples or structures. These include the use of dielectrophoresis for manipulation and separation of different micro-sized samples [1–3], optical tweezers for the manipulation of micro-particles [4–6], acoustic standing wave-based control for rapid and precise control of cells [7–10], and magnetic manipulation techniques for remote control of magnetic materials, structures, or magnetically labeled particles [11–13], among others. These techniques have greatly contributed to the manipulation and characterization of small-sized samples. However, they still possess certain limitations and drawbacks. For instance, dielectrophoresis manipulation techniques may induce sample polarization due to the requirement for an electric field. Optical tweezers face challenges when working in opaque media and require strict environmental, sample, and equipment

D. Tang · C. Zhang (✉) · Z. Hu · P. Zhao
The State Key Laboratory of Fluid Power and Mechatronic Systems, College of Mechanical Engineering, Zhejiang University, Hangzhou, China
e-mail: zhangcq@zju.edu.cn

conditions, along with extensive calibration. Moreover, the high energy density at the optical focus may lead to temperature elevation and potential thermal damage during continuous operations [14]. Acoustic surface wave-based manipulation techniques are limited by the compressibility differences between samples, and their sensitivity and effectiveness still need improvement. Magnetic manipulation techniques are constrained by the magnetic response characteristics of the samples, requiring the use of ferromagnetic samples or samples with completed magnetic labeling, thereby increasing the complexity of the procedures and potentially inducing changes in the sample's properties. As a novel non-contact manipulation method that allows stable capture, movement, and levitation of samples within a gradient static magnetic field, magnetic levitation cleverly exploits the difference in magnetic susceptibility between weakly magnetic samples and the surrounding medium. It does not necessitate complex detection, feedback control processes, or circuit structures. In recent years, magnetic levitation has become an important research topic for non-contact manipulation and performance characterization of small-sized weakly magnetic samples.

The non-contact manipulation of micro-sized samples is fundamental for further characterization and testing, and it is essential in the development of modern scientific and technological advancements. For instance, in fields such as life sciences, deep Earth exploration, and deep-sea research, the ability to capture, transport, and separate micro-sized particles in enclosed or extreme environments enables precise and controlled manipulation of these particles, as well as characterization of their mechanical properties under extreme conditions. The development of such techniques helps to fill the gap in traditional material characterization methods for detecting micro-sized samples in enclosed or extreme environments [15]. This chapter provides a comprehensive review of the current researches on Maglev based manipulation methods, starting with fundamental principles for Maglev based non-contact manipulation techniques. Furthermore, an analysis is conducted to evaluate the advantages and disadvantages of existing magnetic levitation methods as a novel non-contact magnetic manipulation technique.

10.2 Manipulation Principles

The fundamental principle of the Maglev based manipulation method is to construct a potential well using a magnetic field and trap the sample at the position where satisfies the condition of the potential energy being at a local minimum when subjected to the combined effects of the gravitational field and the magnetic field (Fig. 10.1). In the context of particle and cell manipulation in paramagnetic salt solutions or ferrofluids under weak magnetic fields, it is important to consider the magnetizations of both the body and the magnetic liquid [16].

The magnetic force, under a weak field approximation, can be described by Eq. 10.1, which is commonly referenced in the literature.

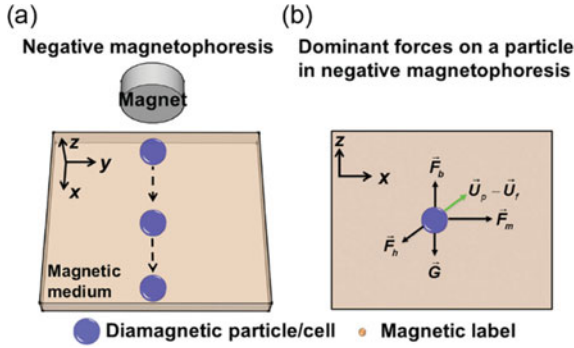


Fig. 10.1 **a** Negative magnetophoresis—magnetization of diamagnetic particles/cells is less than its surrounding medium; particles/cells move towards the location of field minima when a magnetic field is applied. **b** Dominant forces include magnetic force \vec{F}_m , hydrodynamic drag force \vec{F}_h , gravitation force \vec{G} , and buoyancy force \vec{F}_b on a particle in negative magnetophoresis. \vec{U}_p is the velocity of the particle and \vec{U}_f is the velocity of the medium flow. Reproduced with permission from Ref. [16]. Copyright 2016 Wiley

$$\vec{F}_{\text{mag}} = \frac{(\chi_p - \chi_m)V}{\mu_0} (\vec{B} \cdot \nabla) \vec{B} \tag{10.1}$$

When manipulating particles and cells in ferrofluids under strong magnetic fields, Eq. 10.1 becomes invalid due to the nonlinear dependence of a superparamagnetic particle’s magnetization on the applied field, as well as the magnetization of the ferrofluid. Both the superparamagnetic particle and the ferrofluid can be accurately modeled using the classical Langevin theory, which treats magnetic nanoparticles as non-interacting magnetic dipoles in a superparamagnetic particle and the ferrofluid. This approach leads to the Langevin function of magnetization, as described in Eq. 10.2 [17].

$$M = nm_{\text{eff}} \left(\coth x - \frac{1}{x} \right) \tag{10.2}$$

where $x = \frac{m_{\text{eff}}\mu_0 H}{k_B T}$.

In the case of positive magnetophoresis, the magnetization of the superparamagnetic particle (Mp) is always greater than that of the surrounding medium (Mf). Under a non-uniform magnetic field, the magnetic force (Fm) applied to the particle is directed towards field maxima. Conversely, for negative magnetophoresis, the magnetization of the particle or cell (Mp) is always lower than that of the surrounding magnetic liquid (Mf), and the direction of the magnetic force (Fm) on the particle or cell is directed towards field minima.

The Reynolds number in a typical Magneto-Archimedes levitation-based manipulation device is much less than 1, resulting in laminar flows. Hydrodynamic viscous drag force \vec{F}_v thus plays a significant role in particle and cell manipulation; its expression on a spherical particle with diameter D_p is,

$$\vec{F}_v = -3\pi\eta D_p(\vec{v}_p - \vec{v}_m)f_D \quad (10.3)$$

Here, η represents the viscosity of the paramagnetic medium, \vec{v}_s and \vec{v}_m refer to the velocity vectors of the particles and the magnetic liquids, respectively. f_D is the hydrodynamic drag force coefficient experienced by a particle due to the presence of a nearby solid surface, commonly known as the “wall effect”.

The net force of gravitational and buoyant forces \vec{F}_b on a spherical body can be expressed as Eq. 10.4. Due to the low Reynolds number and resulting laminar flow in MagLev-based manipulation systems, inertial effects can be neglected. Therefore the dynamics of particles in Maglev-based manipulation are determined by the balance of all dominant forces.

$$\vec{F}_b = \frac{\pi D_p^3}{6}(\rho_p - \rho_m)\vec{g} \quad (10.4)$$

$$\vec{F}_{\text{mag}} + \vec{F}_v + \vec{F}_b = 0 \quad (10.5)$$

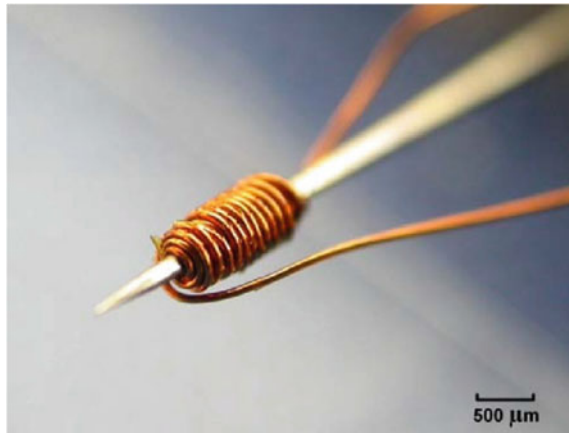
It is clear from the above equations that the dynamics of a particle in paramagnetic medium is determined by its physical properties including size, density, as well as the contrast of magnetization between itself and surrounding medium. These three physical properties are currently being exploited for MagLev-based manipulation. It should be noted that the volume concentration of superparamagnetic nanoparticles used for particle and cell manipulation is typically around 1%. Therefore, the magneto viscous effect, which refers to the formation of chain structures due to inter-particle interaction, can be neglected for the purpose of analysis.

10.3 Manipulating Particles Using Magnetic Tweezer

10.3.1 Magnetic Tweezer

The ability to trap and manipulate very small objects, also known as “tweezing,” is fundamental to numerous disciplines in modern science. Compared with optical and acoustic tweezers, there are no restrictions for magnetic tweezer technique on the medium’s transparency and objects’ refractive index and compressibility. Careful engineering of magnetic tweezers, often in the form of sharp magnetic tips, is necessary to generate localized magnetic field gradients for the generation of sufficient magnetic force.

Fig. 10.2 A complete electromagnetic probe. Reproduced with permission from Ref. [18]. Copyright 2008 Springer Nature



There are two primary types of magnetic tweezers widely utilized: scanning magnetic microneedles and magnetic multipole tweezers: (i) Scanning magnetic tweezers involve utilizing a magnetic microneedle for manipulating target objects (Fig. 10.2) [18]. The microneedle can be magnetized by passing an electric current through a coil wound around it. Precise manipulation of the target object is achieved by controlling the translational motion of the magnetic tweezer. This type of magnetic tweezers is suitable for two-dimensional manipulation, allowing movement and rotation of the target object in various directions. (ii) Magnetic multipole tweezers employ multiple magnetic poles to generate local magnetic field gradients [19]. Each individual pole can be activated independently, resulting in a complex magnetic field configuration. By individually controlling the activation of magnetic poles, three-dimensional manipulation of the target object, including rotation and translation, is achievable. Magnetic multipole tweezers provide high precision and programmability, allowing for precise manipulation within complex magnetic field environments. Both types of magnetic tweezers offer distinctive advantages and applications.

It should be noted that these magnetic tweezers were initially designed to manipulate the magnetic object other than diamagnetic object. The sharper the tip of a magnet is, the smaller the region in which stable Magneto-Archimedes levitation can be achieved, as shown before in Fig. 4.3. Therefore, the magnetic tweezer utilized for MagLev-based manipulation is commonly design with a flat tip, where a region with localized minimum magnetic potential of diamagnetic object can be generated.

10.3.2 Manipulation of Single Particle

In general, the Magneto-Archimedes levitation experiments carried out using superconducting magnetic solenoids and strong magnet devices can also be considered as

magnetic tweezing experiments. This section specifically focuses on research that investigates the manipulation of small-scale diamagnetic objects. The first MagLev-based tweezer for single cell was proposed in 2004 [20]. The experimental setup involves placing a paramagnetic aqueous solution between two cone-shaped rare earth magnets with opposing magnetic fields. By utilizing two magnets with opposite poles facing each other, a strong magnetic gradient can be created between them, allowing for sufficient magnetic force to manipulate living cells at a lower concentration of paramagnetic aqueous solution. The distance between two magnets is 30 μm , and each magnet has a radius of curvature of 76 μm and magnetic field of 0.4 T at the surface. An aqueous solution containing gadolinium (III) salt, which has a high magnetic susceptibility ($2.8 \times 10^{-2} \text{ cm}^3/\text{mol}$) and high biocompatibility, was employed as the paramagnetic medium. The magnetic trapping force on a diamagnetic sphere with a radius of 2.5 μm in a 40 mM solution of gadolinium (III) ions was calculated to be 5.5 pN through finite element analysis, which is comparable to those used in optical traps for biological species. Magnetic traps offer several advantages, such as the capability to capture a wide range of materials, including most biomaterials. Additionally, magnetic traps can accommodate larger objects and be positioned deeper within a medium compared to optical traps. Moreover, magnetic traps can provide larger capture volumes, surpassing those of traditional optical tweezers.

Magnetic tweezer systems actuated by electromagnet rather than permanent magnet are more flexible and dynamic during particle manipulation [21]. The ability to switch “on” and “off” ensure that the object will not be affected by the magnetic tweezer after manipulation. The “micropen” tweezer is proposed as a hollow coaxial structure that consists of a non-magnetic inner core (Fig. 10.3a–c), typically made of a thin tungsten wire ($\chi \approx 7 \times 10^{-5}$; diameter $D \approx 1\text{--}100 \mu\text{m}$), and an outer shell made of a nearly hysteresis-free, soft-ferromagnetic supermalloy ($\chi \approx 10^5$). An electromagnetic coil was placed coaxially with the pen to generate an external magnetic field, which magnetizes the tweezer and creates a magnetic gradient around the tip of the tweezer. There are two regions with different magnetic force distribution below the tip of tweezer (Fig. 10.3b): In region I, the magnetic force acting on the particle is directed both toward the axis and the bottom surface of the tweezer. In region II, the magnetic force is only directed to the symmetry axis. With the help of supermalloy and high concentration of paramagnetic solution, the magnetic force that the sample experience in this system is on the order of nN. Therefore, the micropen possess unique characteristics that enable a variety of tweezing modalities. For instance, non-magnetic particles such as large and heavy particles, such as 50 μm glass beads, can be lifted, manipulated, and released in both 2D and 3D (Fig. 10.3d). When utilizing the biocompatible paramagnetic medium (suspension of $\approx 1\text{--}3 \mu\text{M}$ iron oxide NPs coated with 15–25 kDa dextran), the “micropen” magnetic tweezer system can realize 3D manipulation of single cell (Fig. 10.3e). The dextran can not be uptaken by the cells and therefore the cells won’t become magnetic when immersed in such suspensions. The ability to manipulate single cell holds significant potential for applications in studying cellular interactions and mechanisms.

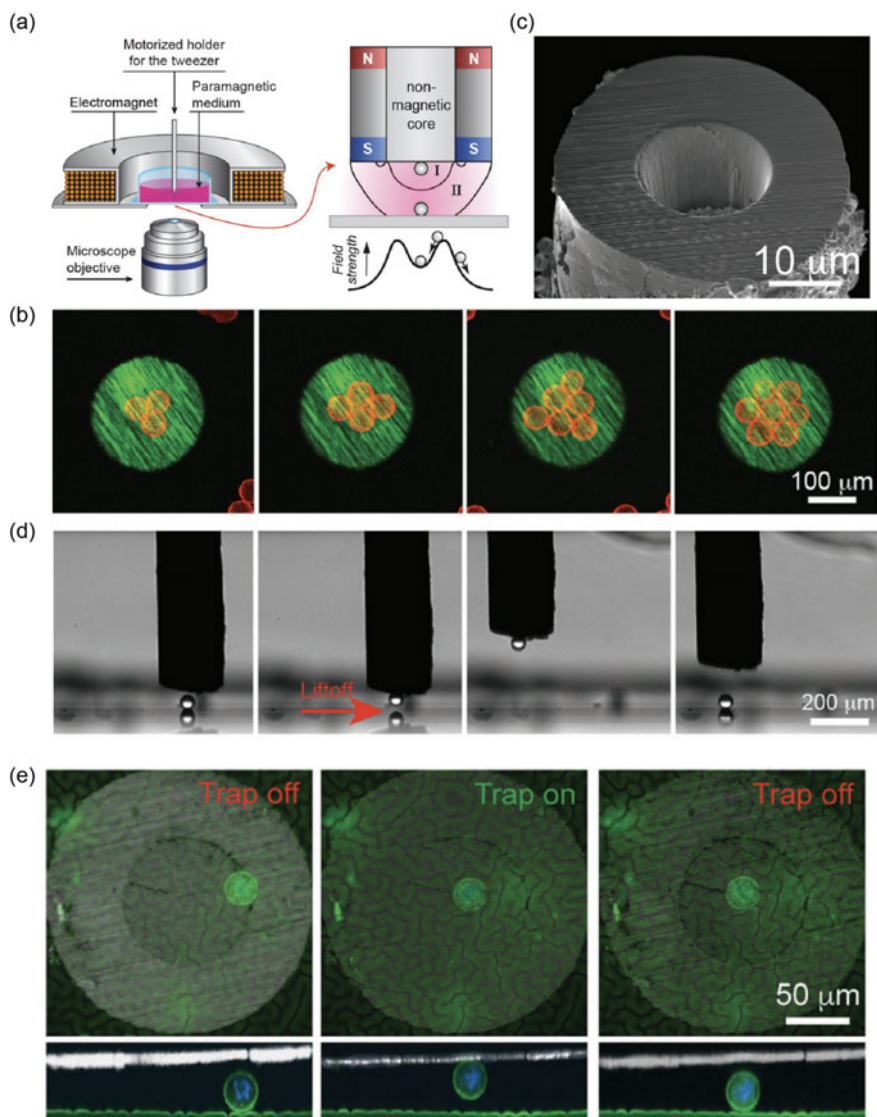


Fig. 10.3 **a** Scheme of the “micropen” magnetic tweezer system; **b** different regions below the tip; **c** SEM image of a FIB-milled hollow microtip; **d** the trapping and releasing of 50 μm glass beads using magnetic tweezer; **e** single-cell manipulation using “micropen” magnetic tweezer system. Reproduced with permission from Ref. [21]. Copyright 2016 Wiley

10.4 Assembling Particles via Magnetic Pattern

MagLev can be used to guide the self-assembly of diamagnetic objects without directly contact with solid surfaces. Since the gravitational and magnetic forces on the mm-scale samples are comparable, fragile object such as living cell clusters or hydrogel, which are inconvenient to handle without hard contact, can be easily to self-assemble through MagLev based manipulation.

Standard MagLev device has the capability of determining the objects' densities and defects through their levitation heights and postures, respectively. Therefore, various objects with specifically designed density distributions can be levitated stably and assembled by magnetic forces. For a particular MagLev system with fixed parameters (i.e., magnetic field and paramagnetic medium), the average density of an object determines its levitation height at equilibrium; the pattern of heterogeneous density within the object defines the orientation of the object relative to the axis of gravity. Through this method, alignment and positioning of self-assembly optical elements in a standard MagLev system is achieved (Fig. 10.4a) [22]. The levitating mirrors are fabricated by a layering reflective Mylar tape onto the surface of polymethylmethacrylate (PMMA). The levitation height and tilt angle can be programmed by layering different materials, i.e., labeling tape on the top mirror, and aluminum tape on the bottom mirror. MagLev technology enables the alignment and assembly of mm-scale objects with varying density distributions into functional three-dimensional structures, all achieved without the need for direct contact. Furthermore, it is possible to assemble and bring the levitating components into contact by removing the paramagnetic medium. Combining the capability of coaxial levitation and the control of liquid level, the levitating objects in different heights can be assembled into a pre-designed multicomponent structures (Fig. 10.4b). The individual components were programmatically assigned specific densities in order to levitate at designated heights and assemble into predetermined configurations based on their respective shapes. The magnetic force-induced coaxial alignment can be treated as a soft templates for self assembling objects in a MagLev based system. For the levitating clusters of both spherical and non-spherical objects, introducing hard templates (both levitating objects and the walls of the container) can promote the packing and shaping of the assembly structures (Fig. 10.4c). The objects, suspended within the paramagnetic medium and situated between the two magnets, undergo spontaneous assembly and orientation. The final arrangement of the objects in the liquid, as well as their self-assembly process, are influenced by a combination of gravitational forces, magnetic forces, and steric interactions (mechanical forces resulting from physical contact) among the objects and the container. Furthermore, customizing the size and shape of the hard templates also proved advantageous in facilitating the formation of organized structures.

By adjusting the shape of magnet to a high length/height ratio, the MagLev-based system can generate sufficient magnetic force in a low concentration of paramagnetic medium to levitate and manipulate living cells [24]. The high length-to-height ratio of the magnet ensures that the horizontal component of the magnetic force along

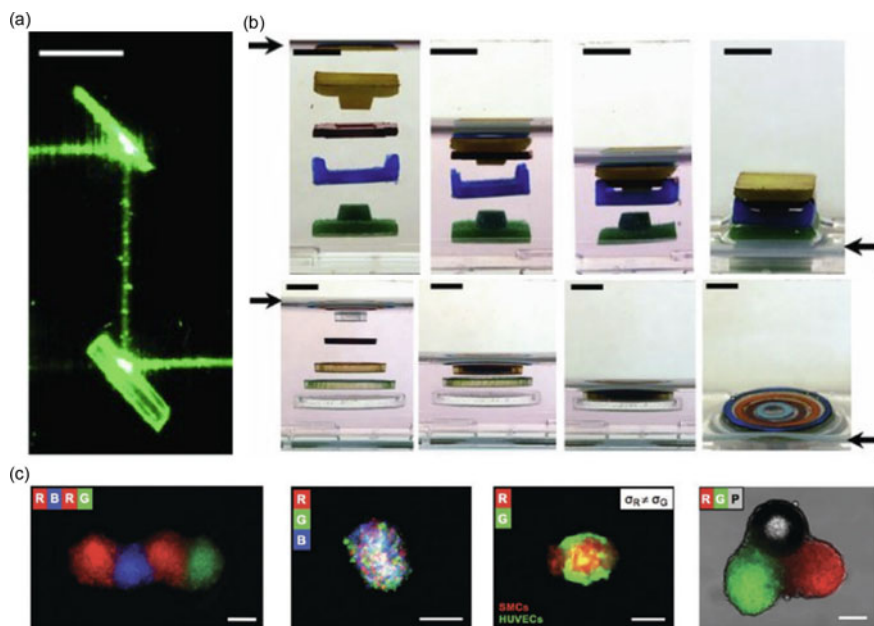


Fig. 10.4 **a** Photographs of self-assembly mirrors in 1.5 M MnCl_2 aqueous solution. **b** The assembly of multilayered structures in 1.8 M MnCl_2 aqueous solution. Black arrows indicate the level of liquid level. Reproduced with permission from Ref. [22]. Copyright 2011 Wiley. **c** Coding of spatially controlled cellular architectures. Reproduced with permission from Ref. [23]. Copyright 2017 Wiley. Scale bars are 5 mm in **(a, b)** and 100 μm in **(c)**

the length axis is weak. Consequently, it will not cause the levitating cells to move towards the center axis within a ten-minute time frame. 3D cellular aggregates start to consolidate after 8 h in levitation, reaching a uniform size after 24–48 h [23]. The temporal and spatial reconfigurability of living materials in a three-dimensional can be guided using this MagLev based device. Four coding schemes were presented for the coding of spatially controlled cellular architectures: serial, parallel, surface tension, and hybrid. These results demonstrate the ability to program the positioning of living clusters for the incorporation of three-dimensional non-living objects into pre-organized 3D structures. The hybrid coding experiments exhibit great potentials for spatiotemporal release of biochemical factors at the microscale to the assembled cells, as well as the facilitation of dynamic modification of cellular microenvironments. However, these benefits are still challenging to achieve using existing technologies once the cellular constructs/organoids have been assembled.

Microfabrication of ferromagnetic (e.g., nickel and cobalt) grids with well-defined trapping regions allowed better control over magnetic forces. Micro-nickel grid covered with a thin layer of polymer can generate magnetic gradients in the region very close to the surface when placed above a permanent magnet (Fig. 10.5a) [25]. The purpose of the grid was to concentrate the magnetic field locally and generate

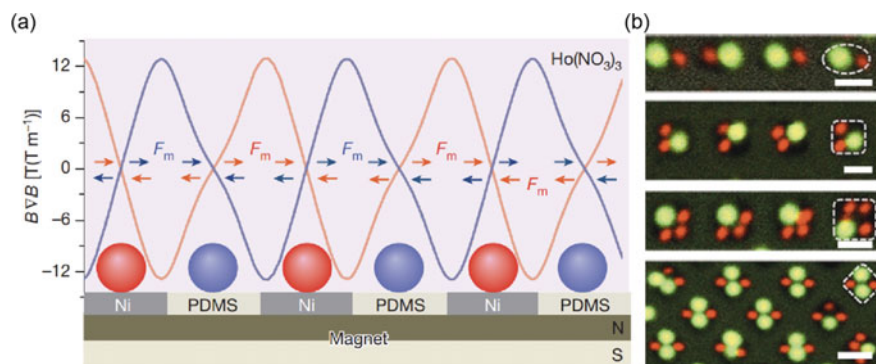


Fig. 10.5 **a** Schematic of the experimental arrangement for assembling of both magnetic and nonmagnetic particles. **b** Examples of colloidal molecules comprising two types of diamagnetic particle (1.2 μm (green) and 800 nm (red)). Scale bars, 2 μm . Reproduced with permission from Ref. [25]. Copyright 2013 Springer Nature

lateral magnetic forces that acted within the plane of the support, directed towards the voids of the grid. In the presence of nonmagnetic particles in a paramagnetic salt solution, these particles accumulated in the voids, forming large, regular arrays that were centimeter-sized. The paramagnetic particles (red) localize onto nickel islands, the diamagnetic particles (blue) centre in the spaces between nearby islands. A series of interesting patterns using particles with different sizes are achieved (Fig. 10.5b). To manipulate microparticles more freely, electromagnets are preferred [26]. A particle assembling and transporting microparticles can be achieved using a field rotating out-of-plane. By adjusting the orientation of the external magnetic field generated by solenoids in relation to the in-plane magnetization, the movement of the minima regions caused the microparticles to be pushed from one trap to the next. A single 7 μm latex bead is transported over an array of circular traps.

References

1. Sun M, Agarwal P, Zhao S, et al. Continuous on-chip cell separation based on conductivity-induced dielectrophoresis with 3D self-assembled ionic liquid electrodes. *Anal Chem*. 2016;88(16):8264–71.
2. Kang KH, Kang Y, Xuan X, et al. Continuous separation of microparticles by size with direct current-dielectrophoresis. *Electrophoresis*. 2006;27(3):694–702.
3. Alshareef M, Metrakos N, Juarez Perez E, et al. Separation of tumor cells with dielectrophoresis-based microfluidic chip. *Biomicrofluidics*. 2013;7(1).
4. Brzobohatý O, Karásek V, Šiler M, et al. Experimental demonstration of optical transport, sorting and self-arrangement using a ‘tractor beam.’ *Nat Photonics*. 2013;7(2):123–7.
5. Ashkin A, Dziedzic JM, Bjorkholm JE, et al. Observation of a single-beam gradient force optical trap for dielectric particles. *Opt Lett*. 1986;11(5):288–90.
6. Ashkin A, Dziedzic JM, Yamane T. Optical trapping and manipulation of single cells using infrared laser beams. *Nature*. 1987;330(6150):769–71.

7. Laurell T, Petersson F, Nilsson A. Chip integrated strategies for acoustic separation and manipulation of cells and particles. *Chem Soc Rev.* 2007;36(3):492–506.
8. Armstrong JPK, Puetzger JL, Serio A, et al. Engineering anisotropic muscle tissue using acoustic cell patterning. *Adv Mater.* 2018;30(43):1802649.
9. Piyasena ME, Austin Suthanthiraraj PP, Applegate RW Jr, et al. Multinode acoustic focusing for parallel flow cytometry. *Anal Chem.* 2012;84(4):1831–9.
10. Ding X, Lin SCS, Kiraly B, et al. On-chip manipulation of single microparticles, cells, and organisms using surface acoustic waves. *Proc Nat Acad Sci.* 2012;109(28):11105–9.
11. Cho MH, Lee EJ, Son M, et al. A magnetic switch for the control of cell death signalling in vitro and in vivo systems. *Nat Mater.* 2012;11(12):1038–43.
12. Robert D, Pamme N, Conjeaud H, et al. Cell sorting by endocytotic capacity in a microfluidic magnetophoresis device. *Lab Chip.* 2011;11(11):1902–10.
13. Etoc F, Lisse D, Bellaiche Y, et al. Subcellular control of Rac-GTPase signalling by magnetogenetic manipulation inside living cells. *Nat Nanotechnol.* 2013;8(3):193–8.
14. Huang NT, Zhang H, Chung MT, et al. Recent advancements in optofluidics-based single-cell analysis: optical on-chip cellular manipulation, treatment, and property detection. *Lab Chip.* 2014;14(7):1230–45.
15. Li G, Chen X, Zhou F, et al. Self-powered soft robot in the Mariana Trench. *Nature.* 2021;591(7848):66–71.
16. Zhao W, Cheng R, Miller JR, et al. Label-free microfluidic manipulation of particles and cells in magnetic liquids. *Adv Funct Mater.* 2016;26(22):3916–32.
17. Rosensweig RE. Magnetic fluids. *Annu Rev Fluid Mech.* 1987;19(1):437–61.
18. Yapici MK, Zou J. Permalloy-coated tungsten probe for magnetic manipulation of micro droplets. *Microsyst Technol.* 2008;14:881–91.
19. Chen L, Offenhäusser A, Krause HJ. Magnetic tweezers with high permeability electromagnets for fast actuation of magnetic beads. *Rev Sci Instrum.* 2015;86(4): 044701.
20. Winkleman A, Gudiksen KL, Ryan D, et al. A magnetic trap for living cells suspended in a paramagnetic buffer. *Appl Phys Lett.* 2004;85(12):2411–3.
21. Timonen JVI, Demirörs AF, Grzybowski BA. Magneto-fluidic tweezing of nonmagnetic colloids. *Adv Mater.* 2016;28(18):3453–9.
22. Mirica KA, Ilievski F, Ellerbee AK, et al. Using magnetic levitation for three dimensional self-assembly. *Adv Mater.* 2011;23(36):4134–40.
23. Tocchio A, Durmus NG, Sridhar K, et al. Magnetically guided self-assembly and coding of 3D living architectures. *Adv Mater.* 2018;30(4):1705034.
24. Durmus NG, Tekin HC, Guven S, et al. Magnetic levitation of single cells. *Proc Nat Acad Sci.* 2015;112(28):3661–8.
25. Demirörs AF, Pillai PP, Kowalczyk B, et al. Colloidal assembly directed by virtual magnetic moulds. *Nature.* 2013;503(7474):99–103.
26. Yellen BB, Hovorka O, Friedman G. Arranging matter by magnetic nanoparticle assemblers. *Proc Natl Acad Sci.* 2005;102(25):8860–4.

Chapter 11

Separation via MagLev



Chengqian Zhang, Jun Xie, Chenxin Lyu, and Peng Zhao

11.1 Introduction

Magnetic labels are widely used to aid in the separation and purification of chemical and biological samples. These labels typically consist of superparamagnetic nano- or microspheres, such as Invitrogen's Dynabeads, which can be covalently attached to a variety of chemical and biological samples. For instance, immunomagnetic separation involves the use of antibodies, often monoclonal, bound to magnetic particles, enabling the removal of prokaryotic and eukaryotic cells from suspension. Various techniques, including cell separation, free flow magnetophoresis, and immunoassays, have been developed for integration into microfluidic devices for lab-on-a-chip technology. However, these magnetic labeling methods have certain limitations: (i) the separations are limited to binary outcomes, with magnetic particles being separated from diamagnetic particles; (ii) the labeling of a diamagnetic material requires a chemical reaction; (iii) the presence of a magnetic particle attached to a diamagnetic material, such as a cell, antibody, or protein, can alter the functionality and properties of the surface; and (iv) the magnetic label must be removed after separation to obtain a pure diamagnetic sample [1].

Novel label-free techniques for manipulating and separating diamagnetic materials based on Magneto-Archimedes levitation technology, which can overcome the aforementioned limitations, is highly valuable in broader applications. Magnetic media such as ferrofluids, which exhibit excellent magnetic response, is commonly utilized for separating diamagnetic particles, especially living matter. Over the past decades, the magnetic levitation of diamagnetic materials has become more

C. Zhang (✉) · C. Lyu · P. Zhao

The State Key Laboratory of Fluid Power and Mechatronic Systems, College of Mechanical Engineering, Zhejiang University, Hangzhou, China
e-mail: zhangcq@zju.edu.cn

J. Xie

College of Mechanical Engineering, Zhejiang University of Technology, Hangzhou, China

accessible in standard laboratory facilities, with the earlier experimental setup involving superconducting magnets and a pressurized oxygen atmosphere being replaced by smaller, cheaper rare-earth magnets and high-density and high-magnetic-susceptibility aqueous paramagnetic salt solutions. As an extension of levitation, MagLev technique is developed to separate cells and polymer particles with various physical parameters.

11.2 Dynamic MagLev

11.2.1 Separation Method

Magneto-Archimedes levitation technique has the capability of positioning objects according to their densities. The MagLev method exhibits inherent stability in levitation and can effectively separate diamagnetic samples with different densities based on their respective heights during stable levitation. However, the key challenge in achieving separation of diamagnetic samples using MagLev lies in effectively utilizing differences in levitation positions to separate and obtain samples with different densities. Currently, there are two main types of MagLev-based separation techniques, as shown in Fig. 11.1. The first involves transitioning the paramagnetic medium from a static state to a dynamic state within the magnetic field and utilizing the flow of liquid to carry away the samples in different positions. The second method involves imparting an initial velocity to the samples to be separated, allowing them to pass through a static liquid under the external magnetic field and generate a displacement difference at the receiving end under the combined effects of magnetic force, hydrodynamic drag force, and buoyancy. The former technique is limited in achieving large-scale separation and high flow rates due to the significant impact of turbulence on the separation efficiency, therefore it is predominantly utilized in microfluidic systems. Importantly, this separation method does not necessitate stable levitation of the sample in the magnetic field, providing flexibility in selecting magnetic sources. It does not require the generation of magnetic field for stable levitating. Instead, the key is to generate sufficient magnetic forces that can cause trajectory deviations during motion. Consequently, regions on the surface of a single magnet with a strong magnetic gradient are often selected as the separation zone.

11.2.2 Dominant Forces

The types of forces in MagLev systems have been summarized in previous sections. The most relevant ones among them for separation are magnetic force \vec{F}_m , gravitational/buoyant force \vec{F}_b , and hydrodynamic/viscous drag force \vec{F}_v . In previous

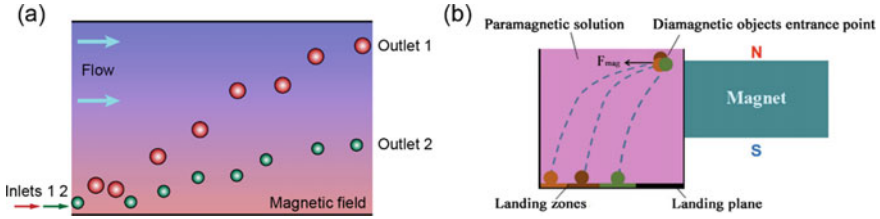


Fig. 11.1 Two separation method in **a** dynamic flow liquid, and **b** static liquid. Reproduced with permission from Ref. [2]. Copyright 2019 Elsevier

chapters, only a few applications, such as manipulation, have considered the hydrodynamic drag force, while the majority have focused on the stable levitation of objects in MagLev systems and ignored the drag force. Hydrodynamic drag force \vec{F}_v plays a significant role in MagLev-based separations when there is a difference in speed between the stream and particles, and always tends to decrease fluid velocity relative to the solid object in the fluid's path. Unlike other resistive forces, such as dry friction, which are nearly independent of velocity, the drag force exhibits a dependence on velocity. For low-speed flow, the drag force is directly proportional to the velocity, while for high-speed flow, it is proportional to the square of the velocity. The specific point at which the transition occurs between low and high speed is determined by the Reynolds number, Re as shown in Eq. 11.1.

$$Re = \frac{\rho v D}{\eta} \quad (11.1)$$

where, ρ is the density of liquid, v is the speed of the object relative to the fluid, D is the diameter of the object, η is the dynamic viscosity.

The drag force is influenced by the characteristics of the fluid as well as the size, shape, and speed of the object. This relationship is commonly represented by the drag equation:

$$F_v = \frac{1}{2} \rho v^2 C_D S \quad (11.2)$$

where C_D is hydrodynamic drag force coefficient (a dimensionless number) of a particle experiencing the effect of having a solid surface in its vicinity, which is often referred to as a "wall effect", S is the cross sectional area. At low Reynolds numbers, the drag coefficient C_D exhibits an asymptotic relationship with Re^{-1} , indicating that the drag is linearly proportional to the speed. This can be observed in the case of a small sphere moving through a viscous fluid, as described by Stokes Law:

$$\vec{F}_v = 6\pi\eta R\vec{v} \quad (11.3)$$

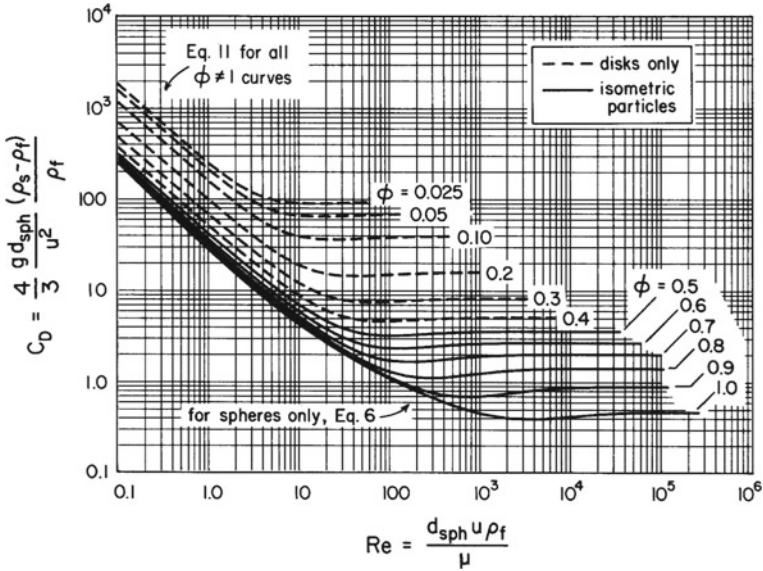


Fig. 11.2 Design chart for drag coefficients of single free-falling particles. Reproduced with permission from Ref. [3]. Copyright 1989 Elsevier

where R is the radius of the sphere. For most microfluidic separations, Eq. 11.3 is widely employed to calculate the drag force experienced by the particles.

At high Reynolds numbers, the drag coefficient C_D is more or less constant and drag will vary as the square of the speed. Figure 11.2 shows how C_D varies with Re for the case of a sphere [3]. Because the power required to counteract the drag force is the result of multiplying the force by the speed, the power required to overcome drag will increase with the square of the speed at low Reynolds numbers and with the cube of the speed at high Reynolds numbers.

The combined forces affecting on the object in a flowing stream, therefore, reflects the physical characteristics of both the object (density and the size) and the flowing medium that suspends the object (viscosity and velocity). When appropriately designed, MagLev systems and fluidic flows could be exploited to carry out separations that reflect both density and size/shape and fluidic characteristics of the flowing medium.

11.3 Separation Methods Using Continuous Flow in MagLev Device

The separation of samples within a MagLev device using continuous flowing liquids has been widely applied for the separation of particles and cells. This method relies primarily on three characteristics of the objects being separated: magnetism, density, and size (including shape), as shown in Fig. 11.3. According to the magnetic force equation, the magnetization contrast between the particles and the surrounding paramagnetic medium ($\chi_p - \chi_m$) is the dominant factor when exposed in an external magnetic field. A higher magnetization contrast leads to a higher magnitude of magnetic force, and thus a higher velocity for separation. Assuming that there are two types of particles with different magnetizations (χ_{p1} and χ_{p2}) moving perpendicularly to the direction of gravity in a magnetic liquid (χ_m), the effectiveness of separating these particles depends on the difference in their magnetization values. If both types of particles are diamagnetic, with a magnetization difference much smaller than that of paramagnetic media ($|\chi_{p1} - \chi_{p2}| \ll \chi_m$), the difference in magnetic forces acting on the two types of particles is not sufficient for effective separation. However, if the condition $\chi_{p1} > \chi_m > \chi_{p2}$ is met, particles with a magnetization of χ_{p1} will be attracted to the region with the highest field strength, while particles with a magnetization of χ_{p2} will be pushed towards the region with the lowest field strength. This method proves to be effective in effectively separating particles with different magnetizations. In addition, the density difference between the particles and the paramagnetic medium also plays a crucial role in the dynamics. Density-based separation primarily follows the basic principles applied in MagLev density measurement methods, which require specific sample sizes and liquid viscosities to ensure that gravity and buoyancy are the main forces acting on the particles in the separation system, and that the particle motion plane within the flow channel is designed to be parallel to the direction of gravity. Besides these separation methods, particle size (including shape) also plays a crucial role in particle separation. Assuming that the particles have the same magnetism and their velocity is perpendicular to the direction of gravity, the magnetic and buoyant forces are proportional to the sample's volume ($V = \pi D^3/6$), while the liquid resistance is proportional to the sample's diameter (D). Therefore, larger particles achieve higher velocities due to the stronger magnetic force acting on them. Combined with microfluidic systems, this method can effectively handle micron-sized particles or cells.

11.3.1 Separation Based on Magnetization Contrast

Traditional particle separation based on magnetization contrast is the process of separating components of mixtures by using a magnet to attract magnetic substances. The is traditional process was mainly utilized to distinguish between non-magnetic substances and those that exhibit magnetic properties. This technique is particularly

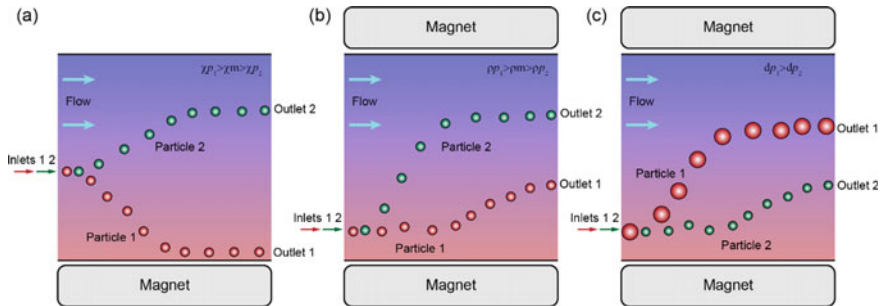


Fig. 11.3 Diagram of separation methods through the differences in **a** magnetism, **b** density, and **c** shape (size)

valuable for the separation of a small number of minerals that are ferromagnetic (containing iron, nickel, and cobalt) and paramagnetic. Cells with surface antigens penetrated by the antibodies coated with superparamagnetic nanoparticles can also be separated with those without magnetic nanoparticle penetrations using a simple magnet in a non-magnetic solution. Magnetic cell separation is considered very promising in bioengineering, clinical diagnostics, and food engineering. The limitations of this method include the presence of antibodies applied to the surface of the target organism, the need for a significant concentration of free antigen to the target cell, and the low throughput of particles separation.

Traditional particle separations mostly based on magnetization occur in diamagnetic solutions based in water. In this process, magnetic particles are captured while diamagnetic particles flow through without being influenced by the magnetic field. Replacing the weakly magnetic medium with a paramagnetic solution can significantly increase the throughput of magnetic and diamagnetic particle separation. This enhancement is attributed to the simultaneous magnetic influences on both magnetic and diamagnetic particles, respectively.

Figure 11.4a depicts a microfluidic device utilized for magnetic and diamagnetic particles separation based on MagLev method. A polydimethylsiloxane (PDMS) device with a T-shape microchannel of main-branch (400 μm wide and 40 μm in depth) and two side-branches (200 μm wide and 40 μm in depth) are fabricated through the standard soft lithography technique. One neodymium-iron-boron (NdFeB) permanent magnet (B221, K&J Magnetics, Inc.) with the magnetization direction perpendicular to the main-branch is placed and fixed at a distance of 500 μm from the main-branch and 3 mm from the side-branch inside the PDMS device. Magnetic particles with a diameter of 2.85 μm (from Bangs Laboratories, Inc.) and diamagnetic polystyrene particles with a diameter of 10 μm (from Duke Scientific Corp.) were mixed and suspended in a 0.1 \times EMG 408 ferrofluid (Ferrotec Corp.) for preparation. The magnetization of the ferrofluid used in this study was higher than that of the diamagnetic particles, but lower than that of the magnetic particles. Consequently, the 10 μm magnetic particles were drawn towards the magnet, while the 2.85 μm diamagnetic particles were repelled.

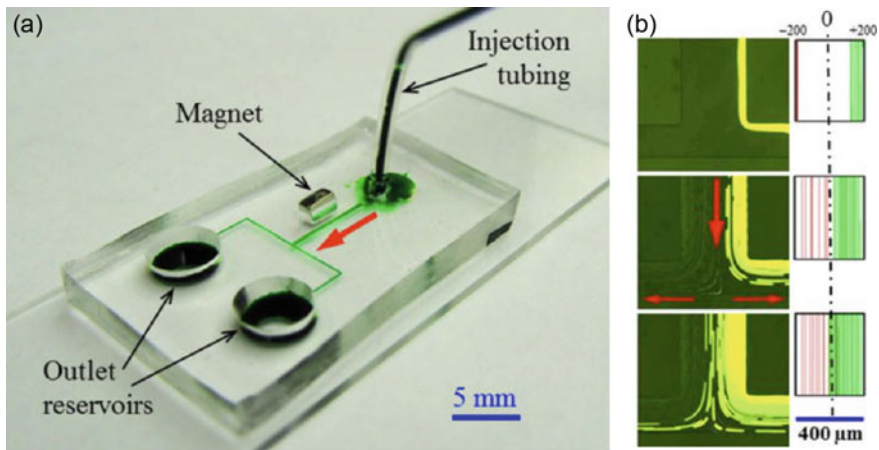


Fig. 11.4 **a** Picture of a microfluidic device for magnetic and diamagnetic particles separation. **b** The experimentally obtained streak images (left column) and theoretically predicted trajectories (right column, red and green lines for magnetic and diamagnetic particles, respectively) at the junction of the T-microchannel under the ferrofluid flow rate of 200 $\mu\text{l/h}$ (top row), 240 $\mu\text{l/h}$ (middle row), and 300 $\mu\text{l/h}$ (bottom row), respectively. Reproduced with permission from Ref. [4]. Copyright 2013 AIP Publishing

The paramagnetic flow rate has significant effect on the performance of particles separation, as shown in Fig. 11.4b. This phenomenon is clearly evident in the particle streak images and trajectories presented in the top row of Fig. 11.4b. On the flow rate of 200 $\mu\text{l/h}$, the 2.85 μm magnetic particles were fully trapped by the magnet. As the flow rate of the ferrofluid increases beyond 240 $\mu\text{l/h}$, the magnetic and diamagnetic particle streams begin to overlap at the T-junction, resulting in a decrease in their respective lateral deflections. This incomplete separation is clearly demonstrated by the particle images in the bottom row of Fig. 11.4b at a flow rate of 300 $\mu\text{l/h}$.

11.3.2 Separation Based on Density

Density-based method was first employed in the 1960s as a means of separating minerals, metals, and plastics from one another when they are immersed in a ferrofluid or a solution containing paramagnetic salts [5]. As we mentioned in Chap. 4, the magnetic forces acting on these objects immersed in a paramagnetic solution are determined by their size, external magnetic field, and the contrast in susceptibilities between the objects and the paramagnetic carrier. When the size and susceptibility of these objects are consistent, diamagnetic objects with varying densities in the same magnetic liquid can be separated solely based on their differences in density.

One straightforward approach is to expand the existing standard MagLev device from a static levitation system into a dynamic flow separation system [1], as shown

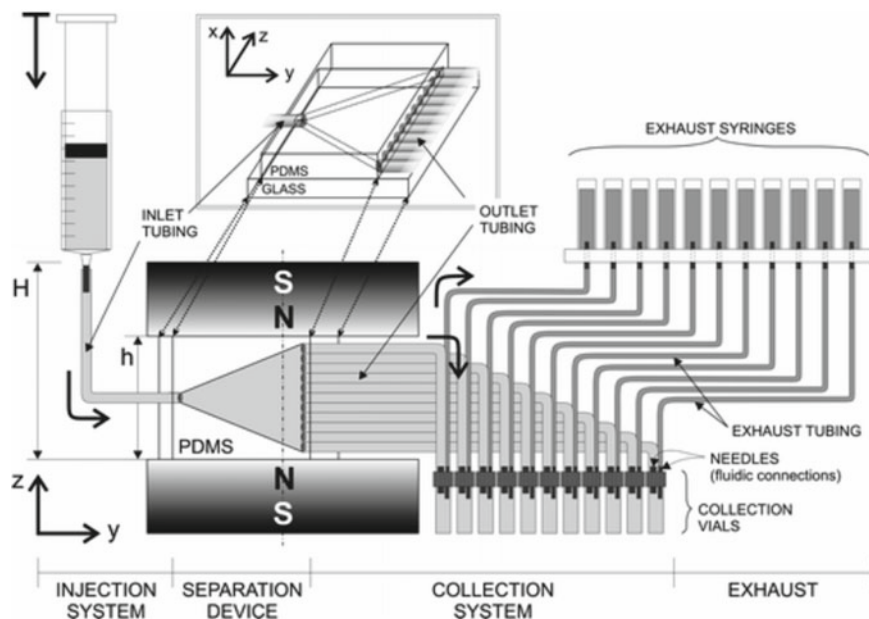


Fig. 11.5 Schematic representation of the separation and collection system based on standard MagLev device. Reproduced with permission from Ref. [1]. Copyright 2007 American Chemical Society

in Fig. 11.5. To avoid the turbulence in streams, the separation system is developed as a microfluidic device, where flow in streams is laminar flow and would not disrupt separations. The device is fabricated of PDMS using soft lithography, which is a widely used techniques in manufacturing microfluidic device.

There are four sections in this separation system, as shown in Fig. 11.5: the injection system, the separation device, the collection system, and the exhaust.

- (I) **Injection System:** A syringe pump is employed to inject the samples for separation from a vertically held syringe above the separation device, which allows the combination of fluidic and gravitational forces to direct the beads into the device. It should be noted that the syringe pump cannot be hold horizontally since the particles will settle inside the barrel.
- (II) **Separation Device:** A vertically placed triangular PDMS channel, aligned with the magnet axis, minimizes regions of low flow rate (dead volume) for all particles to flow from a single inlet to multiple outlets. In the absence of flow, diamagnetic particles experience magnetic forces directed along the axis. Laminar flow in the channel consists of y - and z -components due to its triangular shape. Flow rates were chosen to ensure beads separated in the magnetic field before reaching the outlet, in line with a laminar, quasi-equilibrium protocol. This additional z -component created a slight difference in observed height between static and flowing modes. Depending on the sample

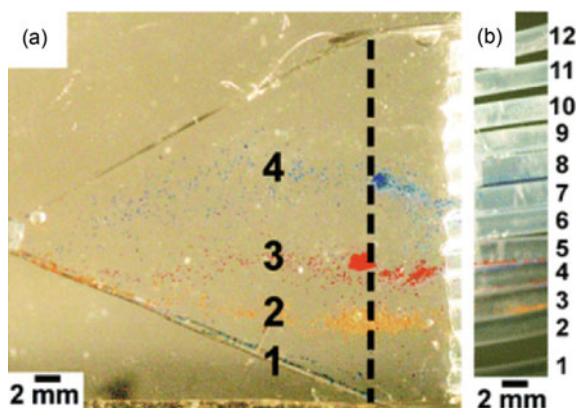
volume (100 μL to several milliliters), separation times ranged from minutes to over 1 h.

- (III) **Collection System:** After passing through the separation device, only fluidic forces and gravity influenced the particles. The collection system simplified sample removal: each outlet led to a glass vial with a septum top, maintaining a sealed fluidic system. The vials were positioned lower than the device for gravitational settling of beads, efficient collection, and minimal tubing clogging. Removal of the septum tops allowed easy collection of samples without disrupting the tubing or fluidic connections.
- (IV) **Exhaust System:** To maintain a constant flow rate, each collection vial was connected to an exhaust tube open to the atmosphere. Placing the tubes at the same height as the syringe ensured consistent back pressure and prevented pressure drop due to gravity between the bottom and top outlets of the device. This exhaust system guaranteed uniform flow rates across all outlets.

The system is filled with a 250 mM GdCl_3 solution and the mixture of dyed spheres is introduced using a syringe pump. The spheres enter the separation channel from a single left inlet (Fig. 11.6a) and exited through multiple collection outlets on the right (Fig. 11.6b). The device successfully separated all four batches of beads, even when the proportions of the batches were unequal. The densest green beads has the fewest collected particles since some of them adhere to the bottom wall and others are trapped at the junction of the outlet tubing and PDMS microfluidic device.

With the development of microfluidic technology, the density-based MagLev separation method is extended to distinguish the small density differences between cells, as shown in Fig. 11.7a [6]. A microcapillary tube with a square cross-section measuring 1 mm \times 1 mm is placed between two permanent neodymium magnets (NdFeB) in a configuration where like poles face each other. This configuration allows the magnets to exert magnetic forces on the objects that oppose the buoyancy forces, resulting in the levitation of the objects at a height that depends on their density. To induce strong magnetic forces on the objects, high-grade (N52) NdFeB

Fig. 11.6 Photographs of four different Merrifield resins with different amounts of chloromethyl functionality separated in the MagLev-based separation system. Reproduced with permission from Ref. [1]. Copyright 2007 American Chemical Society



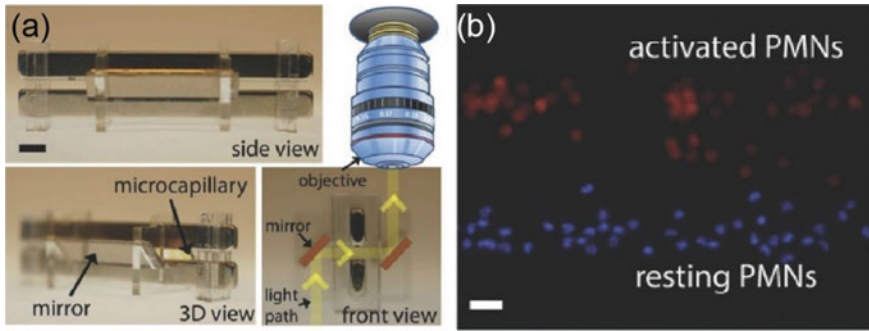


Fig. 11.7 **a** Front, 3D, and side views of the MagLev-based cell separation system. **b** Low-magnification fluorescence image of magnetically separated PMNs. Scale bar, 40 μm . Reproduced with permission from Ref. [6]. Copyright 2015 Wiley

magnets are chosen and positioned close to each other (1 mm apart). Two mirrors coated with gold are placed at each open side of the microcapillary at a 45° angle, creating a device that is compatible with conventional microscopy systems for high-resolution and spatiotemporal monitoring of cells during levitation. This proposed MagLev-based separation device with high length–width ratio has attracted great attention since its introduction and has achieved many accomplishments in the field of cell detection and separation.

Three typical separations are introduced here: (i) Separation between the active and resting phagocytes (PMN) [6], as shown in Fig. 11.7b; (ii) Separation between the anti-CR1 antibody-coated bead and red blood cell (RBC) complexes [7]; (iii) Separation between the live and dead yeast cells [8].

PMN can selectively bind and internalize foreign microorganisms or particles. Phagocytosis leads to the generation of reactive oxygen species (ROS) and the activation of ROS-mediated hydrolytic enzymes. The production of ROS and reactive nitrogen species (RNS) can cause changes in the magnetic characteristics of phagocytes. The dynamic interaction between internalization and exocytosis during phagocytosis directly affects the volumetric mass density, which shows more significant effect on the separation performance than the transient increase in magnetic properties. To investigate the impact of cell activation on suspension height and cell morphology, freshly isolated PMN were incubated with phorbol myristate acetate (PMA) (10×10^{-9} M) for 10 min. As a control, PMN were left undisturbed in a buffer for 10 min. Subsequently, the cells were washed, fluorescently labeled, mixed together, and loaded into the magnetic suspension device. As a result, the height of suspended activated cells was higher than that of the control group.

CR1 (CD35), a unique human protein, is expressed on circulating red blood cells (RBC) in a genetically determined manner. The individual expression levels of CR1 on RBC can vary, with some cells expressing 90 copies, while others can express either 500 or 1200 copies of CR1 per RBC [7]. The interaction of anti-CD35-beads and RBCs will cause a significant change in densities and the levitation heights. This

approach offers several advantages. Firstly, it eliminates the need for background subtraction operations, simplifying the process. Additionally, it yields results rapidly, with a turnaround time of as little as five minutes. Furthermore, by incorporating capture beads of various colors, shapes, or densities, this approach can be multiplexed to simultaneously analyze a blood sample for multiple viruses or both soluble and membrane-bound antigens.

The platform was also employed to separate cells with/without drug treatment through the difference in levitation height caused by changes in cell activity [8]. Upon drug treatment live and dead microorganisms have distinct density signatures. Hence, changes in cellular levitation height and density are correlated with the efficacy of a drug treatment. There is significant need for point-of-care tools to distinguish resistant strains from nonresistant strains, especially for slow-growing species. Thus, this platform has the potential to rapidly test the efficacy of antimicrobial treatments and it can be used for antimicrobial susceptibility testing.

11.3.3 Separation Based on Shape

The MagLev separation method based the shape, primarily employed in microfluidic devices, relies on the significant changes in particles trajectories through alterations in hydrodynamic drag induced by their shapes. The schematic diagram in Fig. 11.8a illustrates a prototype of a microfluidic separation device. In this device, non-magnetic particles are mixed with a water-based ferrofluid (EMG 408) and introduced into a microfluidic channel [9]. The flow of the ferrofluid sheath layer enables fluidic focusing within the channel. Once the non-magnetic particles enter the separation region, they undergo deviation from their original channel path due to the influence of an inhomogeneous magnetic field and magnetic buoyancy. Notably, larger particles experience a stronger magnetic force as the magnetic buoyancy is directly proportional to particle volume. Conversely, fluidic drag is proportional to the particle diameter. Consequently, larger particles are more susceptible to deviation compared to their smaller counterparts. Exploiting this phenomenon, continuous separation of non-magnetic particles/cells from the ferrofluid based on size becomes feasible [10].

Particle and cell shape is a crucial characteristic that can provide valuable information for applications such as cell synchronization and disease diagnostics. To achieve shape-based separation, two approaches have been utilized: hydrodynamic filtration [11] in a complex network of microchannels [12], and deterministic lateral displacement in a high-resolution array of posts [13, 14]. It can be concluded that the variation in the shape of particles leads to discrepancies in hydrodynamic drag forces experienced during flow within the streams. A continuous-flow separation method of equal-volumed spherical and peanut-shaped diamagnetic particles is developed [15]. When the flow rate is set at 120 $\mu\text{l/h}$, it is observed that spherical particles are capable of reaching the sidewall, approaching it closely in proximity. In contrast, peanut-shaped particles are only able to reach about a quarter of the channel width.

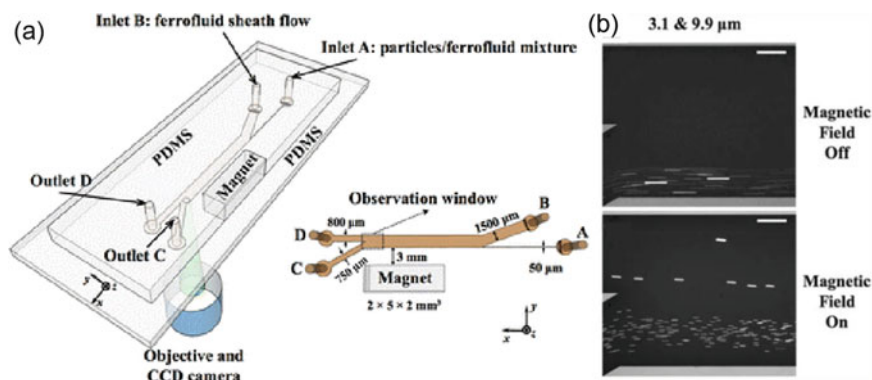


Fig. 11.8 **a** Schematic representation of the separation setup. **b** Fluorescent images of 3.1 and 9.9 μm particles mixture motions with/without magnetic field. Scale bar, 300 μm . Reproduced with permission from Ref. [9]. Copyright 2010 Springer Nature

As a consequence, evident from the overlay images, a distinct gap emerges between the sub-streams of the two particle types. Upon further increase in the flow rate, the residence time of both particle types within the main branch diminishes. This reduction has a dual effect—not only does it decrease the absolute displacement experienced by the particles, but it also leads to a decrease in their relative displacement. Furthermore, as a consequence of the velocity gradient induced by the flow, particles begin to disperse in the depth direction of the channel, as it is important to note that the sheath fluid solely concentrates the particles in the width direction of the channel. Consequently, with the augmentation of the flow rate, the span of each particle sub-stream progressively expands.

11.4 Separation Using Magnetic Projection

Inspired by the principles of magnetic levitation, a novel magnetic separation method called magnetic projection separation that aims at separating multiple mixed particles without strict restrictions on the particle sizes has been proposed. This method is based on a simple structure: a container filled with paramagnetic media placed adjacent to a permanent magnet. Under the action of diamagnetic force, particles of different densities follow different trajectories and eventually land in separate collection areas. This method is primarily applied to the separation of mixed plastics, aiming to overcome the limitations of existing plastic separation methods that can only separate binary mixtures. Different from the typical two-magnets configuration of magnetic levitation, magnetic projection method is firstly introduced based on a novel configuration: a single permanent magnet is placed beside the container that full of static paramagnetic solution [2]. The magnetic force is no longer employed for levitation, but is exploited to project the diamagnetic objects, i.e., the particles to

be separated, in the solution to desirable landing zones. Magnetic projection method has no requirement for the stream to take away the levitated particles in microfluidic separation system. Instead, the particles fall freely into the designed separation zones in a static liquid medium under the combined effect of magnetic force, hydrodynamic drag force, and gravitational/buoyant forces. As illustrated in Fig. 11.9a, the magnetic projection device, which was initially proposed, utilizes a rectangular magnet with poles positioned along the gravitational axis. The free-falling samples are initially positioned at the point nearest to the magnet on the upper surface of the magnet, where the magnetic field can generate sufficient forces to create distinct discrepancies in the landing position (dotted line). Three baffles divided the collection part into four cubicles: cubicle 1 for collecting polyvinyl chloride (PVC, density $1.54 \pm 0.01 \text{ g/cm}^3$, blue); cubicle 2 for collecting polyethylene terephthalate (PET, density $1.34 \pm 0.01 \text{ g/cm}^3$, red); cubicle 3 for collecting polycarbonate (PC, density $1.22 \pm 0.01 \text{ g/cm}^3$, green); cubicle 4 for collecting polymethyl methacrylate (PMMA, density $1.18 \pm 0.01 \text{ g/cm}^3$, yellow). The experimental results of multiple particles separation are shown in Fig. 11.9b. 1.5 M MnCl_2 was used as paramagnetic solution, its density and the magnetic susceptibility are 1.148 g/m^3 and 5.48×10^{-4} , respectively. The purities of PVC, PET, PC and PMMA reached 100 wt%, 98.1 wt%, 96.2 wt% and 95.9 wt%, respectively, as shown in Fig. 11.9c. The results provide confirmation that magnetic projection can be effectively utilized for the separation of multiple mixed plastics. The experimental findings demonstrate the successful separation of multiple mixed particles using the proposed method, which does not require an energy supply, reagent input, or impose size restrictions. This method shows promise in addressing the problem of waste plastics.

The magnetic projection device depicted in Fig. 11.9 has a key limitation, which is the requirement for denser samples compared to the paramagnetic solution in order to achieve a free-falling trajectory. In order to generate a substantial lateral magnetic force to facilitate projection and maximize the utilization of upwelling and sinking regions for the separation of a diverse array of samples, a novel enhancement has been implemented in the design of the magnetic projection separation device. Specifically, the orientation of the magnet's magnetic poles has been adjusted to be perpendicular to the direction of gravity, while the initial release point of the sample is precisely positioned at the central surface of the magnetic pole, as shown in Fig. 11.10a. Additionally, a mathematical model specifically tailored for magnetic projection is not provided, thus relying entirely on simulations to calculate the collecting zones. Furthermore, the current approach limits the projection of samples solely in a downward direction, thereby restricting its processing capacity. As a result, the determination of particle landing zones necessitates repeated experimental trials, ultimately impeding its potential for commercialization. Therefore, dynamics model for moving trajectory is proposed as follows:

$$m \frac{d^2x}{dt^2} = F_{\text{mag},x} - F_{v,x} \quad (11.4a)$$

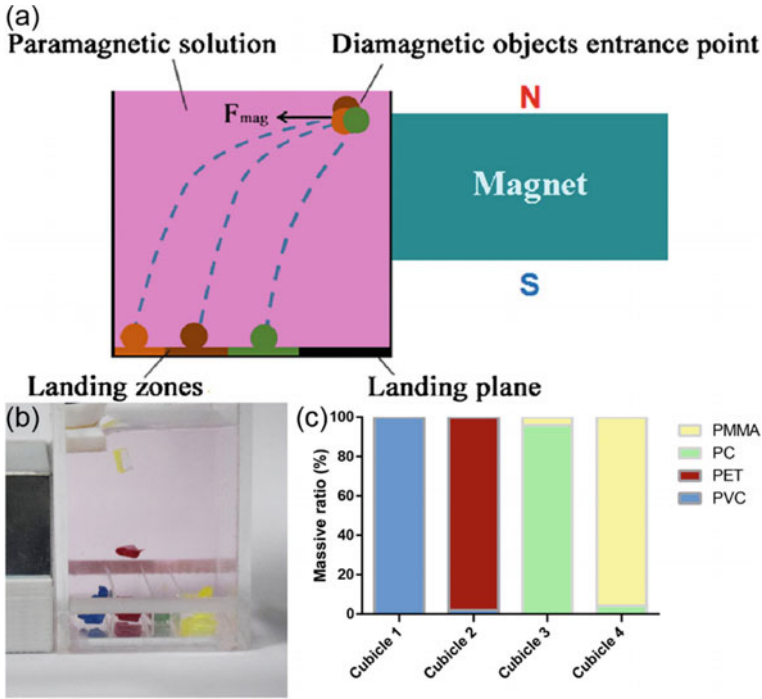


Fig. 11.9 a Schematic representation of the magnetic projection separation method. b Photographs depicting the separation experiments conducted on PVC, PET, PC, and PMMA materials. c Results displaying the successful separation of four mixed plastic samples. Reproduced with permission from Ref. [2]. Copyright 2019 Elsevier

$$m \frac{d^2z}{dt^2} = F_b + F_{mag,z} + F_{v,z} - F_g \tag{11.4b}$$

where, m is the mass of the sample, $F_{mag,x}$ denotes the magnetic force along the x axis, and $F_{v,x}$ represents the drag force, F_b is the buoyancy force, F_g is the gravitational force, $F_{mag,z}$ is the magnetic force along the z axis, $F_{v,z}$ is the drag force.

The magnetic force acting on the sample can be calculated through the spatial magnetic field distribution formula for a rectangular magnet [16]. To obtain precise trajectory of sample, Eq. 11.4 and an empirical formula for drag coefficient C_D (Eq. 11.5) are employed to calculate the hydrodynamic drag forces [3].

$$C_D = \frac{24}{Re} [1 + 8.1716 * e^{-4.0655\psi}] Re^{0.0964+0.5565\psi} + \frac{73.69Re * e^{-5.0748\psi}}{Re + 5.378 * e^{6.2122\psi}} \tag{11.5}$$

where, $\psi = Se/Ss$ denotes the sphericity of the object (Fig. 11.10b).

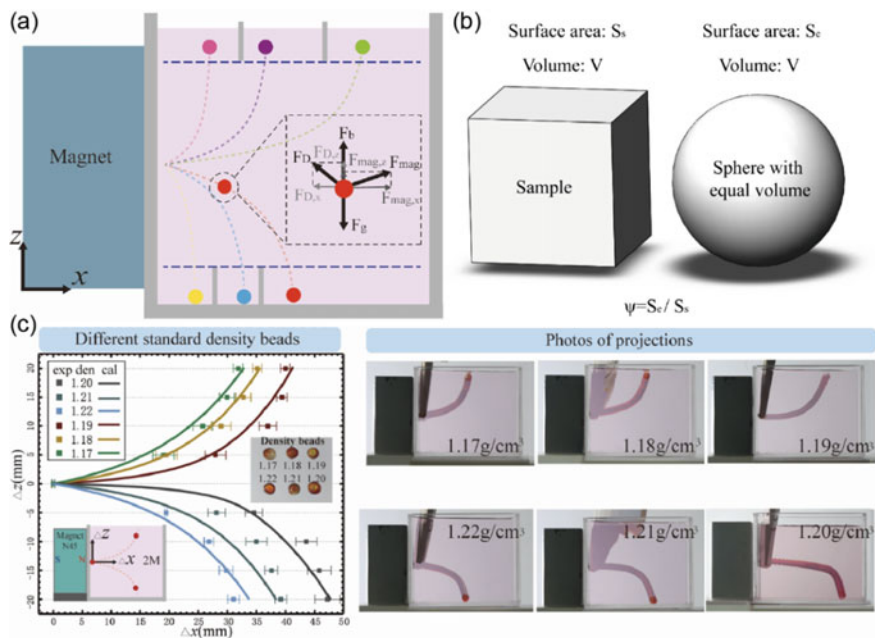


Fig. 11.10 **a** Schematic of bidirectional magnetic projection device. **b** Calculation of sphericity (ψ). **c** Test results and trajectories for the samples of different densities. Reproduced with permission from Ref. [17]. Copyright 2020 American Chemical Society

This model takes into account various parameters, including the object's size, density, and sphericity, as well as the magnetic susceptibility, density, and viscosity of the paramagnetic medium. Additionally, the size and strength of the magnetic source are also considered. Experimental results also exhibit great consistence between the theoretical and experimental trajectories, as shown in Fig. 11.10c.

According to the proposed mathematical model, the relatively low recovery rates of polyvinyl chloride (PVC) and polyethylene terephthalate (PET) in the separation of simulated plastic waste using a 2.2 M $MnCl_2$ aqueous solution can be attributed to the minimal density difference between them, which is only 0.04 g/cm^3 . Upon observing Fig. 11.11a, it becomes apparent that the heavier particles, namely polytetrafluoroethylene (PTFE), PVC, and PET, are not adequately separated. However, these materials still achieved high recovery rates, exceeding 95% by weight as shown in Fig. 11.11b. This validates the effectiveness of bidirectional magnetic projection in separating multiple mixtures. By utilizing the proposed mathematical model, the collection zones can be precisely designed, resulting in high recovery rates even for materials with slight density variations. It should be noted that the separation of PTFE, PVC, and PET would be particularly noticeable in larger containers, making them suitable for commercialized bidirectional magnetic projection. In such cases,

the recovery rates of multiple mixtures could surpass those observed in this experiment, highlighting the significant commercial potential of this approach. Additionally, the inability to separate polypropylene (PP) and acrylonitrile–butadiene–styrene (ABS) is attributed to the significant density discrepancies between the paramagnetic medium, which is a 2.2 M MnCl_2 aqueous solution with a density of 1.216 g/cm^3 , and the two types of plastics. This is due to the decreasing sensitivity of bidirectional magnetic projection with an increasing difference between ρ_s and ρ_m (as depicted in Fig. 11.11c).

The advantages of one-step separation include higher efficiency, lower costs, and the potential for advanced processing capabilities. However, the maneuverability and automation of magnetic projection still remain as major bottlenecks due to the difficulties in achieving automatic feeding and consistent release positions that align with square magnets. Therefore, a groundbreaking approach that utilizes ring magnets for automatic magnetic projection is developed in order to improve the manipulability of

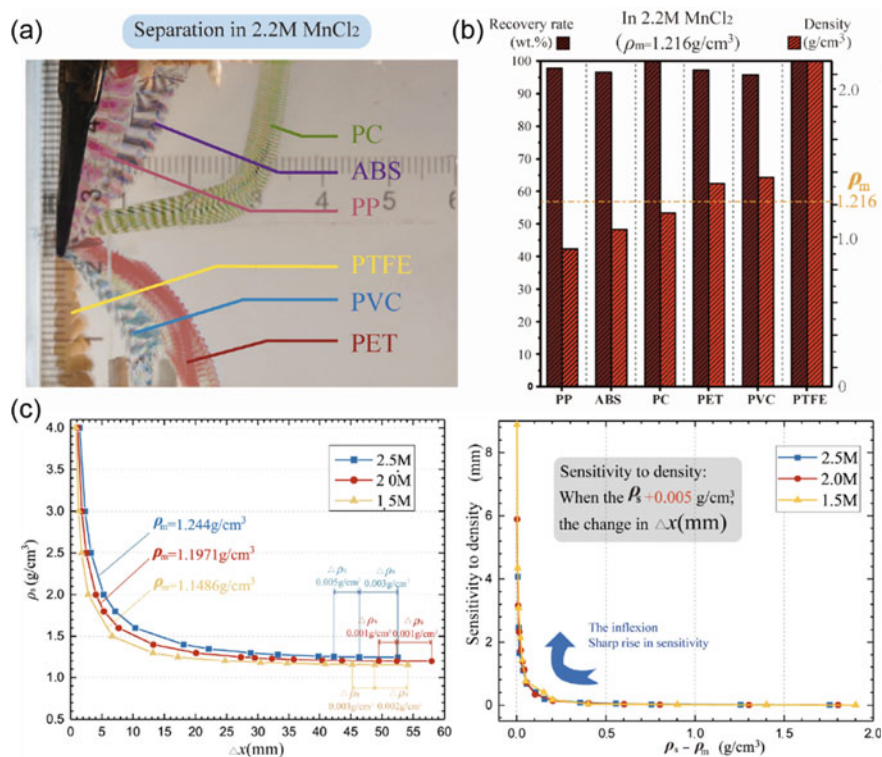


Fig. 11.11 **a** The synthesized photo of separating the simulated plastic wastes in 2.2 M MnCl_2 . **b** The results of the separation of the simulated plastic wastes in 2.2 M MnCl_2 . **c** Change in Δx (defined as density-related sensitivity) against the densities of samples in bidirectional magnetic projection (left), and density-related sensitivity against the differences between ρ_s and ρ_m (right). Reproduced with permission from Ref. [17]. Copyright 2020 American Chemical Society

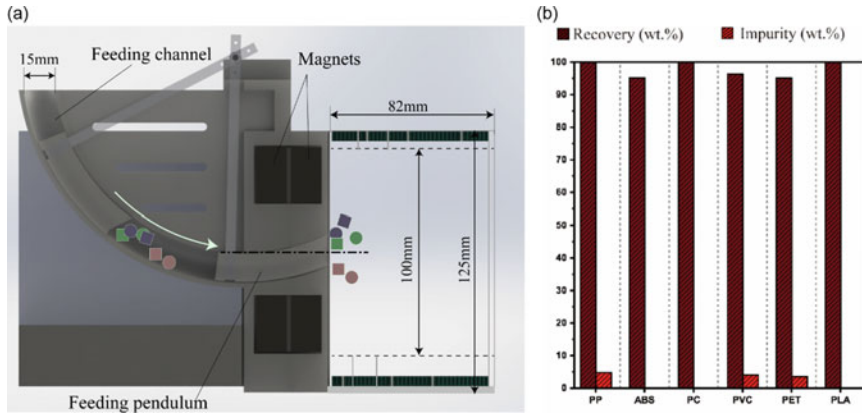


Fig. 11.12 **a** Automatic magnetic projection device—cross section. **b** Recovery and impurity results of the separation process. Reproduced with permission from Ref. [18]. Copyright 2021 Elsevier

the separation process and enhance its potential in industrial waste management, as shown in Fig. 11.12a [18]. One limitation of ring magnets is their reduced magnetic field strength due to the presence of a hole in the center. To overcome this challenge, magnet stacking is applied to increase the magnetic field strength. Through extensive simulations, the trapping area which limits growth of the projection distance of the stacked magnets is determined. Moving forward, a specialized experimental setup is optimized based on the simulation results. This apparatus facilitated the implementation of separation experiments involving various plastic mixtures to evaluate the efficiency of the proposed automatic magnetic projection technique. Six common types of plastics, namely polypropylene (PP), acrylonitrile butadiene styrene (ABS), polycarbonate (PC), polyvinyl chloride (PVC), polyethylene terephthalate (PET), and polylactide (PLA), are chosen to represent diverse plastic mixtures encountered in waste management scenarios, as shown in Fig. 11.12b. Notably, PLA is a polymer that gained increasing popularity as an alternative to non-biodegradable plastics and is widespread used in industry and academia. PLA is often intermixed with other recyclable materials in waste management operations, yet there is limited research on its separation process. Hence, investigating its potential for separation was an important aspect of the magnetic projection separation method. The global production and demand for plastics when selecting the other five types. These choices were based on the fact that these plastics collectively account for approximately 40% of the total global production and demand. The outcomes of separation experiments are highly promising, as a remarkable recovery rate of over 95% for all the tested materials is achieved. This result underlines the effectiveness of automatic magnetic projection as a viable method for plastic separation in waste management processes. Furthermore, this automatic magnetic projection system highlights the potential for using MagLev-based separation method to promote recycling and resource recovery.

References

1. Winkleman A, Perez-Castillejos R, Gudiksen KL, et al. Density-based diamagnetic separation: devices for detecting binding events and for collecting unlabeled diamagnetic particles in paramagnetic solutions. *Anal Chem.* 2007;79(17):6542–50.
2. Zhang X, Gu F, Xie J, et al. Magnetic projection: a novel separation method and its first application on separating mixed plastics. *Waste Manage.* 2019;87:805–13.
3. Haider A, Levenspiel O. Drag coefficient and terminal velocity of spherical and nonspherical particles. *Powder Technol.* 1989;58(1):63–70.
4. Liang L, Zhang C, Xuan X. Enhanced separation of magnetic and diamagnetic particles in a dilute ferrofluid. *Appl Phys Lett.* 2013;102(23).
5. Andres U. *Magneto-hydrodynamic and magneto-hydrostatic methods of mineral separation.* Wiley; 1976.
6. Tasoglu S, Khoory JA, Tekin HC, et al. Levitational image cytometry with temporal resolution. *Adv Mater.* 2015;27(26):3901–8.
7. Cockburn IA, Rowe JA. Erythrocyte complement receptor 1 (CR1) expression level is not associated with polymorphisms in the promoter or 3' untranslated regions of the CR1 gene. *Int J Immunogenet.* 2006;33(1):17–20.
8. Durmus NG, Tekin HC, Guven S, et al. Magnetic levitation of single cells. *Proc Natl Acad Sci.* 2015;112(28):3661–8.
9. Zhu T, Marrero F, Mao L. Continuous separation of non-magnetic particles inside ferrofluids. *Microfluid Nanofluid.* 2010;9:1003–9.
10. Zhao W, Zhu T, Cheng R, et al. Label-free and continuous-flow ferrohydrodynamic separation of HeLa cells and blood cells in biocompatible ferrofluids. *Adv Func Mater.* 2016;26(22):3990–8.
11. Yamada M, Seki M. Microfluidic particle sorter employing flow splitting and recombining. *Anal Chem.* 2006;78(4):1357–62.
12. Sugaya S, Yamada M, Seki M. Observation of nonspherical particle behaviors for continuous shape-based separation using hydrodynamic filtration. *Biomicrofluidics.* 2011;5(2):024103.
13. Beech JP, Holm SH, Adolffson K, et al. Sorting cells by size, shape and deformability. *Lab Chip.* 2012;12(6):1048–51.
14. Zeming KK, Ranjan S, Zhang Y. Rotational separation of non-spherical bioparticles using I-shaped pillar arrays in a microfluidic device. *Nat Commun.* 2013;4(1):1625.
15. Zhou Y, Xuan X. Diamagnetic particle separation by shape in ferrofluids. *Appl Phys Lett.* 2016;109(10):102405.
16. Xiao-Fan G, Yong Y, Xiao-Jing Z. Analytic expression of magnetic field distribution of rectangular permanent magnets. *Appl Math Mech.* 2004;25:297–306.
17. Zhao P, Zhang X, Gu F, et al. Bidirectional magnetic projection: one-step separation for recycling mixed wastes. *ACS Sustain Chem Eng.* 2020;8(29):10774–85.
18. Zhang X, Zhang W, Xie J, et al. Automatic magnetic projection for one-step separation of mixed plastics using ring magnets. *Sci Total Environ.* 2021;786:147217.